Confidential

Experimental and Numerical Investigations on Excimer Laser Lithography in Various Environmental Conditions

By

James Jacob M

ENGG01201304022

Bhabha Atomic Research Centre, Mumbai

A thesis submitted to the

Board of Studies in Engineering Sciences

In partial fulfilment of the requirements

For the degree of

Doctor of Philosophy

of

HOMI BHABHA NATIONAL INSTITUTE

November , 2019

Homi Bhabha National Institute

Recommendations of the Viva Voce Committee

As members of the Viva Voce Committee, we recommend that the dissertation prepared by James Jacob M entitled "Experimental and Numerical Investigations on Excimer Laser Lithography in Various Environmental Conditions" may be accepted as fulfilling the thesis requirement for the award of Degree of Doctor of Philosophy.

Chairman - Dr. B. K. Dutta		Date: 21.02.2020
Guide - Dr. Ramesh K. Singh		Date: 21/02/20
Co-Guide/Convener - Dr. R. Balasubramaniam		Date: 21/2/2020
Examiner - Prof. Suhas Joshi , IIT Bombay		Date: 21.02.2020.
Technology Advisor - Shri. P. Shanmugavelu		Date: 21-02-2020
Member 1 - Dr. J. Chattopadhyay		Date: 21/2/2020.
Member 2 - Dr. T. A. Dwarakanath		Date: 21/02/2020.
Member 3 - Dr. Imran Ali Khan		Date: 21/2/2020

Final approval and acceptance of this dissertation is contingent upon the candidate's submission of the final copies of the dissertation to HBNI.

I hereby certify that I have read this thesis prepared under my direction and recommend that it may be accepted as fulfilling the thesis requirement.

Date: 21.2.2020

Place: Mumbai

(Dr. R. Balasubramaniam)
Co-Guide

(Dr. Ramesh K. Singh)
Guide

STATEMENT BY AUTHOR

This dissertation has been submitted in partial fulfilment of requirements for an advanced degree at Homi Bhabha National Institute (HBNI) and is deposited in the library to be made available to borrowers under rules of the HBNI.

Brief quotations from this dissertation are allowable without special permission, provided that accurate acknowledgement of source is made. Requests for permission for extended quotation from or reproduction of this manuscript in whole or in part may be granted by the Competent Authority of HBNI when in his or her judgment the proposed use of the material is in the interests of scholarship. In all other instances, however, permission must be obtained from the author.

James Jacob M

DECLARATION

I, hereby declare that the investigation presented in this thesis entitled "***Experimental and Numerical Investigations on Excimer Laser Lithography in Various Environmental Conditions"*** has been carried out by me. The work is original and has not been submitted earlier as a whole or in part for a degree / diploma at this or any other Institution / University.

James Jacob M

List of Publications arising from the thesis

Journal

1. James Jacob M, P. Shanmugavelu, R. Balasubramaniam, 'Investigation of the performance of 248 nm Excimer Laser Assisted Photoresist Removal Process in Gaseous Media by Response Surface Methodology and Artificial Neural Network', Manufacturing Processes, Elsevier, 2018, Vol. 49, Page: 122-135. IF:2.237

2. James Jacob M, P Shanmugavelu, R. Balasubramaniam, Ramesh K Singh, 'Study of Excimer Laser Ablation of Photo Resist Polymer in Presence of Hydrogen Gas Environment for Micro-fluidic Applications', IOP Publishing, Material Research Express 6 (2019) 085316

Journal (Communicated)

1. James Jacob M, P Shanmugavelu, Ramesh K Singh, R. Balasubramaniam, 'A comparative Study of Different Regression Models for Etch Depth Prediction during KrF Excimer Laser Ablation of Photoresist in Hydrogen gas medium' under review for publication in " The International Journal of Advanced Manufacturing Technology"

Book Chapter

1. James Jacob M, P Shanmugavelu, Ramesh K Singh, R. Balasubramaniam, Contributed one chapter titled 'Excimer Laser Micromachining and its Applications' to a book titled 'Laser material Processing' published by Springer, 2015

Conferences

1. James Jacob M, P Shanmugavelu, R. Balasubramaniam, Ramesh K Singh, 'Study and Analysis of Thermal Effects during the Excimer Laser Ablation of Polymers in Different Gaseous Environment, International Conference AIMTDR 2014 which was held in IIT Guwahati during 12th-14th December, 2014

2. James Jacob M, P Shanmugavelu, Ramesh K Singh, R. Balasubramaniam, 'Development of gas assisted excimer laser based polymer resist removal process', International Conference COPEN, December, 2015

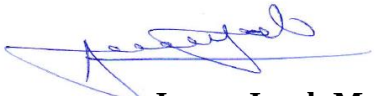

James Jacob M

DEDICATION

To my Lord and my God Jesus Christ

to whom

I owe everything

ACKNOWLEDGEMENTS

I would like to express my sincere gratitude to my guide Prof. Ramesh K. Singh, Indian Institute of Technology Bombay Mumbai, for his invaluable guidance, critical comments encouragement and loving concern during the course of this work. It was an enriching experience learning the theoretical aspects of Laser Materials processing from my guide as part of my course work at IITB, for which I will ever remain grateful. It was indeed a wonderful experience, sitting in a classroom in this institute during one's early fifties, with fellow post graduate / PhD students who are mostly in their twenties.

I am extremely obliged to Dr. R. Balasubramaniam, my Co-Guide from BARC for the motivation, guidance and support that he has provided during the course of this research work. He has always given critical and constructive comments holding me to a higher standard, which helped in improving the quality of the thesis and meeting my research targets in a timely manner. His constant encouragement and comments have enabled me to focus on key issues related to this research work. Above all he has been a very fine human being.

I greatly acknowledge the contributions of my doctoral committee members Prof. B. K. Dutta, Prof. J. Chattopadhyay, Prof. T. A. Dwarakanath and Prof. I. A. Khan who spared their valuable time for periodical critical assessment of my work. Their constructive suggestions have greatly enhanced the quality level of my Ph.D. work.

The present research work on 'Experimental and Numerical Investigations on Excimer Laser Lithography in Various Environmental Conditions' is truly in the multi-disciplinary domain. It would not have been possible to pursue such a work without the help of a true scientist in the field of Chemistry, in the person of Mr P. Shanmugavelu, my Technology Advisor and officer-in-Charge, Analytical Control Labs BARC. The numerous discussions on both the design of experiments and the analysis thereafter has enhanced the quality of the thesis and

timely completion of the work. I shall for ever be indebted to him for the help extended in conducting the chemical etching experiments in his Lab.

I am extremely thankful to Dr. V.K. Suri my colleague and former Head, Precision Engineering Division, BARC, who was the driving force behind my taking up this research work.

My gratitude goes to Prof. Suhas Joshi, currently the Dean, Indian Institute of Technology Bombay Mumbai, who was my teacher in the subject of Ultra Precision Machining. He has been a source of a great inspiration. His displayed focus on both academic and application aspects of the research was inspiring.

I would like to thank Dr. Prabhat Ranjan my younger colleague and classmate in the course of Ultra Precision Machining in a special way for his enthusiasm and active discussions in the areas of FEA modelling. I also thank Shri Tarun Dewangan, Dr. Tribeni, Dr. Anuj Sharma, Shri Karim and Shri Nagaraju for the useful discussion we had.

I greatly appreciate the help I received from Shri Praveen Vijaya Kumar in the areas of Data Driven Prediction Modelling work. I also appreciate the help received from ShriA R Rakesh, Shri Manoj and Shri K Shekhar during the writing of this Thesis.

My thanks are due to Prof. C D Sebastian and the number of friends in the IIT campus who made the life in the Institute really a wonderful one during the course work and even afterwards.

My sincere gratitude goes to my former senior colleagues and friends Dr. T K Bera, Shri S Sarkar, Shri M R Srikanthan and Shri A Nandakumar for providing me this opportunity to carry out this challenging task. I just can't forget my friends and colleagues Shri H A Balasubramanya, Shri Asokan, Shri V Sugadan, Shri Anto Kurian and Shri A S Patil who

were a constant source of encouragement. This work would not have been possible without the help of Shri Abhishek Singh, Shri Raghunath, Shri George Joseph, ShriD S Cyril, Shri Rajashekhara Biradar, ShriMadhukumar, ShriV S Vishwanathan, ShriM S Prabhakar, Shri Gopalakrishnan, Shri Adi Lakshmi Narayan, Shri Mariyappan and Shri Lalchand for their contribution in helping me develop this technology.

My thanks are also due to Shri Deepthi Kumar, Shri M T Manjunath, Shri R Murugan, Shri Nagaraju S, Shri S R Patil for some fruitful discussions during this research work.

I am deeply indebted to my parents, brothers and sisters, and my own family for their true blessings, especially my wife Minnie who has always been my steadfast strength and support. My children Jacob, Tina, Titus and Riya stood by me in this testing phase of my life even at the cost of a lot of things which were very dear to them.

I have received both direct and indirect support from BARC, not the least of which is providing me this opportunity.

There are many others who helped / contributed to this work, that I have not named here, but I am grateful to all of them.

James Jacob M

CONTENTS

Synopsis v

List of Figures viii

List of Tables xiii

List of Symbols xv

List of Abbreviations xvi

Chapter 1 1

Introduction 1

1.1 Relevance and Motivation of Work 1

1.2 Problem Definition 5

1.3 Objective of the Present Research Work 6

1.4 Organization of the Thesis 9

Chapter 2 12

Literature Survey and Gap Areas 12

2.1 Micromachining Process 12

2.2 LASER 13

2.3 Excimer Laser 16

2.4 Laser Ablation Process 20

2.5 Laser Machining Techniques 26

2.6 Review of Laser Machining Applications 28

2.7 Data Driven Predictive Models 34

2.8 Photochemical Machining 35

2.9 Effect of PCM Parameters on Machining 37

2.10 Gap Areas 43

2.11 Scope of Work 44

Chapter 3 46

Experimental Study of Excimer Laser Ablation under Different Gaseous Environments 46

3.1 Introduction 46

3.2 Experimental Setup 47

3.3 Results and Discussion 66

3.4 Summary 73

Chapter 4 74

Experimental Study of Excimer Laser Ablation of Photoresist Polymer in Hydrogen Media 74

4.1 Experiments to Study Effects of Laser Ablation under Hydrogen Gas Environment 74

4.2 Proposed Mechanism for Photoresist Removal by Laser in Hydrogen Gas Media ... 82

4.3 Result and Discussion 84

4.4 Summary 86

Chapter 5 87

Mathematical Modelling of Laser Ablation Process and FEA Simulation 87

5.1 Interaction of Laser Beam with Polymer Material 87

5.2 The Role of Atomic Hydrogen in Enhancing Removal Rate of Photoresist 90

5.3 Computation of the Surface Temperature 92

5.4 FEA simulation 94

5.5 Experimental Study 97

5.6 Results and Discussion 103

5.7 Summary 106

Chapter 6 108

Data Driven Prediction Models for Ablated Depth 108

6.1 Introduction 108

6.2 Linear Regression 110

6.3 Gaussian Process Regression(GPR) 114

6.4 Cubic SVM 120

6.5 ANN 127

6.6 Response Surface Methodology 130

6.7 Comparison of Prediction Results 133

6.8 Summary 140

Chapter 7 141

Experimental Study of Chemical Etching 141

7.1 Introduction 141

7.2 Experimental Procedure 143

7.3 Preliminary Etching Studies in ‘macro scale’ 152

7.4 Study of Chemical Kinetics 158

7.5 Surface Roughness Characteristics 161

7.6 Effect of Excimer Laser Machining on the Depth of Chemically Etched Surface .. 170

7.7 Manufacturing of SSGB 174

7.8 Optimization of Chemical Etching Process 176

7.9 Outcome of Research work in Chemical Etching 198

7.10 Testing with Modified Process 204

7.11 Summary 207

Chapter 8 208

Conclusions 208

8.1 Scientific Contributions of Present Research 209

8.2 Future Scope of Work 210

References 211

Synopsis

This thesis work aims towards improving the performance of Spherical Spiral Groove Bearing (SSGB) by developing a hybrid-manufacturing process which can attain more than 90% functional acceptance. The SSGB is manufactured in three major stages involving diamond turning operation followed by excimer laser lithography for generation of 3D micro grooves and Chemical Micro Machining (CMM). In general, excimer laser micromachining is carried out under normal atmospheric conditions without the use of any assisting gases. The present study is focused to explore the enhancement of laser micromachining rates. Hence bringing down the operating cost of the process, and also the edge definition of micro machined feature by changing the gaseous environmental conditions under which laser ablation is carried out. Further, the chemical micromachining technique is optimised to generate a desired microgroove depth with minimum surface roughness value. The research is thus aimed at developing a hybrid manufacturing process, with consistent functional acceptance, to generate micro-grooves on hemispherical cavity surface on large numbers of Cu-Be alloy components for deployment in the strategic application areas of Department of Atomic Energy (DAE).

Based on a detailed literature survey it was found out that there is a need for in-depth scientific understanding and detailed investigations in the field of excimer laser lithography under different gaseous environment and also chemical etching of DTM machined parts made of Cu-Be alloy. An Excimer laser ablation system comprising of KrF laser source of Coherent make and Beam Delivery unit CNC controlled X-Y table with pulse energy monitor were used for experimental studies. A gas handling setup was fabricated for admitting gas at a predefined flow rate over the surface of polymer during the laser ablation process. A total

number of 540 experiments were conducted involving five different gases by varying laser pulse energy, pulse repetition frequency and gas flow rate. Based on these experimental results under different gaseous media like air, nitrogen, argon helium and hydrogen, it was found that hydrogen gas showed remarkably superior performance in both the machining rate and edge definition of the machined feature, compared to other gases. This enhanced material removal could considerably bring down the operating cost of the laser micromachining system as the consumption of the costly pre-mix gas mixture would come down substantially, resulting in increased throughput per re-fill of the gas in the laser source. It was confirmed, based on extensive experiments carried out under hydrogen gas medium as well as under vacuum conditions that Laser Assisted Chemical Reaction (LACR) is happening under hydrogen gas medium, resulting in enhanced mass removal. The mathematical modelling work has been carried out on material removal phenomena during a single pulse of excimer laser irradiation. Subsequently, the total material removal or the ablated mass in a given number of pulses is derived. The interaction between hydrogen and polymer molecules at the interface in presence of excimer laser results in the formation of nascent hydrogen due to the local heating which raises the temperature and thereby providing the required activation energy for LACR. To carry out the FEA simulation, COMSOL 4.3a software was used to couple multiple physics such as Heat transfer and Arbitrary Lagrangian-Eulerian (ALE) method. Subsequently suitable post processing on simulated data has been carried out to compute surface temperature, mass ablated and surface morphology. The simulated results have been validated with experimental data.

Five Data Driven Prediction Models, such as RSM, Linear Regression (LR), Gaussian Process Regression (GPR), Cubic Support Vector Machine Regression (Cubic SVM) and Artificial Neural Network (ANN) were employed to model the Laser Micromachining

process and their prediction capability for ablated depth. The predicted values were in good agreement with that of experimental data, within 10% variation for most of the cases.

The third stage of manufacturing process of SSGB is chemical micromachining which is carried out after laser lithography to produce micro features on metal. Etch rate as a function of time, concentration and temperature is establised from experimental results. The variation in surface roughness for different combination of etchant and metal was studied. It was observed that Cu-Be alloy is having better surface finish than Cu metal. A relationship of etchant temperature, concentration and time were obtained with MRR and surface roughness. Chemical surface composition of the chemically etched metal surface was studied by GDOES technique. It was found that Beryllium rich surface layer is formed on CuBe alloy after CMM, which offers a harder surface. Optimisation was achieved based on a full factorial experimentation on chemical etching of CuBe alloy using $FeCl_3$ etchant to get a desired micro-groove depth 7 lowest possible surface roughness value.

The major Scientific contributions of present research work done can be summarized as;

A new phenomenon of Laser Assisted Chemical Reaction (LACR) of polymer with hydrogen gas in presence of laser beam at the polymer hydrogen gas interface is observed to be the scientific reason behind the experimental observation of higher MRR.

A better surface roughness of the order of few hundred nanometres is experimentally obtained on Cu-Be material after chemical etching, after optimising the process parameters.

Direct Impact of this work on SSGB: A consistently enhanced performance value and increased acceptance rate of 98% was obtained by adopting the techniques developed by this research work.

List of Figures

Figure 1.1 Three Major Stages of the Manufacturing Process of SSGB 2

Figure 1.2 High Speed Rotating (HSR) Machines [3] 4

Figure 1.3 Spherical Spiral Groove Bearing used in HSR Machines 5

Figure 1.4 Methodology of Work 8

Figure 1.5 Schematic Representaion of Organitaion of Thesis 11

Figure 2.1 Classification of Micromachining Process 12

Figure 2.2 Photon Energy of Various Types of Laser Source 15

Figure 2.3 Schematics of the Excimer Laser Transition. The Exited State Lifetime is Around 5 ns, Whereas the Ground State is Dissociative. 18

Figure 2.4 Pictorial Representation of Interaction between Laser and Material [14]. 23

Figure 2.5 Principle of Direct Laser Writing with xy-Galvanometer Scan-head [16] 27

Figure 2.6 Principle of Mask Projection Technique [16] 28

Figure 2.7 SEM Micrograph of an Array of 50 µm Diameter Holes Percussion Drilled in PET, at 300 Hz and a Fluence of 3500 mJ/cm^2 [19] 29

Figure 2.8 SEM Images of Siemens stars Fabricated by Laser Ablation [26]. 30

Figure 2.9 Research Plan 45

Figure 3.1 Photograph Showing Different Components of Experimental Setup 47

Figure 3.2 Block Diagram of LASER Source 49

Figure 3.3 Block Diagram of LASER Control System 50

Figure 3.4 Excimer Laser Beam Delivery Unit 51

Figure 3.5 Schematic Representation of Experimental Setup 51

Figure 3.6 Gas Handling Setup used for Preliminary Ablation Experiments 53

Figure 3.7 Sectional View of Gas Purging and Ablation Product Extraction Assembly 54

Figure 3.8 Gas Handling Setup used for Detailed Ablation Experiments for Hydrogen 57

Figure 3.9 Helium Dectector 58

Figure 3.10 MSLD Setup 59

Figure 3.11 Vaccum Baking oven for Curing of Polymer Layer on Workpiece 62

Figure 3.12 Schematic Representation of Image Shown by Through the Laser Camera 64

Figure 3.13 Ablated Mass as a Function of Flow Rate 70

Figure 3.14 Variation of Ablation with Different Gas Media 70

Figure 3.15 Ablated Mass as a Function of Pulse Repetition Frequency 71

Figure 3.16 Ablated Mass as a Function of Laser Pulse Energy 71

Figure 3.17 Photographs of 5mm dia. Circular Pattern Ablated on the Photoresist Under Different Gaseous Media. 72

Figure 4.1 Variation of Ablation Rate with Laser Energy for Fixed H_2 Flow Rate (60 lph) ..75

Figure 4.2 Comparison of Mass ablated in H_2 and He media.....76

Figure 4.3 Comparison of Photoresist Removal in Vacuum (10^{-2} mbar) and Hydrogen Gas (400 mbar).....78

Figure 4.4 Ablated Surface (5mm diameter) under Hydrogen (Left) and Vacuum (Right) 79

Figure 4.5 Comparison of Photoresist Removal for 3000 Laser Shots in Vacuum (10^{-2} mbar) and Hydrogen gas (600 mbar).....79

Figure 4.6 Comparison of FTIR Spectrum of Experimental Photoresist with Vapor Phase Produced During Laser Irradiance in Vacuum and Hydrogen Gas Environments 81

Figure 4.7 Comparison of FTIR Spectrum of Vapour Phase Produced During Laser Irradiance of Experimental Photoresist in Vacuum and Hydrogen Gas Environments.....82

Figure 4.8 Showing Polymer-Gas Interaction Leading to Hydrogen Molecule Bond Breaking by π Electron Cloud of Polymer 83

Figure 4.9 Variation of Ablation Depth with Hydrogen Flow Rate 85

Figure 4.10 Variation of Ablation Depth with PRF of Laser 85

Figure 4.11 Variation of Ablation Depth with Laser Pulse Energy.....86

Figure 5.1 Schematic Potential Energy Diagram for a Hydrogen Molecule Approaching an Electron Rich Surface. 89

Figure 5.2 Schematic Diagram of Hydrogen Radical Generation Apparatus [106] 90

Figure 5.3 Homogenized LASER Beam Profile at the Work-Stage. (a) Energy Distribution in 3D for Experimental Work. (b) Energy Distribution in 2D for Experimental Work. (c) Energy Distribution in 3D for Simulation Work. (d) Energy Distribution in 2D for Simulation Work. 92

Figure 5.4 Infinitesimal Element Considered for Heat Balance 93

Figure 5.5 Temperature Variation with Time During Single Pulse of Ablation of Different Energy Level (Time axis is log Scale).....96

Figure 5.6 Temperature Variation with Time During Single Pulse of Ablation of Different Energy Level 97

Figure 5.7 Effect of Laser Ablation on the Morphological Aspect of the Photoresist Polymer for Different Energy Levels as well as Two Level of Gaseous Environment 101

Figure 5.8 Experimental Validation of the Material Removal Under Presence of Argon Gas as well as Hydrogen Gas with Varying Pulse Energy with 2000 Number of Pulses. 101

Figure 5.9 Surface Ablated under Hydrogen Gas 106

Figure 5.10 Surface Ablated under Argon Gas 106

Figure 6.1 Illustration of Trade-off between Training Complexity and the Number of Epochs 110

Figure 6.2 Deviation of Predicted Ablation Depth by LR from Experimental Data 113

Figure 6.3 Deviation of Predicted Ablation Depth by LR from Experimental Data 114

Figure 6.4 Deviation of Predicted Ablation Depth by GPR from Experimental Data 118

Figure 6.5 Deviation of Predicted Ablation Depth by GPR from Experimental Data 119

Figure 6.6 Epsilon Loss Function 121

Figure 6.7 Graphical Representation to Control Complexity 124

Figure 6.8 Epsilon Tube 125

Figure 6.9 Deviation of Predicted Ablation Depth by SVM from Experimental Data 126

Figure 6.10 Deviation of Predicted Ablation Depth by SVM from Experimental Data 127

Figure 6.11 Artificial Neural Network Training Structure. 128

Figure 6.12 Deviation of Predicted Ablation Depth by ANN from Experimental Data 130

Figure 6.13 Regression Graph of Actual and RSM Predicted Values for Validation Sets (R^2=0.96) 132

Figure 6.14 3-D Response Surface Plots on interaction effects of (a) energy and flow (b) energy and PRF (c) Flow and PRF on photoresist ablation depth in Excimer micro-machining in H_2 environment. 133

Figure 6.15 Comparison of Different Prediction Models with Experimental Data 135

Figure 6.16 Comparison of R^2 Value of Different Prediction Models 139

Figure 6.17 Comparison of RMSE Value of Different Prediction Models 140

Figure 7.1 Typical phototools for laser lithography (a) Mask for generating spiral grooves 145

Figure 7.2 Chemical Etching set-up 150

Figure 7.3 Chemical Etching Lab 152

Figure 7.4 Macro-scale Mass Removal Rate Variation with Time for Different Etchant Concentrations 153

Figure 7.5 Variation of etch rate with temperature 154

Figure 7.6 Comparison of etch rate of Cu and CuBe with $FeCl_3$ etchant with temperature from 40ºC to 70ºCin steps of 10°C and etching time from 5min to 30min in steps of 5min. 158

Figure 7.7 (a) Variation of logarithm of slope (reaction rate) with inverse of temperature in K for Cu and 2% Be-Cu alloy (CuBe) with $FeCl_3$ etchant 160

Figure 7.8 Definition of R_a value, the surface roughness parameter 162

Figure 7.9 (d) The variations of surface roughness with etch depth for CuBe alloy $CuCl_2$ ..165

Figure 7.10 Variation of Surface Roughness for Different Combination of Etchant and Metals 166

Figure 7.11 Typical roughness surface records of chemically etched surface of Cu and CuBe alloy (a to d) with $FeCl_3$ etchant carried out on FTS instrument 170

Figure 7.12 'Alicona' Images and Depth Profile after Chemical Etching of two Specimens 171

Figure 7.13 Surface Composition by GDOES 173

Figure 7.14 Manufacturing process flow sheet to produce micro grooves 174

Figure 7.15 Stages of Photochemical Machining 175

Figure 7.16 Experimental plans for Chemical etching 175

Figure 7.17 Profile Showing Relation of Responses with Independent Variables 180

Figure 7.18 Regression graph of actual and predicted values for etch depth and R_a.....182

Figure 7.19 Optimization profile for Design 1 with a target value of 25±2 µm etch depth with minimum possible R_a Value by RSM 183

Figure 7.20 Optimization profile for Design 2 with a target value of 30±2 µm etch depth with minimum possible R_a Value by RSM 184

Figure 7.21 Optimization profile for Design 3 with a target value of 35±2 µm etch depth with minimum possible R_a Value by RSM 184

Figure 7.22 Structure of Neural Network 186

Figure 7.23 Prediction graph of actual values and predicted values.....186

Figure 7.24 3D graphs showing the interaction effects of etching parameters on the dependent variables of etch depth and R_a value 187

Figure 7.25 Optimization profile for Design 1 with a target value of 25±2 µm etch depth with minimum possible R_a Value by ANN 188

Figure 7.26 Optimization profile for Design 2 with a target value of 30±2 µm etch depth with minimum possible R_a Value by ANN 188

Figure 7.27 Optimization profile for Design 3 with a target value of 35±2 μm etch depth with minimum possible R_a Value by ANN.....189

Figure 7.28 Experimental Validation Records for 'Design:1' of ANN.....192

Figure 7.29 Experimental validation records for 'Design:2' of ANN.....194

Figure 7.30 Experimental validation records for 'Design:3' of ANN.....196

Figure 7.31 SSGB Performance Test Setup to Measure the Deceleration Value.....205

Figure 7.32 Performance Indicators and their spread: Old and New Techniques.....206

List of Tables

Table 2.1 Bond dissociation energy 20

Table 3.1 Specification of Excimer laser system 48

Table 3.2 Technical Specifications of the MSLD Equipment 54

Table 3.3 Valves Description of Gas Handling Setup 56

Table 3.4 Thermal Conductivity of Different Gases 64

Table 3.5 Experimental Input Parameters 65

Table 3.6 Ablation Depth for 500 Laser Shots 67

Table 4.1 Experimental Input Parameters 75

Table 5.1 FEA Parameters to Simulate Material Removal during Laser Ablation 94

Table 5.2 Simulation Parameters 95

Table 5.3 Energy of Laser Beam at different Location in its Path 98

Table 5.4 Experimental Results of Material Removal Under Two Different Gaseous Environments with Varying Pulse Energy Level 104

Table 6.1 Parameters used in MATLAB Toolbox 117

Table 6.2 Parameters used in MATLAB Toolbox for SVM 125

Table 6.3 Experimental Data for Hydrogen Gas Medium Compared with Predicted Values of Predictive Regression Models 136

Table 6.4 Comparison of Accuracy of Different Prediction Models 139

Table 7.1 Composition of Wrought CuBe alloy as per ASTM Standard B194-15 (UNS number C17200) 143

Table 7.2 Comparison of Chemical Etchants used for CuBe Alloy 146

Table 7.3 Part List of Chemical Etching set-up 151

Table 7.4 Cu and CuBe Alloy Etching Rates while using $FeCl_3$ and $CuCl_2$ Etchants at Different Temperatures 156

Table 7.5 Experimental conditions and responses on etch depth and surface roughness for CuBe alloy 177

Table 7.6 Statistical Significance for Etch Depth 181

Table 7.7 Statistical Significance for R_a 181

Table 7.8 Achieved optimal parameters with respect to etchant concentration, temperature and etching time for 25±2 µm, 30±2 µm and 35±2 µm etch depth and minimum surface roughness by ANN Modelling 189

Table 7.9 Comparison of R^2 Values of RSM and ANN Models 190

Table 7.10 Comparision of Etch Depth (µm) Predicted by the ANN Model with Experimental Results 197

Table 7.11 Comparision of Surface Roughness (µm) Predicted by the ANN Model with Experimental Results 197

Table 7.12 Modifications Introduced in Manufacturng Process of SSGB 199

List of Symbols

Symbol	Description
A	Absorbance of Media
A_c	Absorbance Coefficient
l	Thickness of the Media
c	Media Concentration
I_o	Intensity of Incident Light
I_t	Intensity of Transmitted Light
T_r	Transmittance
F_T	Ablation Threshold Fluence
x	Etch Rate
α	Absorption Coefficient
F	Laser Fluence
η	Quantum Yield
hv	Photon Energy
R	Surface Reflection Loss
L_e	Thermal Penetration Depth
K	Thermal Diffusivity
t	Laser Pulse Width
C_p	Heat Capacity
k	Thermal Conductivity
ρ	Density
V	Etch Rate
E_A	Activation Energy
R_g	Universal Gas Constant
β	Attenuation Co-efficient of the Polymer
E_a	Activation Energy
Q_{in}	Heat Input
V_f	Velocity of Gas
T	Temperature

List of Abbreviations

Abbreviation	Full Form
PR	PhotoResist
SSGB	Spherical Spiral Groove Bearing
Cu	Copper
Be	Beryllium
HSR	High Speed Rotating
DAE	Department of Atomic Energy
FE	Finite Element
LR	Linear Regression
GPR	Gaussian Progress Regression
SVM	Support Vector Machines
ANN	Artificial Neural Network
RSM	Response Surface Methodology
LASER	Light Amplification by Stimulated Emission of Radiation
LUMO	Lowest Unoccupied Molecular Orbital
HOMO	Highest Occupied Molecular Orbital
UV	Ultra Violet
Kr	Krypton
F	Fluorine
DLW	Direct Laser Writing
MP	Mask Projection
HAZ	Heat Affected Zone
PCM	PhotoChemical Machining
PCB	Printed Circuit Board
EMM	Electrochemical MicroMachining
FFBPN	Feed Forward Back Propagation Network
GA	Genetic Algorithm
SA	Simulated Annealing
ACO	Ant Colony Algorithm

PSO	Particle Swarm Optimisation
WBS	Work Breakdown Structure
MMCs	Metal Matrix Composites
MRR	Material Removal Rate
WGRA	Weighted Grey Relational Analysis
ELM	Excimer Laser Micromachining
BDU	Beam Delivery Unit
MSLD	Mass Spectrometry Leak Detection
DDPMs	Data Driven Prediction Models
MDS	Molecular Dynamics Simulation
CI	Communication Interface
PT	PhotoThermal
LACR	Laser Assisted Chemical Reaction
NFPA	National Fire Protection Agency
GDOES	Glow Discharge Optical Emmision Spectrometer
SSE	Sum of Squared Error

Chapter 1
Introduction

1.1 Relevance and Motivation of Work

Hydrodynamic bearings of the Pivot-Jewel configuration, is extensively used in ultra-high speed machines. These bearings have two components in which one forms the spherical-ended shaft and other comes with micro fluidic grooves etched into it. Functional acceptance of high speed rotating machines which uses these types of bearings, are highly dependent on the performance of these bearings. The bearing performance of this type of hydrodynamic bearings not only depends on the size, shape and form accuracies of both the components of the bearing pair, but also on the number of micro fluidic grooves, groove shape, its width, depth, surface finish and the edge quality of the grooves. These design parameters of the bearing are controlled by the stringent requirements in their manufacturing. Thus manufacturing of these micro fluidic channels are extremely important in the performance of such high precision, high speed machines.

In the present work Spherical Spiral Groove Bearing (SSGB) made of Cu-be alloy has been selected for the study. Currently, the SSGB is manufactured in three major stages, the first stage includes Diamond Turn Machining (DTM) operation of both male and female spherical components to achieve high precision. Then the second stage involves generation of 3D micro grooves on the hemispherical cavity of the female spherical component made of Cu-Be alloy using the Excimer Laser Micromachining (ELM). In this process the photo resist-polymer is coated on the metallic work piece and is cured before subjecting it to laser ablation by mask projection technique. In the third stage the component with ablated polymer is subjected to Chemical Micro-Machining (CMM) by chemical etching technique. Figure 1.1

gives a schematic outline of the entire process involved in manufacturing of spherical spiral grooved bearings used in the present thesis work. As the DTM process is well established and enough literature is available in the field, the present work is more focussed in the other two aspects involved in manufacturing of SSGB.

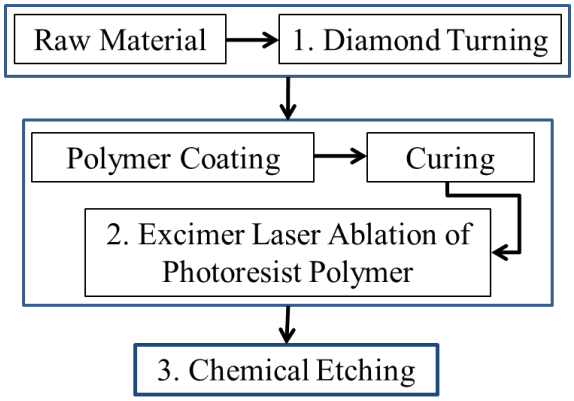

Figure 1.1 Three Major Stages of the Manufacturing Process of SSGB

The second manufacturing step of laser ablation process can easily affect the quality of microgrooves produced on the metallic work piece during the third manufacturing step of chemical micromachining. This can occur in the form various factors such as residuals of photo resist in the work piece, quality of edge definition obtained etc. The significant parameters of the chemically etched microgrooves viz. groove depth, definition of the groove edge, and the surface roughness, are significantly affected by, the pre-processing done by Excimer laser.

In the present age of technological advancements in engineering, electronics, MEMS and MOEMS and biomedical fields, there is requirement of precision parts in the micro-domain, made of different materials like Ferrous and non-Ferrous metals, glass, ceramics and polymers. The functional requirements and the type of raw materials often call for developing newer manufacturing techniques.

Conventional machining processes like turning, milling, drilling, grinding etc., are based on direct mechanical contact between the workpiece and tool. The direct mechanical contact poses problem of increase in temperature of the workpiece. Therefore conventional machining processes cause unwanted changes such as residual, thermal and mechanical stresses. This may lead to deterioration of the properties of the workpiece, which necessitate further processing to remove these problems. Hence there is inexorable need to develop new machining processes and improve present techniques which have a cost-effective ability while using special materials.

Non-conventional machining processes are commonly used to manufacture geometrically intricate [1] and precise parts from new materials in industries such as aerospace, electronics and automotive manufacturing [2]. There are numerous geometrically designed parts / features like deep internal cavities, miniaturized microfluidics, and microelectronics which can be produced by unconventional machining processes.

Microfluidic grooves find very wide application area especially in hydrodynamic bearings for high speed application. Microfluidics comes into an intermediate range within the spectrum of applications for microfabrication systems. The width and depth of most microfluidic channels is of the order of 10-1000 μm, and this feature size is quite difficult to manufacture by microfabrication based on conventional machine tools, but photo-lithographically defined etching processes is quite capable of generating such features especially on 3-D surfaces. Spherical Spiral Groove Bearing (SSGB) made of Cu - 2% Be is extensively used in High Speed Rotating (HSR) machines shown in Figure 1.2 [3]. Figure 1.3 shows the SSGB used in HSR Machines. Functional acceptance of such machines is highly dependent on performance of SSGB. No manufacturing process was able to give more than 35 % functional acceptance of these bearings. Hence, the prime motivation was to

improve the performance of SSGB by developing manufacturing technology to attain higher functional acceptance.

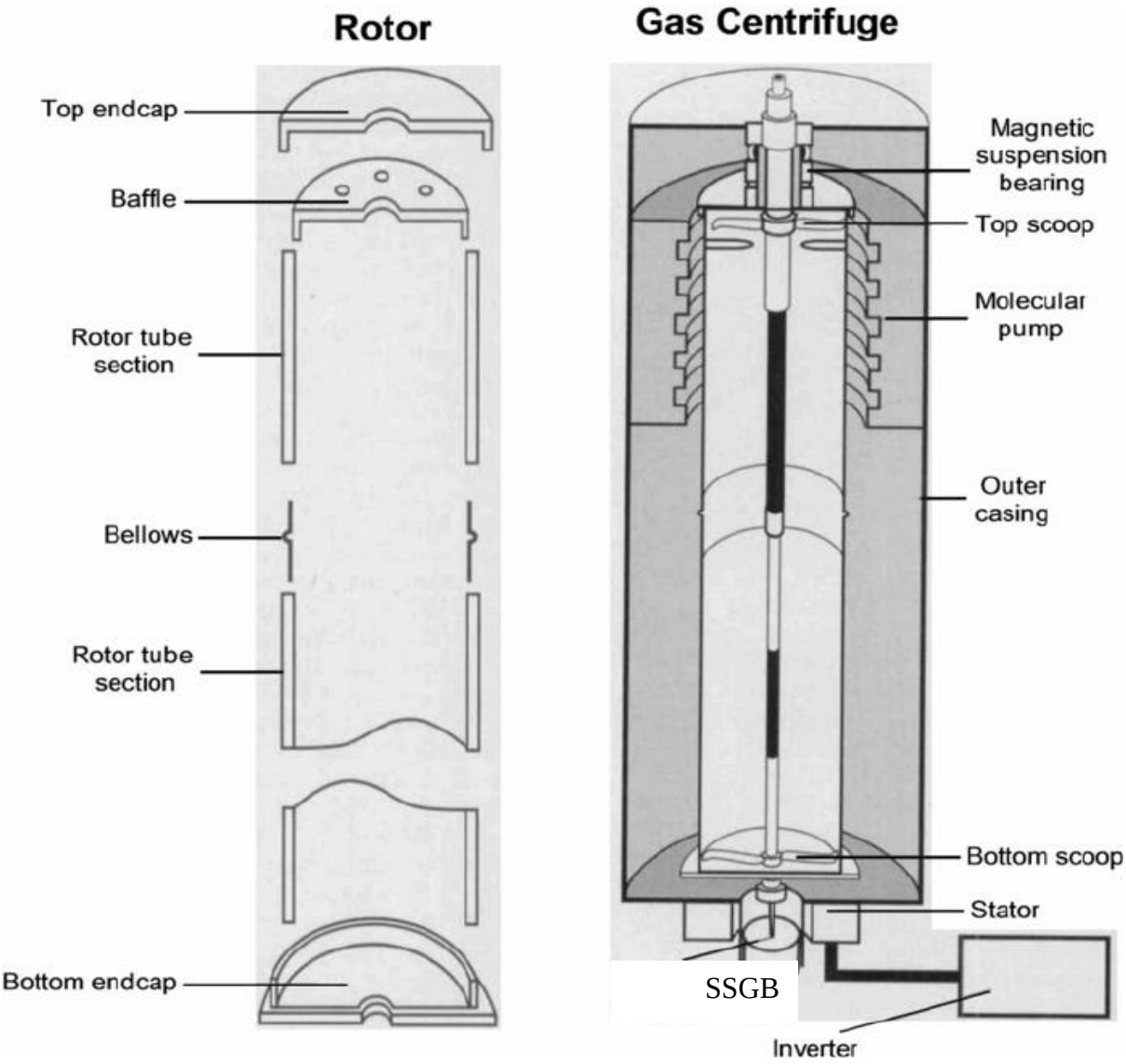

Figure 1.2 High Speed Rotating (HSR) Machines [3]

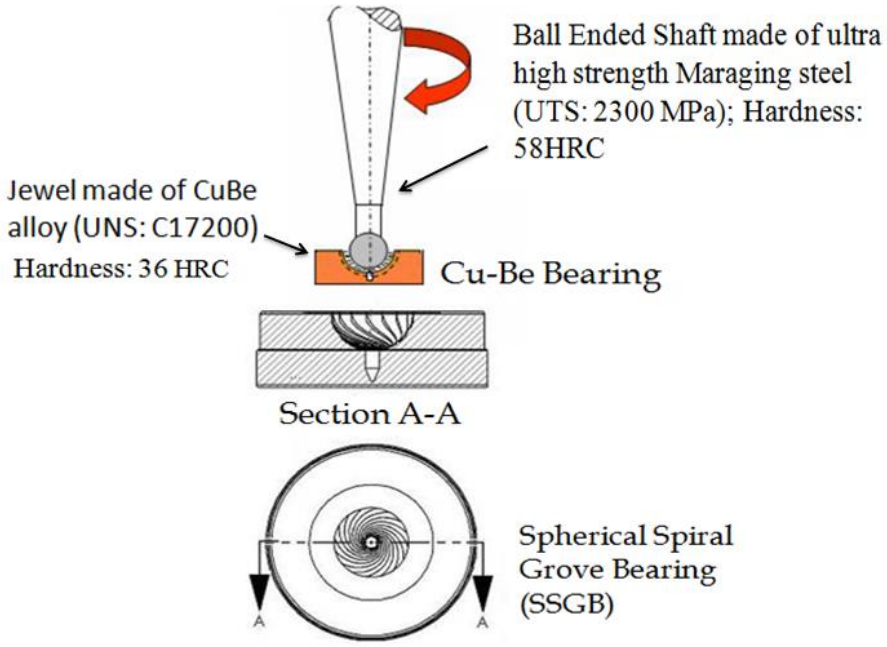

Figure 1.3 Spherical Spiral Groove Bearing used in HSR Machines

The ability of the Laser beam machining, conducted as the major-stage Number -2 in the Figure 1.3 above, to form complex patterns with close tolerances, enables to manufacture wider range of products for different applications.

1.2 Problem Definition

The following are some of the design factors which need very stringent quality control of the components of SSGB.

- Operating speed of HSR is 50,000 RPM
- Axial load on SSGB is 30 N to 100 N
- Minimum life expected from SSGB is 10 Years
- Spherical diameter of SSGB is 4mm to 6 mm
- Operating Temperature of SSGB is of the order of 80^{o}C
- Environment under which SSGB is to perform is corrosive.
- SSGB has to function without any maintenance throughout its life

Higher performance of the SSGB can be achieved by understanding the science behind the manufacturing processes, studying the effect of various machining parameters on the quality of micro fluidics groove and subsequently optimization of the same. This may likely to increase the functional acceptance of the ultra-high speed rotating machines.

1.3 Objective of the Present Research Work

The entire objective is development of a hybrid manufacturing process, with consistent functional acceptance, to generate micro-grooves on hemispherical cavity surface on large numbers of CuBe alloy components for deployment in the strategic application areas of Department of Atomic Energy (DAE). To achieve this objective, the existing hybrid manufacturing process for micro fluidic grooves is to be suitably modified by following the below mentioned targets.

- One of the target of the work is to understand the behaviour of the Excimer laser ablation process of regular photo-resist polymer under various gaseous environmental conditions, with the intention of achieving a higher material removal rate along with good edge definition.
- The study also involves development of proper set up for administering metered quantity of blanketing gas medium to the zone of ablation, to enhance the performance of excimer laser lithography operation.
- In general, the ablation rates depend on the material, wavelength of the laser, ambient atmosphere and geometry of the beam [4]. More than 90% of the operating cost of an Excimer laser system is due to the cost of the consumable Pre-Mix gas [4] and hence the higher ablation rate has got a direct bearing on the economics of operation of the laser system.

- The present study is primarily focused to achieve the twin objectives of - enhancement of (a) laser micromachining rates and (b) the edge definition, of micro-machined feature by changing the environmental conditions.
- Many researchers have studied effects of environmental conditions during laser ablation with specific reference to ablation plume [5]. No literature is available on the usage of different environmental conditions to enhance the ablation rate and the edge definition of the machined feature.
- Further, there are many research papers that deal with the chemical machining of different materials like Copper, brass, stainless steel, monel etc. However, similar publications on the chemical machining studies of DTM-finished parts made of CuBe alloy material is not available in the literature.

1.3.1 Methodology of Work

In order to meet the above objectives / targets, the following methodology of work was planned and flow chart form is shown in Figure 1.4.

- Experimental Study: In order to conduct the detailed experimentation on Excimer laser micromachining of polymer under different environmental conditions, a state of the art excimer laser micro-machining System was designed and developed.
- Development of laser beam conditioning system to have beam of 'hat-top' cross section, resulting in uniform energy density and desired fluence at the work piece
- Incorporate the Beam profiling and energy monitoring systems at appropriate locations in the beam path.
- Integrate the laser firing system with the CNC controller of the X-Y work stage
- Development of proper masks for excimer laser lithography study

- Design and development of systems for the safe admission and exhaust of purge gases including hydrogen to the zone of excimer laser micromachining.
- Development of dedicated Chemical micromachining systems to carry out etching experiments using different etchants and varying the parameters of etchant concentration, temperature and time with provision for effective agitation.
- Identification of suitable characterization techniques and instruments for both the laser machined and chemically etched specimens.

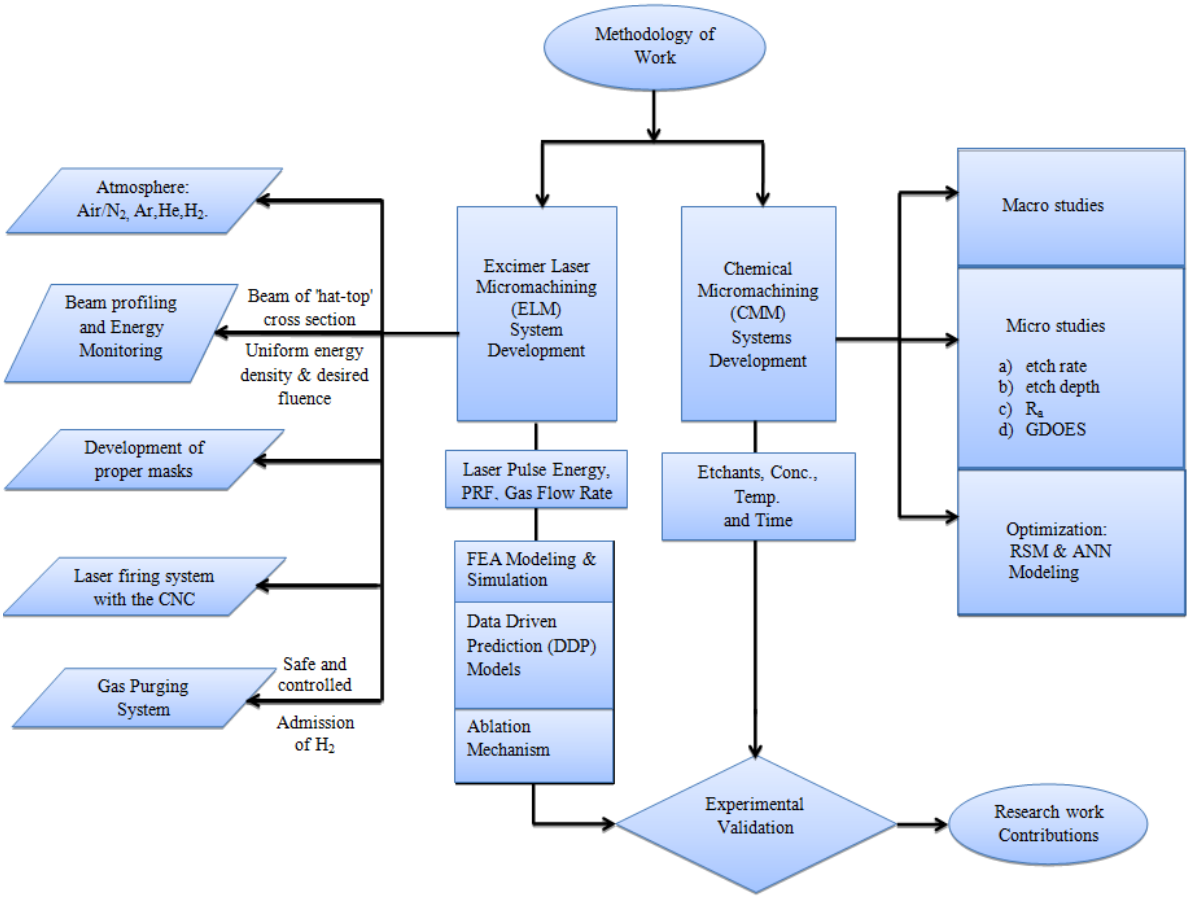

Figure 1.4 Methodology of Work

Thus, the present research work focuses on the enhancement of Excimer laser lithography techniques, involving laser ablation of photo-resist polymer and chemical micromachining of DTM machined parts made of CuBe alloy material to produce micro-grooves on the spherical surface.

1.4 Organization of the Thesis

In **Chapter-1**, relevance and motivation are discussed with objectives of the present research work. The need to enhance the hybrid manufacturing process of Excimer laser lithography involving chemical micromachining of CuBe alloy parts are brought out in this chapter. In addition, the need for the new research area of developing Excimer laser micromachining process, on regular polymer Photo-resist material, having higher machining rate and improved edge definition is also high-lighted.

Chapter-2 is devoted to the literature survey including understanding of lasers in general and Excimer lasers in particular, followed by Excimer laser micromachining processes. It also discusses about the research gaps and the scope of work. This chapter also brings out the scope of research work in the field of experimental as well as numerical investigations on Excimer Laser Micromachining (ELM) and chemical micromachining.

In **Chapter-3**, Experimental Study of Excimer Laser Ablation under Different Gaseous Environments and their outcome is discussed. The effects of different gaseous media like air, nitrogen, argon, helium and hydrogen on the ablation process is studied. Preliminary experimental results obtained with hydrogen gas showed remarkably superior machining rate compared to other gases.

Chapter-4 presents the elaborate experimental study of Excimer Laser Ablation of photoresist polymer in hydrogen media. It also discusses the results of the ablation experiments carried out under hydrogen, helium and also vacuum environments. A mechanism is also proposed on the Photoresist Removal by Laser in Hydrogen Gas Media.

In **Chapter-5** Mathematical Modelling of Laser Ablation Process and the FE Simulation is discussed in detail. The theoretical aspects on the observed facts on the Interaction of laser beam with the polymer material, the computation of the Surface

Temperature, FE simulation on the material removal and the experimental validation are also covered in this chapter.

Chapter-6 deals with the different Data Driven Prediction Models like Linear Regression (LR), Gaussian Progress Regression (GPR), Cubic Support Vector Machines(Cubic SVM), Artificial Neural Network (ANN) and Response Surface Methodology (RSM) to compute the Ablated Depth. As a part of this study, individual and interaction effects of three key operating parameters (i.e. laser pulse energy, pulse repetition rate and gas flow rate) on the laser assisted photoresist removal in hydrogen gas medium were also investigated. The results of the predicted ablated depth values by these various prediction models are compared with the experimental result; Good agreement of the prediction is reported with the experimental values.

Chapter-7 deals with Experimental Study of Chemical Etching of copper as well as copper beryllium alloy materials in two different etchants, viz, Ferric chloride and cupric chloride. Effects of etchant concentration, etching time and etching temperature on the etch depth as well as surface roughness are reported and discussed in this chapter.

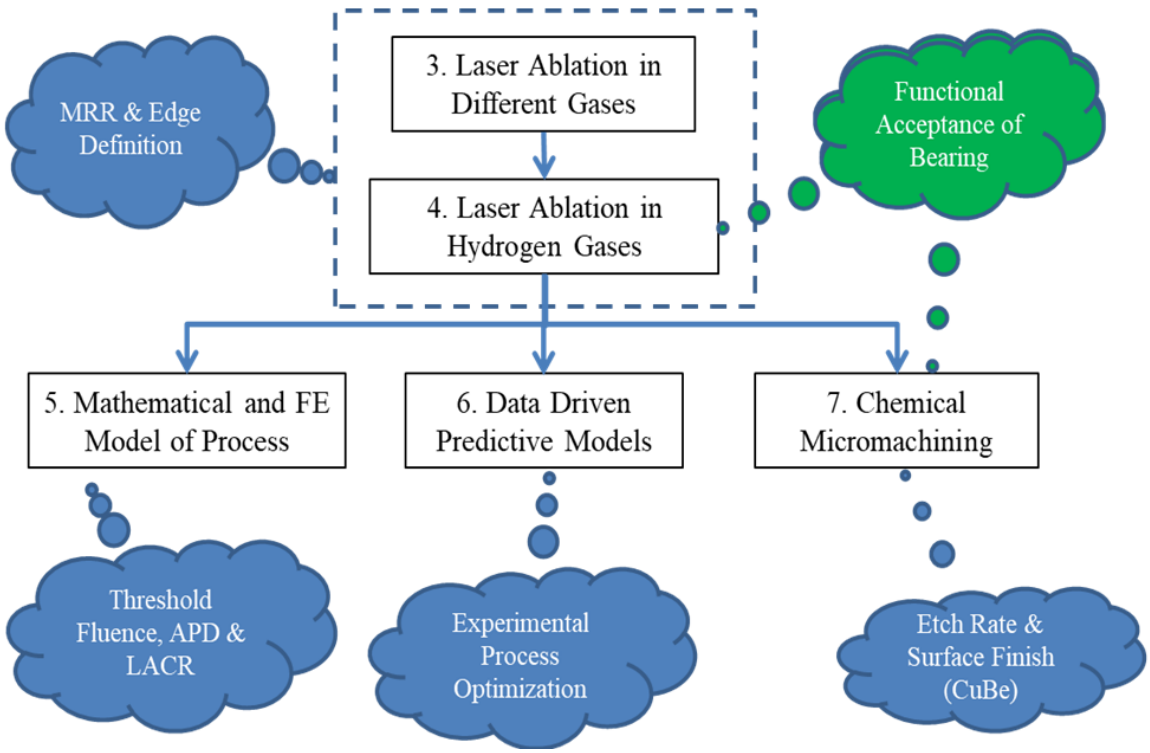

Figure 1.5 Schematic Representaion of Organitaion of Thesis

The concluding remarkson the scientific contribution of this research workand the future scope of further work is indicated in **Chapter-8.** Figure 1.5 shows the overall organization of the chapters and their inter relationships.

Chapter 2

Literature Survey and Gap Areas

This chapter gives glimpse of the fundamentals of various Photochemical Machining (PCM) processes involving excimer laser and chemical etching, and their parameters which govern quality of product. Different materials, chemicals and techniques used in PCM have also been discussed in this chapter. Research work carried out by various investigators are studied and the gap areas are identified.

2.1 Micromachining Process

Micromachining need is increased to meet the fast pace of technological advancement. Various unconventional methods or processes are introduced for micromachining. The classification of various micromachining techniques is shown in Figure 2.1. The present study is focused on Excimer LASER micromachining of polymers, followed by chemical etching of the metallic substrate of the laser ablated workpiece.

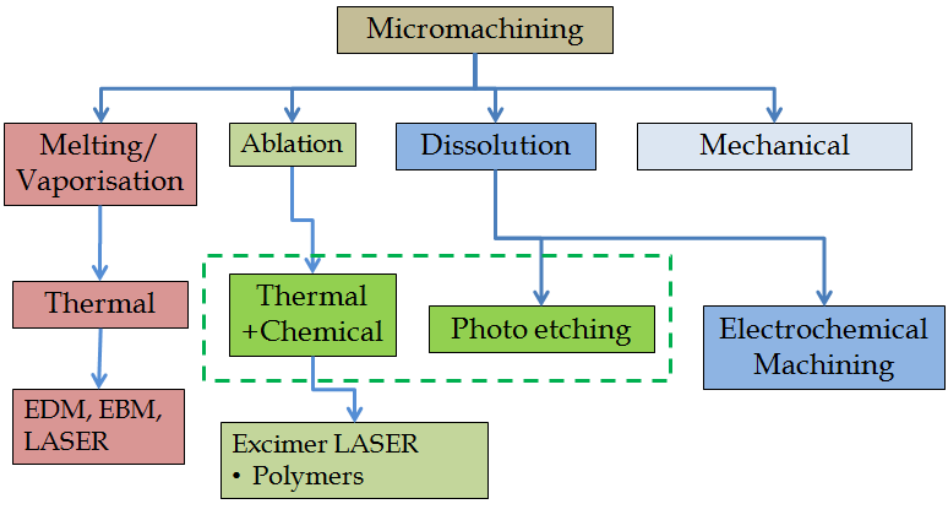

Figure 2.1 Classification of Micromachining Process

Lasers have been used to solve fine machining problems in numerous fields, including those of medical devices, telecommunication, microelectronics, fibre optics, data storage, instrumentation, and micro optics Lasers have been proven as effective tools for micromachining. There are certain advantages associated with laser machining which are listed below.

- Laser based machining process is of Non-contact type, and thus does not pose tool wear issues which happens in traditional machining or EDM processes.
- Damage of material due to shock or handling is not present in this process.
- Selective material removal can be done by proper selection of laser power on-target which allows removal of one type of material from workpiece consisting different layers of materials without damaging bottom layers, for example skiving and wire stripping.
- Laser machining is flexible in incorporating advanced computer control with programming interfaces that permit soft retooling.

Before further investigating laser micromachining, concept of laser, its characteristics and types are discussed in briefly in next section.

2.2 LASER

Stimulated emission was theoretically predicted by Albert Einstein in 1917 and Theodore Maiman produced first Laser (Ruby Laser) in 1960[6]. Laser immediately found its application in various fields which helped in advancement of technology. Basow, Prochorow, Townes used laser for quantum electronics in1964 and Dénes Gábor introduced holography in 1971. Both efforts were recognised and honoured with Nobel Prize.

The first report of material removal by lasers had appeared in the literature during mid-1960's [7]. At present, laser ablation is extensively used in the areas of medicine, Art conservation, Thin film deposition and MEMS manufacturing [8].

2.2.1 Characteristics of Laser

The word LASER is the acronym for Light Amplification by Stimulated Emission of Radiation. Laser has got the unique capability of being coherent in both spatial and temporal modes. Divergence of laser beam is very less compared to ordinary light and can be focused on desired location with excellent precision. Characteristics of LASER beams are following.

- **Monochromatic ---** means single wavelength of photon.
- **Directiona**l --- means low divergence, beam spreads very little
- **Intense ---** means high density of usable photons
- **Coherent ---** means same phase relationship

These characteristics of laser make it suitable for various machining applications. Photon energy of laser beam is one of the deciding factors for defining machining process. Photon energy of different types of laser sources is shown in Figure 2.2.

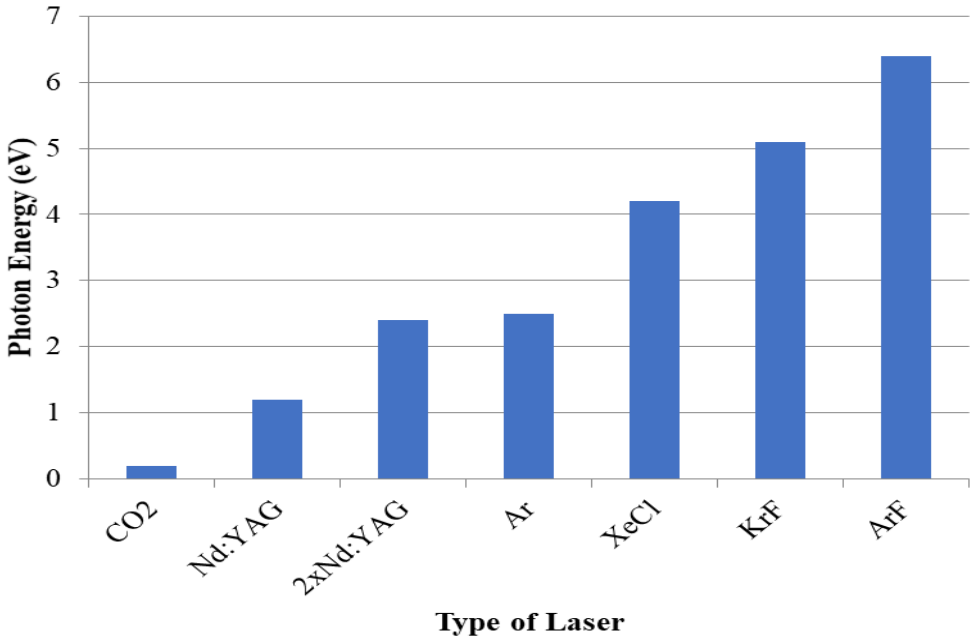

Figure 2.2 Photon Energy of Various Types of Laser Source

Laser is mostly categorized as continuous or pulsed laser by the modes of its operation. The output of laser operating in continuous mode is continuous over time. This type of laser requires stable pumping energy supply, to keep the population inversion in the gain medium. Generally speaking, laser that requires high pumping power cannot produce continuous laser because it will destroy laser equipment by producing extreme heat.

Pulsed laser's output is in pulsed form and is fired at some repetition rate. Pulsed laser's peak energy can be altered by decreasing the frequency because the energy is equal to the average laser power divided by laser frequency, then more energy can be imparted on workpiece within a single laser pulse.

2.2.2 Optical Absorption

The most important principle of laser micromachining is that the laser wavelength must be one which is strongly absorbed by the material to be machined. If the material is extremely transparent to the wavelength of the laser, then optical absorption and energy transfer will not happen. For semiconductors and other crystalline materials, this generally

means that the photon energy must be more than the energy band gap of material. The photon energy must be more than the energy difference between the Lowest Unoccupied Molecular Orbital (LUMO) and the Highest Occupied Molecular Orbital (HOMO) for polymers and other amorphous materials. For both of these cases, that usually requires a laser emitting in the visible or UV range with photon energies of approximately 1 eV or greater.

2.3 Excimer Laser

Excimer laser is an extensively used laser nowadays in scientific and industrial application. It was invented in 1970 by Nikolai Basov *et. al.* from Lebedev Physical Institute in Moscow. Its wavelength was at 172 nm which was produced by using electron beam to excite xenon dimer. The research work was then further progressed by other groups and excimer laser of other wavelengths in ultraviolet range were developed. All these wavelengths in UV range have high energy photons which enabled them in the ablation of a large range of materials.

Excimer lasers are gas lasers and some are discharge pumped also, but apart from this, there are not many resemblances between the most commonly used gas laser viz, CO_2 laser and excimer laser. Excimer laser operation depends on excited dimers and hence the name excimer laser is given to this laser. An excimer is a molecule, which does not have a stable ground state or the ground state which is dissociative and can therefore only exist in a metastable excited state. Firmly speaking, an excimer is a homo-nuclear/ diatomic molecule (e.g. Kr_2, $Ar_2$of the same element).Whereas the one really used in lasers, such as KrF and ArF, is hetero-nuclear and should be called exciplexes. However, this fact has long been ignored, and excimer is the common term used in literature as well [9].

The gain medium of excimer laser is typically gas mixture of noble gas such as argon, krypton or xenon with reactive gas like fluorine or chlorine. The active medium in an excimer laser consists a rare gas (1–9%), a halogen (0.05– 0.3%) and an inert buffer gas (90–99%). The total gas pressure is around four times atmospheric. The gas mixture is circulated rapidly (up to 50 m s^{-1}) and augmented to maintain the desired composition. It is cooled in a heat exchanger and filtered, since changes in temperature and gas composition create difficulties in maintaining a stable beam mode. The laser gas slowly degrades – halogen is depleted and impurities including HF, CF_4, SiF_4 and CO_2 form – resulting in a gradual reduction of gain.A pseudo-molecule, named excimer will be produced under high pressure and electrical stimulation. This excimer is formed by the chemical bond between the atoms of inert gas and reactive halogen atom, or with themselves under the electrical stimulation. The electrical stimulation is generally given by a high voltage electrical discharge or by high-energy electron beams. This excimer can only exist in excited state and will emit photons which form laser light in UV range by spontaneous or stimulated emission.

There are numerous ways to make an excimer laser, in terms of gas composition, pumping mechanism, output power, etc. Their important characteristic is their spectral properties, and the spectral properties are also the major reason behind the use of this laser type for micromachining. All of the excimers emit in the ultraviolet range and capable of producing high intensity focused beams.

The real pumping mechanism is extremely complex and difficult to represent by mathematical equations. Hundreds of different rate equations are used to describe the pumping scheme in detail [10]. It is not essential to explain the mechanisms in detail here which is later explained in short, but a few crucial reactions are the ionisations of the active species Kr and F. This is the key function of the discharge, and the buffer gas (Ne in this

case) intensify the process by charge-transfer collisions. The ionised species combine to form the excited dimer KrF*. The excited state of this molecule is actually the upper laser energy level, which exists for around 5 ns only. Since the ground state is dissociative (with a lifetime of the order of the vibration period ~10^{-13} sec) a population inversion is easily achieved. Figure 2.3 demonstrates the pumping scheme.

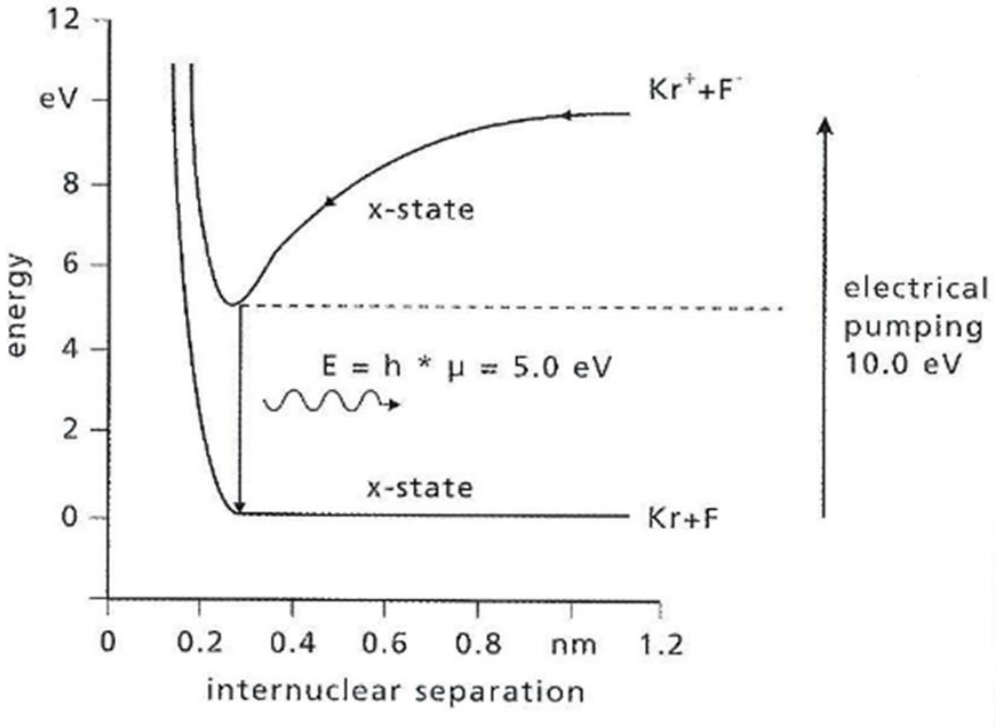

Figure 2.3 Schematics of the Excimer Laser Transition. The Exited State Lifetime is Around 5 ns, Whereas the Ground State is Dissociative.

As indicated earlier, excimer lasers, as such are a family of pulsed lasers, operating in the ultraviolet region, generally produced by a fast electrical discharge in a high-pressure mixture of rare gas (krypton, argon or xenon) and a halogen gas, providing a photon pulse energy in the range of 3-10 eV. The ablation process of polymeric material with a pulsed UV Laser is named as ablative photo decomposition by Srinivasan *et. al.* [11]. The ablation process is characterized by pulse-by-pulse removal of small amount of material at submicron thickness, with minimal damage to the surrounding areas.

Excimer laser is able to break the chemical bond of material by ablation instead of thermal effect. Following are the unique characteristics of machining associated with excimer laser.

1 No heat affected zone

2 High resolution (~1 μm)

3 Precise control of depth

4 High productivity.

Numerous models have been proposed to explain the observed ablation behaviour of various polymeric materials by Garrison *et. al.* [12]. These models invariably assume the ablation to be either photochemical or photo-thermal process. In photochemical process, the material absorbs photons, leading to bond breaking. In photo- thermal process, the deposited energy is converted to heat, leading to thermal decomposition. It has been generally accepted that ablation proceeds by a combination of these two mechanisms [12]. The photon of short-wavelength associated with excimer laser, has energy ranging from 4 to 10 eV, which covers the bond energy of most of the organic polymeric materials. The bonding energies of different types of covalent bonds of organic polymeric materials are shown in Table 2.1. It is evident that a photon of 248 nm KrF excimer laser having energy of 5.1 eV, is sufficient to break most of the covalent bonds of organic polymeric materials. As a result, Excimer lasers are used in the first step of pre-process pattern printing method for metals.

UV laser pulses from excimer have the following characteristics

- Energy in the range mill joules to joules;
- Average power up to several hundred watts;
- Repetition rates up to 1000 Hz;
- Pulse duration from a few to tens of nanoseconds

- Peak power values up to 50 MW.

Table 2.1 Bond dissociation energy

Covalent Bond	Bonding Energy(eV)
O - O	1.47
N - N	1.69
C–Br	2.95
C - N	3.16
C– Cl	3.43
C–C	3.60
H - N	4.03
C=O	4.2
C–H	4.25
N=N	4.33
H–H	4.52
O–H	4.81
C–F	5.08
O=O	5.15

2.4 Laser Ablation Process

August Beer formulated Lambert-Beer's law from the observations of his own experimental results, in combination with experiments of Johann Heinrich Lambert. Lamber-Beer's law states that relationship between absorbance (*A*) and the product of the absorbance coefficient (A_c), thickness of the media (*l*), and the media concentration (*c*) is logarithmic as shown in equation 2.1.

$$A = \log_{10} \frac{I_o}{I_t} = \log_{10} \frac{1}{T_r} = A_c . l . c \qquad \text{---(2.1)}$$

Where parameters *A* represent the absorbance of light, I_o *is* intensity of incident light, I_t is intensity of transmitted light and T_r is transmittance respectively. The parameters A_c is absorption coefficient, *l* is thickness of the light-absorbing media, and *c* is the concentration of media.

2.4.1 Ablation Threshold

Ablation threshold is the minimum energy required for material removal from the material body to happen. At the molecular level, it is necessary to induce molecular or atomic displacement or separation with laser energy. Not only for UV range laser, for a broad wavelength range (from infrared to vacuum ultraviolet) of laser the removal of materials starts to happen when the applied fluence is equal to or more than the ablation threshold. Ablation occurs (not only in the UV laser range, but in a broad wavelength range from infrared to ultraviolet) when the ablation threshold fluence, F_T, is exceeded. For UV and Vacuum UV laser, the ablation threshold fluence is lower than other wavelength range; it can be as low as 20-200 mJ/cm^2. The specific threshold fluence is decided by laser wavelength and the material ablated. One important characteristic of the ablation threshold is that even a high number of laser pulses with a sub-threshold fluence will not be able to remove any material whereas a single pulse with a fluence above the threshold, will be able do so. For solid state laser and excimer lasers, whose pulse duration is normally less than 100ns, the threshold fluence is independent of pulse duration. However, for other types of laser whose pulse duration is longer, threshold fluence is affected by pulse duration.

It is found that the laser etch rate can be written in a form which is consistent with Beer's law

$$x = \alpha^{-1} \ln \frac{F}{F_T} \qquad \text{--- (2.2)}$$

Where x is ablation rate of laser, α is empirical absorption coefficient, F is laser fluence and F_T is laser ablation threshold fluence.

2.4.2 Laser Ablation Mechanisms

In general, there is no mechanical ablation mechanism involved in laser ablation process. However, if light is considered as a stream of photons, then physical pressure is also applied. The beam of light is stream of photons striking at the object/sample, which transfer their momentum to the sample's surface, applying a pressure. Light pressure also has its own effects on the ablation process. The pulsed excimer laser has high peak power density and energy because of which the ablation causes the particles of ablation products' to be blown away from the surface. Whereas the enormous peak light intensity and plasma shockwave helps to blow away the re-deposited materials and part of residues. Some of the vaporized materials are deposited around ablation site and forms pattern of wrinkles. Surface quality of excimer ablation is affected by all these particles and wrinkles. Light pressure is defined as p= [power of light beam]/c, where c is speed of light. This pressure becomes significant at the nanoscale and active research is going on, which focuses on the application of light pressure as driving force in NEMS.

However, light pressure is ignored due to the high magnitude of c (the velocity of light). In general excimer laser ablation is still the photothermal and photochemical ablation mechanism that controls the entire process. Photons of 193 nm (6.4 eV) ArF and 248 nm (5 eV) KrF excimer laser transfer their high energy to surface of materials and remove the material from solid surface. This one-step material exclusion process can be explained in two mechanisms: photochemical and photothermal ablation. Photochemical ablation occurs when the energy of laser photon is absorbed completely which breaks chemical bonds and the material is removed without any thermal effect. Photothermal ablation includes heating

of material surface and removes the material because of thermal effect. Laser energy is transformed into lattice vibration energy that melts and vaporizes the material/polymer. Both ablation mechanisms occur simultaneously in most ablation processes to varying degrees depending on wavelength of laser and bond energy of material [13].

Wavelength or frequency of excimer laser lies in UV range. As explained above that ablation occurs, because of simultaneous occurrence of photochemical and photothermal processes. They have different relation to laser ablation rate which depends on different material properties.

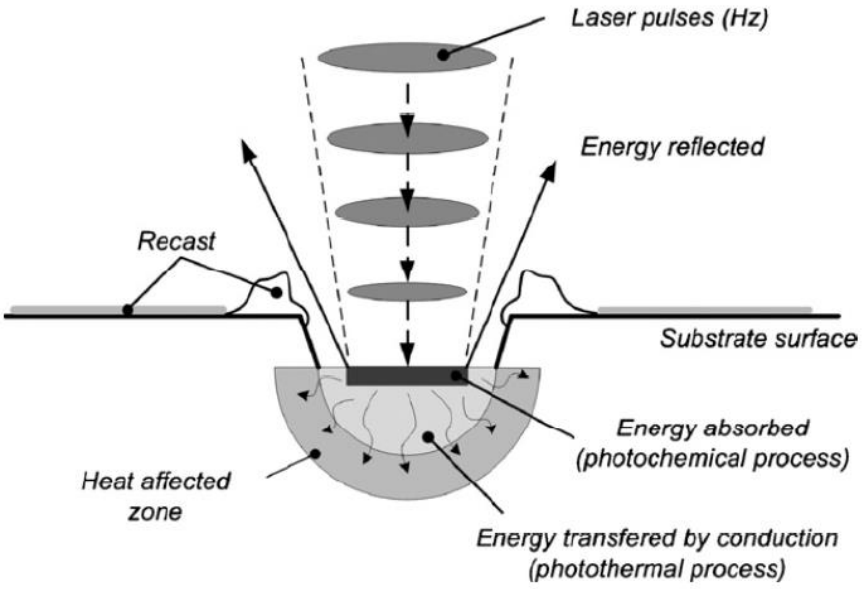

Figure 2.4 Pictorial Representation of Interaction between Laser and Material [14].

Figure 2.4 is simplified to represent two distinct zones. Both zones are dominated by the two laser ablation processes respectively. The first zone is closer to material's surface where laser pulses are bombarded directly. In this zone, photon energy is directly absorbed to break chemical bond which is known as photochemical process zone. The second zone, which is heat affected zone, refers to the portion of energy being transferred by conduction which leads to photothermal process.

2.4.2.1 Photochemical Ablation

During photochemical ablation, there is minimum thermal damage or melting of material, because chemical bonds are directly broken by absorbing high energy photons. For example, ArF excimer laser photon energy is 6.4 eV, while KrF excimer laser photon energy is 5.1 eV which are sufficient to break many chemical bonds. After absorption of photons, decomposition reactions take place inside bulk material. These decomposed parts are removed from the material. This whole process consumes photon energy in direct bond breaking and confines heat diffusion [15]. It is mostly dependent on material's absorption coefficient, α. This absorption coefficient characterizes a given material's capacity to absorb laser energy. It is defined as the inverse of optical penetration depth which indicates the depth upto which laser energy will be absorbed and photochemical ablation process will happen.

For photochemical process F_T, fluence required for ablation threshold is given by equation (2.3).

$$F_T = \frac{nhv}{\eta\alpha(1-R)} \qquad \text{--- (2.3)}$$

Where parameter *n* is the number of bonds that must be broken to achieve material removal, η is the quantum yield for chain scission, hv is the photon energy (assumed to exceed the chemical bond energy of material), and *R* is the surface reflection loss.

Quantum yield: η= no. of molecule decomposed/ no. of photons absorbed.

2.4.2.2 Photothermal Ablation

Photothermal ablation mostly happens in molecules of ground state energy level. In this process, photon energy is not utilized in breaking of chemical bonds. It converts in vibration lattice energy which leads to heating and vaporization of materials. The volatile

products are formed and its rate is highly dependent on temperature. This complete process is largely governed by material properties and laser pulse width. The thermal penetration depth, L_e is defined as

$$L_e = 2(Kt)^{\frac{1}{2}} \quad \text{--- (2.4)}$$

Where, K is the thermal diffusivity and t is laser pulse width. Thermal diffusivity is defined as

$$K = \frac{C_p k}{\rho} \quad \text{--- (2.5)}$$

Where C_p is heat capacity, k is thermal conductivity and ρ is the density of material.

If material thermal diffusivity K is low and laser pulse width is lesser than 1ns, then photothermal ablation effect will be insignificant. Based on the assumption that Arrhenius equation is valid for this process, the volatile products formation rate V can be defined as:

$$V = Ae^{-E_A/R_g T} \quad \text{--- (2.6)}$$

Where A is pre-exponential factor for the decomposition path, E_A is the activation energy for the decomposition path, R_g is universal gas constant, and T is absolute temperature. Hence V must attain a high value to ensure the existence of ablation, i.e. the threshold of thermal ablation. Thermal ablation threshold can be defined as:

$$F_T = C\,(T_D - T_R)/\alpha(1 - R) \quad \text{--- (2.7)}$$

Where C is the specific heat capacity of the material, T_D is the temperature at which quantifiable decomposition occurs, T_R is the initial temperature of the surface, α is empirical absorption coefficient and R is surface reflection loss. Both photochemical and photothermal ablation mechanism are significant and these two processes usually occur simultaneously

during excimer laser machining. In ultraviolet range, photochemical ablation will play predominant part particularly for low ablation energy. If experiments are designed to use infrared laser with high temperature, then photothermal ablation mechanism will be primarily responsible for ablation of material.

2.5 Laser Machining Techniques

The unique characteristics of laser radiation combined with a high degree of flexibility, contact-less machining, wear-less machining and the opportunity of highly automated process allows usage of this tool for wide range of applications. It is used for machining of numerous materials which include silicon, ceramics, metal and polymer. The world of laser machining production is divided into two categories known as micromachining and macro-machining. This classification is not based on the size of the work piece; instead the size of the machined feature processed by the laser tool governs the classification. The laser system used for micromachining application generally uses pulsed beams with an average power lesser than 1 KW whereas, laser system used for macro-machining mostly employs continuous-wave (CW) laser beams having power more than 1KW.

Lasers for micromachining have a wide range of frequencies/wavelengths, pulse duration ranging from femtosecond to microsecond and repetition rates (from single pulse to MHz). These traits of laser permit micromachining with high resolution in both dimensions (depth and lateral).The use of extremely short nanosecond, picoseconds and even femtosecond pulse duration assists minimization of thermal effects such as melting and burr formation. Thus, eradicating the necessity for any post processing actions. Laser micromachining is accomplished with two methods which are listed below.

I. Direct Laser Writing (DLW) using solid state lasers with a 2D galvanometer scan head as shown in Figure 2.5.

II. Mask Projection technique (MP) using mostly Excimer lasers and conventional fixed masks as shown in Figure 2.6.

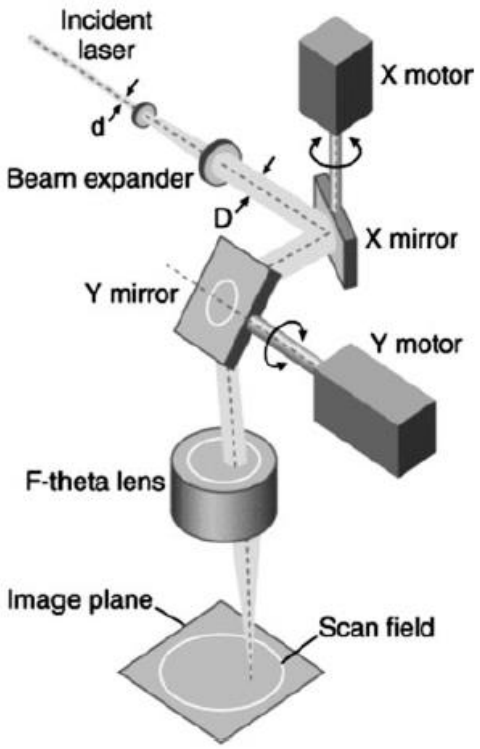

Figure 2.5 Principle of Direct Laser Writing with xy-Galvanometer Scan-head [16]

For sensitive materials like organic materials, Excimer lasers are preferred. These lasers are frequently used in mask projection techniques (MP). Similar to photolithography, the mask projection technique permits to transfer all information contained in a fixed transmissive mask at once which is shown in Figure 2.6.

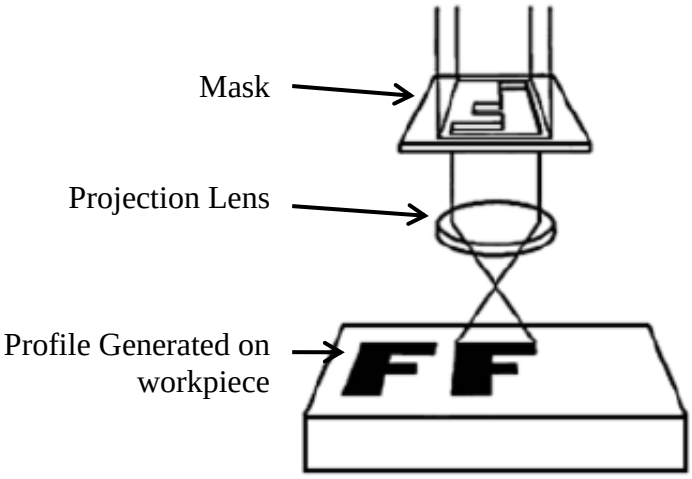

Figure 2.6 Principle of Mask Projection Technique [16]

2.6 Review of Laser Machining Applications

The laser based micro-machining technology has potential applications for manufacturing of challenging parts in the field of engineering as well as bio-medical industries such as complex micro-channels of micro fluidic devices [17]. Laser micro machining technology allows high degree of flexibility, noncontact and thus tool wear free machining, on a wide variety of engineering materials. The possibility of high automation as well as easy integration allows laser micromachining techniques to be used for many materials including silicon, ceramics, metals and polymers. One of the most critical laser parameters is the pulse duration, which ranges from femtosecond to nanosecond (ns), to millisecond [18].

Holes as small as a few microns can be drilled, with wall angles close to 90^0 – often 85^0– 89^0. The wall angle will become steeper with higher pulse energy, and with higher absorption of the substrate. The aspect ratio of the holes can be high, the limit being the conical shape of the holes caused by the wall inclination - values for the aspect ratio has been reported in literature to reach 600 [19], but more common values are 5 - 10 as shown in Figure 2.7.

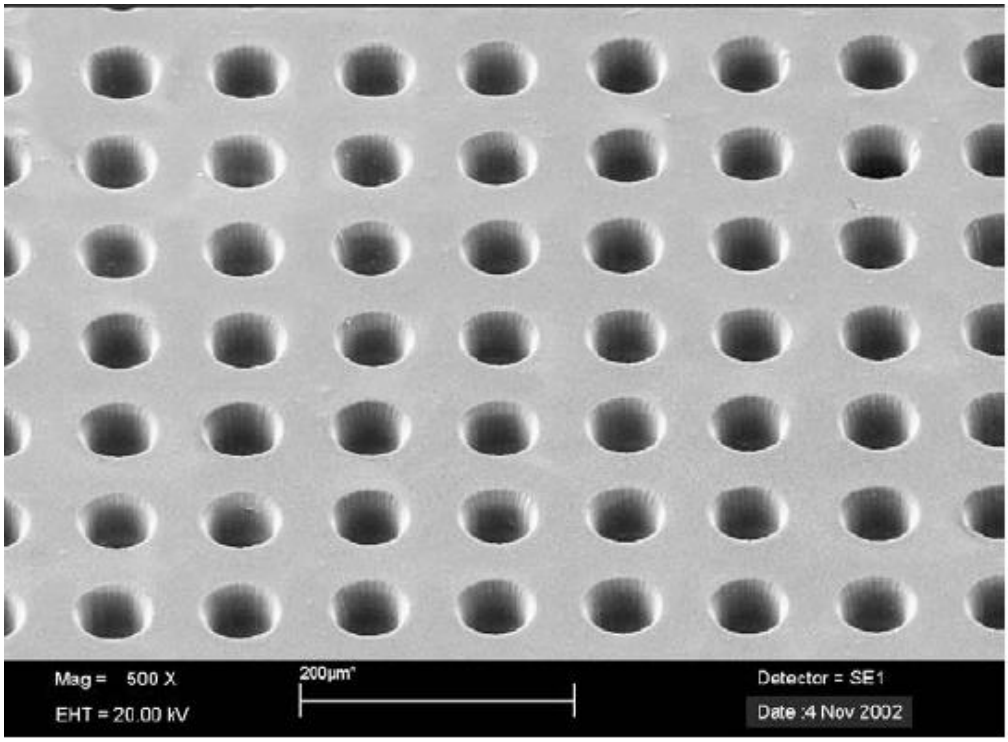

Figure 2.7 SEM Micrograph of an Array of 50 µm Diameter Holes Percussion Drilled in PET, at 300 Hz and a Fluence of 3500 mJ/cm^2 [19].

Attributes like wavelengths, pulse duration and repetition rates allow micro-machining with high resolution in depth as well as in lateral dimensions [20]. As laser beam absorption varies for different materials, an appropriate laser needs to be used in a specific application [21].

Though laser micromachining offers many advantages, it invariably has thermal related issues. The thermal effect induces the Heat Affected Zone (HAZ) which needs to be reduced or even eliminated [22]. Excimer Laser ablation of polymers was first reported in 1962 as a technique of photolithography [23]. However, compared to conventional photolithography, this new technique of excimer laser ablation has unfortunately had mainly, two disadvantages, firstly, carbonization upon irradiation [23]. Secondly, debris contaminating both the ablated surface and the optical elements of the laser micromachining set up [24]. Researchers T. Lippert *et. al.* [25] had suggested to use specially designed

polymers, which incorporates the photo-chemically active chromophore groups into the main polymer chain, to overcome these problems.

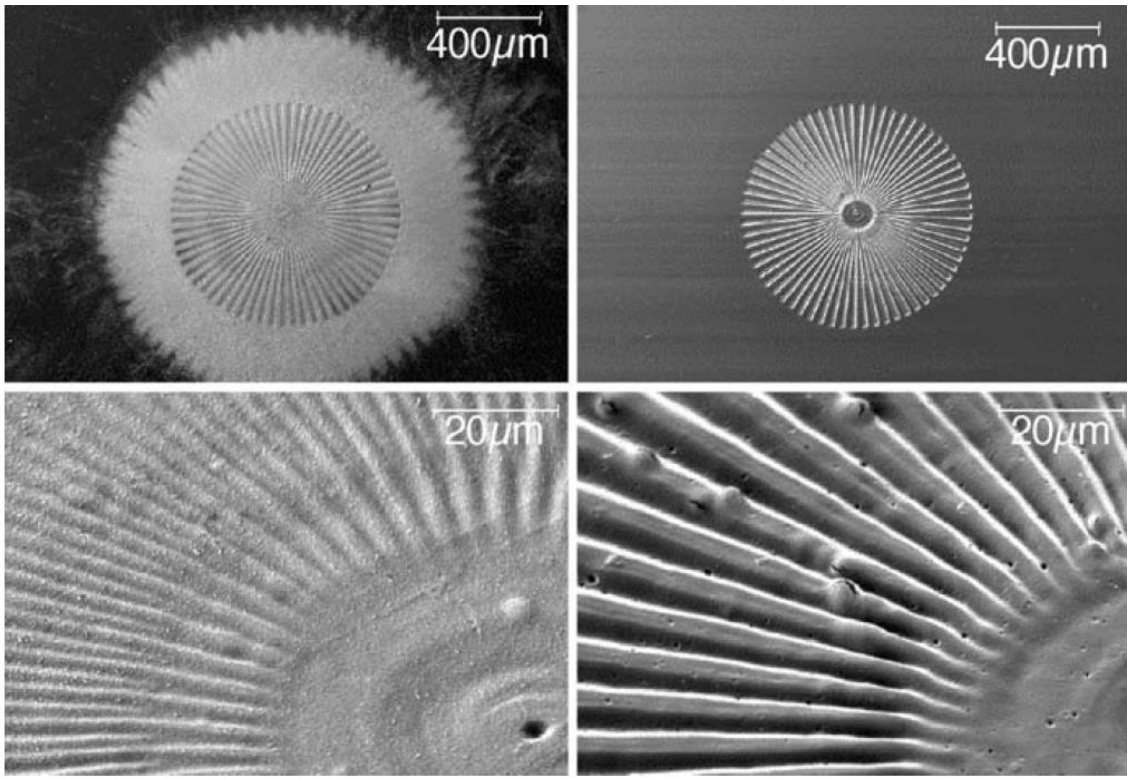

Figure 2.8 SEM Images of Siemens stars Fabricated by Laser Ablation [26].

However, to overcome such problems, various types of environments such as liquid and gaseous media were used by some other researchers Perrie *et. al.* [27] and Ju Sun *et al.* [28]. Other than these issues, another area that needs to be given attention to enhance the quality of micro- machined surface is the debris-control. Figure 2.8 shows SEM images of siemens stars fabricated by laser ablation. Top left image is siemens stars in polyimide and top right is in the triazene polymer using 5 pulses. Bottom row of figure is magnification of the siemens stars in the top row.

Dowding and Lawrence have reported the beneficial effects of debris control by means of closed thick film filtered water immersion. Sun and Longtin have reported that the focused femtosecond laser pulse can be dramatically distorted in air due to the Kerr Effect

and the Plasma effect on account of the very high optical intensities of the order of 1016 - 1019 W/cm^2 associated with femtosecond lasers [28]. However, they have reported that the ill-effects can be mitigated by using a helium gas medium. Perrie *et. al*. [27] have reported that the use of flowing He gas is of major benefit when micro structuring aluminium with NIR femtosecond laser by minimizing plasma breakdown and surface oxidation and helps to remove fine debris. In case of submerged laser cutting under liquid medium using ns-pulsed green fibre laser, researchers have reported that the beam enlargement or reduction due to change in refractive index does not significantly reduce the fluence. However, the absorptivity of the liquid can cause significant energy loss [30].

Excimer laser is a good tool when it comes to micromachining of polymers. The short pulse duration, in the nanosecond regime of Excimer laser, helps in direct ablation of the polymer without adverse thermal effects. In this case the mechanism of material removal is by Ablative Photo Decomposition (APD) phenomenon, which breaks the molecular bonds without any appreciable thermal effect [31]. The energy of the UV photons of the excimer laser is high enough to interact with organic molecular bonds, causing APD and direct ablation of material by using short pulse duration [32].

Hence, for micromachining of organic polymers, excimer lasers are extensively used. As far as the excimer laser beam geometry is concerned, beam dimensions and beam divergence are determined by electrode geometry. Most excimer lasers have highly non-Gaussian beam profile about the longer axis, of the nearly rectangular beam with large cross-section. Excimer lasers have thus typically broad spatial profile and poorly defined mode structure and hence not suitable for focal point application like direct writing, because of the very high value of M^2 factor [33]. Additionally, thanks to low thresholds of ablation of polymers, focusing of laser beam is not necessary, and large surface areas can be treated [34]. Hence excimer lasers are commonly used in mask projection techniques like

photolithography for making of 2½D structures by means of homogenized laser beam, as reported for fabrication of micro-fluidics devices [35]. The development of laser-assisted surface micro-patterning or modification of polymers has thus taken a considerable interest in the past. Excimer lasers such as KrF (248 nm) and ArF (198 nm) were widely reported to be an efficient tool for precision micro-structuring of polymer materials. In general ablation rate of polymers are expressed as a function of incident fluence and the threshold fluence of the polymer used. The threshold fluence values are, however, very low for polymers, in the order of tens of mJ cm^{-2} unlike metals and ceramics [36]-[38]. Moreover, the amount of ablated material for polymers shows a direct linear proportionality for a wide range of fluence.

Removal of Photoresist (PR) is an important manufacturing stage in the fabrication of solid- state devices/microelectronics. Attempts have been made to develop dry cleaning process of PR removal using oxygen plasma and ozone gas [40]-[42]. This method has its inherent demerits due to the oxidation of the substrate, apart from degradation of device properties due to the bombardment of high-energy ions on the substrate. Oxygen/ozone plasma ashing may also cause oxidation of substrates and metal wiring due to its operating process temperature of higher than 250 °C [43], [44]. To overcome the problems associated with plasma cleaning process, researchers have studied an alternate resist removal method using hydrogen radicals. The main disadvantage of this process is the requirement of high temperature of the order of 2000 °C to generate hydrogen atoms using hot tungsten filament [45]-[49].

One considerable disadvantage of excimer laser ablation of polyimide is the soot and debris that gather around the ablation zone during the irradiation. Kuper *et. al.* [50] inspected the surface debris that results from KrF excimer laser ablation of polyimide. Effect of the pressure, and atomic or molecular weight of several ambient gases: H_2, He, Ne,

air, Ar, Kr, and Xe on debris formation was analysed. A linear relation between the measured debris radius and the inverse third root of the ambient pressure was found which was consistent with the predictions of blast wave theory. No quantifiable debris could be observed under helium or hydrogen gases up to 1 atm environment. Earlier the recommendation was made that the reason for debris-free polyimide films under He gas environment was due to the high thermal conductivity of gas. The present data suggest that thermal conductivity of the ambient gas is not a primary reason for the debris reduction. The resultant value of the blast energy, approximately equal to 5% of the incident pulse energy, was used to evaluate a nascent blast pressure of approximately 150 atm. The major assumption is that surface debris will form if the ablation fragments are restricted in a small volume for sufficient time. Conclusions from blast wave theory suggested method to decrease the amount of debris produced.

Extensive research has been conducted in the area of water assisted laser processing of metals and ceramics and compared their performance with air. It had been established by Brook *et. al.* [51] and Simakin *et. al.* [52] that water assisted laser etching provided better tolerances and smaller heat-affected zone widths and avoided the re-deposition of debris. Water-assisted laser etching mainly eliminated re-deposition of debris in the machined area, resulting in cleaner and more precise surface profile, avoiding any need for subsequent work piece cleaning. Dupont *et.al.* [53] also observed a difference between etching of steel in air and water. In water, the etching was considerably faster than air.

Gieger *et. al.* [54] conducted KrF excimer laser ablation tests under a thin water film to modify the micro-structure of mainly, ceramic materials. They compared dry machining with underwater machining and found that in underwater machining, the re-deposition of ablated material was completely eliminated, resulting in better quality of finished surface. They reported that for some ceramic materials the ablation rate is increased significantly.

Shafeev *et al.* [55] proposed dissociation of water producing hydrogen during the laser etching of diamond in water. Lou Q [56] reported that laser irradiation of PTFE under water-film was found to improve wet-ability and adhesive strength with epoxy resin. The increase in the wetting of the PTFE surface and adhesion strength was explained by laser aided chemical reaction of water with PTFE surface.

2.7 Data Driven Predictive Models

Regression analysis is extensively used to express the relationship between response and predictor variables. Relation between functional data analysis and high-dimensional statistics were discussed by Bongiorno *et. al.* [57] whereas Aneiros and Vieu [58] investigated the variable selection of functional linear regression with multiple functional predictors in the infinite dimensional variable problems.

Chiou *et. al.* [59] projected a multivariate functional linear regression (mFLR) approach to analysis and prediction of multivariate functional data in cases in which both the response and predictor variables contain multivariate random functions. To overcome the problems of over-fitting resulting from high-dimensional sequential data and difficulty in predicting due to dynamic behaviour of real world data. Zhu *et. al.* [60] proposed a multi-kernel Gaussian process latent variable regression model for high-dimensional sequential data modelling and prediction.

Support vector machines (SVMs), have been used as a regression (SVM) predicting tool due to its several advantages like, few model parameters to be chosen, avoidance of overfit to the data etc. SVM is generally applied to many real issues like predicting the performance of compact heat exchangers [61], modelling of heat transfer in a thermosyphon reboiler [62], biosorption process studies [63].

2.8 Photochemical Machining

PhotoChemical Machining (PCM) is a typical unconventional machining method which uses photoresist and chemical etching procedures. Metal is removed through its etching by chemical solutions to dissolve the surface of the work piece that has been selectively exposed with the help of photographic technique. PCM is also called as photoetching, photofabrication and photochemical milling. It can be used for a very wide range of metals and alloys but up to a typical thickness of 2 mm [64].

Chemical etching, which is one of the key elements of PCM, was a well-known machining method in Ancient Egypt in 2300 BC. The Egyptians used to etch copper with citric acid [65]. Till 19^{th} century this process was broadly used for etching of decorative items. The development of photography proved to be a novel improvement in chemical machining and J. N. Niepce was the first to use a photoresist made from bitumen of Judea asphalt for etching pewter in 1826 (an alloy of 80-90% of tin and 10-20% of lead). William Fox Talbot patented a PCM process used for etching of copper with ferric chloride, using a photoresist made from bichromated gelatin in 1852. John Baynes in 1888, introduced a process for etching material on two sides using a photoresist, which was patented in the USA [66].

The major industrial application of chemical machining was established after the world war like many other techniques. In 1953, North American Aviation Inc, California USA used the PCM process to etch aluminium components required for rockets. The company termed the process as chemical milling and patented it in 1956 [67]. During this time, Kodak successfully promoted a new type of photoresist named KPR and the development of more photoresist followed [68]. The industrial application of chemical machining and the advancement of photoresist technology shaped a machining process

which found its application in the newly developed Printed Circuit Board (PCB) manufacturing industry [69].

Researchers Black and Cutter, etched copper with cupric chloride ($CuCl_2$). They used hydrochloric acid (HCl) in $CuCl_2$ as major solution and found improved etch rate [70]. Andes and Saubestre used etchants like $FeCl_3$, $CuCl_2$, nitric acid (NHO_3), chromic sulphuric acid (CrO_3-H_2SO_4) and peroxysulphate and found $FeCl_3$ and $CuCl_2$ were better etchants for copper [71], [72], [73].

Sharpe and Garn conducted studies on copper etching with $CuCl_2$ and chemical additives sodium chloride (NaCl), hydrochloric acid (HCl) and ammonium chloride (NH_4Cl) and performed a comparative study on $CuCl_2$ and $FeCl_3$ etchants. They found that $CuCl_2$ produced less undercut and better surface finish compared to $FeCl_3$ [74].

During the last fifty years, the use of PCM has increased significantly in the electronics industry (predominantly in the production of printed circuit boards and lead frames), precision engineering and decorative industries to fulfil the demand for thin, flat and complex metal components. This process was also kwon as the most secretive machining process in the USA [75]. The major advantages of PCM are that it is independent of the metal's physical and mechanical properties. Its level of precision is high and tooling cost is very low [76]. PCM is also very competitive when compared with other unconventional and advance machining processes such as Wire-Electro Discharge Machining (WEDM), laser beam machining, stamping and photo-forming [77].

The development of all manufacturing technologies in itself has some difficulties and PCM is no exception. One of the most important considerations is the environmental effect of the disposal of industrial/chemical waste generated from PCM process. This has created problems throughout the world. Heavy penalties have been imposed on factories to

enforce the stringent environmental regulations. The rapid rise in demand of industrial waste disposal has forced both the manufacturing industries and research centres to find efficient and effective solutions [78], [79].

2.9 Effect of PCM Parameters on Machining

The impact of etchant concentration, additives and etching temperature on etch rate was examined by Cakir [80]. Copper etching with $CuCl_2$ formed a stable and high etch rate and low undercut. The etching temperature was limited to 50-55^oC because of peak operating temperature of etching machine. The molarity of $CuCl_2$ etchant was 2.33–2.5 mol. The Oxidation-Reduction Potential (ORP) of $CuCl_2$ was controlled and kept around 510–530mV. These etching parameters provided a desired copper etching results. It is necessary to regenerate/recycle the waste etchant from environmental point of view. Thus, various cupric chloride etchant regeneration processes were explored.

Hibi *et. al.* [81] developed an effective method for machining of ceramic by using a krypton fluoride (KrF) excimer laser with a 248-nm wavelength (excimer laser assisted chemical machining). A soft hydrous oxide layer was formed by photochemical reaction due to laser irradiation on SiC in presence of water. The soft layer was then machined with a diamond tool to form a mirror surface finish. The conditions were optimised for high machining rate and better surface integrity of SiC.

Muhl *et. al.* [82] developed a new technique to directly deposit a controlled ink film on metal surface which act as etch resistant mask. This process was done by microprocessor-controlled printer. The process was similar to photochemical machining but it proved helpful in removing of two stages of photo-processing and mask making. The process had been demonstrated in laboratory for the application of texturing rollers for the production of textured steel sheet in automotive industry. The potential of this process is

huge in other areas of PCM because of its ability to mask wide range of surface geometries with the help of computer software.

Makino *et. al.* [83] examined the heat resistance ability and chemically inert behaviour of cyclised polybutadiene rubber, to find its suitability as a photoresist material for photoetching of alumina ceramic in phosphoric acid. Stencil breakdown, variation in stencil thickness during etching, and etch factor were measured during experimental study. It was found that this material after baking at temperatures of 300°C for 30 min provided good resistance to chemical attack by the acid at 300^{o}C. The effects on etch factor by post-bake temperature, etching temperature, etching time, and original groove width were established.

An experimental assessment of a 2D simulation model of etching, where the role of reaction products dynamics was considered [84]. A 2D Monte Carlo simulation model for PCM was considered and the model proved to be successful in describing temperature and geometric effects of an anisotropic surface disaggregation. To get accurate simulation of the surface at the micro-geometry scale, the coordination number of the surface elements should be included. The experimental results showed that the etching process at lower temperatures shifts towards a reaction-limited regime. It was observed that the etchant motion had a great influence on the macroscopic anisotropy of the universal process.

An exclusive etching technique for fabricating perforated (filigree) magnesium micro components with metal wire widths of the order of the metal thickness using a photochemical machining (PCM) process was developed and optimized [85]. Etchant temperature, concentration and volume, workpiece orientation and metal thickness were controlled in experimental demonstration of PCM. Metal wire widths of 0.15 mm and 0.25 mm thick magnesium foil was fabricated for use in micro air vehicle (MAV) wings or

stents. This etching process varied from the industrial etching process used to manufacture magnesium letterpress printing plates and embossing dies. Hydro-Solve was best-suited photoresist for etching magnesium.

The application of Artificial Neural Network (ANN) for the prediction of undercut in the photochemical machining (PCM) process of SS430 was presented by Saraf *et. al.* [86]. The etching time, etching temperature and etching concentration were used as inputs to the ANN model. A Feed Forward Back Propagation Network (FFBPN) was used to predict the undercut for effective and economic production. The various neural network architectures were considered by changing the number of neurons in the hidden layer. A FFBPN with eight neurons in the hidden layer had been selected as the optimum network. The experimental results show that the ANN model can be used to predict the undercut in PCM in response to machining parameters. Artificial intelligence approaches such as Genetic Algorithm (GA), Simulated Annealing (SA), Ant Colony Algorithm (ACO) and Particle Swarm Optimisation (PSO) were left for future research.

Tehrani *et. al.* [87] examined the process to reduce pitting and obtain better surface finish in chemical machining of stainless steel SS304. A new etchant (H_2O + HCl + HNO_3 + HF + H_2COOH + TEA) was presented for chemical machining of SS304. Experimental results gave good surface finish without any pitting while high machining rate was achieved. Adding 5–10% of TEA to the etchant solution improved surface roughness. Increasing the temperature of the etchant increased the oxidising power (machining rate) and decreased the surface finish values. Adding 5–10% of TEA to the etchant solution decreased the difference between the rate of corrosion of metal grain and grain boundaries, which resulted in better surface finish. The etchant was tested at numerous temperature values and different depths of machining and the results were compared with other etchants.

Roy *et. al.* [88] classified the costs involved in Photochemical Machining (PCM) and presented a cost model for PCM using bottom-up approach. IDEF3 methodology was used in illustration (Work Breakdown Structure, WBS) to categorize the process of PCM. IDEF3 maps were used to allocate the cost drivers of each operation and to build the cost model. The cost drivers for the PCM manufacturing process was recognized. The cost model was developed using WBS and cost drivers, which was more appropriate for stainless steel machining. The cost model was suitable for activities like product costing, process optimisation, and cost controlling. The model was validated by judgement of experts on case studies. Cost model created here can be improvised to comprise additional PCM techniques to machine other materials.

Deepak Kumar *et. al.* [89] explored the effect of the rolling direction on the surface finish and etching depth. Monel 400 alloy was fabricated with microchannel on its surface having widths of 60, 100, 150, 200, and 250 μm. The experimental results discovered that the quality of the microchannel surface finish was smoother along the rolling direction than across the rolling direction, due to the grain boundary orientations along the (001) plane. The etching depth increased along the rolling direction due to the presence of residual stress and plastic strain, which finally improved the microchannel quality. It was proved that lattice plane orientation played vital role in the microchannel etching of Monel 400 alloy.

Metal Matrix Composites (MMCs) have applications in aerospace and automotive industries due to high strength to weight ratio and elevated temperature resistance. Agarwal *et. al.* [90] developed aluminium based silicon carbide particulate MMCs and optimized the process parameters in photochemical machining of composites. Effect of numerous control parameters such as etching time, temperature of etchant and concentration of etchant on Material Removal Rate, Undercut and Etch factor in PCM of Al/SiC has been detected by using integrated DoE and Grey Relational Analysis. Training of ANN model was done

using experimental results and it performed reasonably for trend analysis of given experimental set. The optimal machining parameter was observed at etching temperature of 60^{o}C, etching concentration of 700 gm/lit. and etching time of 12 minutes. The result obtained from experiments verified that improvement in the machining was achieved by setting optimum machining parameters.

Wangikar *et. al.* [91] optimized the Photochemical Machining (PCM) of brass and German silver using ferric chloride as etchant. The effect of concentration of etchant, etching time, and temperature of etchant (PCM parameters) on surface roughness, material removal rate, and edge deviation was analysed. To minimize edge deviation and surface roughness and to maximize material removal rate, overall evaluation criteria (OEC) was formed by assigning different and equal weight percentage to these parameters. The optimized condition for particular OEC was attained by observing the effect of PCM parameters. Experiments were carried out, which presented that concentration had biggest effect and etching time had least effect on surface roughness, material removal rate, and edge deviation. The surface roughness and material removal rate increased with increase in concentration, temperature and etching time but edge deviation decreased with increase in etching time. The surface roughness was lower for brass, while the edge deviation was lesser for german silver. The material removal rate was higher for brass compared to german silver.

Photochemical Machining (PCM) of stainless steel (SS-304) by ferric chloride as etchant was examined by Agarwal *et. al.* [92]. Weighted Grey Relational Analysis (WGRA) technique was used to optimize the concentration of etchant, etching time, and temperature of etchant (PCM parameters). Weighted grey relational grade was calculated to minimize undercut and surface roughness and to maximize material removal rate and etch factor. The optimized parameters were used to manufacture the microfluidic channel and its assembly

which are required in biomedical application. 750 gm/lit of etchant concentration, 60°C etchant temperature and 50 min of etching time provided the optimum process conditions. It was observed that surface roughness and material removal rate increased with increase in the temperature and time of etchant. This increase was also detected for increase in concentration of etchant up to 650 gm/lit. The dimensions of microfluidic channel and surface topography was studied, which showed the increase in voids across the grain boundary and irregularities across the surface with increase in time, temperature and concentration of etchant.

Pryor and Brock applied peroxydisulphuric acid for the etching of copper alloys and felt the requirement of a cooling system at relatively higher etching temperatures [93]. Ueda found higher etching temperatures produces higher etching rates in copper etching with $FeCl_3$ etchants [94].

The prediction model of the etched topology of circle and right triangle dimples has been proposed with varying etching time for effective machining of carbon steel [95]. The optimization of process parameters in PCM of SS316L is reported for undercut (Uc) and MRR using GRA method [96].

Allen and Cakir investigated various etching parameters in the PCM of copper alloys etching with mainly $CuCl_2$ and $FeCl_3$. HCl additions to CuCl2 etchant were used. They observed that $FeCl_3$ produced better etch rate than $CuCl_2$ only, but the addition of HCl to $CuCl_2$ increased etch rate. High etchant concentration and etching temperature increased etch rate and produced a better surface quality [97], [98].

According to Arrhenius equation [94] using a higher temperature, gives a higher etch rates

$$V = A\, e^{\frac{-E}{R_g T}} \qquad \text{--- (2.8)}$$

where V is Etch rate

A is Frequency factor

E is Arrhenius activation energy

R_g is Universal gas constant

T is Temperature

Visser [99] studied the effect of temperature, using $FeCl_3$ for various stainless steels and indicated that according to Van'tHoft's Law a higher temperature would produce a higher etch rate.

2.10 Gap Areas

The research is aimed at understanding and improving the currently practised hybrid manufacturing process, to have consistent functional acceptance by generating enhanced quality micro-grooves on CuBe alloy components. Based on a detailed literature survey, following gaps have been identified:

1. Influence of different gaseous environmental conditions on Excimer Laser Micro machining (ELM) of polymer.
2. ELM of polymer in gaseous environment, especially under hydrogen and its effect on mass removal and edge definition of the machined geometrical feature.
3. Investigation on the mechanism of material removal during excimer laser micromachining of polymers under hydrogen gas.
4. Comprehensive study of laser lithography involving chemical micro machining
5. ELM of different polymer under H_2 environment with varying wavelength
6. Molecular Dynamics Simulation (MDS) of ELM under gaseous environment
7. Study of chemical micro machining of Cu-Be alloy vis-a-vis plain copper.

8. Effect of Excimer laser micro machining on the quality of the final product made by chemical micro machining.
9. Understanding the mechanism of chemical micro micromachining of Cu-Be alloy.
10. Development of environment driven ELM for enhanced quality and higher throughput.
11. Development of Data Driven Prediction Models (DDPMs) to find the depth of ablation of excimer laser micro machined feature.

These gap areas show that there is a need for in-depth scientific understanding and detailed investigations in the field of excimer laser lithography under different gaseous environment and also chemical etching of Cu-Be alloy material.

2.11 Scope of Work

The scope of research work is found to be enormous and following research work was identified to be carried out.

1 Study of Excimer Laser Micromachining (ELM), as part of the first step of lithography, under various gaseous environments, with a view to enhance the machining rate and edge definition of machined feature.

2 Understanding mechanism of ELM under H_2 environment.

3 Developing Mathematical model and FEM simulation on excimer laser micromachining of polymer under H_2 environment.

4 Experimental investigation in chemical micromachining of Cu-2%Be alloy vis-à-vis pure copper.

5 Development of data-driven process models, namely, Response Surface Methodology (RSM), Linear Regression (LR), Gaussian Process Regression (GPR),

Support Vector Machines (SVM) and Artificial Neural Network (ANN) to predict the ablated depth of laser micro machining under hydrogen environment.

6 Experimental investigation and Optimization of both laser and chemical micromachining processes.

The research works need to carry out various activities, and these activities have been mentioned as per the research work plan of this Ph.D. thesis is shown in Figure 2.9.

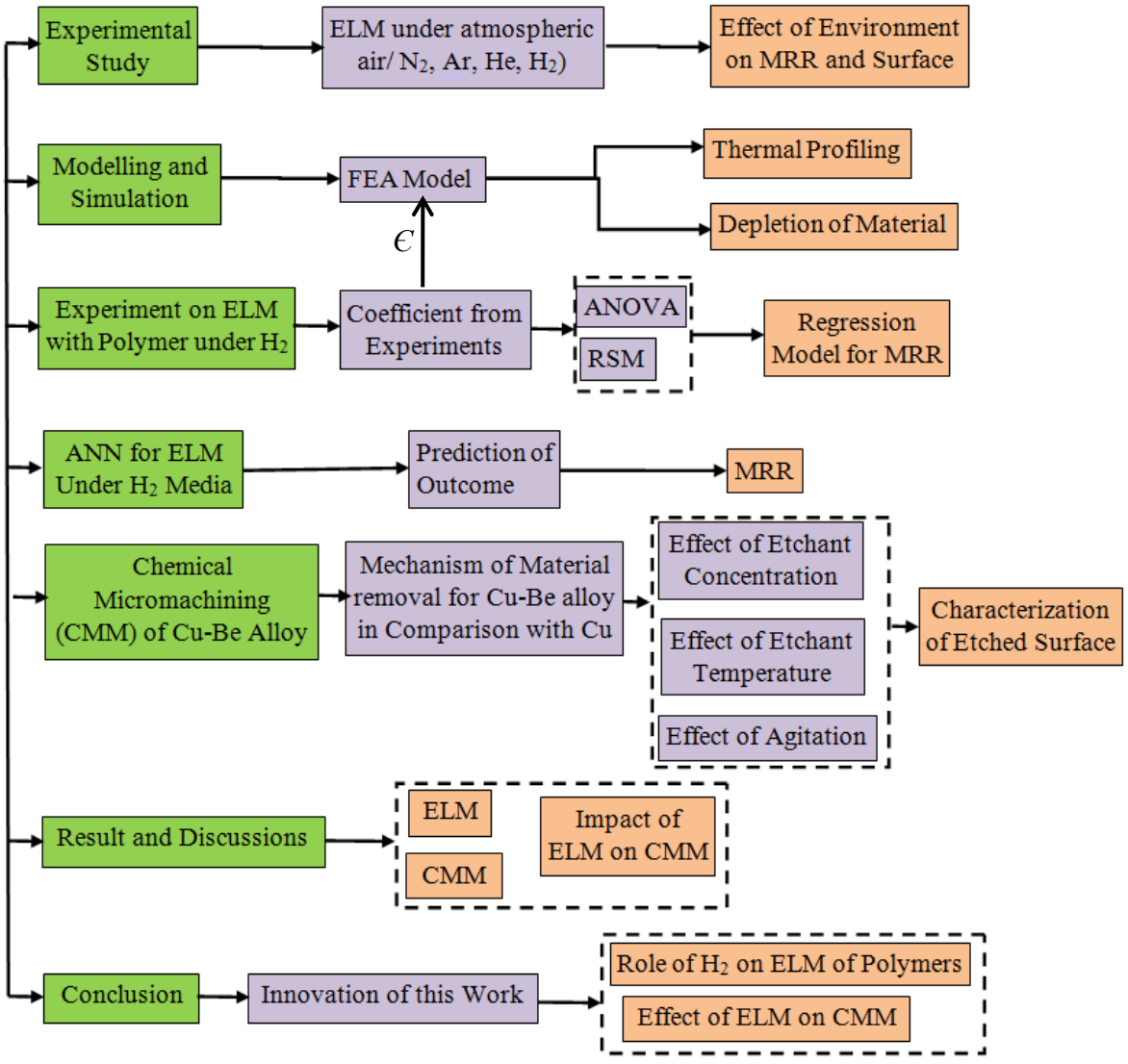

Figure 2.9 Research Plan

Chapter 3

Experimental Study of Excimer Laser Ablation under Different Gaseous Environments

3.1 Introduction

Non-conventional, non-contact type advanced machining process like laser based micro machining process is widely used in modern industries for producing components with geometrically complex profiles. Though laser based micro machining of polymer, by and large, is a cold ablation process, photo thermal process associated with the laser heating may affect the surface characteristics. The present chapter describes the experimental studies on excimer laser ablation of Photoresist polymer in different gaseous environment, viz, Air, N_2, Ar, He and H_2, with an intention to have enhanced MRR and edge definition of the machined feature. A negative photo resist, E-1020 obtained from M/s Cadmosil Chemical Pvt. Ltd, India has been studied using 248 nm KrF Excimer laser. The effect of gas purging on the ablation rate and surface characteristics of the polymer has been studied. Amongst the gases used, hydrogen gas showed distinct results with respect to ablation rate and surface characteristics.

Limited information is available on the use of gaseous coolants during laser ablation of polymeric materials. Hence, this study has been primarily focused on establishing the effect of certain gaseous environment on the ablation rate of polymer during excimer laser ablation. Attempts have also been made to study whether the usage of gaseous cooling media in the laser ablation process has any meaningful bearing on the surface characteristics of the work piece. Five different gaseous media viz, hydrogen, helium, argon, nitrogen and air were selected for the study. Among these gases, hydrogen and helium possess higher thermal

conductivity than the other three gaseous media used in the experiment. The details of the experiments along with the results and observations are presented in this chapter.

3.2 Experimental Setup

Excimer laser ablation system comprising of KrF laser source LPxPro 305 of Coherent make(wavelength of 248 nm and pulse duration of 25 ns), Beam Delivery unit (consisting of attenuator, homogenizer, photo-mask, projection lenses), CNC controlled X-Y table with vacuum chuck and pulse energy monitor, were used for this study. This experimental setup is shown in Figure 3.1. The technical details of system used is given in Table 3.1. Excimer laser pulse with a pulse duration of 25 ns (FWHM) and wavelength of 248 nm is generated for the experiment. A circular mask of 20 mm dia. is used to produce the 5mm dia. flat hole on the polymeric layer of workpiece. The pulse repetition rate was fixed at 20Hz with variable pulse energy for generating data.

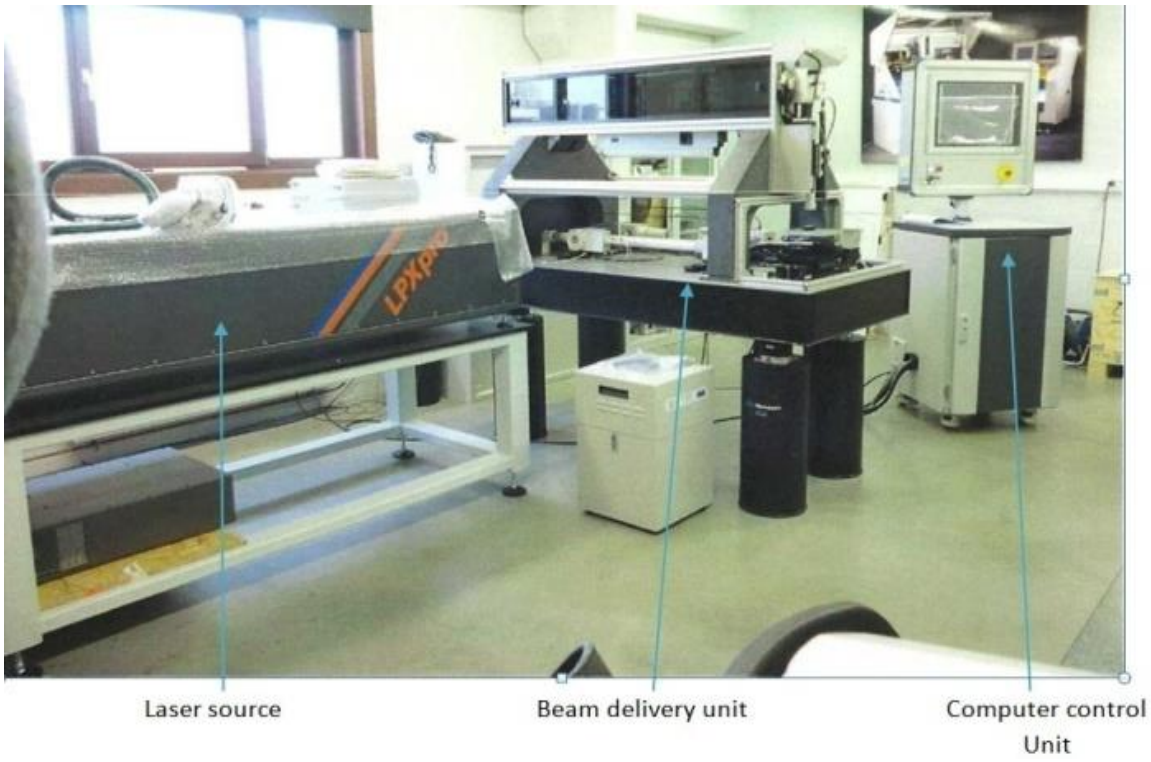

Figure 3.1 Photograph Showing Different Components of Experimental Setup

Table 3.1 Specification of Excimer laser system

Laser type	Excimer
Laser Media	KrF
Wavelength (nm)	248
Maximum Pulse Energy (mJ) at source	1000
Max. Average Power (W)	50
Maximum repetition rate (Hz)	50
Pulse Duration (FWHM, ns)	25
Pulse-to-Pulse Stability	± 1.5 %
Beam Dimensions	10mm x 30mm
Beam Divergence	1 x 3 mrad (V x H)
Spot size on mask plane	30mm x 30mm
X-Y Stage Travel and repeatability	250mm x 150 mm; ± 1 μm
Z-Focus Stage range and repeatability	200 mm; ± 1 μm
Fume Extraction	HEPA filter based suction

3.2.1 Laser Source

Excimer LPX-305 laser source with Krypton Fluoride (KrF) as active laser medium which operates at a wavelength of 248 nm was used for the ablation studies involving organic photoresist polymer E1020, sourced from M/s Cadmosil India. The LASER source used for experiments have following components:

1. An active laser medium capable of emitting laser light
2. An optical resonator for the amplification of the laser light
3. An energy source to stimulate the emission of laser light

Functional block diagram of the laser source LPX-305 LASER source is given below in Figure 3.2.

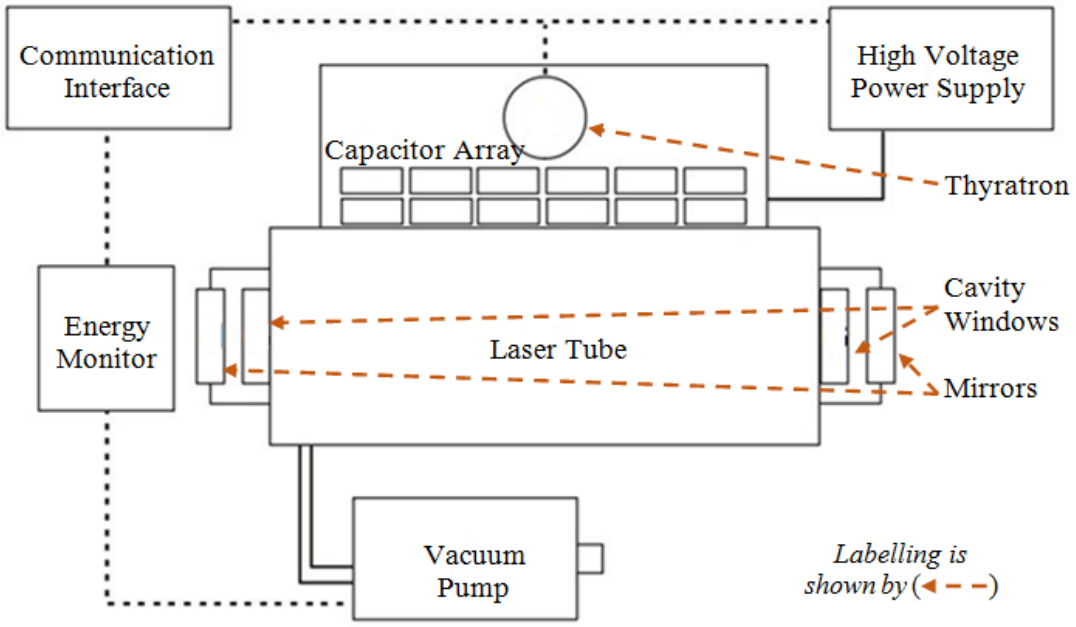

Figure 3.2 Block Diagram of LASER Source

3.2.2 Laser Control System

The Communication Interface (CI) is the central control module. Limited tasks are carried out separately by dedicated sub modules such as the gas handling module, energy monitor and the High Voltage (HV) power supply. The individual modules communicate through a data ring made up of fiber optic light wave guides (FOLs). The user interface to the laser control system is the handheld keypad or external control PC. The LPX-305 operates as a pulsed laser. The electrical discharge and, consequently, the emission of the individual laser light pulses can be triggered either internally or externally. Triggering occurs continuously at the repetition rate (Pulse frequency) set by the user through the laser control software. With external triggering, the laser light pulses are triggered from an external trigger generator that is connected to the external trigger socket on the industrial computer. The fundamental layout of the control system for the LPX-305 shown in Figure 3.3.

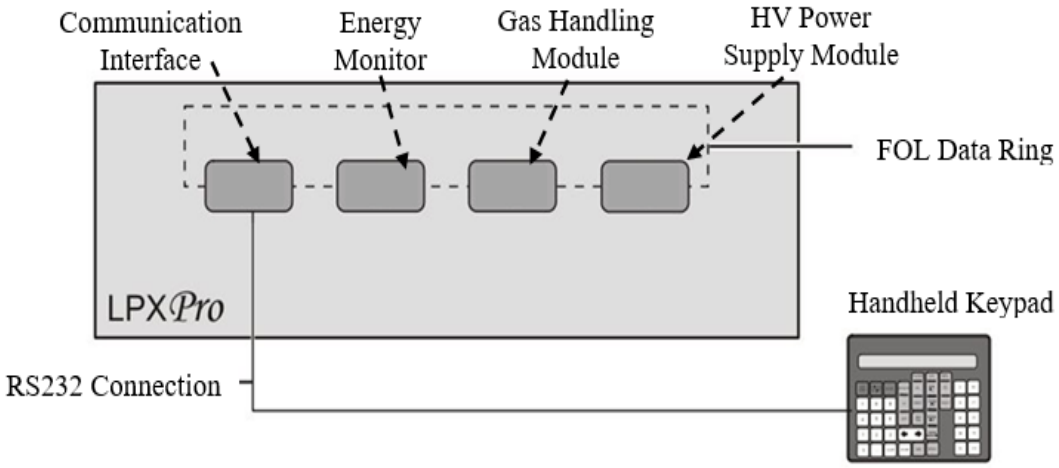

Figure 3.3 Block Diagram of LASER Control System

3.2.3 Beam Delivery Unit

Beam Delivery Unit (BDU) shown in Figure 3.4 consists attenuator, homogenizer, photo-mask, projection lenses, CNC controlled X-Y table with vacuum chuck and pulse energy monitor, was used for the present study. The Raw laser beam of 15mm x 30mm cross section enters the BDU at point number 1 indicated in Figure 3.4. The whole path of the beam, as it travels through the different optical elements of steering mirrors, beam condenser telescopes, homogenizer arrays, field lens, photo-mask, inspection microscope, projection lens marked as 1-2-3-4-5-6-7-8-9-10-11-12-13, until it reaches the job placed at the X-Y table of the BDU. Such a long and folded beam path is provided; first, to satisfy the basic lens formula $\frac{1}{f} = \frac{1}{u} + \frac{1}{v}$ of the projection lens and second, to make the installation a compact one. The experimental setup consisting of beam delivery unit is shown in Figure 3.4. The schematic of beam delivery system along with workpiece is shown in Figure 3.5.

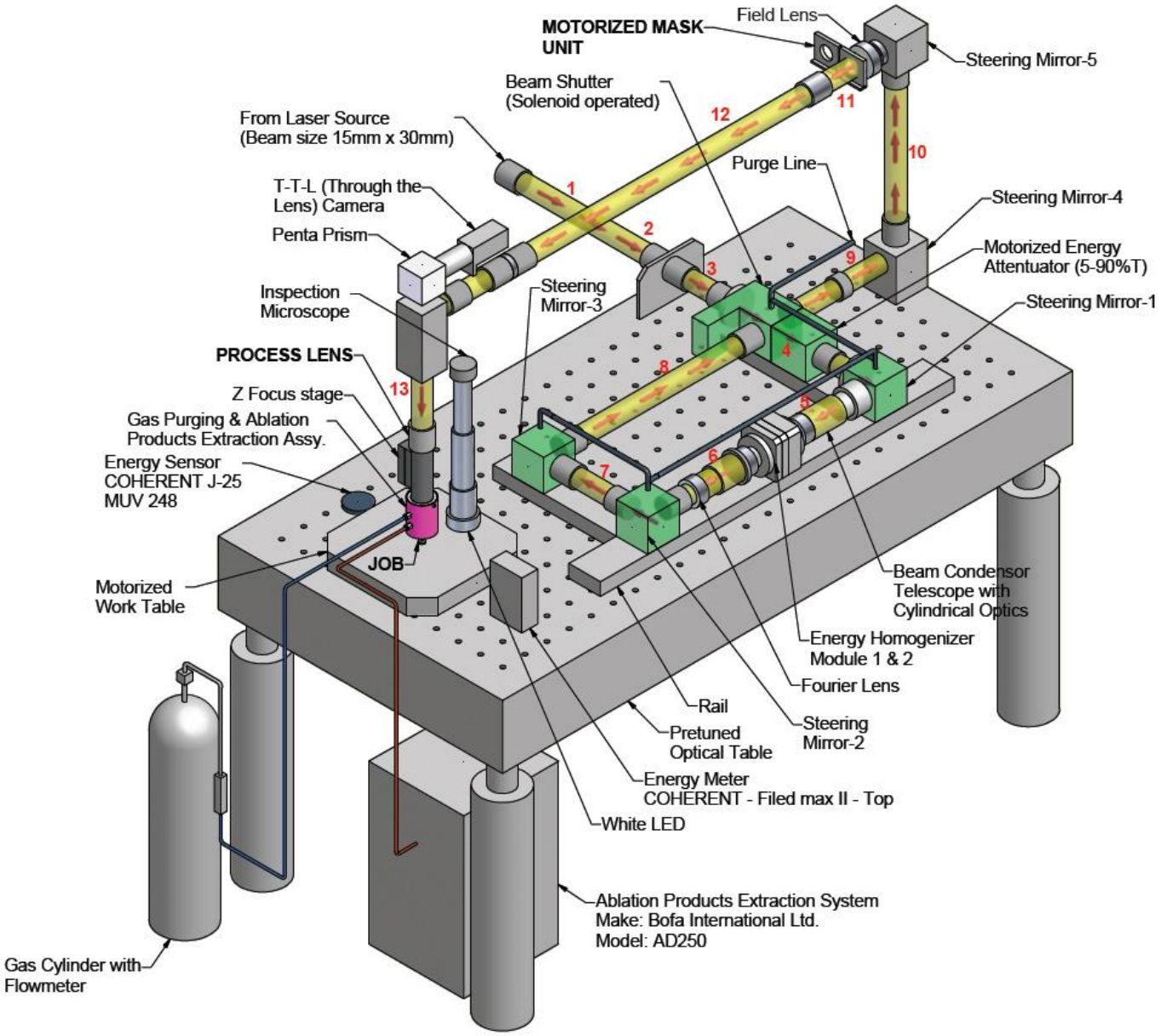

Figure 3.4 Excimer Laser Beam Delivery Unit

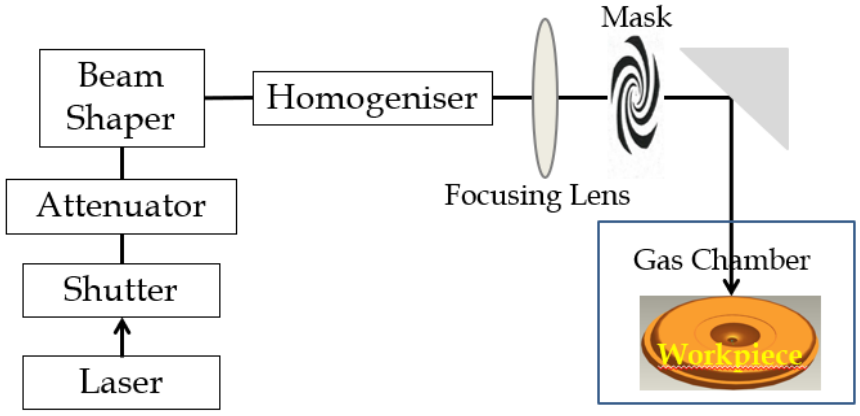

Figure 3.5 Schematic Representation of Experimental Setup

3.2.4 Gas Handling Setup

Gas handling setup used for Preliminary Ablation Experiments as shown in Figure 3.6 was fabricated for purging gas at desired flow rate over the surface of polymer during the laser ablation process [100]. Compressed gases are stored separately in different 20 litre cylinders which are connected to setup and isolated with valve. Flow rate of gas is manually controlled by valve and reading is measured with rotameter. Sectional view of gas purging and ablation product extraction assembly exclusively developed for the present work, is shown in Figure 3.7. The manifold consists of a cylindrical chamber, made up of SS 304, having an effective volume of 100 ml, which was used for photoresist removal study. The chamber has inlet and outlet valves. The chamber can be evacuated with rotary pump or gas could be admitted at a required flow rate. A calcium fluoride window of 50 mm diameter was fixed over ablation chamber, normal to laser beam axis.

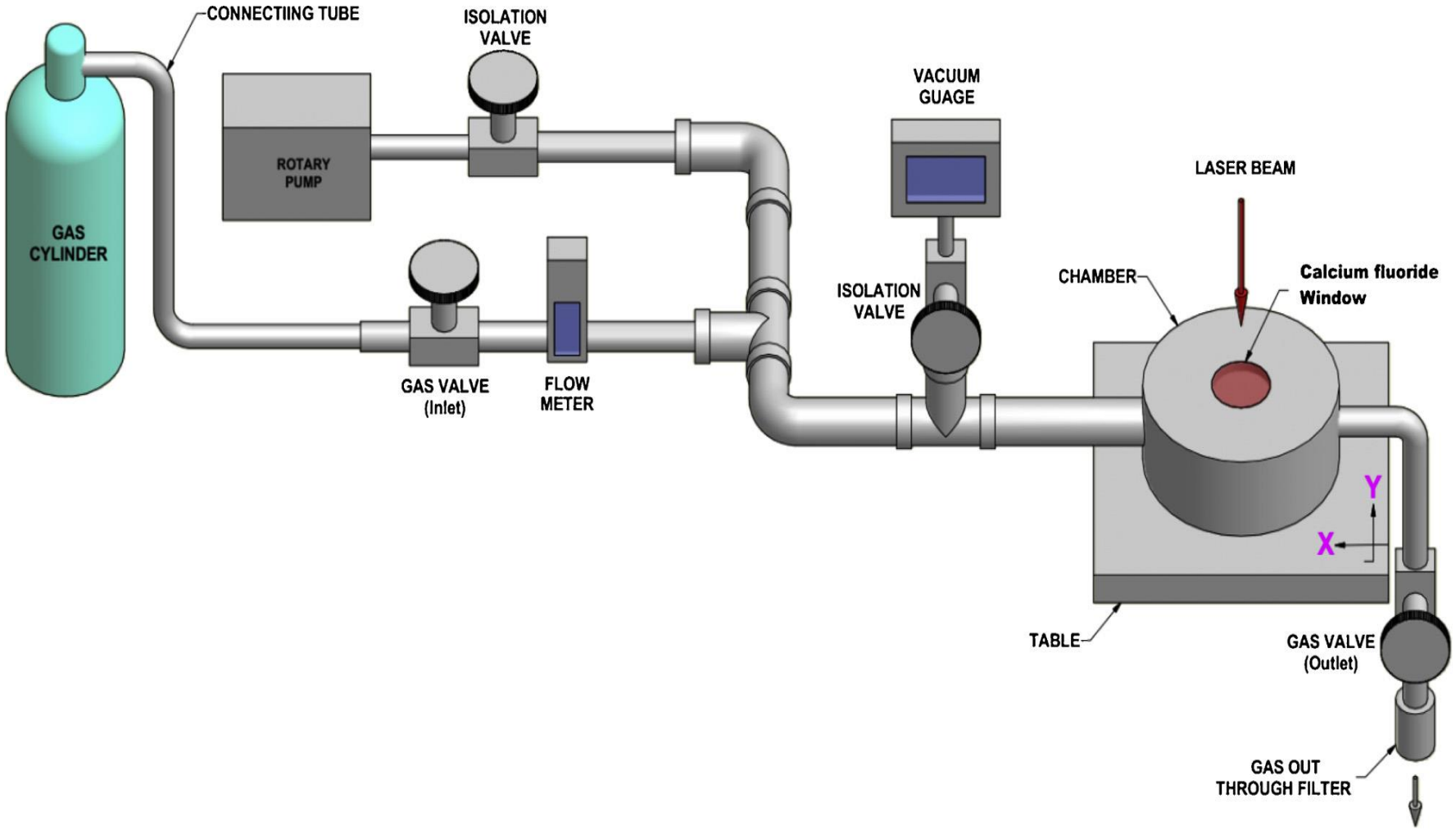

Figure 3.6 Gas Handling Setup used for Preliminary Ablation Experiments

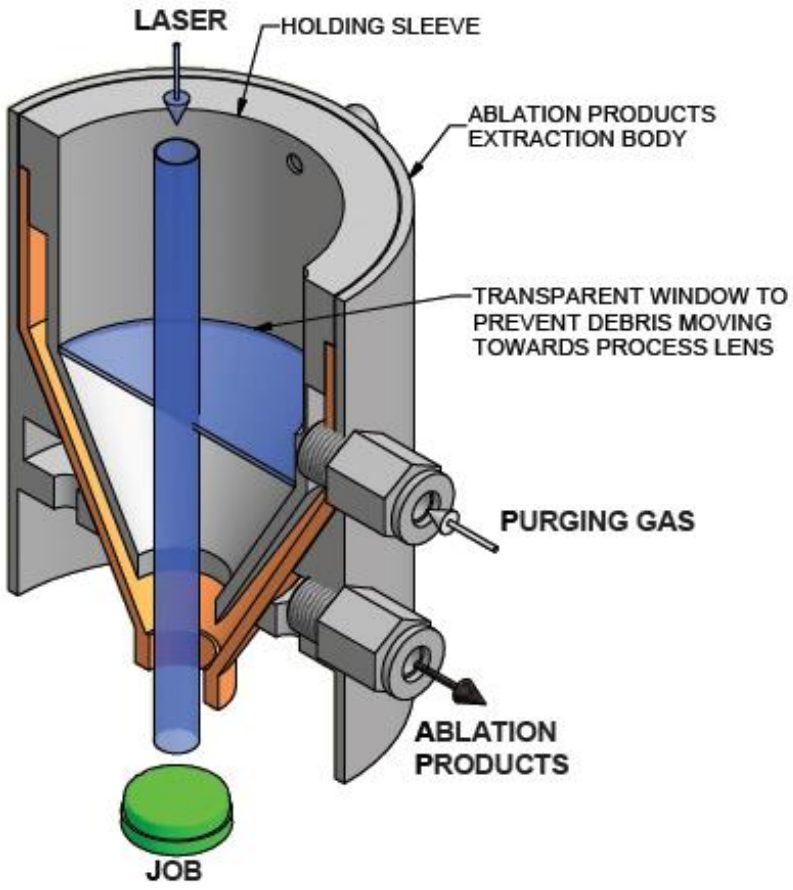

Figure 3.7 Sectional View of Gas Purging and Ablation Product Extraction Assembly

Gas Handling Setup used for detailed ablation experiments for hydrogen is shown in Figure 3.8. The gas handling setup contains Hydrogen which makes it necessary to be leak proof for maintaining industrial safety. Mass Spectrometric Leak Detector (MSLD), Model Number ASM 192 T2 Alcatel, France was used to qualify leak tightness of all joints present in gas handling setup. The important technical specifications of the MSLD equipment are shown in Table 3.2. The working of MSLD equipment is explained later in this section.

Table 3.2 Technical Specifications of the MSLD Equipment

Sr. No.	**Specifications**	**Description**
1.	Make	Alcatel Vacuum Technology, France
2.	Model No.	ASM192T2
3.	Vacuum Circuit	Shown in Figure 3.10

Sr. No.	Specifications		Description
4.	Pumping Capabilities		50 m^3/h (Approximately) 100 l/s (for Turbo Molecular Pump)
5.	Leak Testing Methods		1. Spray Method * 2. Sniffing Method 3. Bombing Method
6.	Measurement range for Spray Method (He) (High sensitivity test mode)		$1x10^{-11}$ to $3x10^{-4}$ mbar.l/s
7.	Analyser cell	(a) Filament	2 tungsten filaments
		(b) Sensitivity	3×10^4A/mbar
8.	Start-up time (at 20°C)	(a) Without auto-calibration	3min 10s ±10%
		(b) With auto-calibration	4min 30s ±10%
9.	Time to reach test mode- Hard Vacuum Test (High Sensitivity test mode)		4s (Inlet port blanked-off)

* In this experimental study, Spray method is used.

The description of valves used to control gas flow in experimental setup is given in Table 3.3. Gas handling setup operation steps are explained below in detail.

- Switch on the Rotary vane vacuum Pump for evacuate the gas handling setup.
- Turn on the valve No. V-101, when we open evacuating starts then open the valves No. V-102, V-103, V-104, V-105 and V-108 for complete evacuating the setup.
- Open the valve No V-106 for measuring the vacuum in the Vacuum Gauge.
- After reaching required range vacuum close the valve No. V-101 and V-102, V-103, V-104, V-105 and V-107.
- Open gas cylinder No-1-cylindervalve and regulate the Pressure. For 01 bar then open the valve No. V-102 measure the pressure at pressure gave up to 1 bar.
- Close the valve No V-102 and gas cylinder valve.
- Open gas cylinder No.2-cylinderValve and regulate the pressure for 2 bar then open the valve No. V-103 observe the pressure 2 bar gauge.

- After reaching the required pressure close V-103 and gas cylinder valve.
- Open the valve No V-104 to flow the gas towards humourized Laser beam and control the gas flow by throttling the flow with flow control valve No V-105 and flow can be measured in the flow meter.

Table 3.3 Valves Description of Gas Handling Setup

S. No	**Valve no**	**Description**	**Specification**
1.	V-101	Vacuum Isolation Valve	Swage Lock Make 1/2" Diaphragm Valve
2.	V-102	Hydrogen Gas Inlet Valve	Swage Lock Make 1/2" Diaphragm Valve
3.	V-103	Argon Gas Inlet Valve	Swage Lock Make 1/2" Diaphragm Valve
4.	V-104	Gas Outlet Valve	Swage Lock Make 1/2" Diaphragm Valve
5.	V-105	Flow Control Valve	Swage Lock Make 1/2" Bellow Sealed Valve
6.	V-106	Isolation Valve	Swage Lock Make 1/2" Diaphragm Valve
7.	V-107	Exhaust Valve	Swage Lock Make 1/2" Diaphragm Valve
8.	V-108	Pressure Gauge Valve	Swage Lock Make 1/2" Diaphragm Valve

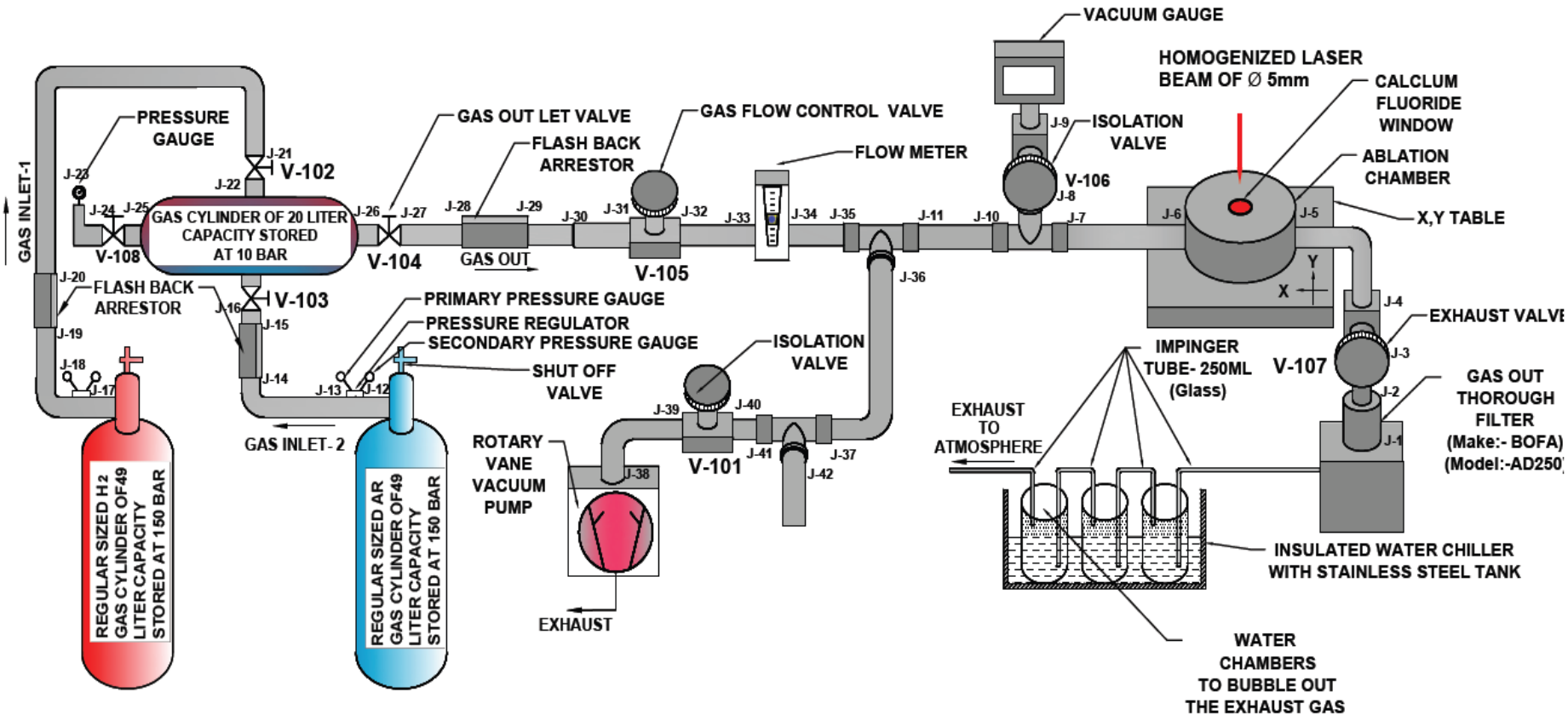

Figure 3.8 Gas Handling Setup used for Detailed Ablation Experiments for Hydrogen

3.2.5 MSLD

As can be seen from Figure 3.8, the gas handling setup has 41 joints which needs to be qualified for leak tightness to follow industrial safety norms of using hydrogen gas. Mass Spectrometry Leak Detection (MSLD) setup as shown schematically in Figure 3.10 was attached with the gas handling setup at joint no 42. Detailed procedure for MSLD is explained later in this section.

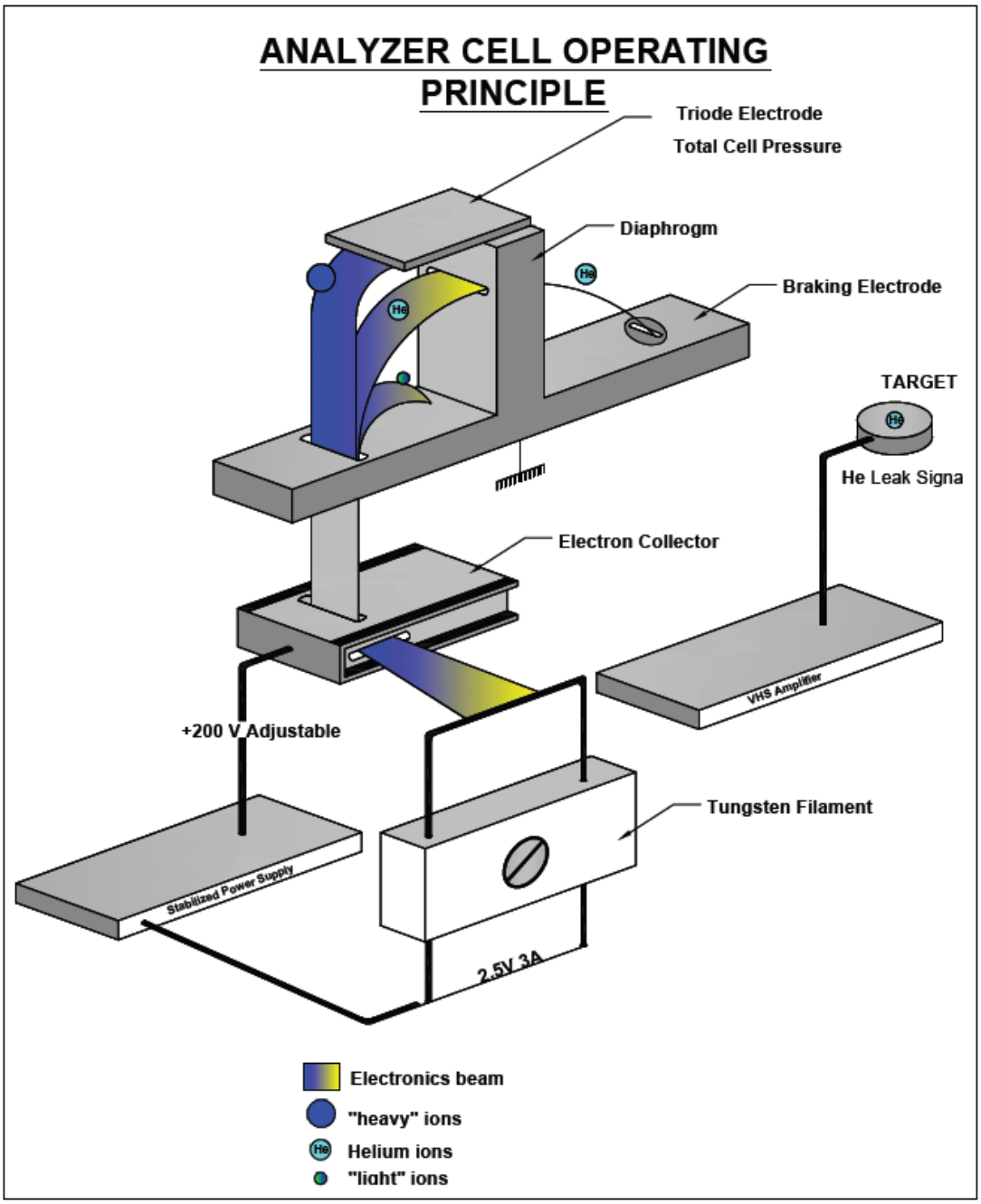

Figure 3.9 Helium Dectector

Figure 3.9 shows the schematic representation of helium detector working. Gas molecules sucked from gas handling setup is ionized by tungsten filament and later accelerated in electric field. These fast-moving ionised gas molecules are subjected to magnetic field in such a way that only helium ions will pass through a window and others are blocked. Helium molecules passed through this window are detected gives the leak rate.

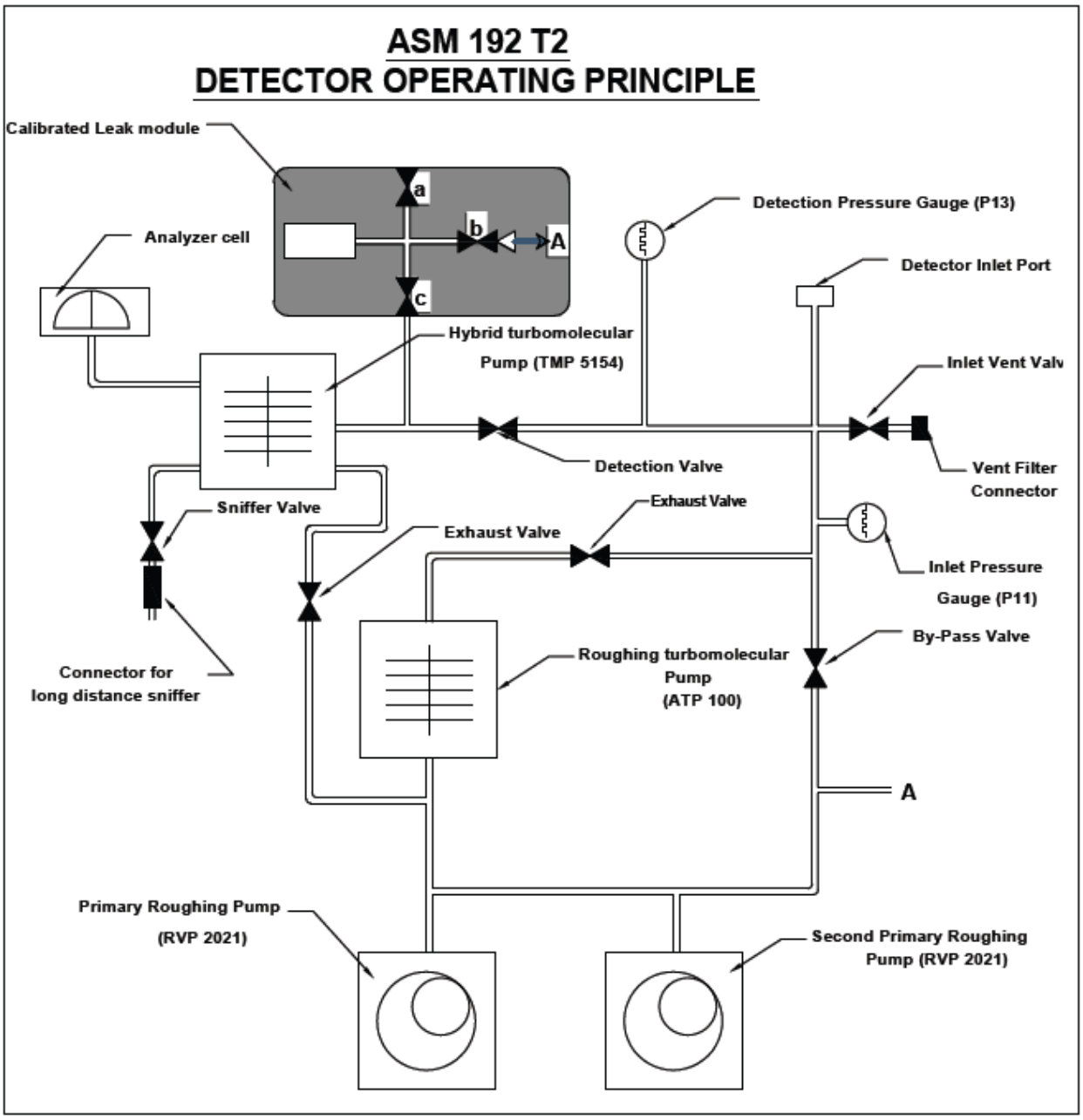

Figure 3.10 MSLD Setup

Gas handling setup operational steps, to certify it for its very high level of leak tightness, using the MSLD are explained below in detail.

- Switch on the MSLD setup and proceed after completion of Auto calibration only.
- Switch on the cycle on the MSLD remote, open the V109 valve to evacuate the gas handling setup.
- After getting high sensitivity mode on MSLD, start probing Helium from joint No. 1 to joint no 11 and note the reading for each joint.
- 2 min time gap is maintained between the probing of one joint to next joint.
- Repeat the same procedure for probing the joints from joint No-12 to joint no-41.
- The gas handling setup has been cleared for an average leak rate of $1.5x10^{-10}$ mbar.lt/s.

3.2.6 Photoresist

A commercially available photoresist polymer E1020 (supplied by M/s Cadmosil Chemical Pvt. Ltd, India) was used for the manufacture of micro grooved metallic parts using the two-stage process of excimer laser lithography of photoresist coated metallic workpiece followed by chemical micromachining.

A film thickness of about 5000 μm was used as a precautionary measure in the experiment in such a way that laser beam does not reach the metal surface.

3.2.7 Photoresist Coating on Metal Substrate

Metal substrate of stainless steel cylindrical cups (50 mm dia. x 5 mm depth) were used, and an epoxy based photoresist is filled and cured. The filling was dried by air and subsequently cured at 110^{o}C for 1 hour under vacuum (10^{-2} mbar absolute pressure). Figure 3.11 shows vacuum baking setup which was manufactured for curing of polymer layer on workpiece. The experimental setup had rotary vane pump for achieving 10^{-2} mbar

absolute pressure and heating coil to maintain 110 ^{o}C temperature. The setup had a capacity of holding more than 60 workpiece inside vacuum chamber for this process.

Uniform coating thickness of the polymer layer, free from entrapped gases, was attained by following the above mentioned procedure using this experimental setup. The test samples were placed inside the ablation chamber of the gas handling system and mounted on the X-Y stage of laser ablation system for photoresist study. Spring loaded jig arrangement was used to fix workpiece on X-Y table. The movement of this motorized X-Y table which has had a resolution of 1 µm was controlled by CNC programme.

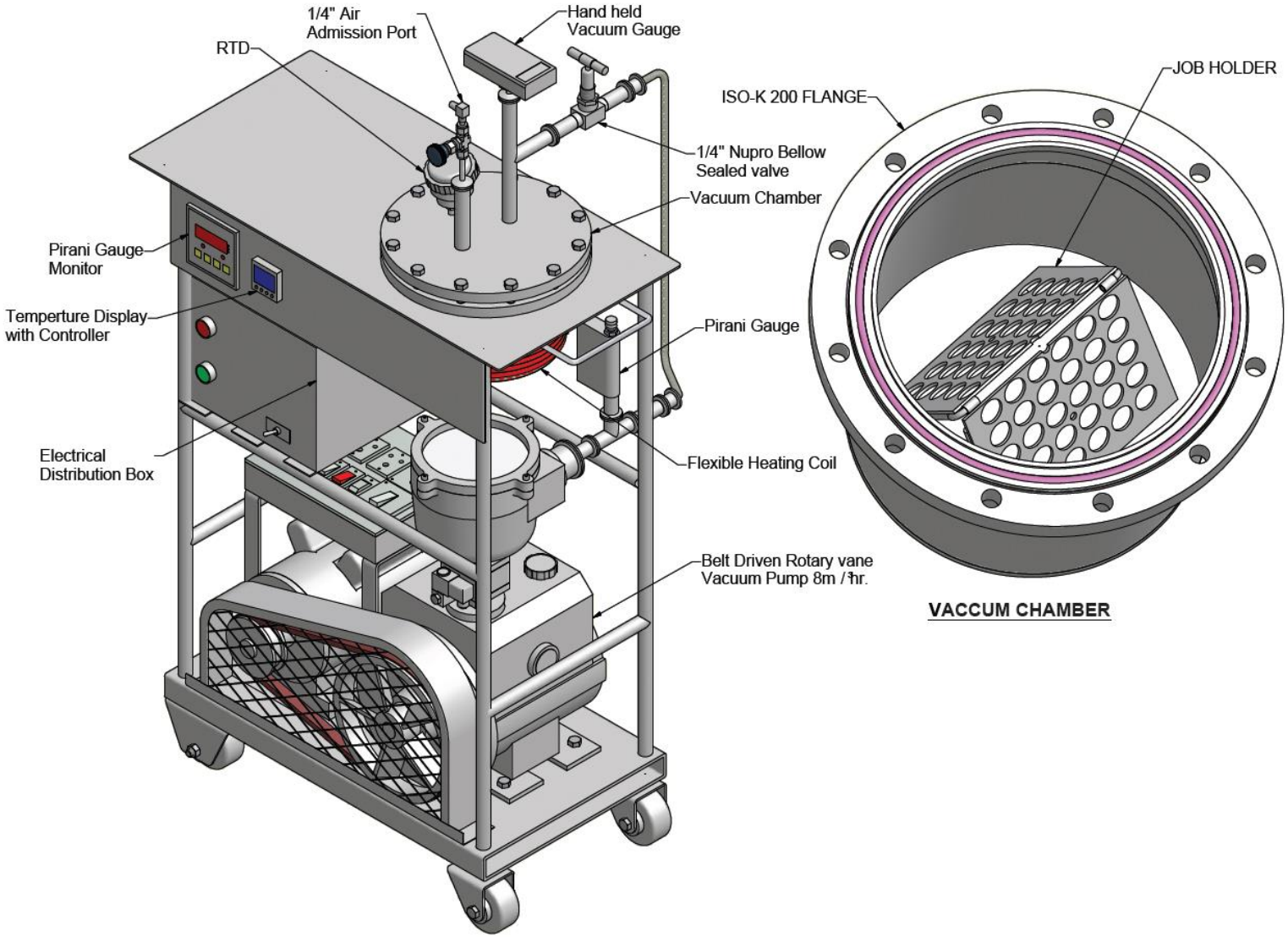

Figure 3.11 Vaccum Baking oven for Curing of Polymer Layer on Workpiece

3.2.8 Experimental Procedure

The workpiece undergoes various pre-processes before carrying out excimer laser ablation for removal of photoresist polymer which are listed below.

1. Raw material of CuBe alloy is machined by CNC to achieve desired shape and dimensions.
2. Machining on DTM is carried out for accomplishingN2 surface finish which is qualified after inspection on Ultra Precision 3D-CMM model UPMC850 CARAT, of Zeis German.
3. Ultrasonic cleaning of workpiece is carried out using ethoxy ethanol as solution.
4. Water washing of workpiece is done to remove ethoxy ethanol and later heated at 80^{o}Cunder vacuum for removing water.
5. Workpiece is coated with photoresist polymer by dipping method and kept 24 hrs for drying of polymer layer.
6. Workpiece is baked at 100 ^{o}C for 5 mins for proper bonding between polymer and workpiece surface
7. Ablation of polymer from workpiece surface is carried out on experimental setup which is shown in Figure 3.1.
8. Chemical Micromachining of workpiece is carried out to generate grooves on workpiece.
9. Photoresist polymer is stripped by ethoxy ethanol in ultrasonic cleaning and final product is produced.

Present study is focused on ablation of polymer by excimer laser. Hence, procedure related to that process only is explained below. The polymer coated workpiece was fixed on a spring-loaded fixture and this fixture was held by vacuum chuck on X-Y table. The

workpiece is aligned (Matching the Centre of workpiece with Laser beam centre) by manoeuvring X-Y table using industrial computer. Live image of workpiece is shown by 'Through The Lens' (TTL) camera on computer screen with Laser beam centre marking. Schematic representation of workpiece fixed on X-Y table is shown in Figure 3.12. Once the workpiece was aligned, the excimer Laser parameters fed into computer to carry out ablation of polymer.

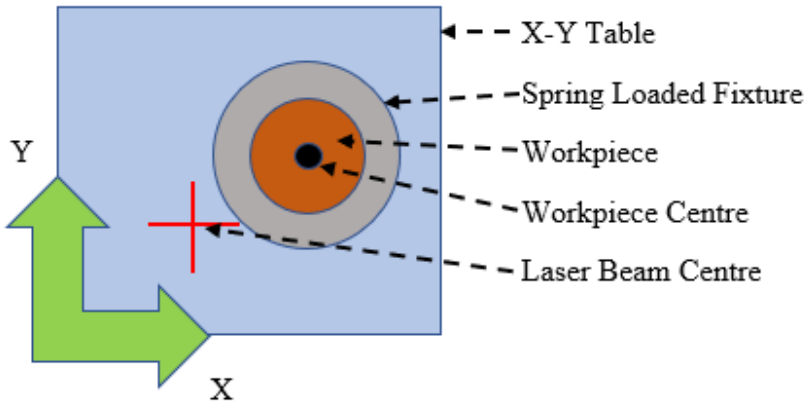

Figure 3.12 Schematic Representation of Image Shown by Through the Laser Camera

3.2.9 Design of Experiments

The gases used for study include hydrogen, helium, nitrogen, argon and air. These five gases were selected for study based on their thermal conductivity values, as shown in Table 3.4, covering a range between 17×10^{-3} W/m.K and 287×10^{-3} W/m.K [101]. In order to compare the photoresist removal process under various gaseous media, the photoresist has exposed to 2000 laser shots under various experimental conditions. For each gaseous medium, totally 36 numbers of experiments were carried out under different parameters as shown in Table 3.5.

Table 3.4 Thermal Conductivity of Different Gases

S. No.	Gas	Thermal Conductivity at 300 K (W/mK x 10^{-3})
1	Argon	17.9

S. No.	Gas	Thermal Conductivity at 300 K (W/mK x 10^{-3})
2	Nitrogen	26
3	Air	26.2
4	Oxygen	26.6
5	Helium	156.7
6	Hydrogen	186.9

Table 3.5 Experimental Input Parameters

Levels for Laser pulse energy (mJ)	30, 40, 50, 60	4 no.
Levels for Pulse repetition rate (Hz)	20, 30, 40	3 no.
Levels for Gas flow rate (lpm)	0.8, 1, 1.2	3 no.
No. of Gases	H_2, He, Ar, N_2, Air	5 no.
No. of repetitions	Triplicate	3 no.
Total Experiments	540 no.	

The Full Factorial experimental design was employed for the design of the experiments to evaluate the effect of three operating parameters, i.e., gas flow rate (l/min), pulse repetition rate (Hz) and laser energy(mJ). These selected parameters are considered as the independent variables and the amount of photoresist ablated (μm) after 2000 laser pulses of irradiation was selected as the dependent variable (response).

In all experimental cases, the laser pulse energy was set to a value which is above the threshold value for the bond breaking of polymeric material. The variation of photoresist mass removed with hydrogen flow rate at different laser pulse energy levels was established. The results of photoresist depth removed for 2000 laser shots are shown in Table 3.6. The data was subjected to statistical analysis using ANOVA (Analysis Of VAriance) methodology to establish the effect of gaseous media on the photoresist removal process by Excimer laser.

3.3 Results and Discussion

Laser ablation rate, in general, is sum of the rates attributed to photochemical and photo-thermal process. Depending upon the conditions in which the ablation process is conducted, the extent of contribution by photo chemical (PC) and photo-thermal (PT) process may vary. Much above the threshold limit of laser energy, photo-thermal process might contribute significantly to the net ablation rate.

Table 3.6 Ablation Depth for 500 Laser Shots

Exp. No.	Input Parameters for Experiments			Ablation Depth (µm) Mean				
	Flow rate (lpm)	Laser pulse repetition (Hz)	Laser Energy (mJ)	Hydrogen Media	Helium Media	Argon Media	Nitrogen Media	Air Media
1	0.8	20	30	61.47	33.05	24.46	23.80	21.81
2	0.8	20	40	87.25	42.30	34.64	31.07	37.02
3	0.8	20	50	101.13	50.24	43.23	46.27	52.62
4	0.8	20	60	114.35	57.51	49.44	55.79	55.66
5	0.8	30	30	52.62	21.81	17.45	16.13	17.71
6	0.8	30	40	82.63	29.75	23.93	21.15	24.46
7	0.8	30	50	101.13	34.37	30.14	31.73	34.24
8	0.8	30	60	103.12	34.37	33.84	36.36	37.54
9	0.8	40	30	47.59	13.88	13.88	12.29	14.01
10	0.8	40	40	73.37	21.81	18.77	15.20	19.70
11	0.8	40	50	87.25	25.12	23.80	23.80	26.44
12	0.8	40	60	99.15	29.75	25.65	27.37	28.03
13	1	20	30	63.46	33.05	23.53	21.02	23.80
14	1	20	40	64.78	60.15	40.32	27.63	39.66
15	1	20	50	105.10	54.20	46.93	48.25	50.90
16	1	20	60	119.91	60.81	54.20	56.19	56.19
17	1	30	30	58.83	23.14	19.17	15.34	18.77
18	1	30	40	69.41	33.05	25.12	19.30	29.75

Exp. No.	Input Parameters for Experiments			Ablation Depth (μm) Mean				
	Flow rate (lpm)	Laser pulse repetition (Hz)	Laser Energy (mJ)	Hydrogen Media	Helium Media	Argon Media	Nitrogen Media	Air Media
19	1	30	50	97.17	35.69	31.07	31.86	34.64
20	1	30	60	114.75	40.72	36.22	37.81	38.34
21	1	40	30	44.29	20.49	14.54	10.58	14.54
22	1	40	40	73.37	23.80	19.57	15.20	21.02
23	1	40	50	92.54	27.10	23.80	25.65	25.51
24	1	40	60	105.10	30.67	27.76	27.10	29.08
25	1.2	20	30	50.50	35.03	27.10	18.51	26.18
26	1.2	20	40	84.87	44.29	39.13	24.46	31.86
27	1.2	20	50	107.08	54.20	48.25	49.97	52.88
28	1.2	20	60	126.52	62.13	55.00	55.52	58.30
29	1.2	30	30	59.23	24.46	20.23	13.22	19.83
30	1.2	30	40	76.81	30.41	27.23	17.58	25.12
31	1.2	30	50	94.92	37.68	31.99	33.05	34.11
32	1.2	30	60	121.62	43.36	34.37	36.49	35.17
33	1.2	40	30	55.52	18.51	14.15	9.92	14.67
34	1.2	40	40	71.92	23.14	20.09	13.75	21.42
35	1.2	40	50	90.16	29.08	24.19	25.78	26.84
36	1.2	40	60	111.71	31.73	27.10	27.63	29.75

The gases used for study included hydrogen, helium, argon, nitrogen and air. In all cases, the laser pulse energy was set to such a value which ensures that laser fluence is higher than the threshold fluence of the polymeric material. The mass ablated (the amount of polymeric material removed for a fixed no. of pulses) was computed as a function of gas flow rate at different laser pulse energy levels. A total number of 540 experiments were conducted involving five different gases, all the experiments were conducted in triplicate; by varying laser pulse energy in four levels (30, 40, 50 and 60mJ), pulse repetition frequency in three levels (20, 30 and 40Hz); gas flow rate in three levels (0.8, 1.0, 1.2lpm). The experimental observations on the variation of the mass ablated as well as the mean value of the same, under five different gaseous media are graphically shown in Figure 3.13, Figure 3.15 and Figure 3.16. From these graphs it is obvious that photoresist removal/ ablation rate in hydrogen gas medium falls under totally different category compared to the rest of the gases studied. Among the five gases used hydrogen gas has highest thermal conductivity as shown in Table 3.4. Higher thermal conduction leads to higher rate of cooling at ablation site which could decrease the mass removal from photothermal mechanism. Despite its higher thermal conductivity, hydrogen gas showed remarkable increase in ablation rate, thus proving to be an assisting chemical agent during the photoresist removal by excimer laser. Its standard deviation on the mean value is also higher compared to other gases. This wide spread standard deviation data may be attributed to the possible influence of main input parameters viz., laser energy, PRF and hydrogen gas flow rate on the etch depth produced. It can be inferred from Figure 3.14 that hydrogen gas environment results in the highest amount of mass removal by laser ablation and detailed explanation of its mechanism is given in next chapter.

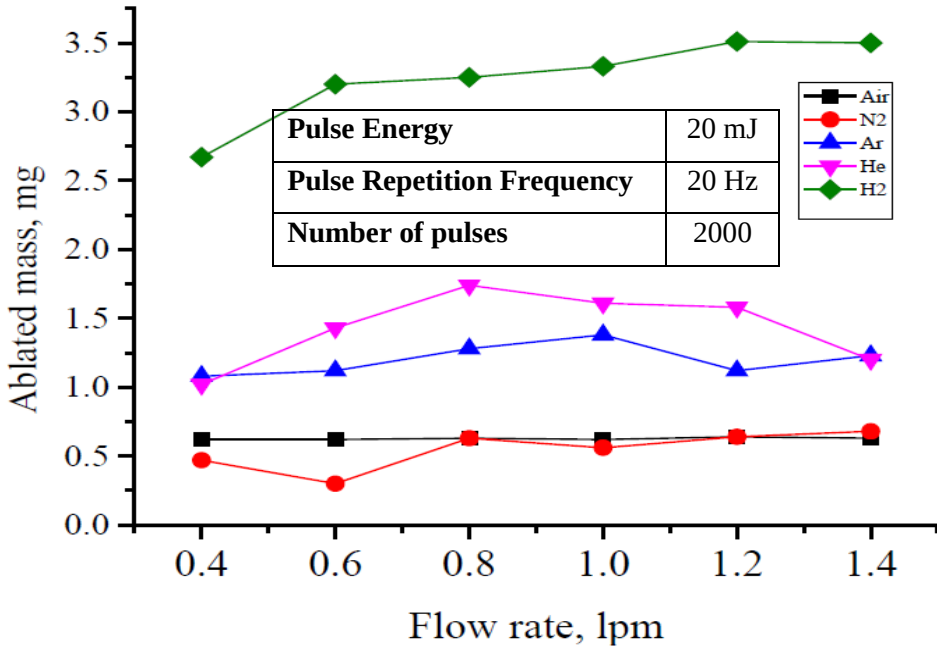

Figure 3.13 Ablated Mass as a Function of Flow Rate

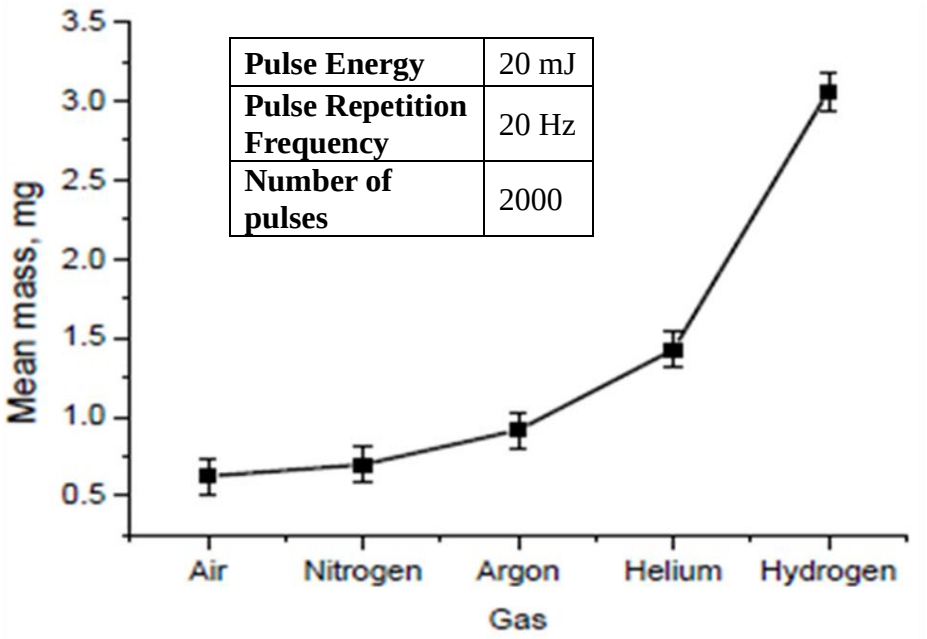

Figure 3.14 Variation of Ablation with Different Gas Media

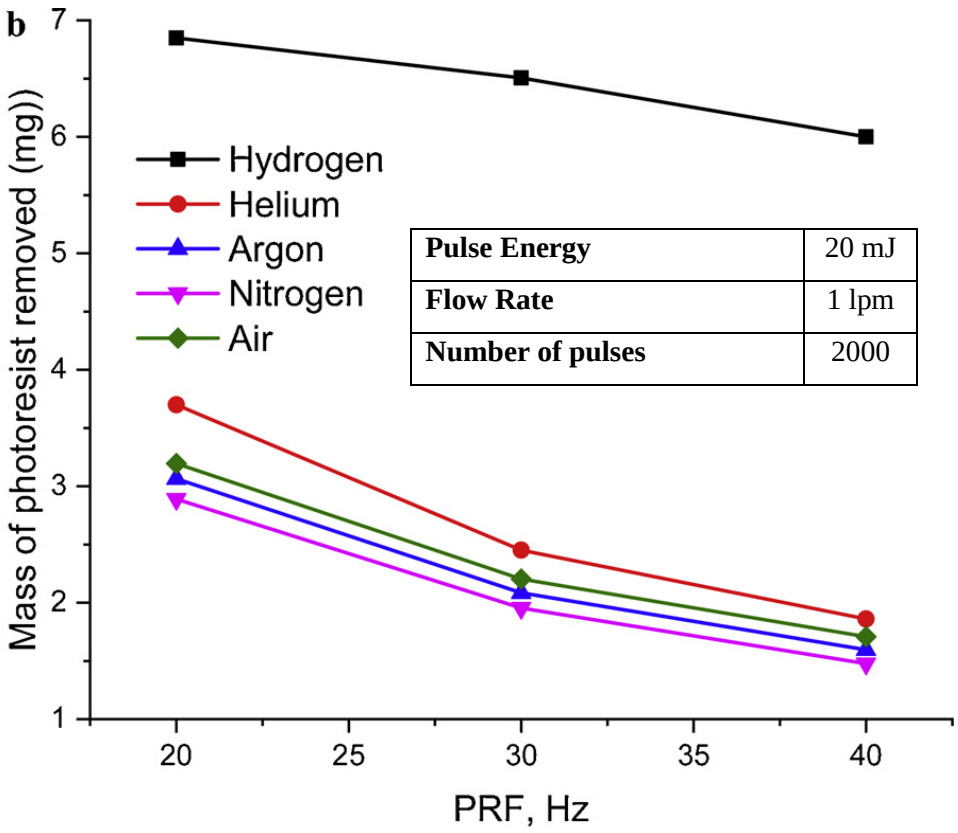

Figure 3.15 Ablated Mass as a Function of Pulse Repetition Frequency

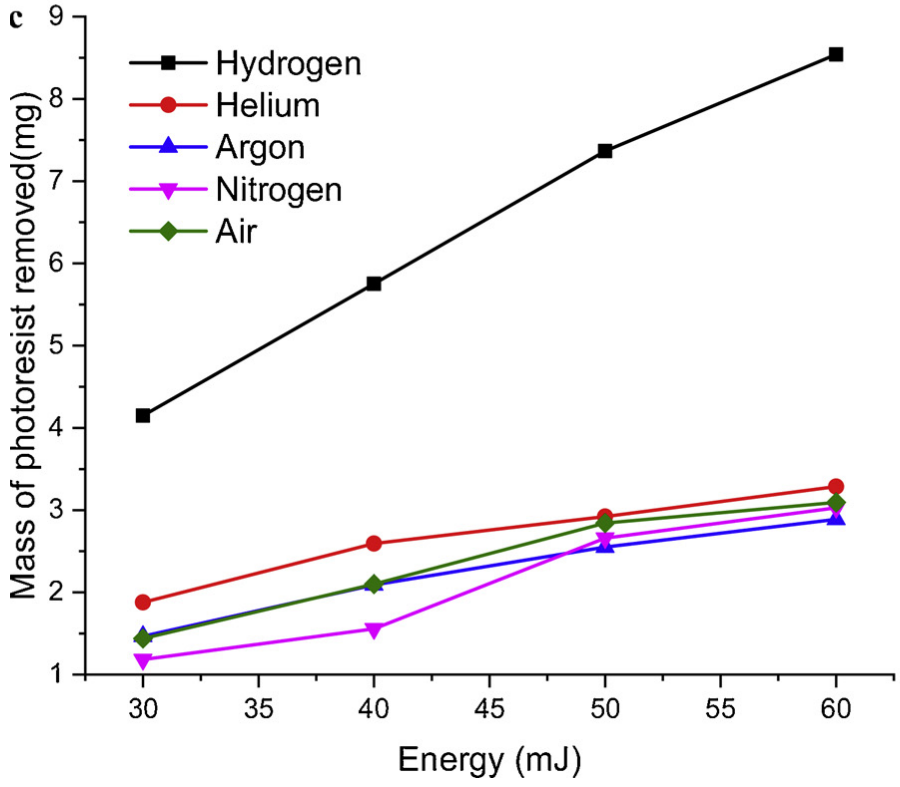

Figure 3.16 Ablated Mass as a Function of Laser Pulse Energy

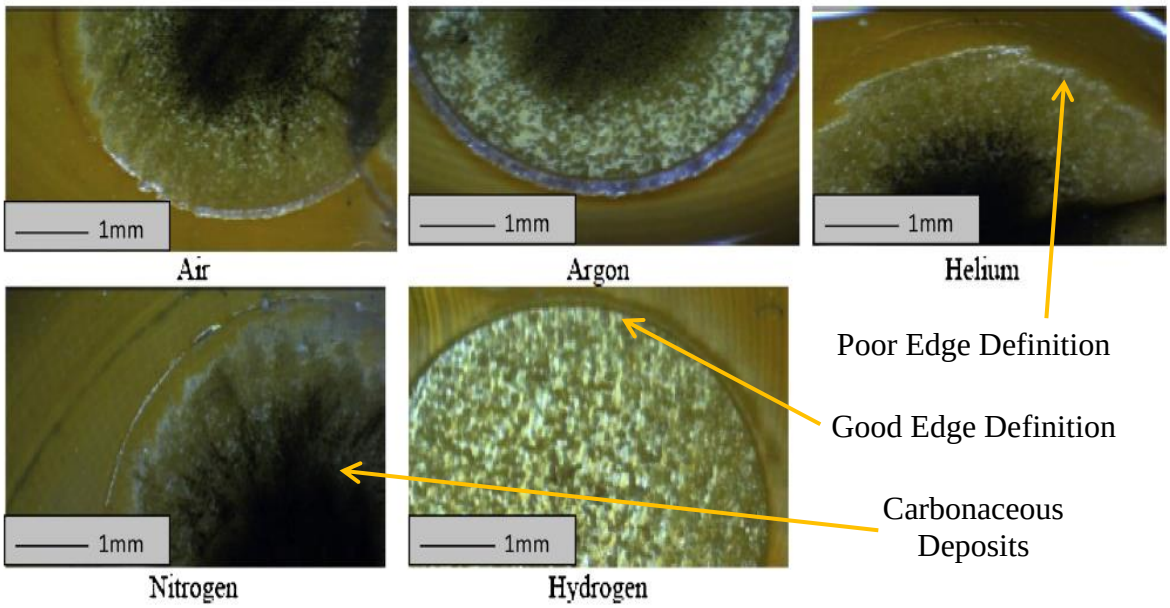

Figure 3.17 Photographs of 5mm dia. Circular Pattern Ablated on the Photoresist Under Different Gaseous Media.

Photographs of 5 mm dia. circular pattern ablated on the photoresist under different gaseous media are shown in Figure 3.17. It is interesting to note that the ablated surface for all the gases, except hydrogen, showed a pattern of irregular etches all along the circumference and black coloration. Formation of black colour on the surface may be explained as detailed below. Laser assisted burning of polymeric material with traces of oxygen present as a contaminant in the gaseous medium might be the reason for producing carbonaceous deposits on the surface. It was also observed that the black colour on the surface is more prominent in central region of the ablated area than the circumference. This is an obvious observation as the central region of laser beam has higher hot spot, resulting in higher rate of burning of the polymeric material with oxygen. In contrast to other gases studied, hydrogen gas showed good quality of surface contour without any black marks. Like other gases, hydrogen gas used for the study might also have traces of oxygen as a contaminant. But, surface blackening is not observed in this case due to the possible laser assisted chemical reaction of oxygen with hydrogen rather than polymeric material.

3.4 Summary

Experimental setup was developed to conduct excimer laser ablation of photoresist polymer under different gaseous environment, viz, Air, N_2, Ar, He and H_2, with an intention to have enhanced MRR and edge definition of the machined feature. Experimental parameters included gas flow rate, laser pulse energy and laser pulse repetition frequency were varied to study their effects on MRR and edge definition of the machined feature. Based on the results of excimer laser ablation experiments carried out under different gaseous media like air, nitrogen, argon helium and hydrogen, it is found that hydrogen gas showed remarkably superior photoresist removal rate compared to other gases. Edge definition under hydrogen media is remarkably superior. It is also observed from Figure 3.15 and Figure 3.16 that MRR increases with laser pulse energy and decreases with PRF.

Chapter 4

Experimental Study of Excimer Laser Ablation of Photoresist Polymer in Hydrogen Media

The effect of different gaseous medium like air, nitrogen, argon and helium on the ablation process was explained in previous chapter. The results obtained with hydrogen gas showed remarkably superior photoresist removal rate compared to other gases. A mechanism for photoresist removal by laser in hydrogen gas medium is explained in this chapter. As a part of this study, individual and interaction effects of three key operating parameters (i.e. laser energy, pulse repetition rate and gas flow rate) on the laser assisted photoresist removal in hydrogen gas medium were investigated and the results are described in this chapter.

4.1 Experiments to Study Effects of Laser Ablation under Hydrogen Gas Environment

Experimental setup explained in previous chapter was used for conducting further experimental study. A Full Factorial experimental design was employed for the experiments to evaluate the effect of three operating parameters, i.e., gas flow rate (l/min), pulse repetition rate (Hz) and laser energy (mJ). These selected parameters were considered as the independent variables and the depth of photoresist ablated (μm) after 500 laser pulses of irradiation has been selected as the dependent variable (response). The experimental ranges and their levels were decided based on experiments described in the previous chapter. Accordingly, 48 tests were defined for these three independent variables in four levels for PRF and flow rate each and three levels for energy, as shown in Table 4.1.

Table 4.1 Experimental Input Parameters

Levels for Laser pulse energy (mJ)	40, 50, 60	3 no.
Levels for Pulse repetition rate (Hz)	10, 20, 30, 40	4 no.
Levels for Gas flow rate (lpm)	0.6, 0.8, 1, 1.2	4 no.
No. of Gases	H_2	1 no.
No. of repetitions	Triplicate	3 no.
Total Experiments	144 no.	

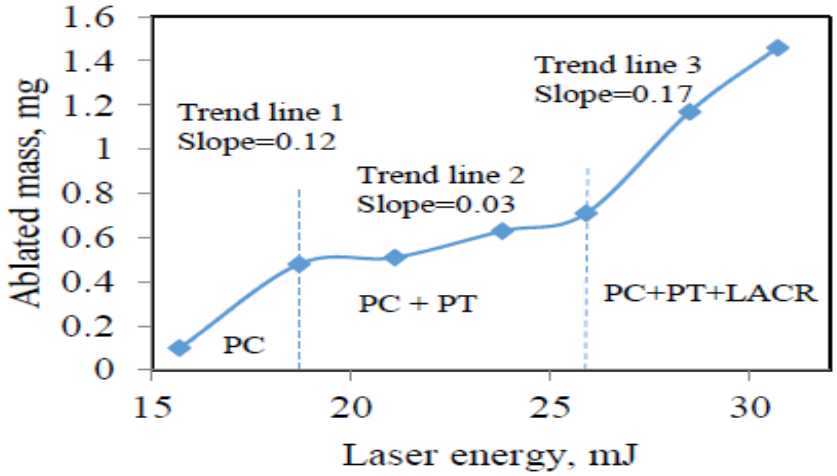

Figure 4.1 Variation of Ablation Rate with Laser Energy for Fixed H_2 Flow Rate (60 lph)

Figure 4.1 shows the variation of the ablated mass with laser energy for fixed H_2 flow rate of 60 lph. It could be identified from above graph that, relation of ablated mass with laser energy could be separated in three different regions based upon the slope. The slope of the third trend line is 0.17, which is about 40% higher compared to the first trend line. This increase may be attributed to additional contribution by the Laser Assisted Chemical Reaction (LACR). The condition for minimum activation energy, which is a prerequisite for the LACR of polymeric material with hydrogen, is met in this laser energy region.

4.1.1 Laser Ablation under H_2, Helium and Vacuum

Experiments of excimer laser ablation of photoresist polymer under hydrogen gas, helium gas and vacuum are conducted. Laser ablation experiments were conducted by varying the laser pulse energy, laser pulse repeation rate and gas flow rate and results were shown in previous chapter. Based on the observations explained in previous chapter that MRR increases with pulse energy and decreases with PRF, further experimental study was conducted by varying gas flow rate only with an intention to understand the mechanism involving hydrogen. The results are presented in this section and role of hydrogen in laser ablation process is discussed.

4.1.2 Comparison of Laser ablation under H_2 and Helium gas

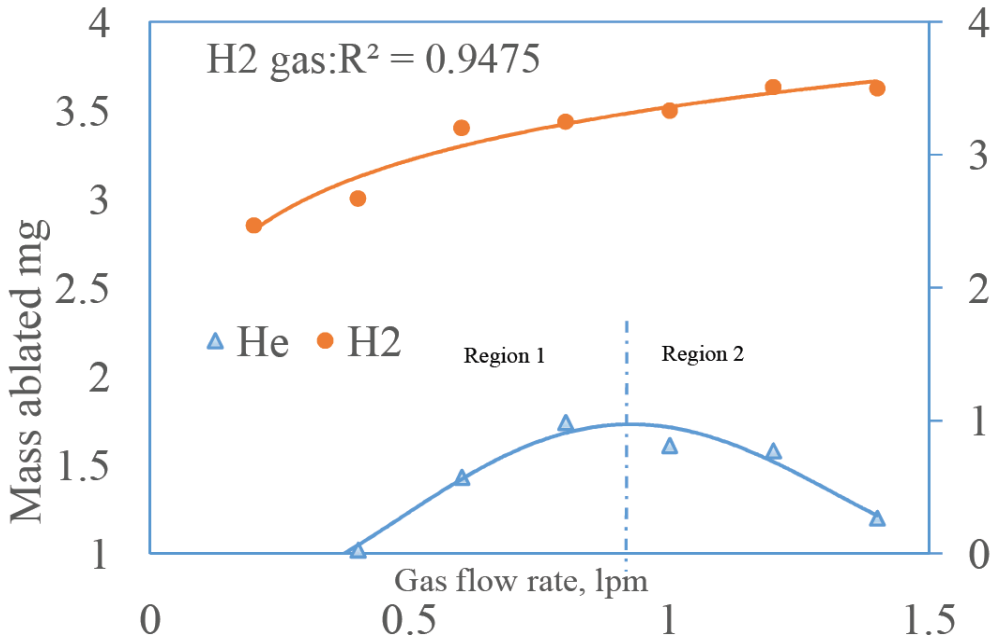

Pulse Energy	20mJ
Pulse Repetition Frequency	10 Hz
Number of pulses	2000

Figure 4.2 Comparison of Mass ablated in H_2 and He media

Experimental observation of laser ablation under (a) He gas and (b) H_2 gas is shown in Figure 4.2. Here the ablated mass as a function of the flow rate of hydrogen and helium

gases are shown. Mass ablated in helium gas media can be categorized into two distinct regions. In region 1, where an increasing trend is seen, the continuous flow of helium gas aids in effective removal and transport of ablated debris away from the polymer surface. In contrast, region 2 exhibits a decreasing trend because helium gas not only aids the removal and transport of ablated debris away from the polymer surface, but also acts as a cooling medium and effectively minimizes that part of the ablation, which is contributed by the photothermal action. Hydrogen gas shows the trend that follows an exponential relation (correlation coefficient>0.94). This reveals that hydrogen gas undergoes laser activated chemical reaction with the polymeric material during laser ablation. The exponential relation of ablation with hydrogen gas flow rate is in accordance with Arrhenius chemical reaction rate relation mentioned by, Reaction rate = $Ae^{-Ea/RgT}$

As discussed in the previous chapter, the mean mass of the photoresist removed under different gaseous media, provide information that air, nitrogen, argon and helium did not show significant change in mass of photoresist removed. The standard deviation or the experimental scatter in the measured ablated mass is similar for all the gases, except hydrogen. However, the hydrogen gas showed different behaviour compared to other gaseous media studied. Despite its higher thermal conductivity, hydrogen gas showed remarkable increase in ablation rate, thus proving to be an assisting chemical agent during the photoresist removal by excimer laser. Its standard deviation on the mean value is also higher compared to other gases. This wide spread standard deviation data may be attributed to the possible influence of main input parameters viz., laser energy, PRF and hydrogen gas flow rate on the depth of ablation.

4.1.3 Comparison of Laser ablation under H_2 and Vacuum

In order to confirm whether any laser assisted chemical reaction (LACR) is happening or not under hydrogen gas medium, experiment was carried out under vacuum (10^{-2} mbar) and also at 400 mbar (absolute) hydrogen gas medium. The mass ablated in hydrogen medium was seen to be higher than that obtained in vacuum condition, as shown in Figure 4.3. The photoresist removal rate in hydrogen medium is higher than that of vacuum condition for the entire energy range. Energy of excimer laser beam was varied for conducting experiments as gas flow rate does not exist for vacuum. Ablated surface under hydrogen and vacuum is shown in Figure 4.4. It could be clearly observed from Figure 4.4 that ablated surface quality for work piece under hydrogen media is better than that under vacuum.

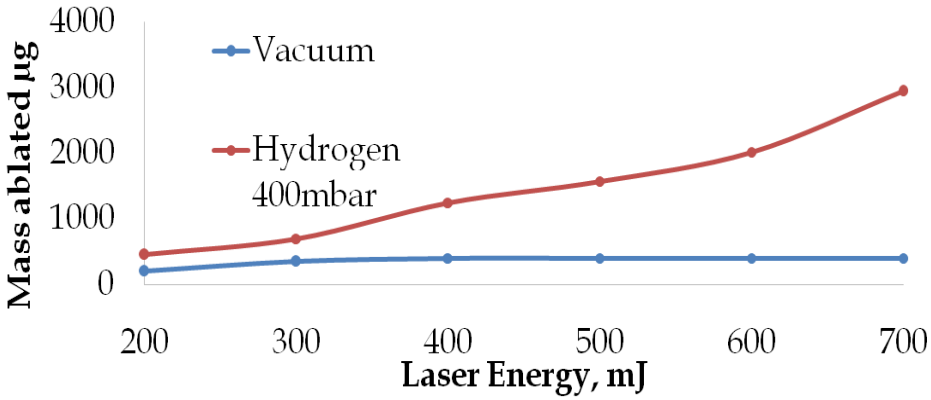

Figure 4.3 Comparison of Photoresist Removal in Vacuum (10^{-2} mbar) and Hydrogen Gas (400 mbar)

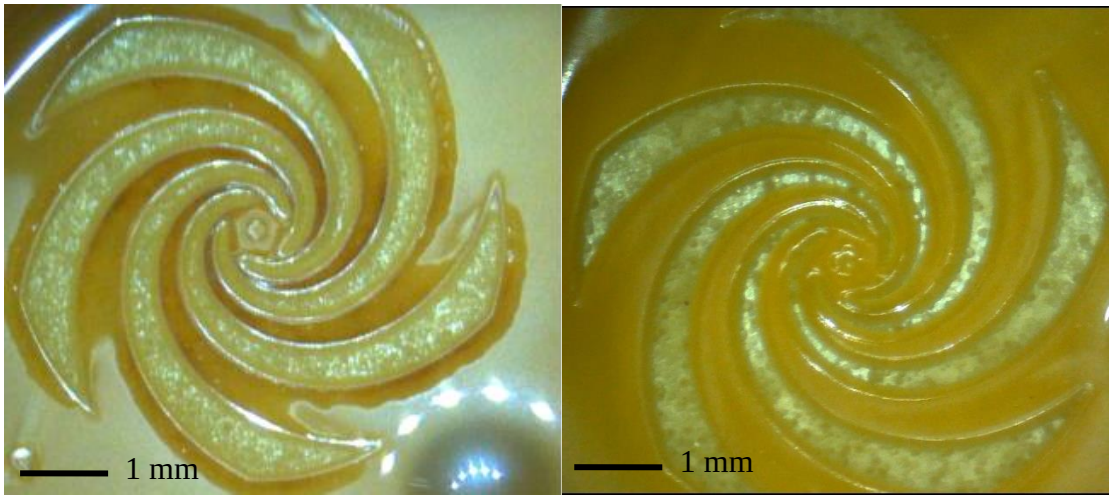

Figure 4.4 Ablated Surface (5mm diameter) under Hydrogen (Left) and Vacuum (Right)

Extensive experiments carried out under hydrogen gas media, shown that hydrogen gets involved in chemical reaction with the polymer thereby enhancing the ablation. Mass ablated in hydrogen media is much higher than that obtained in vacuum condition.

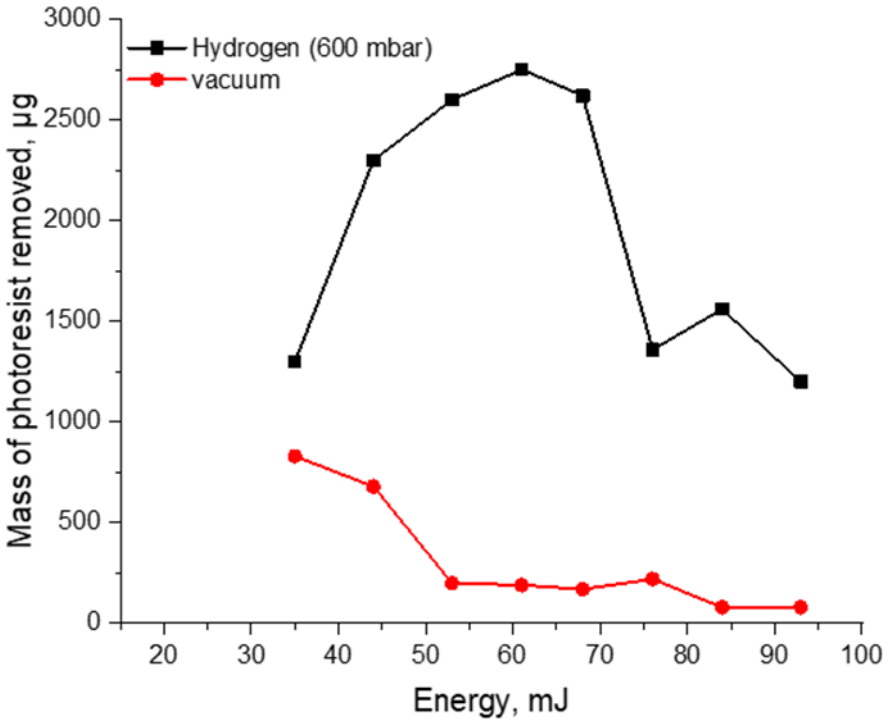

Figure 4.5 Comparison of Photoresist Removal for 3000 Laser Shots in Vacuum (10^{-2} mbar) and Hydrogen gas (600 mbar).

Among the gas media studied, thermal conductivity is highest for hydrogen gas medium. Being a higher thermal conductivity medium, hydrogen gas was expected to minimize photo-thermal contribution for the net photoresist removal rate. This might reduce the net photoresist removal rate in hydrogen gas medium. On the contrary, hydrogen gas showed remarkable increase in ablation rate, thus proving to be an assisting chemical agent during the photoresist removal process. In order to confirm if such laser assisted chemical reaction is happening or not, experiments were carried out under vacuum (10^{-2} mbar) and also at 600 mbar (absolute) hydrogen gas medium. The mass ablated in hydrogen medium was seen to be higher than that obtained in vacuum condition, as shown in Figure 4.5. The photoresist removal in hydrogen medium is observed to be increasing with energy, reaching a maximum value and then showing a decreasing trend for higher energy. However, the photoresist removal rate in hydrogen medium is higher than that of vacuum condition for the entire energy range.

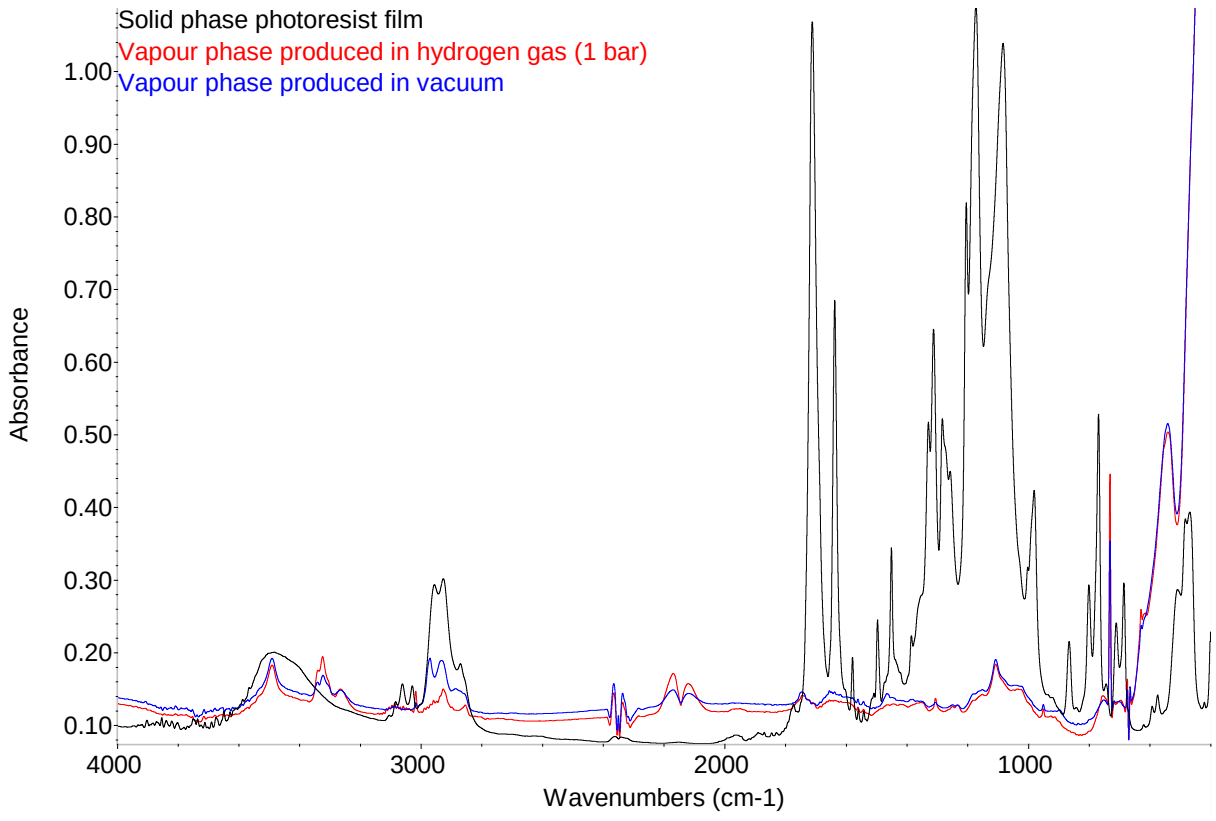

Figure 4.6 Comparison of FTIR Spectrum of Experimental Photoresist with Vapor Phase Produced During Laser Irradiance in Vacuum and Hydrogen Gas Environments

FTIR spectrum of experimental photoresist is compared with vapour phase produced with laser irradiance in vacuum and hydrogen environment is shown in Figure 4.6. It may be noted that the absorption of experimental photoresist is very high compared to vapour phase product generated after laser irradiance as can be seen from Figure 4.6. Therefore, comparison of only vapour phase product formed under vacuum and hydrogen gas media is shown separately in Figure 4.7. From this figure it could be observed that spectral bands in three regions showed change in peak heights. It may be noted that the spectral region in the range 3100-3000 cm^{-1} is due to C-H stretching adjacent to double bond or aromatic ring. 3300-3400 cm^{-1} spectral region is due to N-H stretching. It is obvious from the IR spectra that C-H stretching region is more prominent than N-H stretching region for vacuum experiment. On the contrary, N-H stretching region is more prominent than C-H stretching region for hydrogen gas experiment. This might be attributed to hydrogenation of olefin functional group. A broad spectral band in the range of 3800-3600 is also observed for hydrogen experiment. This is due to -OH of hydrogenated/opened epoxy group. From these observations, we may infer that there might be a Laser Assisted Chemical Reaction (LACR) of hydrogen gas with photoresist polymer. It is well known that atomic hydrogen has the effect of etching sp^2 bonding (unsaturated olefinic bonds, π bonds) fractions in the photoresist polymer films [102], [103].

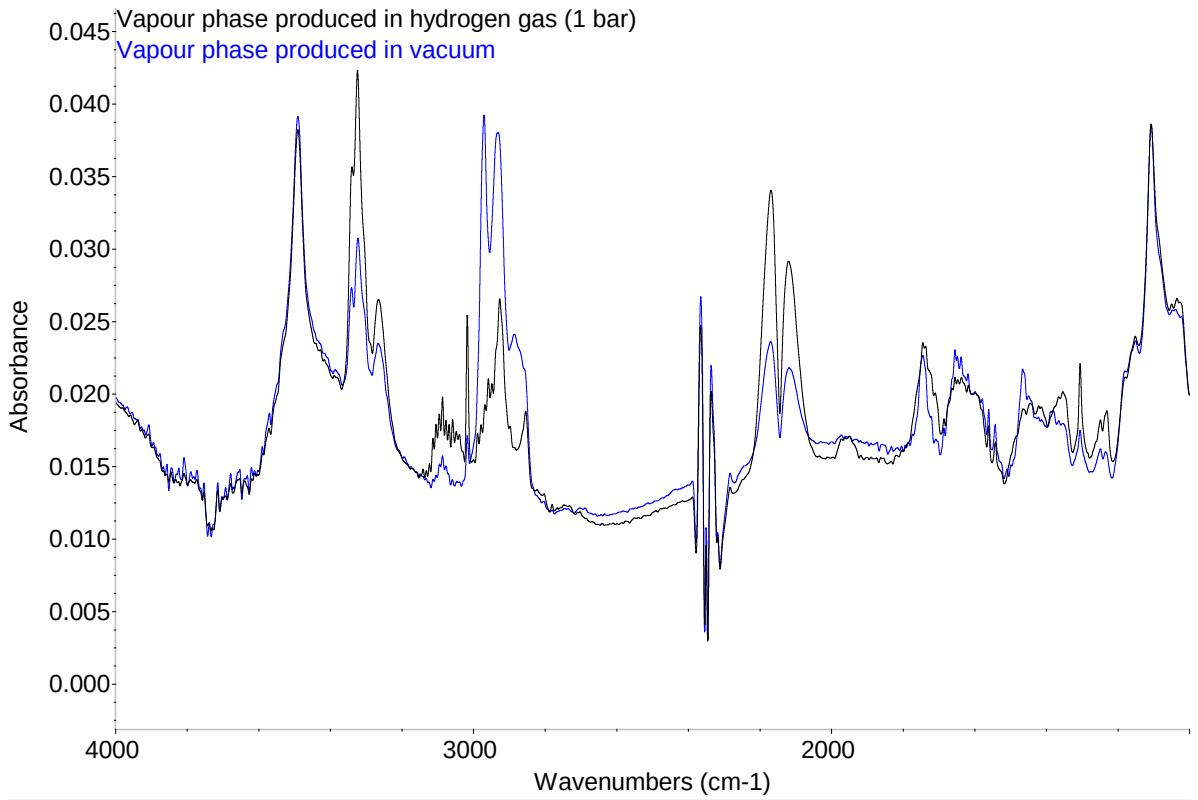

Figure 4.7 Comparison of FTIR Spectrum of Vapour Phase Produced During Laser Irradiance of Experimental Photoresist in Vacuum and Hydrogen Gas Environments

4.2 Proposed Mechanism for Photoresist Removal by Laser in Hydrogen Gas Media

Researchers have studied the photo degradation of polymers in oxygen medium and the mechanism, for photo oxidation of polymer has been proposed. Since oxygen molecule absorbs UV photon, it is electronically excited to singlet state, which exhibits several specific reactions and the one that has been most often invoked in the photo-oxidation of polymers is the formation of a hydro-peroxide by oxidation of an olefin containing an allylic hydrogen, which could further decompose and lead to additional chain scission.

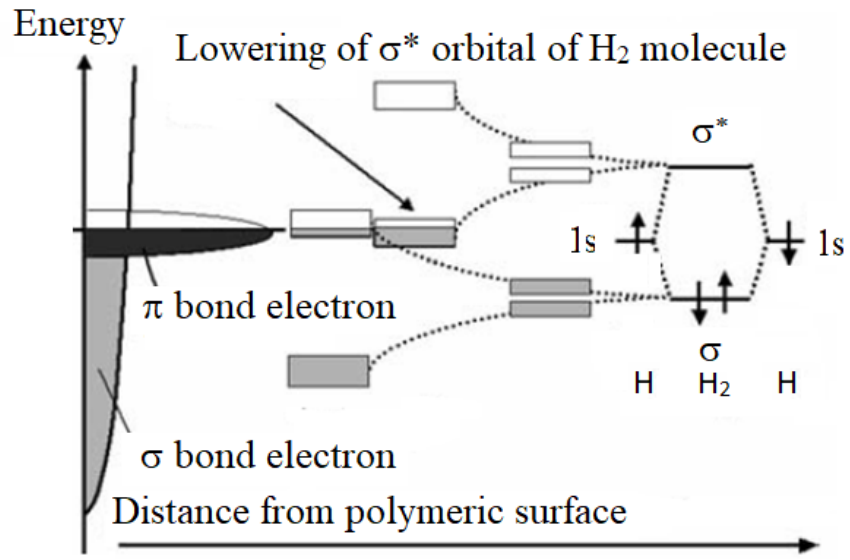

Figure 4.8 Showing Polymer-Gas Interaction Leading to Hydrogen Molecule Bond Breaking by π Electron Cloud of Polymer

In the present study, hydrogen gas, though doesn't absorb UV photon, is showing remarkable increase in photoresist removal rate under laser irradiance. Hydrogen gas, even though transparent to UV photon, may still play some role in enhancing the photoresist removal rate. A mechanism has been proposed here to explain the key role that hydrogen gas plays during the process of photoresist removal by laser. When a hydrogen molecule approaches the polymer surface, as indicated in Figure 4.8, it will first feel the Vander Wal force of interaction, which is a weak interaction due to polarization effects, resulting in physical adsorption. At this stage, the molecular orbitals of hydrogen molecule are interacting with the delocalized π electron cloud of polymeric benzene group or olefinic groups, leading to lowering and broadening of the bonding and anti-bonding orbitals of hydrogen molecule. When hydrogen approaches even closer or at polymer-gas interface, there may be an exchange between π electrons cloud of polymer and hydrogen molecular orbitals, leading to associative chemisorption. This interaction results in weakening of the internal bonding of the hydrogen molecule due to the filling of the otherwise antibonding (empty σ^* state) orbital. The resultant bond breaking leads to generation of hydrogen free radicals. Compared to the

restricted movement of polymeric macro radicals in the polymeric material the hydrogen free radical, being very reactive, unstable and mobile, can diffuse and migrate along the polymer chain attacking SP^2 and SP hybridization carbon centre (unsaturated π bonds around carbon). This is an additional pre-processing step, which converts the polymer into saturated macro-molecules i.e π bond is converted into σ bond due to hydrogenation. This process alters the physical and chemical property of polymeric surface, which aids for easy bond scission by laser photon interaction with polymer. So, it can be easily concluded that increase in photoresist removal rate in hydrogen environment is due to gas assisted chemisorption of hydrogen molecule on polymeric surface resulting in generation of highly reactive hydrogen radicals.

4.3 Result and Discussion

In order to validate our proposed mechanism of LACR of photoresist with hydrogen gas the experimental results were analysed and the same are shown in graphical form in this section.

Photoresist ablation, in general, is sum of the rates attributed to photochemical (PC) and photothermal (PT) processes [104]. Depending upon the conditions in which the ablation process is conducted, the extent of contribution by PC and PT may vary. Figure 4.9 shows that ablation depth is increasing with increase in flow rate of hydrogen which implies MRR is increasing with increase in flow rate of hydrogen. In case photothermal (PT) processes was having significant contribution in MRR then ablation rate should have reduced with increase of hydrogen flow rate. This implies that LACR type of phenomenon is occurring in ablation process udder hydrogen gas media. Figure 4.10 shows variation of ablation depth with PRF of laser and it can be observed that increase in PRF reduces the MRR. This effect of PRF on MRR is not investigated in present research work. Figure 4.11 shows that MRR

under hydrogen media is increasing with laser pulse energy which is in agreement with previous research findings on the effect of laser fluence on MRR.

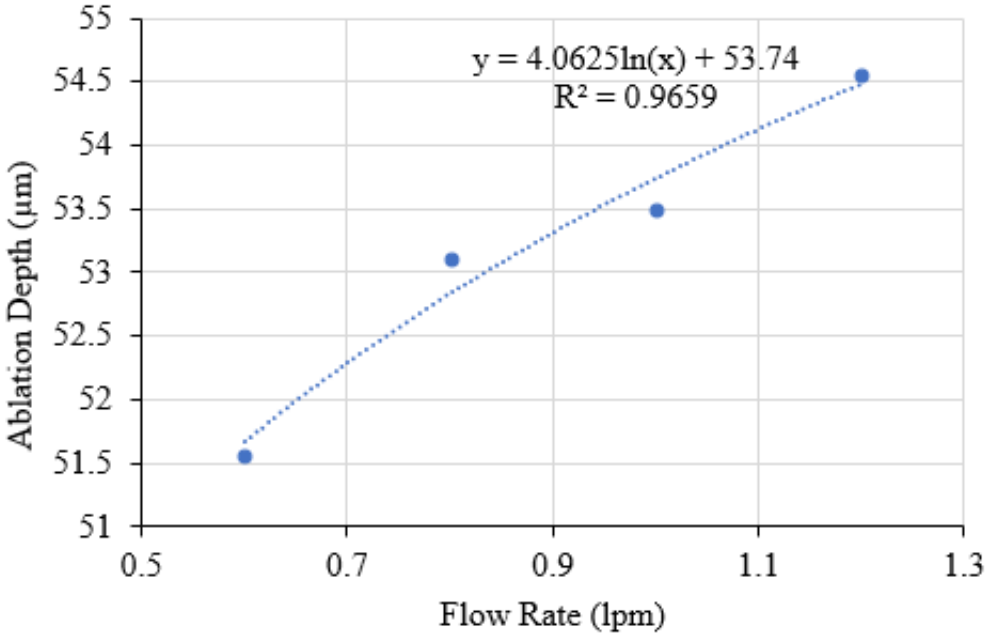

Figure 4.9 Variation of Ablation Depth with Hydrogen Flow Rate

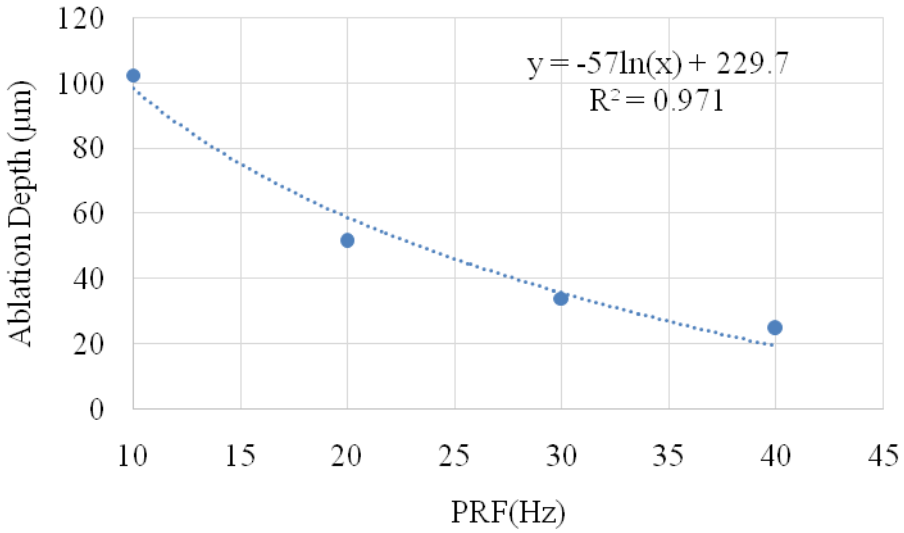

Figure 4.10 Variation of Ablation Depth with PRF of Laser

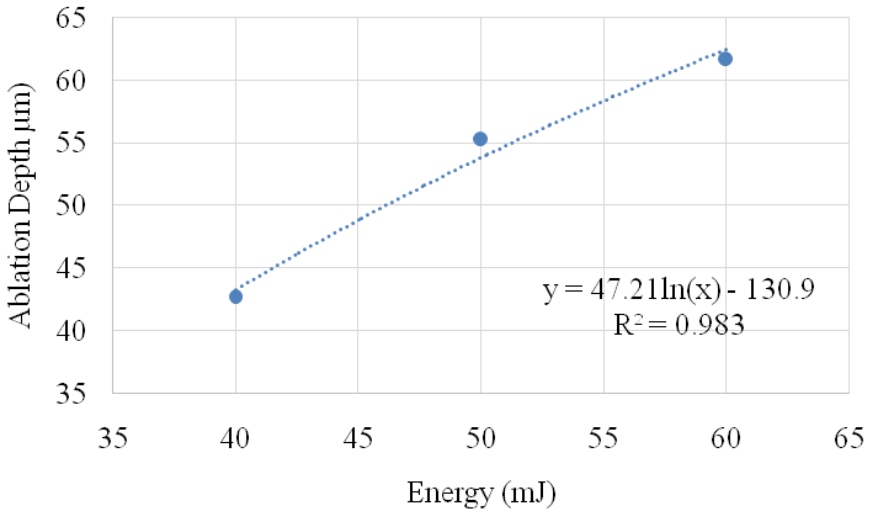

Figure 4.11 Variation of Ablation Depth with Laser Pulse Energy

4.4 Summary

Excimer laser ablation of photoresist polymer under hydrogen gas, helium gas and vacuum environments were studied experimentally in order to see the special effect of hydrogen gas on MRR.

Mass ablated in helium gas media is categorized in two distinct regions. With increase in helium flow rate MRR increases in lower flow rate region and then started decreasing for higher flow rate region. MRR under Hydrogen gas shows continuously increasing trend with in the experimental range, and then follows an exponential relation (correlation coefficient>0.94).This reveals that hydrogen gas undergoes laser assisted chemical reaction with the polymeric material during laser ablation. The exponential relation of ablation with hydrogen gas flow rate is in accordance with Arrhenius chemical reaction rate relation mentioned by, Reaction rate = $Ae^{-Ea/RgT}$. Further experiments by varying the laser pulse energy showed that MRR increases with increase in laser fluence which is no exception to previous research findings.

Chapter 5

Mathematical Modelling of Laser Ablation Process and FEA Simulation

The mathematical modelling work was carried out to understand material removal phenomena during a single pulse of excimer laser irradiation. Subsequently, the total material removal or the ablated mass in a given number of pulses was also derived, which is further used to predict the same by incorporating FEA simulation on the developed mathematical model. Temperature variation in the polymer was computed; subsequently surface morphology and surface quality of the work piece was also simulated. Moreover, experiments were conducted under both hydrogen gas media and an inert gas media of Argon, for the validation of simulated results.

5.1 Interaction of Laser Beam with Polymer Material

Demir *et. al.* [30] had studied optical, chemical and mechanical effects of different submerged liquid laser cutting of AZ31Mg alloy. They have reported that the beam enlargement due to change in refractive index does not significantly reduce the fluence, however, the absorptivity of the liquid can cause significant energy loss. But, the gaseous medium like argon and hydrogen does not affect nanosecond pulse laser because of very small power densities of the order of 10^6 W/cm^2 thereby preventing ionization of the medium and hence change in refractive index of these gases are insignificant.

As far as the chemical effects of laser beam propagation in hydrogen gas media is concerned, the present work discusses about the enhanced material removal rate obtained due to Laser Assisted Chemical Reaction (LACR) between nascent hydrogen, produced as a

result of the three parts interaction between laser-hydrogen gas molecule -polymer, at the hydrogen gas -polymer interface.

As far as the mechanical effects are concerned, the flowing gas media at the laser micro machining area, helps in blowing out the debris formed, making the fresh polymer surface available for continued micro machining. In the present experimental work the micromachining of polymer material is carried out using excimer laser beam of 248nm wavelength to validate the model. It is seen that the mechanism of material removal is Ablative Photo-Decomposition (APD). For these short wavelengths of 248 nm, the large molecules typical of polymers, are broken into smaller fragments by electronic excitation of the bonds. Since the smaller molecules have lower density, the irradiated volume expands rapidly, in fact so rapidly that the surface layers are ejected; thus the excess energy is carried away in the form of kinetic energy by the ejected material and therefore the process is relatively cool.

5.1.1 Mathematical Modelling

When the laser beam irradiates the surface of the polymer, a very small fraction corresponding to the reflectance value of the material is reflected. As the reflectance value is negligibly small for polymer material, this part is not considered in the model. According to Beer-Lambert law, intensity varies along depth as shown in equation 5.1[105].

$$I = I_o e^{-\beta Z} \quad \text{--- (5.1)}$$

Where I is intensity at a depth 'z' from the surface of polymer, I_o is the intensity entering the sample at z = 0, and β is the attenuation co-efficient of the polymer. If the threshold fluence to initiate the ablation of the specific polymer, is equal to φ_{th}, then depth of material removed after time 't' can be expressed as follows shown in equation 5.2.

$Z_t = (1/\beta)\, ln(\varphi/\varphi_{th})$; where, $\varphi = \int I dt = I\, t_{on}$ where, $0 \leq t \leq (t_{on} = 25\ ns)$. --- (5.2)

Eq. (5.2) is valid for a single pulse. If 'N' pulses are applied, the material removal or depth of ablation would be N times Z_t. Hence, Eq. (5.2) can be modified as per equation 5.3.

$$Z_N = (N/\beta)\, ln(I * t_{on}/\varphi_{th}) \quad \text{--- (5.3)}$$

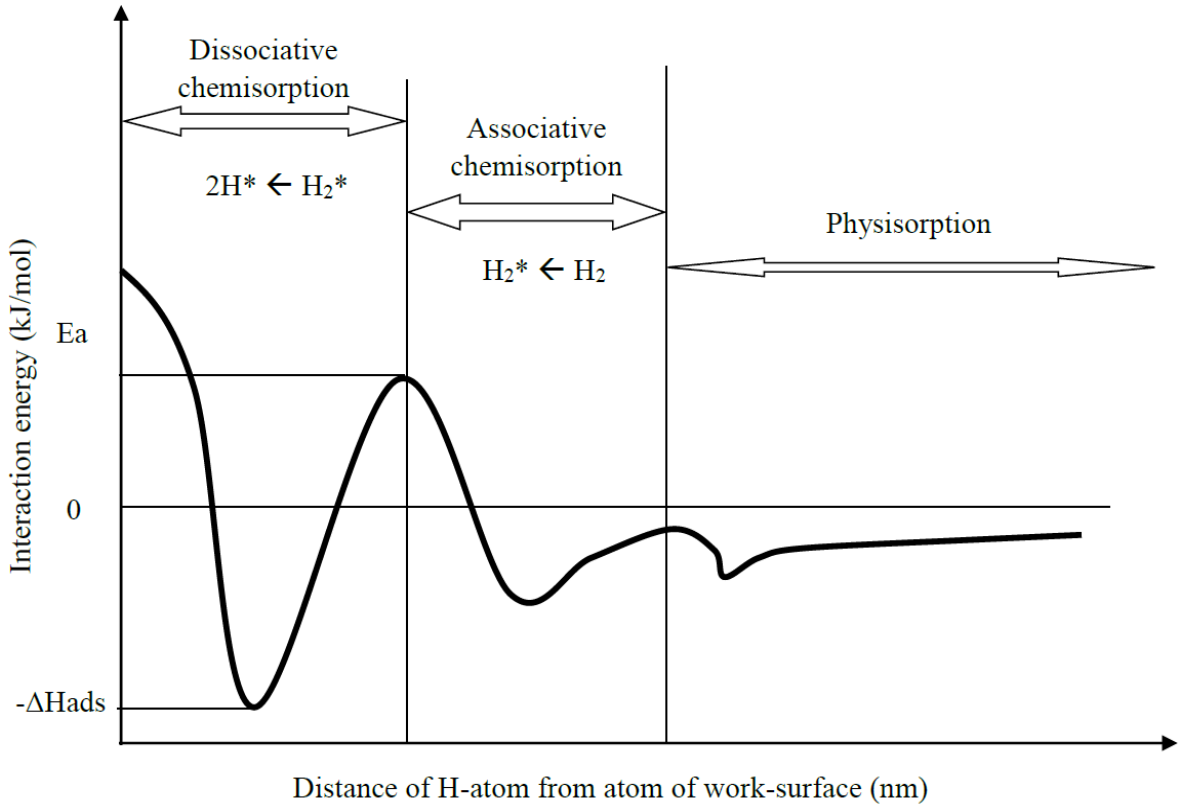

Figure 5.1 Schematic Potential Energy Diagram for a Hydrogen Molecule Approaching an Electron Rich Surface.

The interaction between molecules/atoms of hydrogen and polymer molecules take place when a hydrogen molecule approaches a polymeric surface (having π-bonds like olefinic/aromatic functional groups of electron rich centres), as indicated in Figure 5.1. Figure 5.1 shows that at the region of physisorption, hydrogen gas molecules are absorbed at the polymer surface. When a hydrogen molecule approaches even closer, there may be an exchange of electrons from the polymer surface with the anti-bonding (σ^*) molecular orbital of hydrogen. This results in associative chemisorption. In the excited state (H_2^*) energy level

gets reduced as shown in Figure 5.1. The height of the barrier, E_a, is nothing but activation energy which helps in dissociating the excited state of hydrogen molecule (H_2^*) into hydrogen free radical/nascent hydrogen atom. The free radical/nascent hydrogen atom is highly reactive and unstable. Being highly reactive, nascent hydrogen reacts instantly and spontaneously with olefinic/aromatic functional groups, causing scissoring of triple/double bonds. This invariably reduces the threshold fluence values of the polymer.

5.2 The Role of Atomic Hydrogen in Enhancing Removal Rate of Photoresist

The role of atomic hydrogen generated by tungsten hot-wire catalyser, in the removal of photoresist polymer by chemical reaction, is a well-established phenomenon [106].

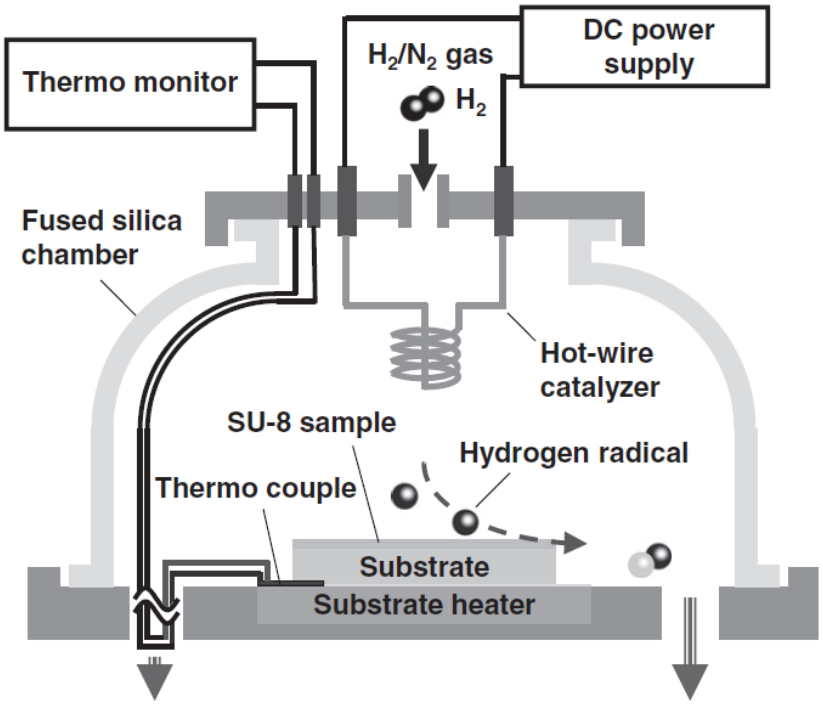

Figure 5.2 Schematic Diagram of Hydrogen Radical Generation Apparatus [106]

The enhanced removal rate of the photoresist observed during excimer laser ablation under hydrogen gas media can be explained as the 'Laser assisted Chemical Reaction' phenomenon involving the - generation of atomic hydrogen at the polymer-hydrogen gas interface- in presence of excimer laser irradiation. During laser ablation, local heating raises

the temperature of the polymer surface thereby providing the activation energy to dissociate the excited hydrogen molecule at the polymer-hydrogen interface. This leads to generation of hydrogen radicals (i.e. hydrogen atoms) which move towards the work-surface and thereby scissoring the electron rich bonds (like π-bonds) of the polymer, resulting in ablation of the polymer. The enhanced material removal under hydrogen gas medium can be modelled based on Eq.(5.2), by replacing the term (φ_{th} in the denominator of Eq.(5.2) with $\varepsilon.\varphi_{th}$), while the value of epsilon is less than unity. This will effectively bring down the value of the denominator in Eq.(5.2), resulting in higher ablation depth per laser pulse, or higher amount of material removal per pulse. The modified mathematical model is presented in Eq.(5.4).

$$Z_{t1} = \frac{1}{\beta}\ln\left(\frac{I*t}{\varepsilon\varphi_{th}}\right) \qquad \text{if } E_a \leq {}^1\!/_2 K_b T \qquad \text{--- (5.4)}$$

where 'ε' is a factor by which the threshold fluence of the polymer is reduced, due to the presence of hydrogen gas.

A circular and flat -hat top laser beam has been used in excimer laser micromachining. Both for the modelling and the experiments, the energy profile of the beam has been mapped using energy meter and sensor (make: COHERENT and model: Energy Max II – TOPTM and J-25 MUV-248), same is presented in Figure 5.3 (a-b). In view of these experimental conditions, flat and circular beam has also been used for the simulation as shown in Figure 5.3 (c-d).

$$Z_t^2 = \frac{1}{\beta} ln\left(\frac{I*t}{\varepsilon\varphi_{th}}\right) \qquad \text{if } E_a \geq {}^1\!/_2 K_b T \qquad \text{--- (5.5)}$$

$$Z_N = \frac{N}{\beta} ln\left(\frac{I*t_{on}}{\epsilon\varphi_{th}}\right)\begin{vmatrix}\varepsilon = 1; if E_a \geq 1/2K_bT \\ \varepsilon < 1; if E_a \leq 1/2K_bT\end{vmatrix} \qquad \text{--- (5.6)}$$

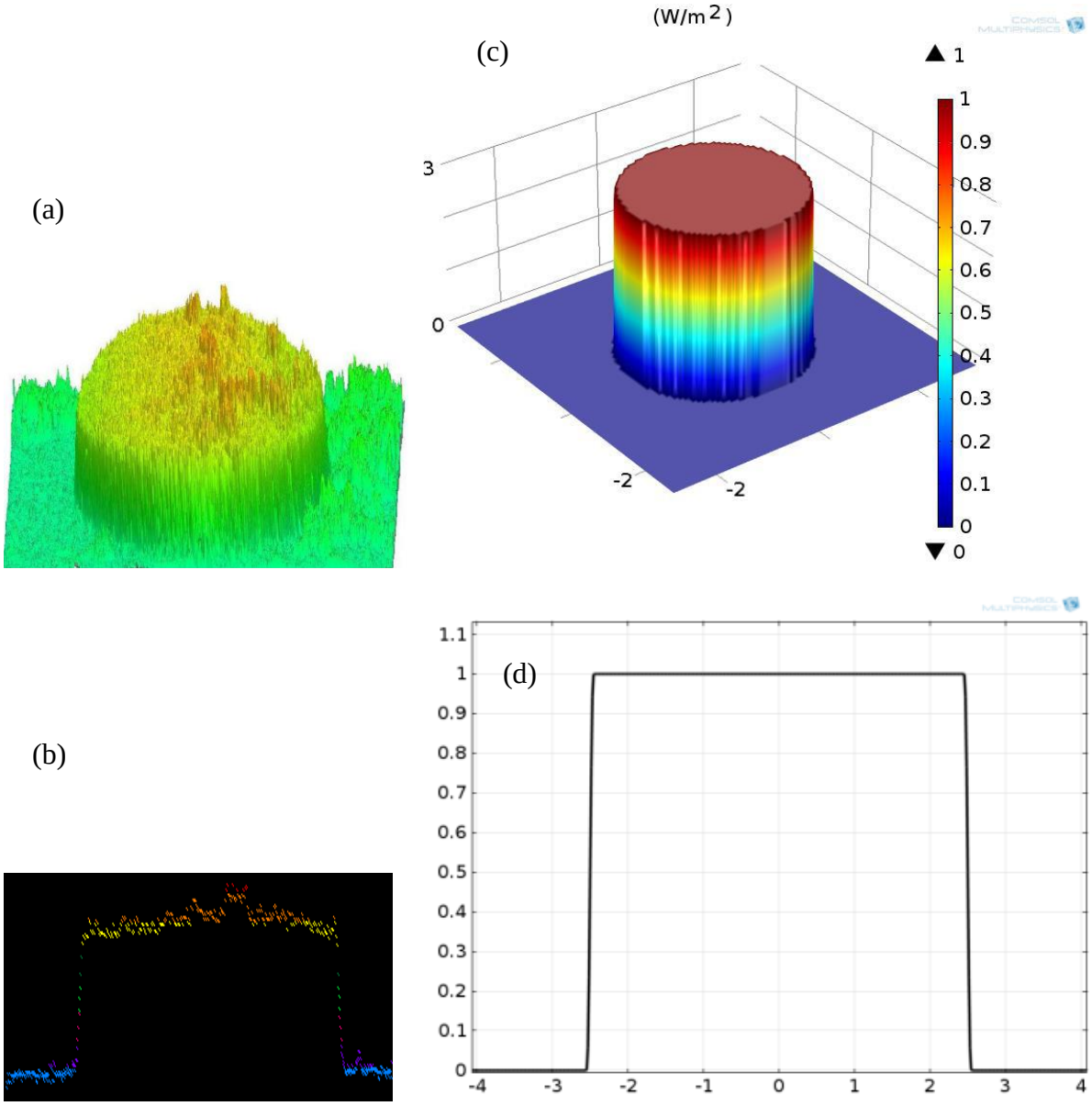

Figure 5.3 Homogenized LASER Beam Profile at the Work-Stage. (a) Energy Distribution in 3D for Experimental Work. (b) Energy Distribution in 2D for Experimental Work. (c) Energy Distribution in 3D for Simulation Work. (d) Energy Distribution in 2D for Simulation Work.

5.3 Computation of the Surface Temperature

Temperature (T) on work-surface can be computed from the heat balance equation as described in Eq. (5.11).

Heat input from laser, $Q_{in} = I_o e^{-\beta z} \pi R^2$ --- (5.7)

Heat out by conduction, $Q_{cond.} = -K\pi R^2 \frac{\partial T}{\partial Z}$ --- (5.8)

Heat out by convection, $dQ_{conv.} = \left(a + bV_f^c\right)2\pi r dr(T - T_\infty)$

$$Q_{conv.} = \int_{r=0}^{r=R_o}\left(a + bV_f^c\right)2\pi r(T - T_\infty)dr \quad \text{--- (5.9)}$$

Where, Q_{in} is heat input by laser at depth z. $dQ_{conv.}$ is the elemental heat transfer by convection from the surface of polymer. Rand R_o are the radius of the laser beam spot and the workpiece respectively. $T_\infty$is ambient temperature. '*K*' is co-efficient of thermal conductivity of the polymer, $\left(a + bV_f^c\right)$ is the flow dependent heat transfer co-efficient for convection. 'a', 'b' and 'c' are arbitrary constant and V_f is the velocity of gas.

Heat being stored in the workpiece,

$$Q_{Store} = \iint \rho C_p \frac{\partial y}{\partial x} 2\pi r dr dz \quad \text{--- (5.10)}$$

From heat balance, temperature distribution profile can be calculated using the following equation which can be applied on infinitesimal element shown in Figure 5.4.

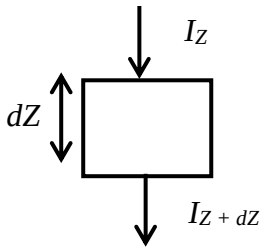

Figure 5.4 Infinitesimal Element Considered for Heat Balance

$$dQ_{in} = dQ_{cond.} + dQ_{conv.} + dQ_{store} \quad \text{--- (5.11)}$$

$$dQ_{in} = -\left(\frac{\partial(I_Z dZ)}{\partial Z}\right) \quad \text{--- (5.12)}$$

Differential equation for temperature calculation can be written in Cartesian coordinate as follows

$$\left(\beta I_o e^{-\beta Z}\right)dZ = -\nabla.(k\nabla T) + \nabla\left\{\left(a + bV_f^c\right)(T - T_\infty)\right\} + \rho C_p \frac{\partial T}{\partial t} \quad \text{--- (5.13)}$$

where, ρ is density, C_p is specific heat capacity.

The unknown coefficients like E_a, a, b, c, ε and β are computed using experimental data. The mathematical model as shown in equations 5.4, 5.5 and 5.6 are simulated using Finite Element Analysis (FEA) as described in the next chapter.

5.4 FEA simulation

To carry out FEA simulation, COMSOL 4.3a multi-physics software has been used to couple multiple physics such as Heat transfer and Arbitrary Lagrangian-Eulerian (ALE) method. Subsequently suitable post processing on simulated data has been carried out to compute surface temperature, mass ablated and surface morphology. Following assumptions are made for conducting the FE simulation.

1. Homogenized LASER beam profile is assumed at the workpiece.
2. Attenuation constant of polymer on LASER=16000 mm^{-1} (Computed from Experiment).
3. Attenuation of LASER due to gas environment is insignificant.
4. Absorbed energy (within the workpiece) per unit volume and time is proportional to the photon flux, i.e. the intensity *I*.
5. Constant amount of material will be removed for each laser pulse delivered.

In this work, finite element analysis was carried out to solve time dependent heat transfer equation using conduction as well as convection.FEA parameters to simulate material removal by laser ablation are shown in Table 5.1.

Table 5.1 FEA Parameters to Simulate Material Removal during Laser Ablation

Solver configuration	Fully coupled of heat transfer and ALE.

Solver type	PARDISO
Non-linear method	Constant (Newton)
Simulation type model	Time dependent and Parametric sweep
Geometry type	Axisymmetric
Parametric sweep for Energy	Range (10 mJ to 60 mJ with step of 5 mJ)
Shape function	Lagrange (Quadratic)
Geometric shape order	Quadratic
Type of mesh	Triangular
Mesh smoothing type	Winslow

A mathematical model for material removal is proposed towards understanding of the process behaviour. Moreover, ALE technique from FEA simulation has been carried out using the proposed mathematical model for response prediction. Eventually, simulated results have been validated by comparing with the experimental results. Parameters for the simulation are listed in Table 5.2.

Table 5.2 Simulation Parameters

Parameters	**Value**	**Description**
Energy	10 to 60 mJ	Pulse energy (initial value)
Pulse	2000	Number of pulses
φ_{th}	70 mJ/cm^2	Threshold fluence
t_{on}	25 ns	Pulse time or on time
PRF	20 Hz	Pulse repetition rate
T duty	1/PRF	on time + off time
β	16000 mm-1	attenuation constant
ϵ	0.5	Constant due to H_2 gas
PP	Energy/ton	Pulse peak power
R	2.5 mm	LASER spot size
p	PP/(πR^2)	Power per unit area
T_{act}	350 K	It comes from activation energy (E_a). $T_{act}=E_a/K_b$
T_a	700 K	Ablative temperature

Parameters	Value	Description
H_{gas}	5 MW/m^2-K	Heat transfer coefficient of gas
C_{pw}	120 J/kg-K	Heat capacity of workpiece
ρ	1190 kg/m^3	Density of workpiece
K	0.19 W/m-K	Thermal conductivity of workpiece
α_w	70 μm/m-K	Thermal expansion (Linear) of workpiece

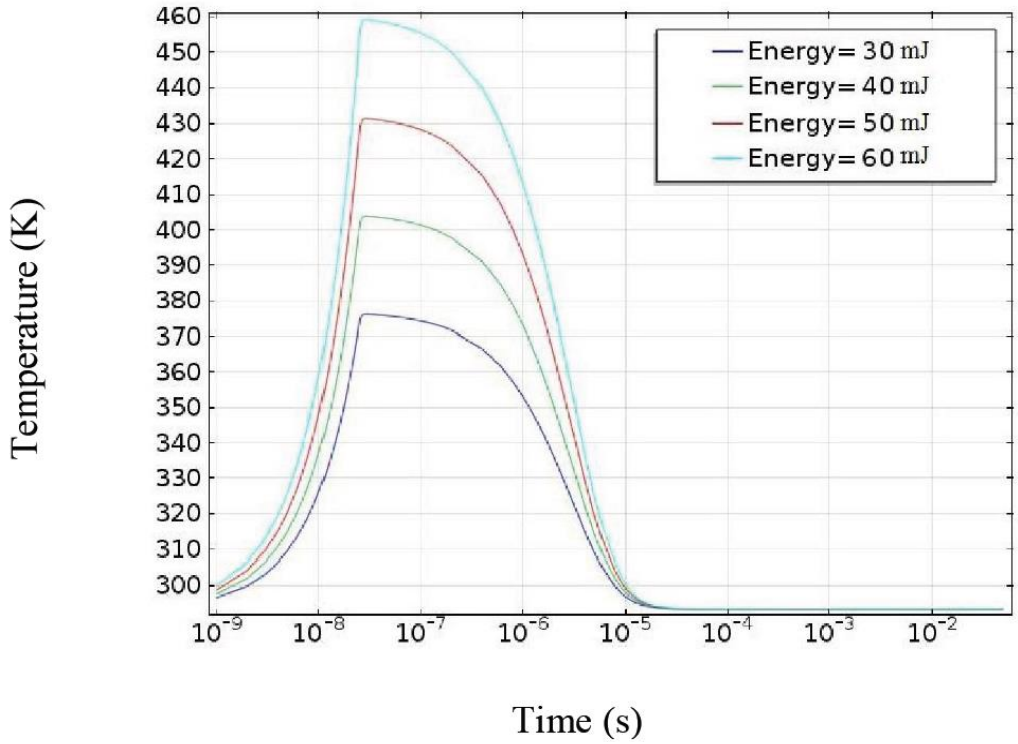

Figure 5.5 Temperature Variation with Time During Single Pulse of Ablation of Different Energy Level (Time axis is log Scale)

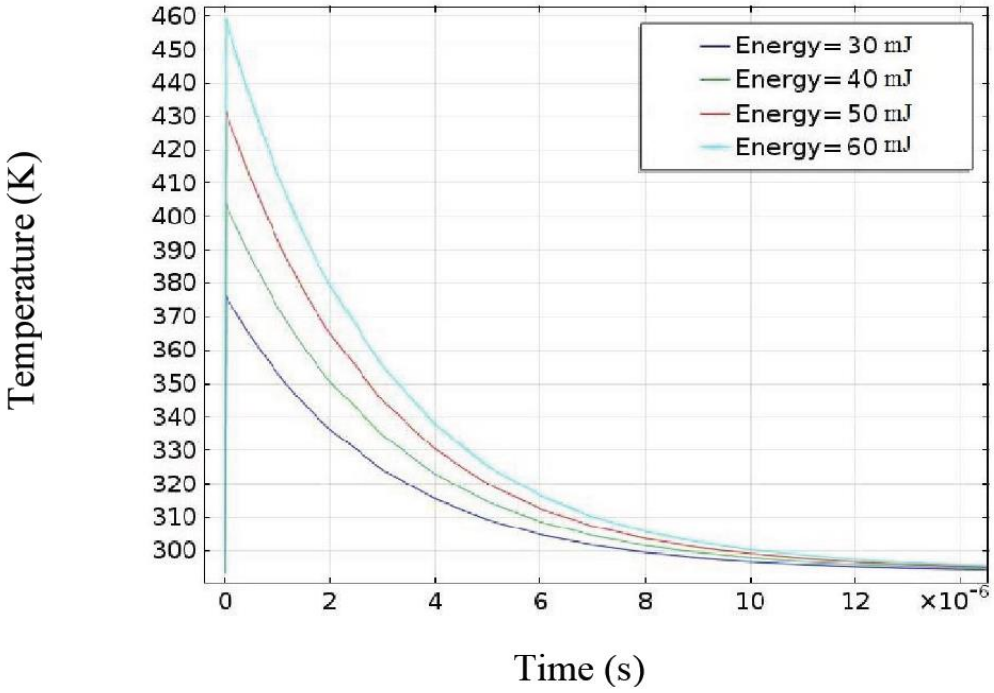

Figure 5.6 Temperature Variation with Time During Single Pulse of Ablation of Different Energy Level

The simulation work was performed to compute temperature as a function of space and time. Then the factor epsilon (ε), (Refer Eq. (5.4)), was computed as a function of time and space within the workpiece by few experiments under hydrogen and argon gas and it is obtained nearly equal to 0.5. The value of epsilon was further evaluated for various pulse energy from 30 to 60 mJ and almost similar result is obtained.

5.5 Experimental Study

The experimental setup explained in chapter 3 was used to validate the FE Results. The laser micro-machining system used for the experiments consisted of the mask projection arrangements. The Excimer laser beam spot size on the mask was designed to be of size 30mm × 30 mm, which is quite big, as is the case with excimer laser sources. Therefore, the mask projection technique has been employed for the micromachining rather than direct writing technique. The optics used in the set-up was designed to ensure a demagnification

ratio of 4 times, thereby beam size on the workpiece will be around 7.5mm × 7.5mm. The system could give maximum energy density 600 mJ/cm^2 on the target.

In order to make optical system containing beam shaper, beam homogenizer, projection lens etc a compact one, five numbers of steering mirrors (M1 to M5) were used as shown in Figure 3.4. Leaving aside the steering mirrors, the optical chain for the experimental set up consisted of the basic elements which included laser source, solenoid operated beam shutter, attenuator, beam shaper, beam-homogenizer, Fourier lens, field lens, mask, process lens, part positioning stage.

Measured pulse energy values at various points of the optical beam processing unit for an input energy of 645 mJ at the entry point of the beam delivery unit, is given in Table 5.3. Fluence of the Laser beam falling on work surface is of the order of 30 mJ cm^{-2} which shows huge amount of energy was lost by due to attenuation by the different optical elements present in Beam Delivery Unit as shown in Figure 3.4.

Table 5.3 Energy of Laser Beam at different Location in its Path

Number of Stages	**Description and Location of the Element in the Optical Path**	**Energy after the Element, mJ**
1	LASER source output to beam delivery unit	645
2	Steering Mirror, M1	480
3	Homogenized laser after Fourier lens	413
4	Steering Mirror, M2	408
5	Steering Mirror, M3	390
6	Steering Mirror, M4	263
7	Steering Mirror, M5 and transmitted through field lens and 20 mm circular	70.3
8	After projection lens with reduced diameter of 5 mm	66.7

A gas handling setup was separately fabricated for admitting gas at a predefined flow rate (gas flow rate= 1.0 lpm, temperature=300 K, and pressure=1 bar) over the surface of polymer during the laser ablation process. The set-up consisted of a cylindrical steel chamber made up of SS304 having a volume of about 100 ml with gas inlet and outlet for gas admittance at predefined flow rates. A calcium fluoride window of 2-inch dia. was fixed over ablation chamber, normal to laser beam axis. The chamber was evacuated with a rotary vane pump and the vacuum created was of the order of 10^{-3} mbar before flowing the working gas, and due to this, the amount of ambient air became insignificant in the chamber as the pressure ratio reached upto 10^{-6}. The lower and upper explosive limits for hydrogen are 4% and 75% by volume respectively. Instead of a normal gas cylinder, it has been ensured to get a small hydrogen gas cylinder of 20 litres capacity filled to 10 bar pressure, so that the total mass of hydrogen gas is very small and the fire potential is thus negligible. Further, in order to ensure an extremely safe operation of handling hydrogen gas, provision was made to evacuate the ablation chamber before admitting pure hydrogen into the ablation zone, which in turn ensured that the whole operation did not fall anywhere within the zone of explosive limits. Moreover, every joint in the hydrogen line was certified to very high level of leak tightness of the order of 1×10^{-9} mbar.litre/s of He. As far as safety aspect of hydrogen gas handling was concerned, hydrogen gas was used within the safety limit as per the safety standard of National Fire Protection Agency (NFPA).Stainless steel coupons (50mm dia. X 5mm thick) are used as metal substrate, over which photo resist polymer has been coated to about 500 μm thickness. The coating has been air dried and subsequently cured at 110 °C for about 1 h under vacuum at 10^{-2} mbar absolute pressure. This is done to achieve uniform coating thickness of the polymer which is free from entrapped gases in the polymeric material. The coated workpiece has been placed inside the steel chamber and mounted on the X-Y translation stage of laser micromachining set up for the experimental study, schematically

shown in Figure 3.5. A new set up as shown in Figure 3.8 is designed and fabricated which has got a capability to undertake laser ablation trials under flowing gas mixture having a predefined composition. A set of experiments were conducted in which pulse energy is varied from 30 mJ to 60 mJ in steps of 10 mJ. The ablation process has been performed under continuous flow of the gas. Two types of gaseous environment viz., hydrogen and argon were used to compare the response on material removal.

To compute the material removal due to the laser ablation, workpiece/sample weight is measured before and after ablation using a weighing machine (make Shimazdu and model AUX220) with resolution of 0.0001 g, and the difference is reported as the material removal.

Further, the experiments were repeated thrice to see the extent of variation from the simulated results.

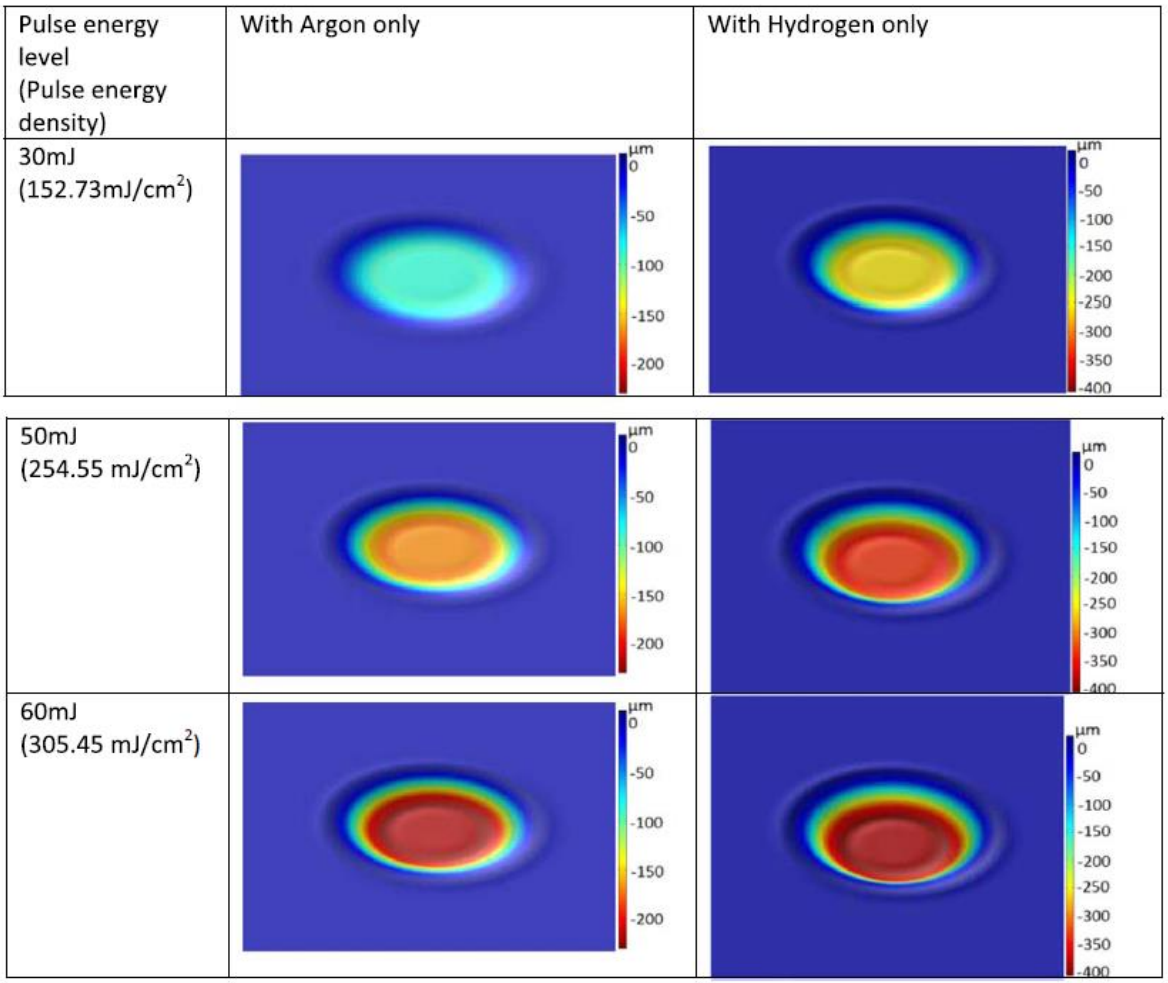

Figure 5.7 Effect of Laser Ablation on the Morphological Aspect of the Photoresist Polymer for Different Energy Levels as well as Two Level of Gaseous Environment

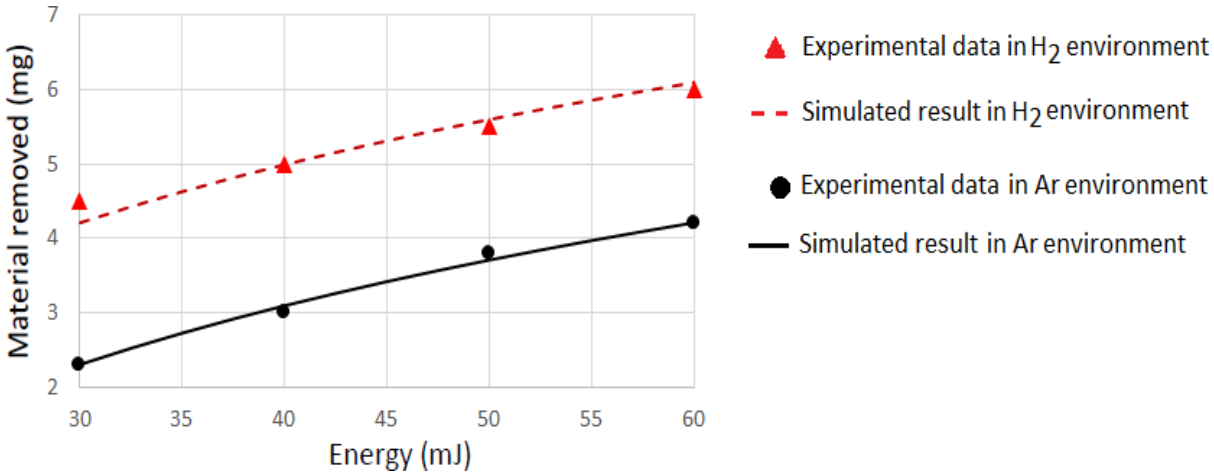

Figure 5.8 Experimental Validation of the Material Removal Under Presence of Argon Gas as well as Hydrogen Gas with Varying Pulse Energy with 2000 Number of Pulses.

ALE technique from FE simulation has been carried out using the proposed mathematical model for the response prediction. The simulated results have been validated with experimental data. The simulated results as shown in Figure 5.5 and Figure 5.6. It shows that the maximum temperature on the work surface does not go beyond 473 K or 200 ^{O}C which supports that the material removal takes place by means of photochemical dissociation only. The surface topography of ablated polymer in the presence of argon gas and hydrogen gas based on the FE simulation are presented in Figure 5.7. In this figure, three different pulse energy levels were used. To validate these simulated results, a set of experimentation were conducted. To experimentally validate the FE simulation, fresh experiments were conducted with argon as well as hydrogen gas and Figure 5.8 shows the comparison. It can be observed from Figure 5.8 that simulated results which are represented by lines are closely following the experimental data points (represented as dots and triangles). The simulation result showed that the material removal in this study occurs because of photo-dissociative phenomena rather than photo thermal phenomena as the maximum temperature does not cross beyond 470 K which is less than the glass transition temperature of the polymer. However, the modest heating of the polymer surface during excimer laser ablation under H_2 gas environment helps in providing the activation energy to generate hydrogen free radical at the polymer surface, resulting in Laser Assisted Chemical Reaction (LACR) of hydrogen atom with polymer, thereby increasing the MRR.

FE simulations of polymer mass ablated by excimer laser under hydrogen and argon medium has been carried out which are in good agreement with experimental results.

5.6 Results and Discussion

Simulated results and experimental results are compared and discussed here. Effect of both gaseous medium on temperature variation, material removal rate, surface morphology and surface quality are discussed in this section.

5.6.1 Temperature Variation

From Figure 5.5 and Figure 5.6, it is observed that the temperature values obtained from simulation, under the experimental conditions of laser parameter, increases and reaches a maximum value of 470 K, 440 K, 410 K, 390 K, 360 K and 330 K at laser pulse energy levels of 60, 50, 40, 30, 20 and 10 mJ respectively. However, the temperature comes down to 300 K (room temperature) and it gets stabilized within 10 micro seconds. It may be inferred from Figure 5.5 that the temperature reaches its maximum value within few nanoseconds and drops down to room temperature within few micro seconds. It means that the material heating occurs during laser 'pulse-on' time in the time scale of nanosecond during which maximum temperature of 470 K is attained. Under this prevailing time scale and temperature, no adverse thermal effect is expected to occur. Moreover, the peak temperature of 470 K is less than the glass transition temperature of the polymer. Thus, it can be stated that the material removal occurs without any thermal effect on the workpiece. But the polymer surface temperature rise may play the role of providing activation energy required for the proposed mechanism of laser assisted chemical reaction (LACR) of polymer with hydrogen gas. This leads to enhanced Material Removal Rate (MRR) under hydrogen gas environment.

5.6.2 Material Removal

Mass of the ablated polymer material is calculated (based on simulation) and plotted along with those corresponding to the experimental data in Figure 5.8. The simulation result is indicated as continuous dotted and solid lines whereas the experimental values are

indicated as discrete points on the plot. This plot shows good agreement between simulated result and experimental data in case of hydrogen gas as well as argon gas environment. These results are also presented in tabular format in Table 5.4. Here, three set of similar experiments were carried out and mean values are tabulated with ± standard deviation.

Table 5.4 Experimental Results of Material Removal Under Two Different Gaseous Environments with Varying Pulse Energy Level.

Laser Pulse Energy (mJ)	**Fluence in ($mJ\ cm^{-2}$)**	**Material Removal (mg) in Gaseous Environment (mean ± standard deviation)**	
		Argon	**Hydrogen**
30	152.73	2.3±0.16	4.5±0.16
40	203.64	3.0±0.08	5.0±.14
50	254.55	3.8±0.14	5.5±.14
60	305.45	4.2±0.08	6.0±0.21

From Figure 5.8 and Table 5.4, it is observed that the material removal is almost getting shifted by 2 mgs in case of pure hydrogen gas environment as compared to pure argon. This shift in the mass removal can be explained by the model discussed earlier. As the polymer workpiece is exposed to the hydrogen gas environment, the top surface of workpiece gets covered by the hydrogen gas adsorption at room temperature, which is temperature dependent phenomenon. When laser radiation is applied on the surface, hydrogen gas molecule splits into atoms and it further move inside of the workpiece. Based on the initial adsorption of hydrogen molecule, a defined number of hydrogen atoms move inside of workpiece and reduces the threshold fluence to ablate. Thus, hydrogen environment leads to an increase in material removal by a constant value of 2 mgs (app.) in case of various pulse energy levels as shown in Figure 5.8.

In addition, it is also observed that the material removal increases with the pulse energy and the same has been validated with the experimental values as presented in Figure 5.8. As the pulse energy increases, more number of laser photons get bombarded for the ablation.

5.6.3 Surface Morphology

The surface morphology of the ablated surface is generated using the simulation of the mathematical model and they are presented in Figure 5.7. In this result it is observed that the depth of ablation increases with energy level. Moreover, the ablation depth is also higher in case of hydrogen gas as compared to argon gas. For example, for 30 mJ pulse energy, the depth of ablation is 110 μm under argon gas, whereas it is 260 μm under hydrogen gas; corresponding depth values for a pulse energy of 60 mJ were 250 μm under argon gas and 400 μm under hydrogen gas respectively. The simulated result of the shape of ablated surface also matches with experimental results.

5.6.4 Surface Quality

Surface quality is another area in which hydrogen gas has influence for better edge quality and haze-free surface. Here, “haze free surface” indicates the surface which is free from stains occurring by oxidation during laser ablation. Experimental results as shown in

Figure 5.9 and Figure 5.10 shows that hydrogen gas is responsible for fabricating micro-features with excellent edge quality and haze free surface. For edge quality and the surface quality, a portion of the ablated feature is zoomed and shown in Figure 5.9 and Figure 5.10. From these photographs it is obvious that the surface ablated under hydrogen gas is superior to surface ablated under the inert atmosphere of argon gas.

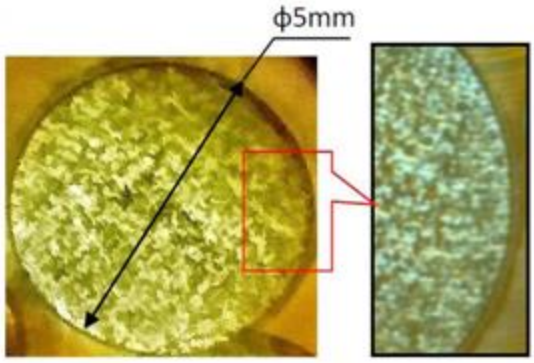

Figure 5.9 Surface Ablated under Hydrogen Gas

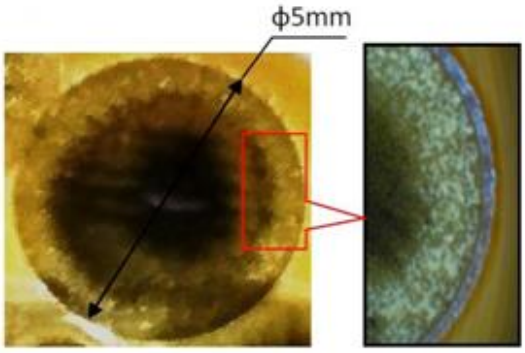

Figure 5.10 Surface Ablated under Argon Gas

5.7 Summary

The present study confirms a novel finding about the effect of hydrogen gas during excimer laser based micromachining of photo-resist polymer. Moreover, the phenomenon of ablation under hydrogen gas environment was modelled and simulated in this chapter. The model was validated with experimental results and the results were discussed. The significant outcome of the present study can be summarized in following points.

1. It was found that material removal rate is almost double in case of hydrogen as compared to inert environment of argon gas. Interaction phenomena of hydrogen gas and polymer under influence of excimer laser is discussed, modelled and simulated. This was attributed to LACR of polymer with hydrogen, which is reported here.

2. The simulation result showed that the material removal in this study occurs because of photo-dissociative phenomena rather than photo thermal phenomena as the maximum temperature does not cross beyond 470 K. However, the modest heating of the polymer surface during excimer laser ablation under H_2 gas environment helped in providing the activation energy to generate hydrogen free radical at the polymer surface, resulting in Laser Assisted Chemical Reaction(LACR) of hydrogen atom with polymer, thereby increasing the MRR.

Chapter 6

Data Driven Prediction Models for Ablated Depth

6.1 Introduction

Regression means finding a function which approximately maps an input domain to the real number output domain on the basis of a training sample. Five data driven models, Linear Regression (LR), Gaussian Process Regression (GPR), Cubic Support Vector Machine Regression (Cubic SVM), Artificial Neural Network (ANN) and Response Surface Methodology (RSM) were employed to model the Laser Micromachining process and their prediction capability for ablated depth. Laser energy, pulse repetition rate, gas flow rate are input parameters and ablation depth is output parameter of laser micromachining process, which are included by these models.

Machine Learning is considered as a subfield of the broader field, Artificial Intelligence (AI) and it is associated with the advancement of techniques and methods which empower the computer to learn. In simple words, it is advancement of algorithms which help the machine to learn and accordingly perform activities related to specific tasks. Machine learning is having connections with statistics in numerous ways. Over the passage of time, several techniques and methodologies were developed for machine learning tasks [107].

6.1.1 Statistical Learning Theory

The statistical learning theory provides a basis for identifying the problem, studying the problem by acquiring knowledge, making forecasts and deciding from the set of data. In simple

words, it enables the selection of the hyper plane space in such a way that it closely characterizes the primary function in the target space [108].

In statistical learning theory the problem of supervised learning is formulated as follows. A set of training data is given as $\{(\mathbf{x}_1,y_1)... (\mathbf{x}_n,y_n)\}$ in $R^n\times$ R sampled space according to unknown probability distribution P(**x**,y), and a loss function V(y,f(**x**)) which measures the error. For a given **x**, f(**x**) is predicted instead of the real value y. The problem comprises of finding a function (f) that minimizes the prospect of the error on new data; means finding a function f that minimizes the expected error [109].

$$\text{Error} = \int V(y, f(\mathbf{x}))\, P(\mathbf{x}, y)\, d\mathbf{x}\, dy \qquad \text{--- (6.1)}$$

In statistical modelling we would select a model from the hypothesis space, which is nearest (with respect to some degree of error) to the underlying function in the target space.

6.1.2 Learning and Generalization

Initial machine learning procedure is intended to learn illustrations of simple functions. Hence, the aim of learning was to yield a hypothesis that achieved the correct classification of the training data. Initial learning algorithms were designed to find such a precise fit to the data [110]. The capability of a hypothesis to properly classify data which is not used in the training set is known as its generalization. SVM performs better in terms of not over generalization when compared to the neural networks which might easily end up doing over generalizing of data [111]. One more thing to consider is that, where to make the best trade-off between training complexity and the number of epochs. The illustration shown in Figure 6.1brings more clarity of the information given above.

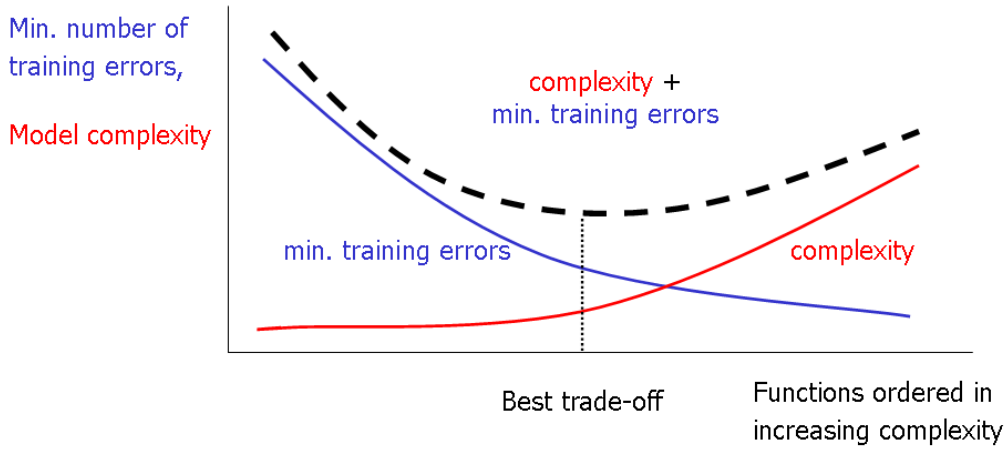

Figure 6.1 Illustration of Trade-off between Training Complexity and the Number of Epochs

6.2 Linear Regression

Linear Regression (LR) employing linear relationship between a quantitative dependant variable and a single quantitative explanatory variable was used in the present study. Flow rate, laser Pulse Repetition Frequency (PRE) and Laser energy are the three explanatory variables and ablation depth is the dependant variable. A linear relationship between the population mean of the outcome and the value of the explanatory variables is postulated and coefficients are calculated.

A simple regression, which implies a single independent variable, can accommodate most of functional relation between the left-hand side [LHS] (*i.e.*, dependent) variable and right-hand side [RHS] (*i.e.*, independent) variable. In general, it is easier to think about the relation between the variables as either linear or non-linear (*i.e.*, concave, convex or some arbitrary polynomial). A simple linear regression equation models the stochastic relation between the dependent and the independent variable as:

$$Y = A + BX + \in \qquad \text{--- (6.2)}$$

At X_i the vertical difference between the estimated, $\hat{Y}_i$, and the actual observation, Y_i is defined as error, e_i

$$e_i = (Y_i - \hat{Y}_i) \quad \text{--- (6.3)}$$

The function which has to be minimized (by choosing a and b) is

$$\sum_i (Y_i - \hat{Y}_i)^2 = \sum_i (Y_i - a - bX_i)^2 \quad \text{--- (6.4)}$$

This is referred to as the Sum of Squared Errors or, SSE. It can be proven that if we choose b as:

$$\boxed{b = \frac{\sum_i (X_i - \bar{X})(Y - \bar{Y})}{\sum_i (X_i - \bar{X})^2} = \frac{\sum_i X_i Y_i - n\bar{X}\bar{Y}}{\sum_i X_i^2 - n\bar{X}^2};} \quad \text{--- (6.5)}$$

and a as

$$\boxed{a = \bar{Y} - b\,\bar{X}}, \quad \text{--- (6.6)}$$

then SSE will be minimized.

Formulas (6.2), (6.3) (6.4) (6.5) and (6.6) give the least-squares estimate of the true model (*i.e.*, the true relation between Y and X) as

$$\hat{Y} = a + b\,X \quad \text{--- (6.7)}$$

While computing the standard deviation for a set of one dimensional (one variable) set of observations, each value is compared to the common mean and the differences are squared. In the least squares formula, each observation is compared to its own (conditional) mean and the differences are squared.

The Coefficient of Determination, r^2, is simply the ratio of SSR (the explained variation in *Y*) to SST(the total variation in *Y*), or

$$r^2 = SSR/SST = 1 - SSE/SST = 1 - \frac{\sum (Y_i - \hat{Y}_i)^2}{\sum (Y_i - \bar{Y}_i)^2} = \frac{a\sum Y_i + b\sum Y_i X_i - n\bar{Y}^2}{\sum Y_i^2 - n\bar{Y}^2} \quad \text{---(6.8)}$$

In present case we have 3 input parameters viz Flow rate(X_1), Laser pulse repetition (X_2) and laser energy (X_3) as input parameters and Ablation Depth(Y) as output.

So the equation becomes $Y = aX_1 + bX_2 + CX_3 + d$ ---(6.9)

The 48 sets of experimental values were used to calculate the coefficients of the equation (6.9).

The coefficients obtained using MATLAB are

a=4.633333,b=-2.5135, c=0.950625 and d=64.31542

So the final equation becomes

Ablation depth = Flow rate*4.633 + Laser pulse repetition*(-2.5135) + Laser Energy*0.950625 + 64.315

The prediction capabilities of linear regression are shown in Table 6.4, and graphically represented in Figure 6.2 and Figure 6.3. It can be observed that prediction response of linear regression model is having root mean square error of 13.22 compared with experimental results.

The Coefficient of Determination R^2, for the predicted Ablation depth using Linear regression is 0.858. Which shows the prediction capability if LR is fairly good, but not very accurate in predicting the Ablation depth, as the relation between ablation depth and input parameters (flow rate, laser pulse repetition and laser energy) is not limited to single order.

Hence coefficient of determination is low which needs to be improved for reliable prediction. But since it is very simple method, we may say that the result is promising.

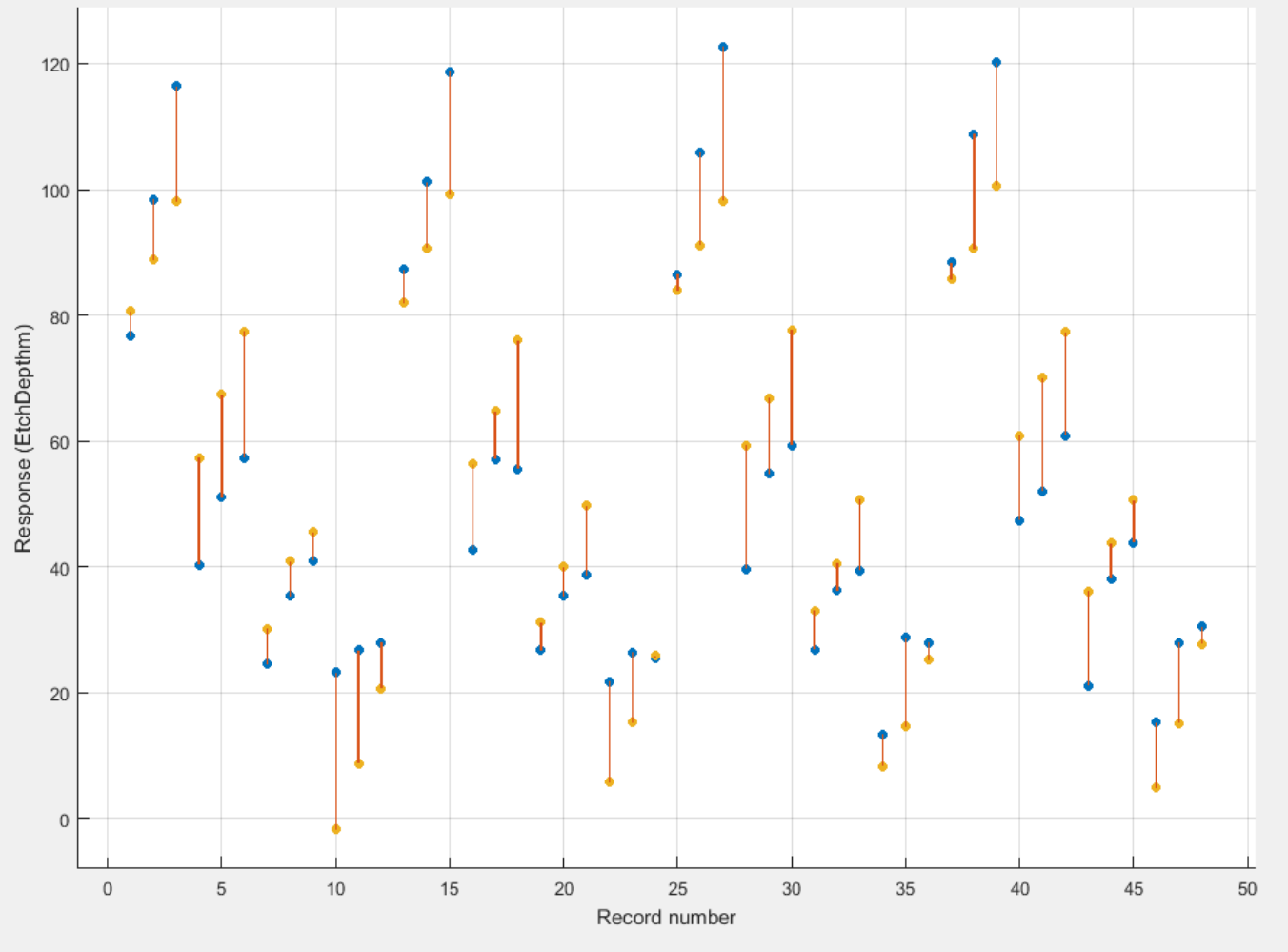

Figure 6.2 Deviation of Predicted Ablation Depth by LR from Experimental Data

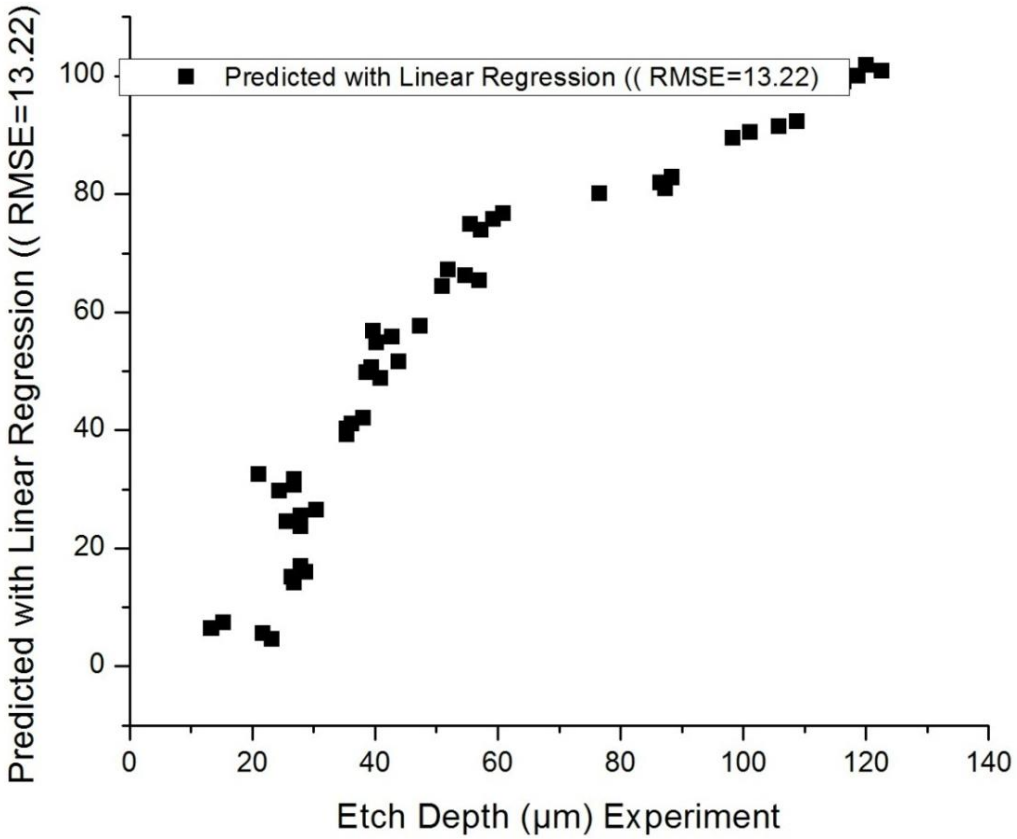

Figure 6.3 Deviation of Predicted Ablation Depth by LR from Experimental Data

6.3 Gaussian Process Regression(GPR)

GPR models are nonparametric kernel-based probabilistic models which helps to quantify uncertainty in prediction resulting from intrinsic noise in the problem and errors in the parameter estimation procedure [112]. Though GPR is a form of supervised learning, the training data are harnessed in a subtler way with the help of 'fitrgp' function of MATLAB. In present study fitrgp function was used to train the GPR model. Unlike other regression methods, in which a function (quadratic, cubic, or even non-polynomial) is assumed and used for model selection to choose from various possibilities, GPR is an even finer approach as it can represent function obliquely and more rigorously.

- A Gaussian process is defined as a probability distribution over functions y(x), such that the set of values of y(x) evaluated at an arbitrary set of points $x_1,..X_n$ jointly have a Gaussian distribution.
    - Probability distribution indexed by an arbitrary set
    - Any finite subset of indices defines a multivariate Gaussian distribution
- Input space X, for each x the distribution is a Gaussian, what determines the GP is
    - The mean function μ(x) = E(y(x))
    - The covariance function (kernel) k(x,x') = E(y(x)y(x'))
    - In most applications, we take μ(x)=0. Hence the prior is represented by the kernel.

Consider the training set $\{(x_i, y_i);\ i = 1,2,...n\}$, where $x_i \epsilon R^d$ and $y_i \epsilon R$, drawn from an unknown distribution. A GPR model addresses the question of predicting the value of a response variable y_{new}, given the new input vector x_{new}, and the training data. A linear regression model is of the form

$$y = x^T\beta + \varepsilon \qquad \text{--- (6.10)}$$

Where $\varepsilon \sim N(0, \sigma^2)$.). ε is the error with mean zero and variance σ^2. The error variance σ^2 and the coefficients β are estimated from the data. A GPR model explains the response by introducing latest variables, $f(x_i),\ i = 1,2,...n,$ from a Gaussian Process (GP), and explicit basis function, h. The covariance function of the latest variables captures the smoothness of the response and basis-functions project the inputs x into p-dimensional feature space.

A GP is a set of random variables, such that any finite number of them have a joint Gaussian distribution. If $\{f(x), x \epsilon R^d\}$ is a GP, then given n observations $x_1, x_2, \ldots x_n$, the joint distribution of the random variables $f(x_1), f(x_2), \ldots f(x_n)$ is Gaussian. A GP is defined by its mean function $m(x)$ and covariance function, $k(x, x')$. That is $\{f(x), x \epsilon R^d\}$ is a Gaussian process, then

$$E(f(x)) = m(x) \quad \text{--- (6.11)}$$

and $$Cov\,[f(x), f(x')] = E\,[\{f(x) - m(x)\}\{f(x') - m(x')\}] = k(x, x') \quad \text{--- (6.12)}$$

Now consider the following model

$$h(x)^T \beta + f(x), \quad \text{--- (6.13)}$$

where $f(x) \sim GP(0, k(x, x'))$, that is $f(x)$ are zero mean GP with covariance function, $k(x, x')$. $h(x)$ are asset if basis functions that transform the original feature vector x in R^d into a new feature vector $h(x)$ in R^p, β is a p-by-1 vector of basis function coefficients. This model represents a GPR mode. An instance of response y can be modelled as

$$P(y_i | f(x_i), x_i) \sim N(y_i | h(x_i)^T \beta + f(x_i), \sigma^2) \quad \text{--- (6.14)}$$

Hence, a GPR model is a probabilistic model. There is a latent variable $f(x_i)$ introduced for each observation x_i which makes the GPR model nonparametric. In vector form, this model is equivalent to

$$P(y | f, X) \sim N(y | H\beta + f, \sigma^2 I), \quad \text{--- (6.15)}$$

Where

$$X = \begin{pmatrix} x_1^T \\ x_2^T \\ \vdots \\ x_n^T \end{pmatrix}, \quad y = \begin{pmatrix} y_1 \\ y_2 \\ \vdots \\ y_n \end{pmatrix}, \quad H = \begin{pmatrix} h(x_1^T) \\ h(x_2^T) \\ \vdots \\ h(x_n^T) \end{pmatrix}, \qquad f = \begin{pmatrix} f(x_1) \\ f(x_2) \\ \vdots \\ f(x_n) \end{pmatrix} \qquad \text{--- (6.16)}$$

The joint distribution of latent variables $f(x_1)$, $f(x_2)$, …$f(x_n)$ in the GPR model is as follows:

$$P(f|X) \sim N(f|0, K(X,X)) \qquad \text{--- (6.17)}$$

Close to a linear regression model, where $K(X,X)$ looks as follows:

$$K(X,X) = \begin{pmatrix} k(x_1,x_1) & k(x_1,x_2) & \dots & k(x_1,x_n) \\ k(x_2,x_1) & k(x_2,x_2) & \dots & k(x_2,x_n) \\ \vdots & \vdots & \ddots & \vdots \\ k(x_n,x_1) & k(x_n,x_2) & \dots & k(x_n,x_n) \end{pmatrix} \qquad \text{--- (6.18)}$$

The covariance function $k(x, x')$ is usually parameterized by set of kernel parameters of hyper-parameters, θ. Often $k(x, x')$ is written as, $k(x, x'|\theta)$ to explicitly indicate the dependence on θ. Parameters used in the MATLAB toolbox to solve the present problem and to get the relation between input and output is shown in Table 6.1.

Table 6.1 Parameters used in MATLAB Toolbox

1	Model Type	Matern 5/2 GPR
2	Basis Function	Constant
3	Kernal function	5/2 Matern
4	Kernal Scale	Automatic
5	Kernal Sigma	Automatic

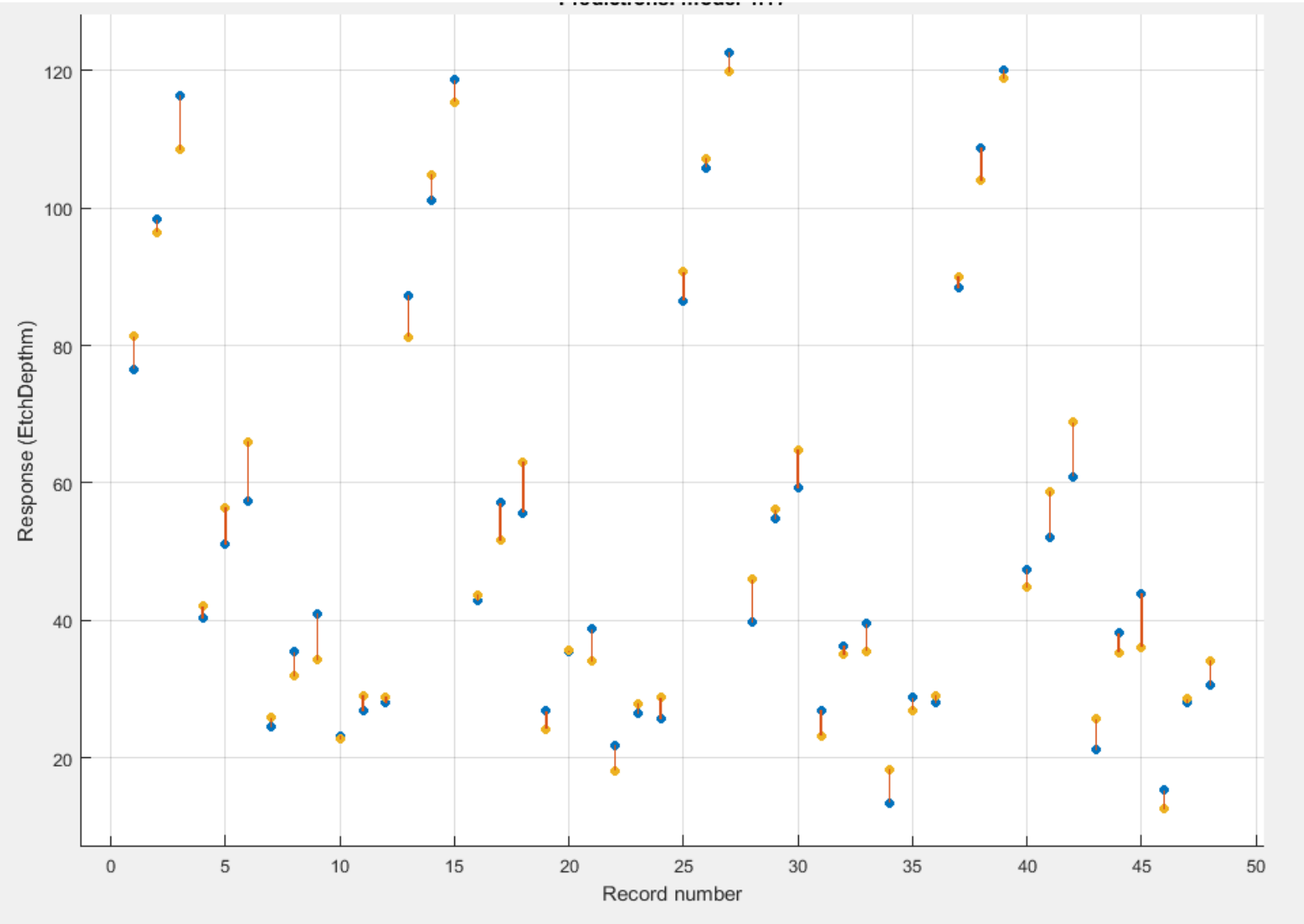

Figure 6.4 Deviation of Predicted Ablation Depth by GPR from Experimental Data

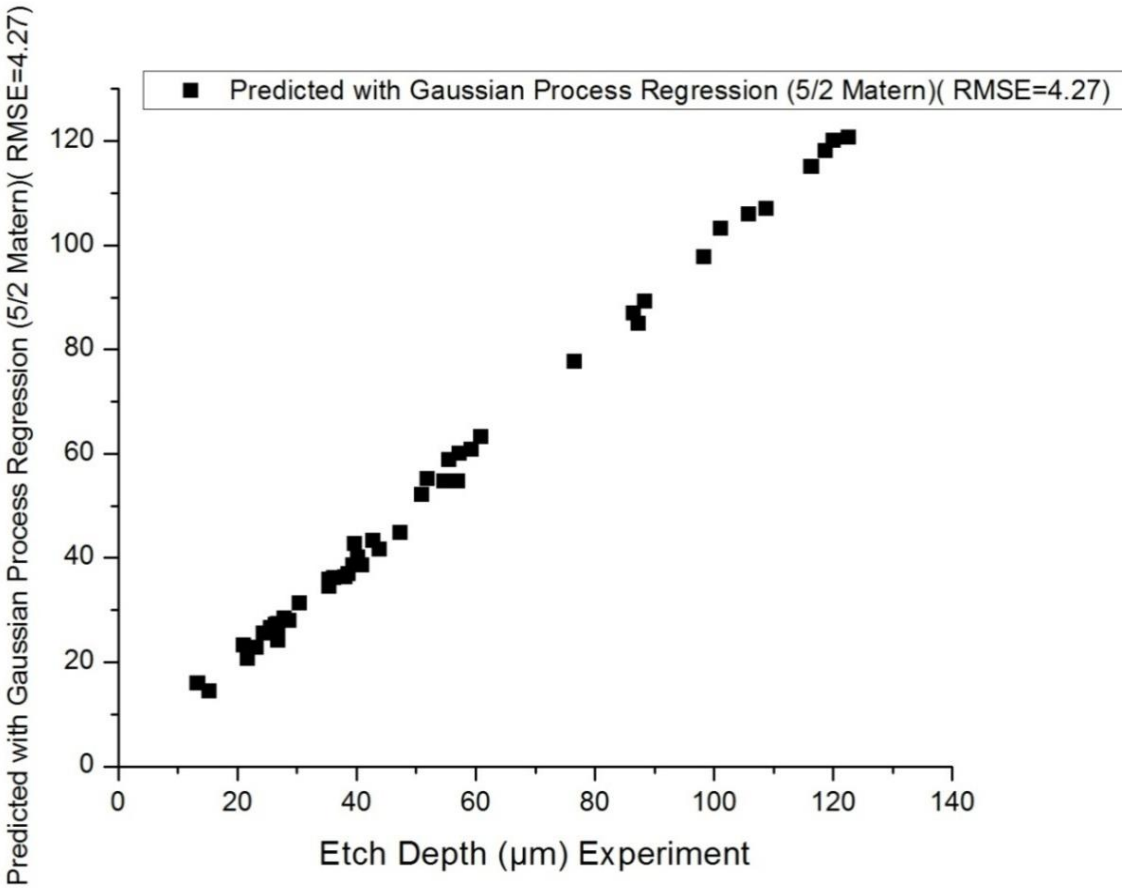

Figure 6.5 Deviation of Predicted Ablation Depth by GPR from Experimental Data

The prediction capabilities of GPR is shown in Table 6.4, and graphically represented in Figure 6.4 and Figure 6.5. It can be observed that prediction response of GPR model is having good agreement with experimental results.

Gaussian Process Regression (GPR) is modelled using MATLAB tool box. The Coefficient of Determination R^2, for the predicted Ablation depth using GPR is 0.996 with RMSE of 4.27. The prediction capability if GPR is very good. It can be used to model the present excimer laser micro-machining process accurately.

6.4 Cubic SVM

Support Vector Machine (SVM) was first perceived in 1992 which was introduced by Boser, Guyon, and Vapnik in COLT-92. Support Vector Machines (SVMs) are a set of connected and supervised learning methods used for either classification or regression [107]. They are associated to a family of generalized linear classifiers. In alternative term, Support Vector Machine (SVM) is a classification and regression forecasting tool that uses machine learning theory to improve predictive accuracy while automatically avoiding the over-fitting to data. Support Vector machines are described as the systems, which use hypothesis space of a linear functions in a high dimensional feature space and trained with a learning algorithm obtained from optimization theory that implements a learning bias derived from statistical learning theory. Support vector machine was originally popular with the NIPS community and later became an active part of the machine learning research all around the globe. SVM becomes famous when it was using pixel maps as input to give accuracy equivalent to sophisticated neural networks with elaborated features in a handwriting recognition task [113]. It is also used for various other applications, like, face analysis. It is especially used for pattern classification and regression based applications.

The foundations of Support Vector Machines (SVM) had been developed by Vapnik [114] and gained popularity due to countless promising features like better empirical performance. The formulation uses the Structural Risk Minimization (SRM) principle, which proved to be superior to traditional Empirical Risk Minimization (ERM) principle used by conventional neural networks [115]. SRM minimizes an upper limit on the probable risk, whereas ERM minimizes the error of the training data. This difference is responsible for providing greater ability of generalization to SVM, which is the objective in statistical learning. SVMs were initially developed to solve the classification problem, but recently they have been extended to solve regression problems as well [116].

6.4.1 SVM Representation

The objective function is a function combining a loss function and flatness

$$\min_{b_j} \sum_{i=1}^{n_v} V_c(r_i) + \sum_{j=1}^{n_b} k_j b_j^2$$

$$V_c(r) = \begin{cases} 0 & if\ |r| < \epsilon \\ r - \varepsilon & otherwise \end{cases}$$

$$r_i = \sum_{j=1}^{n_b} b_i \xi_j(x_i) - y_i$$

The loss function can be any loss function. Most commonly used loss function is epsilon in sensitive loss function because it is more insensitive to a bad data point. Flatness is the measure of curvature with its shape function. An example of flatness function is

$$F = \sum_{i=1}^{n_b} k_i b_i^2$$

We try to minimize the loss function and flatness of the curve. The loss function can be any loss function. Most used loss function is epsilon in sensitive loss function because it is more insensitive to a bad data point. Figure 6.6shows that there is no penalty between the epsilon values. Flatness is the measure of curvature with I_{th} shape function.

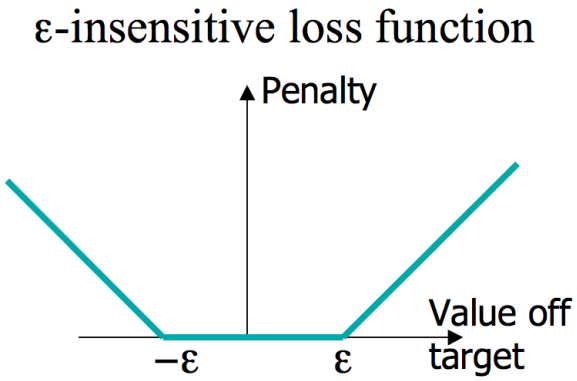

Figure 6.6 Epsilon Loss Function

MATLAB is used to build SVR model. There are different parameters in SVR. If the data point is not linear separable, we can use a kernel trick to transform the data. The original data will transform to a higher dimensional data so the points can be linear separable. The options of kernels in SVR are linear, poly, RBF, and sigmoid. The default kernel is Radial Basis Function (RBF). Choosing the right kernel is very important. R-square score can dramatically change with different choices of kernel. The two most popular non-linear kernels are polynomial kernel and radial basis function (RBF) kernel. Here in our case polynomial of degree 3 ie cubic kernel is used.

6.4.1.1 Kernel Functions

The objective of the kernel function is to facilitate operations to be performed in the input space rather than the potentially multi-dimensional feature space. Hence the inner product need not be calculated in the feature space. The function should perform mapping of the attributes of the input space to the feature space. The kernel function plays a significant role in SVM and its performance.

$$K(x, x') = \langle \phi(x), \phi(x') \rangle, \quad \text{--- (6.19)}$$

$$K(x, x') = \sum_{m}^{\infty} a_m \phi_m(x) \phi_m(x'), \quad a_m \geq 0, \quad \text{--- (6.20)}$$

$$\iint K(x, x') g(x) g(x') dx dx' > 0, \quad g \in L_2 \quad \text{--- (6.21)}$$

If K is a symmetric positive definite function, which satisfies Mercer's Conditions, then the kernel represents a correct inner product in feature space. The training set is not linearly

divisible in an input space, but it set is linearly divisible in the feature space; which is known as Kernel trick [117]. The different kernel functions are given below.

1) Polynomial: A polynomial mapping is a popular method for non-linear modelling. The second kernel is usually preferable as it avoids problems with the hessian becoming Zero.

$$K(x, x') = \langle x, x' \rangle^d. \quad \text{--- (6.22)}$$

$$K(x, x') = \left(\langle x, x' \rangle + 1\right)^d. \quad \text{--- (6.23)}$$

2) Gaussian Radial Basis Function: Radial basis functions most commonly with a Gaussian form

$$K(x, x') = \exp\left(-\frac{\|x - x'\|^2}{2\sigma^2}\right) \quad \text{--- (6.24)}$$

3) Exponential Radial Basis Function: A radial basis function produces a piecewise linear solution which can be attractive when discontinuities are acceptable.

$$K(x, x') = \exp\left(-\frac{\|x - x'\|}{2\sigma^2}\right) \quad \text{--- (6.25)}$$

4) Multi-Layer Perceptron (MLP): The long established MLP, with a single hidden layer, also has a valid kernel representation.

$$K(x, x') = \tanh\left(\rho\langle x, x' \rangle + \varrho\right) \quad \text{--- (6.26)}$$

There are many more kernal functions which include Fourier, splines, B-splines, additive kernels and tensor products[118].

6.4.1.2 Controlling Complexity in SVM

SVM is prevailing to estimate any training data and generalizes superior on given datasets. The complexity in terms of kernel, affects the performance on new datasets [119]. The complexity of SVM is controlled by supporting parameters and SVM is not able to set these parameters which needs to be determined by user by Cross-Validation on the given datasets [120]. The Figure 6.7 given below shows a better illustration.

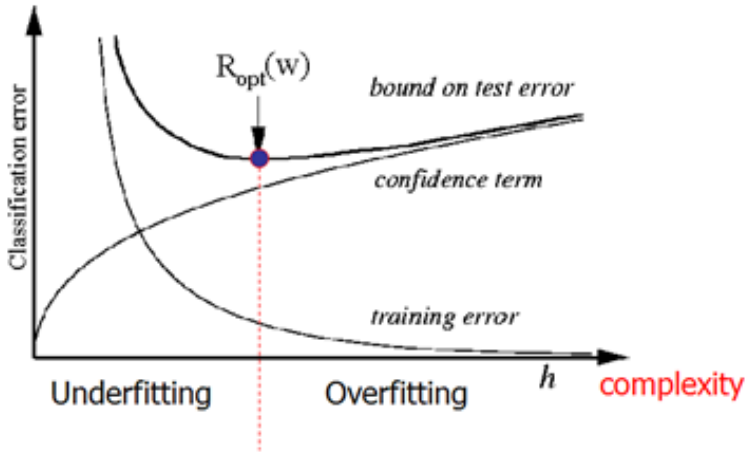

Figure 6.7 Graphical Representation to Control Complexity

6.4.2 SVM Penalty Term

Another important parameter is 'C'. C is the penalty term. It is a tradeoff between mis-classification of training examples and simplicity of the decision surface. A lower C has a smoother decision surface. A higher C tries to classify all training data correctly by giving the model more options to choose support vectors. Epsilon is the epsilon in the epsilon tube. No penalty is associated with the training loss function, when points are inside the epsilon tube as shown in Figure 6.8. The goal is to get as many points fitted within this epsilon tube as possible; here c value of 100 is used in our case, for the SVH modeling.

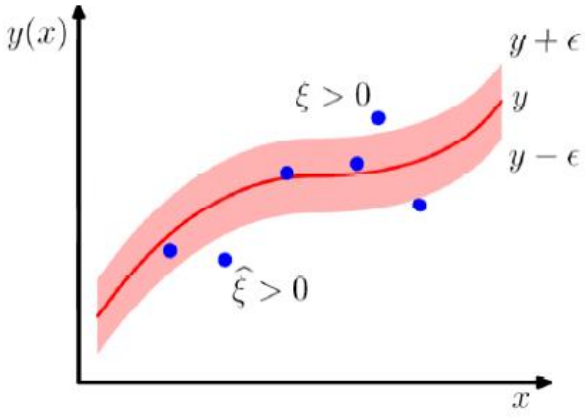

Figure 6.8 Epsilon Tube

Table 6.2 Parameters used in MATLAB Toolbox for SVM

1	Model Type	Cubic SVM
2	Kernal function	Cubic
3	Kernal scale	Automatic
4	Epsilon	100
5	PCA	Not required

The prediction capabilities of cubic Support Vector Machine Regression are shown in Table 6.4, along with those of other prediction models, described in this chapter. It is graphically represented in Figure 6.9 and Figure 6.10. SVM Regression is modelled with MATLAB toolbox. The Coefficient of Determination R^2, for the predicted Ablation depth using SVM is 0.986 and RMSE is 4.90um. It can be observed that prediction response of Cubic SVM model is having good agreement with experimental results because nonlinear kernel function is used for modelling.

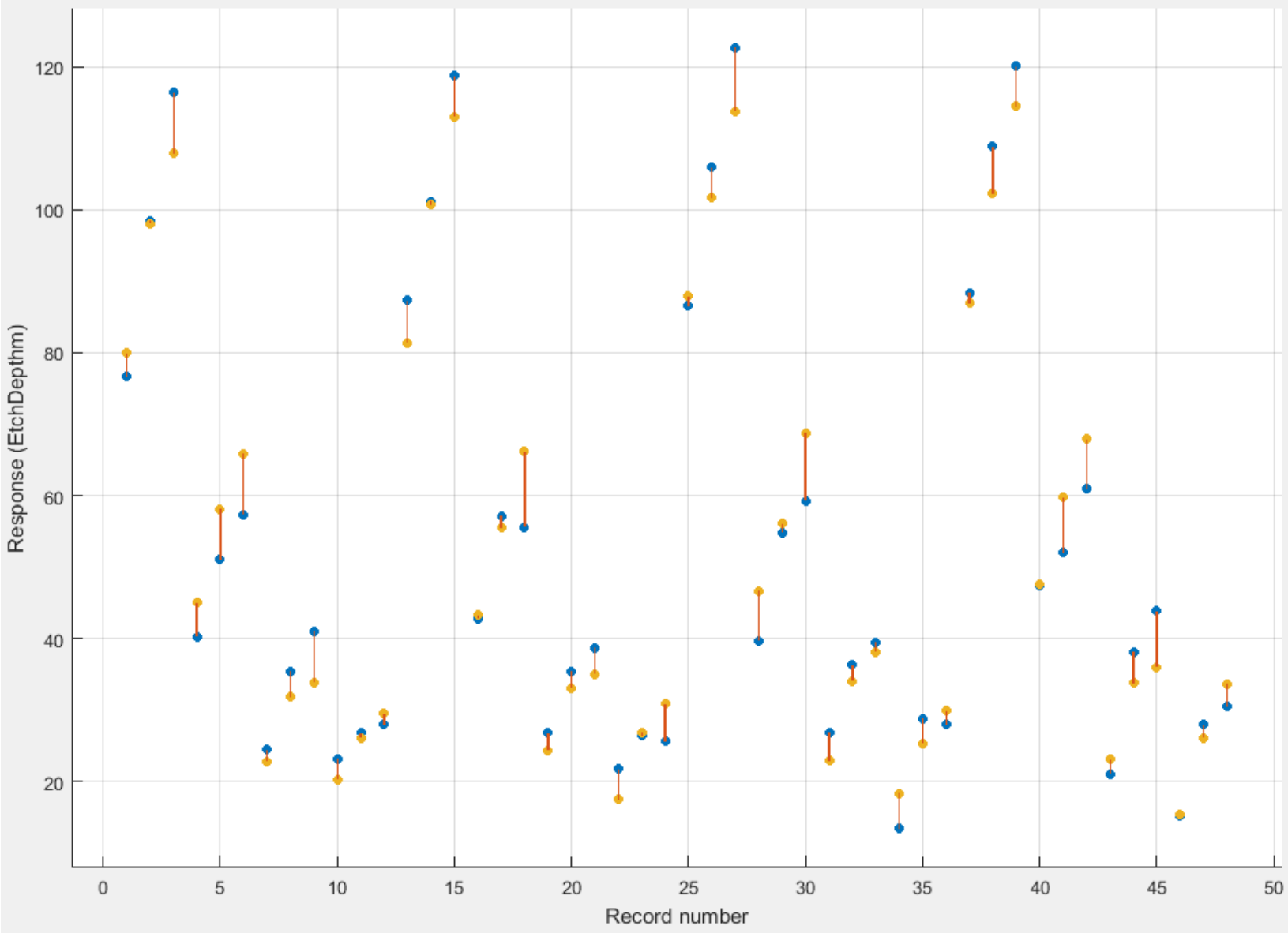

Figure 6.9 Deviation of Predicted Ablation Depth by SVM from Experimental Data

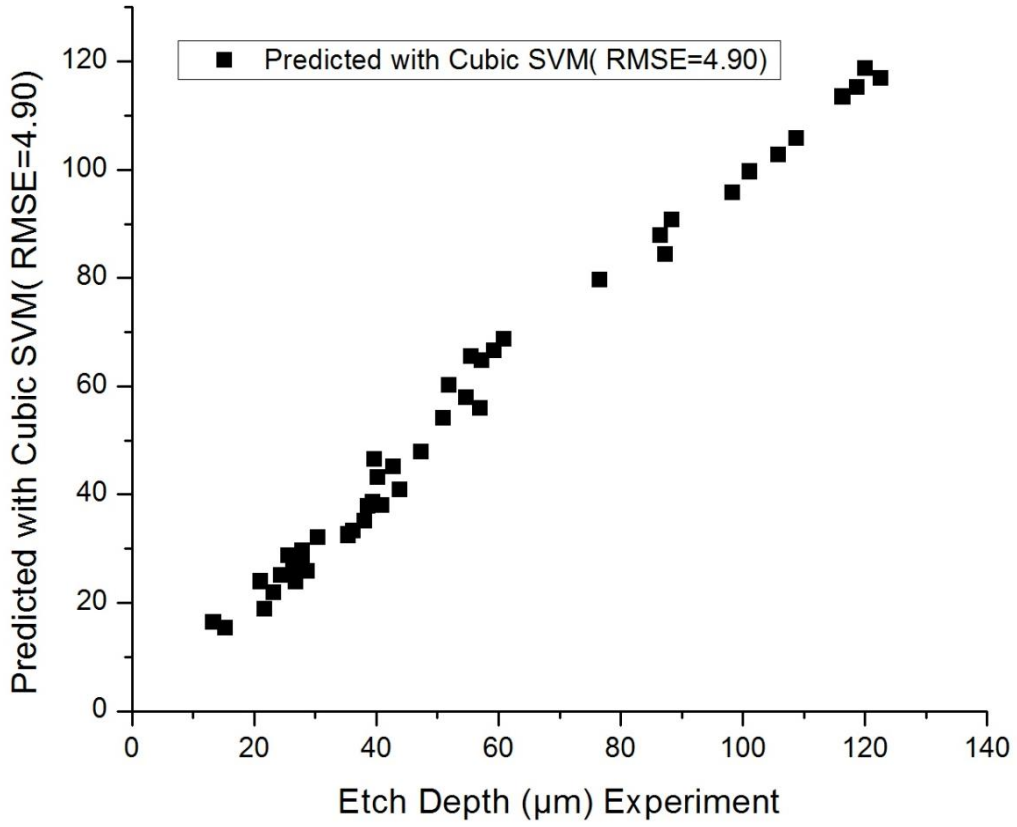

Figure 6.10 Deviation of Predicted Ablation Depth by SVM from Experimental Data

6.5 ANN

For ANN, a three-layer feed-forward neural network was developed and trained by back-propagation gradient-descendent algorithm. The experimental data were randomly classified into two sets containing 32 and 16 data to be employed for training and validation respectively. Training data sets were used for updating weights and biases via Levenberg–Marquardt algorithm and the test data were utilized to evaluate the generalization ability of the trained network. A hyperbolic tangent sigmoid function and two linear functions were used as transfer functions for the neurons in the hidden layer and the neurons in the input and output layers respectively. The input and output layers had 3 and 1 neurons respectively. To determine the optimal number of neurons in the hidden layer, different topologies were examined during which

the number of neurons varied between 3 and 15. Based on the values of R^2 and RMSE, 5 numbers of neurons were observed to be providing satisfactory results. Accordingly, ANN model for hydrogen gas medium was developed with 3 inputs- 5 nodes mono hidden layer-output concept, as shown in Figure 6.11.

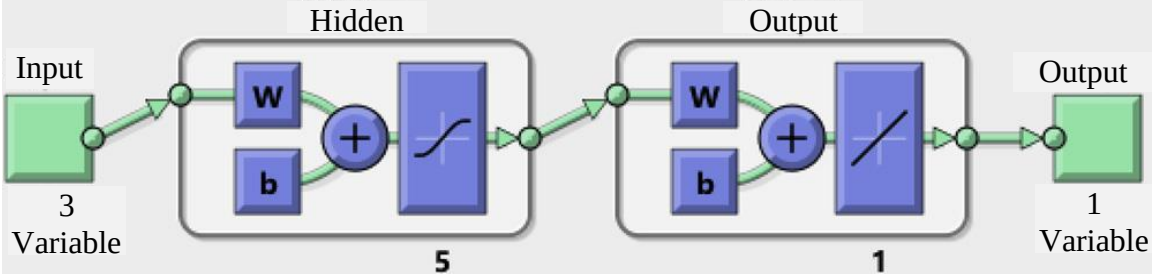

Figure 6.11 Artificial Neural Network Training Structure.

Having understood the main and interaction effects of input parameters viz., laser energy, PRF and hydrogen gas flow rate on the Material Removal Rate (MRR) of photoresist, ANN model is constructed. For this modelling purpose, 48 experiments, each in triplicate were carried out under different input parameters, for a fixed number of laser shots of 500. Each of these input parameters are introduced to ANN structure by an input layer neuron. Experimental data sets are used to train the ANN to make the general understanding of the model. Among the data sets, 2/3 of the data is used for training the ANN model, while 1/3 is used for validation purpose. While training set is used to adjust the network weights and errors in each iteration, validation sets are used to optimize the ANN architecture with respect to number of neurons for the hidden layer. Based on the least mean square error as evaluation criterion, a structure of neural network with single hidden layer with five nodes is, observed to be the appropriate one for ANN modelling as shown in Figure 6.11. Correlation of training and validation data sets with the predicted values showed correlation coefficient>0.99, indicating that the single layer five neural nodes ANN model, is sufficient to explain the result satisfactorily.

The model equation for the prediction of etch depth is given by,

Etch depth (μm) = [106.71 – (17.63*H_1) – (8.04*H_2) - (100.08*H_3) – (49.20*H_4) + (17.47*H_5)]

where H_1, H_2, H_3, H_4 and H_5 are five hidden nodes, which are governed by the following relations;

H_1= tanh [0.5 * ((6.59 – (0.29 *Flow) –(0.038* PRF) – (0.13 *Energy))]

H_2= tanh [0.5 * ((–9.35 + (4.94 * Flow) + (0.075 *PRF) + (0.05*Energy))]

H_3=tanh [0.5 * ((0.48 – (0.136 *Flow) + (0.18 *PRF) – (0.027*Energy))]

H_4= tanh[0.5 * ((–0.56 + (0.26 *Flow) + (0.043*PRF) – (0.028 *Energy))]

H_5= tanh [0.5 * ((1.09 + (3.34 * Flow) + (0.061 *PRF) – (0.102 *Energy))]

Optimization of input parameters to derive maximum etch depth is also carried out. Flow rate of 1.2 lpm, PRF of 10 Hz and energy of 60 mJ are computed to be optimum input parameters. Under this optimum condition, a maximum etch depth of 120 μm was achievable for 500 laser shots.

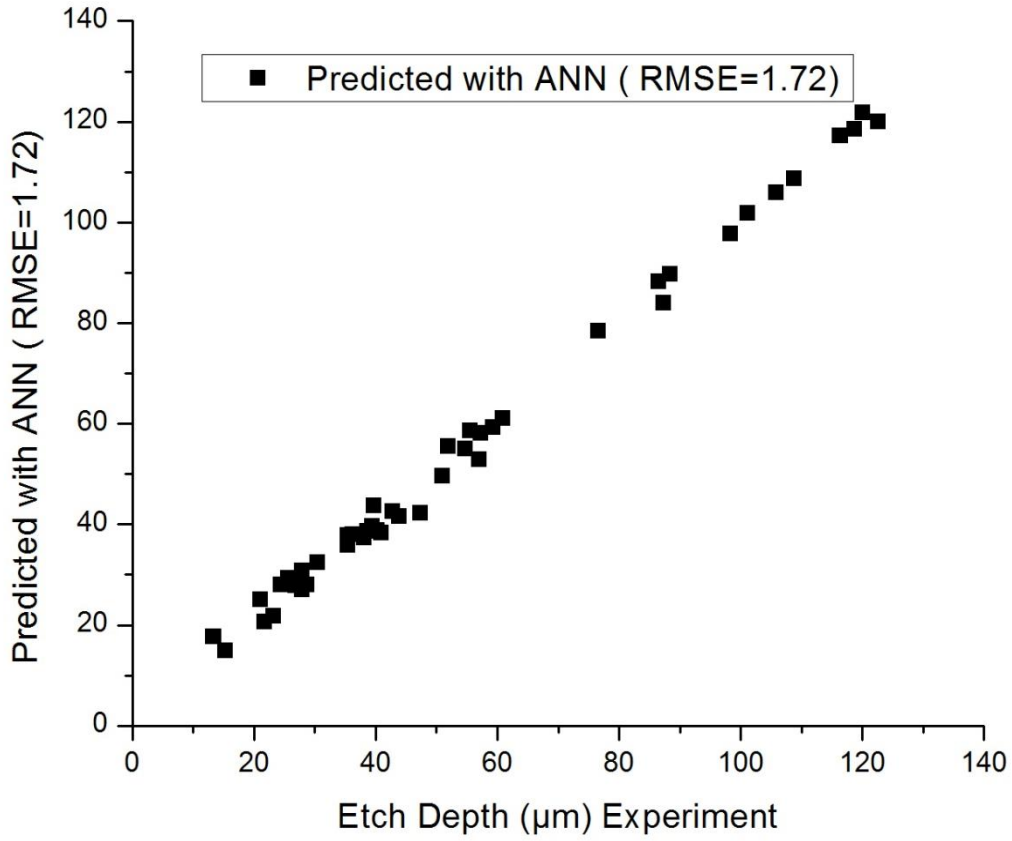

Figure 6.12 Deviation of Predicted Ablation Depth by ANN from Experimental Data

The prediction capabilities of cubic ANN are shown in Table 6.4, and graphically represented in Figure 6.12. It can be observed that prediction response of ANN model is having best agreement with experimental results among these models.

6.6 Response Surface Methodology

A second-order polynomial equation as shown below was used to model the mass removed/ablated depth of photoresist, as a function of the three independent variables mentioned above.

$$Y=\beta_0 + \beta_1 A + \beta_2 B + \beta_3 C + \beta_4 AB + \beta_5 AC + \beta_6 BC + \beta_7 A_2 + \beta_8 B_2 + \beta_9 C_2 \quad \text{--- (6.27)}$$

Where,

Y is the depth of ablation produced under hydrogen gas medium (response)

β_0 represents the intercept,

β_1, β_2 and β_3 are the coefficients of the independent variables,

β_7, β_8 and β_9 are the quadratic terms, and

β_4, β_5, β_6, are the interaction coefficients.

A, B and C are gas flow rate, pulse repetition rate and laser energy respectively.

Moreover, the analysis of variance (ANOVA) and optimization of the photoresist removal process were also performed.

Based on RSM methodology, a mathematical quadratic equation as shown below was obtained.

$$Y = -11.06 + 12.18A - 5.34B + 4.81C - 0.55AB + 0.23AC - 0.037BC - 3.078A^2 + 0.104B^2 - 0.0313C^2 \quad \text{--- (6.28)}$$

Where Y represents the photoresist ablation depth (μm) and A, B, and C are hydrogen gas flow rate (l/min.), pulse repetition rate (Hz) and laser energy (mJ) respectively. The predicted values for the photoresist ablation depth and the relative percentage deviation from the experimental values derived from the RSM model are presented in Table 6.3. Predicted values by RSM model were in good agreement with the experimental values. The predicted values for ablation depth by RSM model were within 10% variation for most of the cases as can be seen from Table 6.3. RSM model fit was satisfactory as its regression coefficient (R^2) is 0.98. Moreover, in the normal probability plot, as shown in Figure 6.13, the residuals for ablation depth fell closer to the straight line, confirming the integrity of developed RSM model. The deviation between experimental and predicted values was less than 10%, for most of the cases.

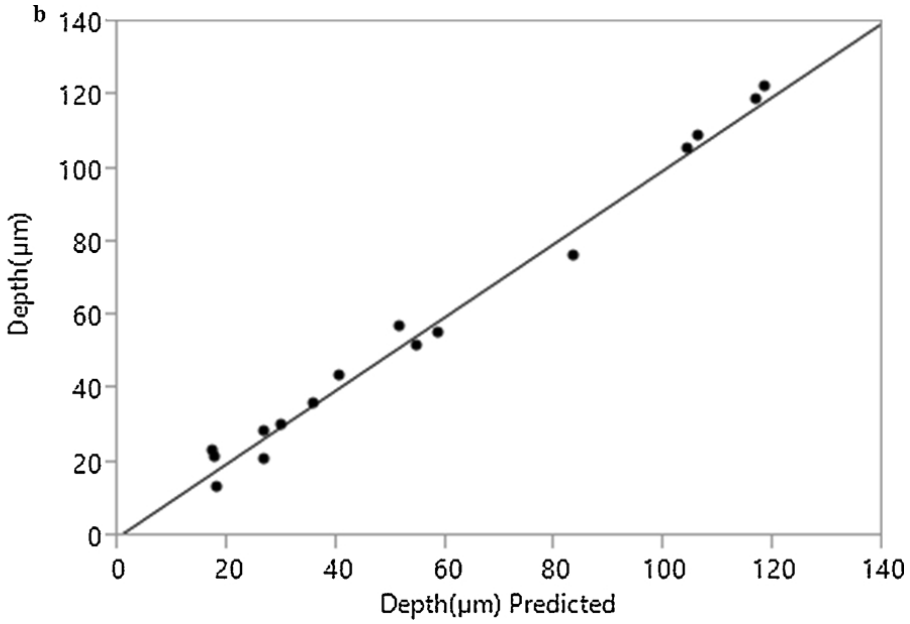

Figure 6.13 Regression Graph of Actual and RSM Predicted Values for Validation Sets (R^2=0.96)

Three-dimensional response surface plots (Figure 6.14 a–c), predicted on the quadratic model, were drawn to study the effect of the input parameters on photoresist ablation removal rate. These plots provide supplementary assessment of the relationship between the response of ablation depth and the three independent variables studied. Figure 6.14 a–c confirmed that PRF has got a negative effect on ablation depth while the other two parameters, namely, pulse energy and flow rate are having positive effects on the ablation depth.

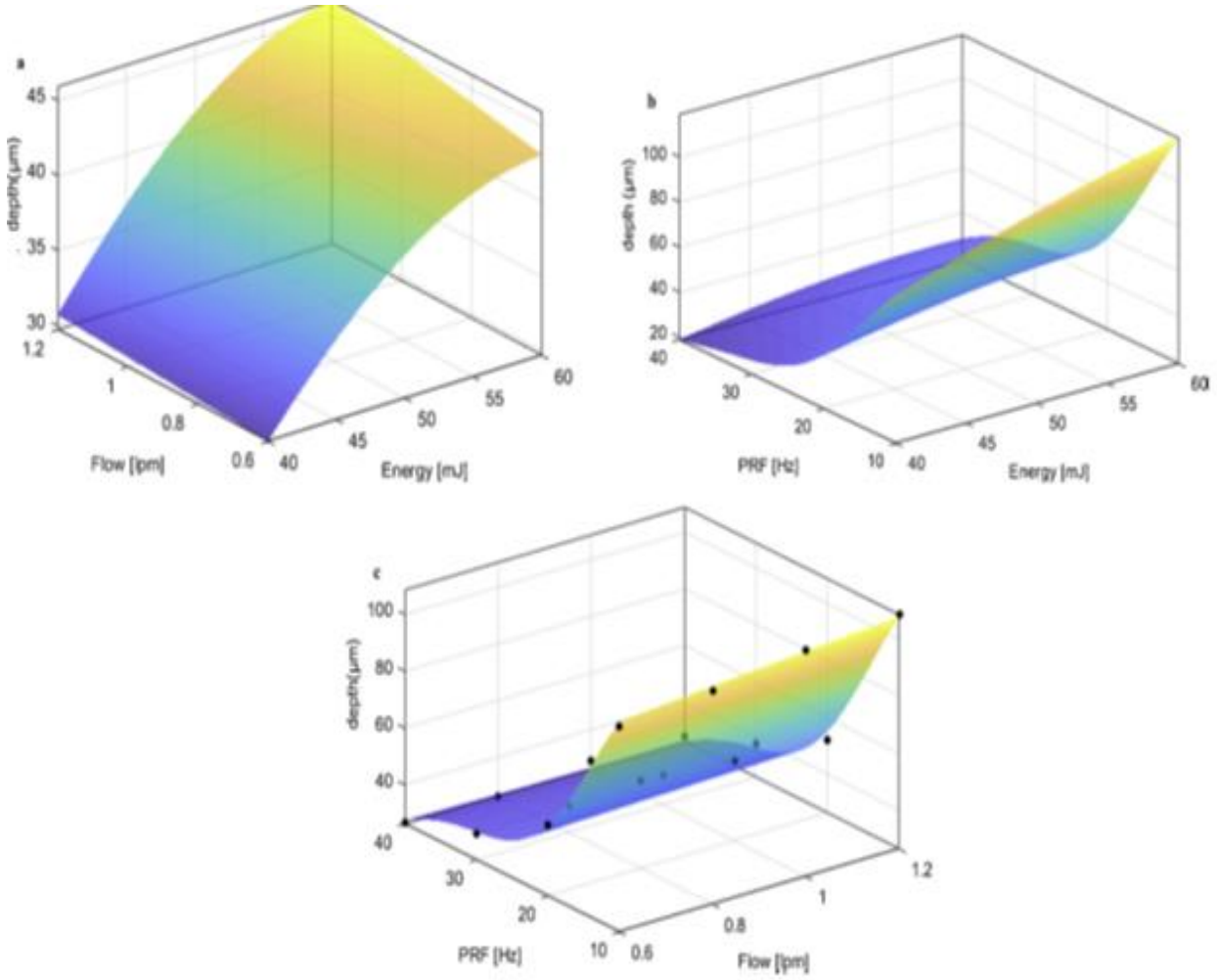

Figure 6.14 3-D Response Surface Plots on interaction effects of (a) energy and flow (b) energy and PRF (c) Flow and PRF on photoresist ablation depth in Excimer micro-machining in H_2 environment.

6.7 Comparison of Prediction Results

Photoresist materials are hydrocarbon polymers with phenyl-, carboxy, keto, olefenic functional groups. The interaction of laser photon with photoresists differ with the type of functional groups that are present. The present study is focused to understand the interaction of laser photon with photoresist, in the presence of hydrogen gas environment. Photoresist removal rate by excimer laser beam is associated with both photochemical (cold ablation by bond

breaking) and photothermal mechanisms [12]. The material removal process is characterized by pulse-by-pulse removal of small amount of material at submicron depth, with minimal damage to the surrounding areas. In photothermal process, the deposited energy is converted to heat, leading to thermal decomposition [12]. It has been generally accepted that material removal proceeds by a combination of these two mechanisms. In general, a photon of short-wavelength excimer laser, has energy ranging from 4 to 10 eV, which covers the bond energy of most of the organic polymeric materials. KrF excimer laser having a photon energy of 5.2 eV, is sufficient to break most of the covalent bonds of organic polymeric materials. Even though the photochemical action dominates over the photothermal process, the photothermal process still has a significant role in the photoresist removal process, which may have detrimental effects on the ablated surface characteristics. Hydrogen gas is of special interest due to its higher thermal conductivity and reduction property. So, it is expected to play dual role, as coolant and reducing agent under appropriate conditions. It is expected to minimize the photothermal contribution part in the net photoresist removal process, due to its higher thermal conductivity. It is also expected to undergo chemical reduction reaction with unsaturated/olefinic/phenyl functional group of polymers, provided hydrogen radical is generated due to laser irradiation.

The ablation depth predicted by different models are compared with experimental results in Table 6.4. The percentage of relative deviation of predicted values from the experimental values is also given in Table 6.4. Prediction performance of both the models are compared based on the correlation of experimental versus prediction values (Figure 6.15) and It can be clearly observed in Figure 6.16 and Figure 6.17 that ANN, GPR, Cubic SVM, RSM are having close predictive performance capabilities.

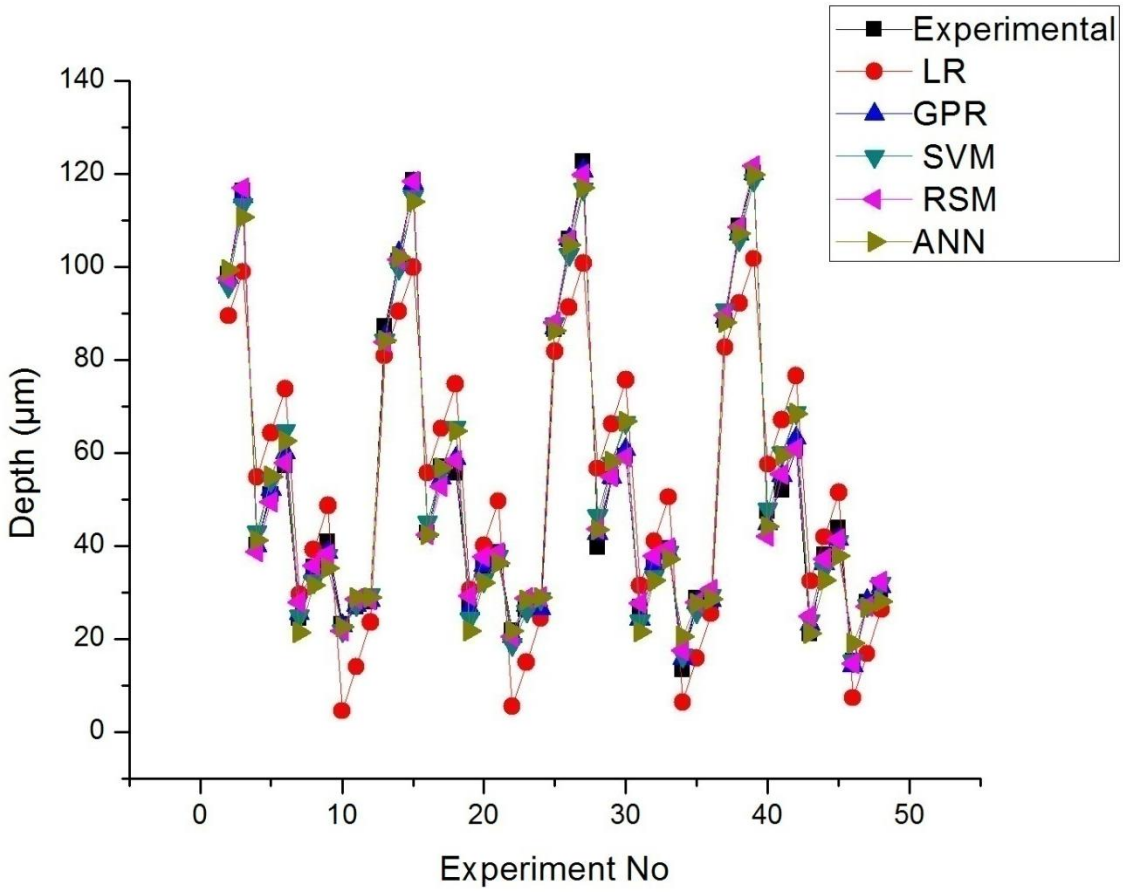

Figure 6.15 Comparison of Different Prediction Models with Experimental Data

Table 6.3 Experimental Data for Hydrogen Gas Medium Compared with Predicted Values of Predictive Regression Models.

Exp. No.	Input Parameters for Experiments			Experimental Value of Ablation Depth (µm) Mean*± SD	Linear Regression		GPR		Cubic SVM		ANN		RSM	
	Flow rate (lpm)	Laser pulse repetition (Hz)	Laser Energy (mJ)		Depth (µm)	RD %	Depth (µm)	RD %	Depth (µm)	RD %	Depth (µm)	RD %	Depth (µm)	RD %
1	0.6	10	40	76.6±7.7	79.99	-4.4	77.67	-1.4	79.61	-3.9	78.3	-2.2	81.8	−6.8
2	0.6	10	50	98.4±0.4	89.49	9.1	97.69	0.7	95.78	2.7	97.6	0.8	99.4	−1.0
3	0.6	10	60	116.4±2.9	99	14.9	115.05	1.2	113.41	2.6	117.1	-0.6	110.7	4.9
4	0.6	20	40	40.3±3.3	54.85	-36.1	40.04	0.6	43.11	-7.0	38.8	3.7	41.2	−2.4
5	0.6	20	50	51.0±2.5	64.36	-26.2	52.06	-2.1	54.02	-5.9	49.5	2.9	55	−8.0
6	0.6	20	60	57.3±1.6	73.86	-28.9	60.04	-4.8	64.75	-13.0	58	-1.2	62.6	−9.3
7	0.6	30	40	24.5±2.6	29.72	-21.3	25.41	-3.7	25.01	-2.1	28	-14.3	21.5	12.1
8	0.6	30	50	35.4±1.5	39.22	-10.8	34.44	2.7	32.39	8.5	35.8	-1.1	31.6	10.9
9	0.6	30	60	41.0±2.2	48.73	-18.9	38.59	5.9	37.98	7.4	38.3	6.6	35.3	13.8
10	0.6	40	40	23.2±2.2	4.58	80.3	22.75	1.9	21.78	6.1	21.7	6.5	22.7	2.3
11	0.6	40	50	26.8±1.3	14.09	47.4	27.31	-1.9	27.39	-2.2	28.6	-6.7	29	−8.1
12	0.6	40	60	28.0±3.3	23.59	15.8	28.32	-1.1	29.58	-5.6	28.5	-1.8	29	−3.6
13	0.8	10	40	87.3±4.4	80.91	7.3	84.94	2.7	84.27	3.5	83.9	3.9	84.2	3.5
14	0.8	10	50	101.2±0.7	90.42	10.7	103.09	-1.9	99.6	1.6	101.7	-0.5	102.2	−1.0
15	0.8	10	60	118.7±2.6	99.92	15.8	117.98	0.6	115.18	3.0	118.5	0.2	114	4
16	0.8	20	40	42.8±3.3	55.78	-30.3	43.28	-1.1	45.06	-5.3	42.5	0.7	42.5	0.6
17	0.8	20	50	57.1±3.1	65.28	-14.3	54.63	4.3	55.95	2.0	52.8	7.5	56.8	0.6
18	0.8	20	60	55.6±1.3	74.79	-34.5	58.84	-5.8	65.47	-17.8	58.5	-5.2	64.8	−16.5

Exp. No.	Input Parameters for Experiments			Experimental Value of Ablation Depth (µm) Mean*± SD	Linear Regression		GPR		Cubic SVM		ANN		RSM	
	Flow rate (lpm)	Laser pulse repetition (Hz)	Laser Energy (mJ)		Depth (µm)	RD %	Depth (µm)	RD %	Depth (µm)	RD %	Depth (µm)	RD %	Depth (µm)	RD %
19	0.8	30	40	26.8±1.1	30.64	-14.3	26.51	1.1	24.4	9.0	29.3	-9.3	21.7	19.1
20	0.8	30	50	35.4±0.4	40.15	-13.4	35.86	-1.3	32.59	7.9	37.7	-6.5	32.2	9.1
21	0.8	30	60	38.7±1.1	49.65	-28.3	36.89	4.7	37.79	2.4	38.6	0.3	36.4	5.7
22	0.8	40	40	21.8±3.4	5.51	74.7	20.62	5.4	18.77	13.9	20.6	5.5	21.8	0.3
23	0.8	40	50	26.4±1.8	15.01	43.1	27.22	-3.1	26.01	1.5	28.9	-9.5	28.5	−8.1
24	0.8	40	60	25.6±2.7	24.52	4.2	26.5	-3.5	28.64	-11.9	29.2	-14.1	29	−13.0
25	1	10	40	86.5±5.8	81.84	5.4	86.84	-0.4	87.81	-1.5	88.2	-2.0	86.3	0.3
26	1	10	50	105.9±1.6	91.34	13.7	105.96	-0.1	102.76	3.0	105.8	0.1	104.8	1
27	1	10	60	122.7±0.4	100.85	17.8	120.64	1.7	116.76	4.8	119.9	2.3	117.1	4.6
28	1	20	40	39.7±5.4	56.7	-42.8	42.74	-7.7	46.48	-17.1	43.7	-10.1	43.5	−9.6
29	1	20	50	54.8±1.7	66.21	-20.8	54.72	0.1	57.81	-5.5	54.9	-0.2	58.3	−6.4
30	1	20	60	59.3±1.4	75.72	-27.7	60.75	-2.4	66.57	-12.3	59.2	0.2	66.8	−12.6
31	1	30	40	26.9±3.1	31.57	-17.4	24.21	10.0	23.86	11.3	27.8	-3.3	21.6	19.8
32	1	30	50	36.3±1.3	41.08	-13.2	36.15	0.4	33.32	8.2	37.9	-4.4	32.6	10.3
33	1	30	60	39.5±1.9	50.58	-28.1	38.49	2.6	38.59	2.3	39.6	-0.3	37.3	5.7
34	1	40	40	13.4±0.8	6.43	52.0	15.91	-18.7	16.43	-22.6	17.6	-31.3	20.6	−53.1
35	1	40	50	28.8±2.0	15.94	44.7	27.85	3.3	25.76	10.6	27.9	3.1	27.8	3.7
36	1	40	60	28.0±2.0	25.45	9.1	28.28	-1.0	29.29	-4.6	30.7	-9.6	28.7	−2.7
37	1.2	10	40	88.4±2.3	82.77	6.4	89.16	-0.9	90.73	-2.6	89.7	-1.5	88.2	0.3
38	1.2	10	50	108.8±2.3	92.27	15.2	107.03	1.6	105.76	2.8	108.7	0.1	107.2	1.5

Exp. No.	Input Parameters for Experiments			Experimental Value of Ablation Depth (µm) Mean*± SD	Linear Regression		GPR		Cubic SVM		ANN		RSM	
	Flow rate (lpm)	Laser pulse repetition (Hz)	Laser Energy (mJ)		Depth (µm)	RD %	Depth (µm)	RD %	Depth (µm)	RD %	Depth (µm)	RD %	Depth (µm)	RD %
39	1.2	10	60	120.1±0.5	101.78	15.3	120.03	0.1	118.64	1.2	121.7	-1.3	119.9	0.1
40	1.2	20	40	47.4±4.0	57.63	-21.6	44.81	5.5	47.88	-1.0	42.2	11.0	44.3	6.7
41	1.2	20	50	52.0±0.5	67.14	-29.1	55.2	-6.2	60.12	-15.6	55.5	-6.7	59.5	−14.5
42	1.2	20	60	60.9±3.8	76.64	-25.8	63.22	-3.8	68.58	-12.6	61	-0.2	68.5	−12.4
43	1.2	30	40	21.1±0.4	32.5	-54.0	23.15	-9.7	23.9	-13.3	25	-18.5	21.3	−0.6
44	1.2	30	50	38.1±0.4	42	-10.2	36.24	4.9	35.09	7.9	37.3	2.1	32.7	14.2
45	1.2	30	60	43.9±3.4	51.51	-17.3	41.53	5.4	40.88	6.9	41.5	5.5	37.9	13.7
46	1.2	40	40	15.3±0.3	7.36	51.9	14.34	6.3	15.26	0.3	14.8	3.3	19.1	−24.6
47	1.2	40	50	28.0±1.8	16.87	39.8	28.36	-1.3	27.15	3.0	27	3.6	26.8	4.2
48	1.2	40	60	30.5±3.0	26.37	13.5	31.3	-2.6	32.03	-5.0	32.4	-6.2	28.2	7.4

*The values shown here is an average value of triplicate experiments conducted for 500 laser shots

Table 6.4 Comparison of Accuracy of Different Prediction Models

S. No.	Method	R^2	RMSE
1.	Linear regression	0.858	13.22
2.	Cubic SVM	0.986	4.90
3.	Gaussian Process Regression (Matern 5/2 GPR)	0.996	4.27
4.	ANN	0.997	1.72
5.	RSM	0.983	5.01

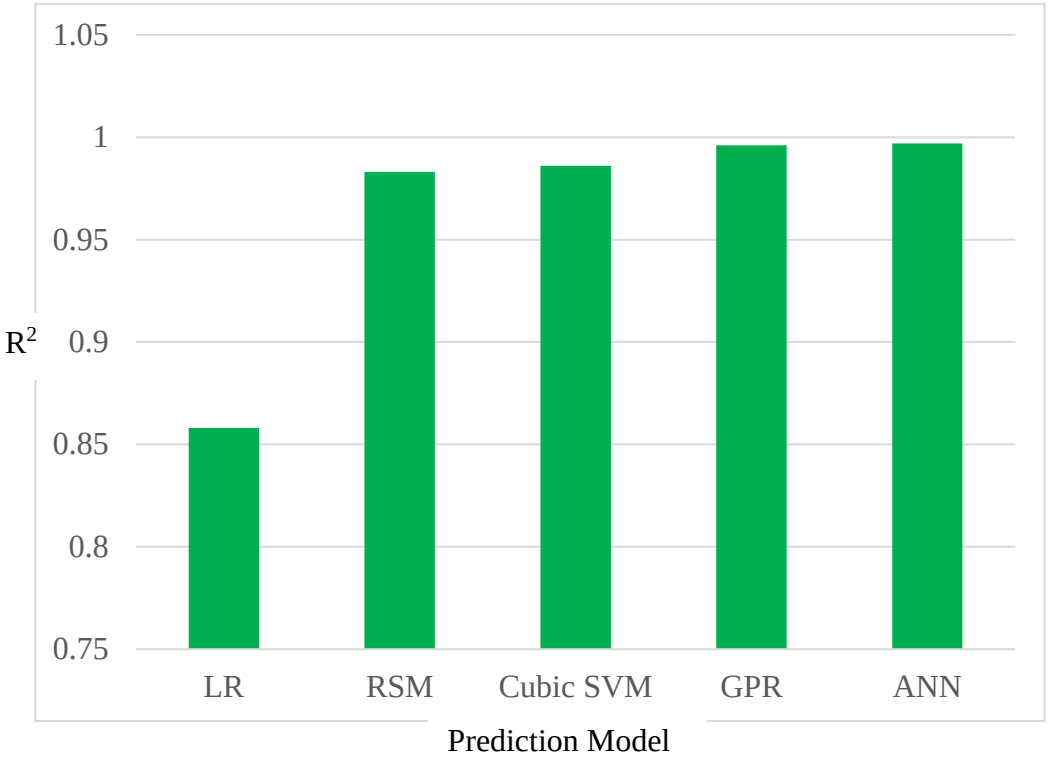

Figure 6.16 Comparison of R^2 Value of Different Prediction Models

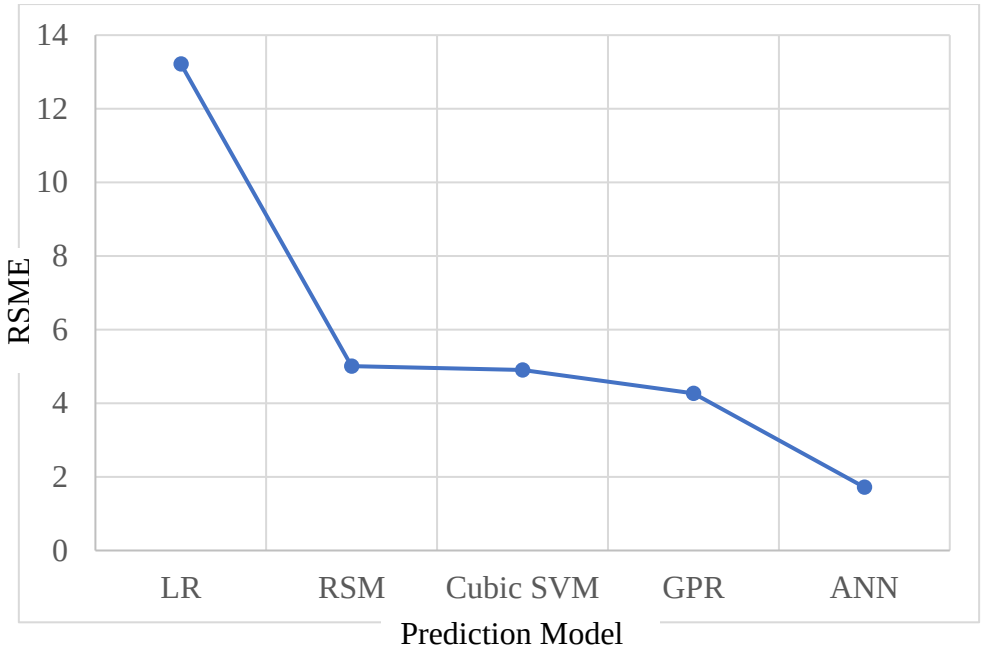

Figure 6.17 Comparison of RMSE Value of Different Prediction Models

6.8 Summary

For the prediction of ablation depth in the Excimer laser micromachining operation under hydrogen gas environment, five different data driven models have been developed. The five different models were developed based on Linear Regression(LR), Gaussian process Regression(GPR), Cubic support vector machine (Cubic SVM), Response Surface Methodology(RSM) and Artificial Neural Network(ANN). The results suggest that SVM, GPR, ANN and RSM models are suitable to predict ablation depth in excimer laser micromachining. It is observed that ablation depth predicted by LR is least accurate among these models. However, ANN and GPR model, appear to be superior for both training as well as validation. Overall, the performance of the models in this study has proven that suitable machine learning techniques can be successfully used for predicting the ablation depth. Based on the close performance of SVM, GPR, ANN and RSM models, we propose that these four models can be used for prediction the ablation depth.

Chapter 7

Experimental Study of Chemical Etching

7.1 Introduction

This chapter discusses the optimisation of the chemical etching process of CuBe alloy parts using $FeCl_3$ etchant, to manufacture micro-fluidic grooves. The process optimisation models were developed using two techniques, namely Response Surface Methodology (RSM) and Artificial Neural Network (ANN). The targeted response variable-set consists of the predefined etch depth and the lowest possible surface roughness values. The optimum etching parameters of concentration, temperature and etching time, to satisfy these conditions were obtained as the outcome from these models. These models were experimentally validated.

Three types of experimental works on chemical etching were carried out as part of the research work. These were: a) Macro level (chemical etching up to 5 hours duration), b) Preliminary micro etching studies and c) Optimization studies on chemical etching of CuBe material using $FeCl_3$ etchant. The overall manufacturing process sheet of SSGB and the importance of chemical etching process in the overall plan of SSGB manufacturing, are also described.

Traditional machining processes like turning, milling, drilling, grinding etc., depend on direct mechanical contact between the tool and workpiece. The direct mechanical contact increases the temperature of the workpiece and therefore traditional machining processes may cause undesirable effects like residual, thermal and mechanical stresses. At times, it may call for further processing of the workpiece to eliminate or minimize these problems. Hence there is inevitably a need to develop new machining processes and improve existing techniques while using advanced materials which often imposes these kinds of problems on larger extent.

Chemical Etching (CE) is one such non-traditional machining process. The birth of this technology as a machining process is credited to Manuel C. Sanz, an engineer with North American Aviation in the year 1953 [122]. This technique can be used for the production of geometrical features having desired contour, through selective removal of material by controlled chemical reaction with acidic / alkaline solutions. In most applications, a photosensitive masking / photoresist is used to define the precise location / contour of the geometric feature on the work piece. Maskants/ photoresists are specially designed materials, that are chemically resistant to the harsh etchants. In order to ensure good adhesion of the maskant, the work piece surface should be cleaned properly prior to the application of the maskant. A good test for efficient cleaning is spraying water on the work piece surface and observing whether individual droplets spread out to form a uniform, continuous, thin film of water. Formation of such a film indicates adequate cleaning, whereas inadequate cleaning produces uneven wetting of the surface. Extremely high adhesion may result in the stripping process of the maskant very difficult after chemical etching. Chemical etching to get the desired contour is generally done by immersion of the workpiece within the etchant solution.

Almost all materials can be chemically etched, although some are etched relatively easier than others. Etching is primarily a corrosion process, which is carried out in a controlled manner to achieve desired output. Thus, corrosion-resistant materials are tough to etch and require extremely corrosive chemical etchants. Metals like tantalum, gold and titanium, special alloys, ceramics, glass and plastics are few examples of above mentioned category. However, many materials used frequently in manufacturing can be etched readily using aqueous solutions comprising ferric chloride, cupric chloride, ferric nitrate, potassium ferricyanide or dilute acids or alkalis. The materials most frequently etched to produce industrial products are stainless steels, copper, copper alloys, nickel, nickel alloys, aluminium, molybdenum and various grades of steels. Chemical etching process also provides various

advantages which includes its independence of work piece hardness, burr free machining, flexible to accommodate design changes and freedom from residual stresses [123].

7.2 Experimental Procedure

Photochemical machining (PCM) is chemical etching process that uses a photoresist (photosensitive masking) to define the locations from where the metal will be etched. The complete photochemical machining process can be divided in six different processes/activities which are listed below.

1. The phototool generation
2. The surface cleaning of work piece
3. The coating of photoresist
4. The exposure of photoresist (PR) with UV light or laser beam.
5. The etching of work piece, from which the PR is selectively removed in the previous step.
6. The removal of the residual photoresist, using proper solvent.

7.2.1 Specimen

The specimen used for this study is CuBe alloy with 2 % Be (UNS No. of the alloy: C17200), the composition of which is shown below in Table 7.1 as per ASTM Standard B194-15. This material is used for manufacturing the female part of the SSGB.

Table 7.1 Composition of Wrought CuBe alloy as per ASTM Standard B194-15 (UNS number C17200)

Composition %weight						**Tensile strength**	**Yield strength**
Be	**Co+Ni**	**Co+Ni+Fe**	**Al**	**Si**	**Cu**	**MPa**	**MPa**
1.80-2.00	0.20min	0.60 max	0.20max	0.20max	Remainder	1140-1345	965

Properties of CuBe alloys:

- The wrought high strength alloy C17200 contains 1.6-2%Be and nominal 0.25%Co and it is a ductile and machinable material.
- C17200 alloy, which is used for the experimental trials, is a precipitation hardenable material that forms the beryllides (Cu, Co) Be. The limited solid solubility of Be in Cu matrix produces highest achievable strength by precipitation hardening by which Copper Beryllium attains the greatest strength to 1,400 MPa, of any copper-based alloys. During Age-Hardening, dissolved Be forms precipitates from substitutional solid solution. It has good thermal conductivity, of the order of 3-5 times of that of tool steel.
- Annealing temperature for high strength alloys are in the range of 760-800^{o}C.
- This alloy is resistant to abrasive wear and to galling so it is used in bearings where antigalling properties are important.

A circular disc of 17mm diameter, 2mm thick is used as specimen. One face of the disc is finished-machined (10-20nm Ra value) on ultra-precision diamond turning machine.

7.2.2 Phototool generation

The photo tool / was manufactured using 0.1mm thick foil made of stainless steel 304 grade material. The overall shape of the mask is of 40mm square, provided with arrangement to hold the same on the mask holder of the laser Beam Delivery Unit (BDU). This mask was used in the Laser micromachining set up to ablate the 'photo resist-coated metallic work piece'.

Two masks shown in Figure 7.1 (a) and (b) were used for the experimental studies of this research work. The chemical etching process optimization studies were conducted and

reported in this thesis making use of the mask for producing 5mm diameter cylindrical hole as shown in Figure 7.1 (b).

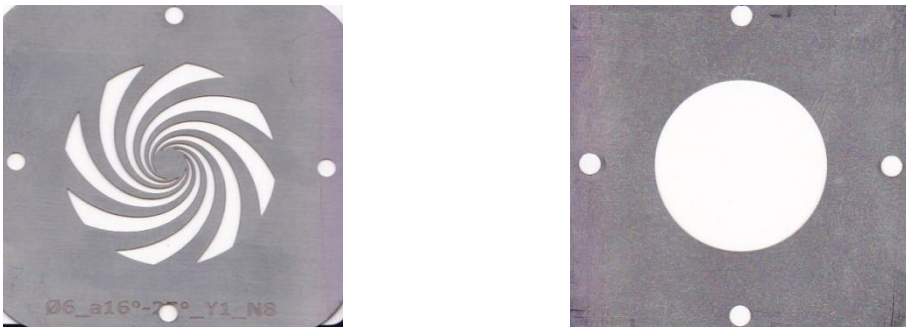

(a) (b)

Figure 7.1 Typical phototools for laser lithography (a) Mask for generating spiral grooves (b) Mask for producing 5mm diameter cylindrical hole

7.2.3 Surface Cleaning of specimens

All the specimens are cleaned in an ultrasonic cleaner, first with surfactant and secondly with Tri-Chloro-Ethylene (TCE) solvent. Subsequently they were dried before applying the photoresist on their surface. The purpose of surface cleaning is to remove the undesired chemical and particulate contamination like oil, wax, grease, rust or any oxide or dirt on the work piece.

7.2.4 Coating of Photoresist

Applying a layer of photoresist, is one of the critical stages in photochemical machining. The application of photoresist has two important roles in the PCM. First of all, it should be possible to transfer the pattern from the mask to the photoresist layer by Excimer laser ablation; secondly it should resist chemical reaction with the etchant and avoid break down during the metal etching. A commercially available photoresist (PR) polymer E1020 (supplied by M/s Cadmosil Chemical Pvt. Ltd, India) was used for photochemical machining. The final thickness of the PR layer after the curing was 1000μm.

7.2.5 Exposure of Photoresist (PR) with UV laser beam

The exposure of the photoresist is another important stage of photochemical machining. A pulsed excimer laser beam of 248 nm wavelength is used for the lithography. A homogenized excimer laser beam having flat top energy density profile has been projected on to the photoresist layer. During the Excimer laser ablation, the laser exposed area is ablated, leaving the unexposed metal surface coated with PR.

7.2.6 Etching of specimens

Various etchants are commercially employed for chemical etching of copper and copper based alloys. After giving due considerations to factors like the unwanted aggressiveness, its effects on the alloying metals and etch rates, the selection of etchants for CuBe alloy components, the selection of the etchants was narrowed down to $CuCl_2$ and $FeCl_3$.The characteristics of these two etchants used for CuBe alloy are compared in Table 7.2.

Table 7.2 Comparison of Chemical Etchants used for CuBe Alloy

Etchants	Observations
$CuCl_2$	• One of the major etchants for copper and CuBe alloys • Chemical reaction is simple and easy to understand • More environment friendly process compared to $FeCl_3$ etching process
$FeCl_3$	• Commonly known as universal etchant in the photochemical machining industry. • Chemical reaction of etching more complex • Higher etch rate compared to $CuCl_2$ etchant.

In the chemical etching study, the objective is to make a comparative experimental investigation of CuBe alloy vis-à-vis ETP grade pure copper. In this study, both the above referred etchants namely, $FeCl_3$ and $CuCl_2$ were used.

The chemical reaction of copper with $FeCl_3$ is as follows:

$$FeCl_3 + Cu \rightarrow FeCl_2 + CuCl \ldots\ldots\ldots\ldots\ldots\ldots\ldots\ldots (1)$$

Here, Copper is oxidized by the ferric ions, giving cuprous chloride (CuCl) and ferrous chloride ($FeCl_2$).

CuCl is oxidized further in the etchant solution to produce $CuCl_2$ as follows:

$$FeCl_3 + CuCl \rightarrow FeCl_2 + CuCl_2 \ldots\ldots\ldots\ldots\ldots\ldots (2)$$

This built-up of $CuCl_2$, produced during the reaction, reacts with copper and forms CuCl shown below:

$$CuCl_2 + Cu \rightarrow 2CuCl \ldots\ldots\ldots\ldots\ldots\ldots\ldots\ldots\ldots\ldots (3)$$

From the above chemical redox reactions, we can conclude that $FeCl_3$ etchant in copper machining apparently generates the effects of two etchants in the same etching process, in which the main etchant is $FeCl_3$ and the second etchant is the by-product etchant i.e. $CuCl_2$. The combined effect of the both etchants produces higher etch rate in comparison to $CuCl_2$ etchant.

In the present research work, the work piece made of CuBe alloy is chemically etched to dissolve that part of the specimens-surface which has been selectively exposed using laser ablation technique. The basic chemical reaction involved in the etching of the work piece using $FeCl_3$ etchant, wherein ferric ions are reduced to ferrous ions and copper metal is

oxidised to cupric ions is shown below. Similarly, the redox reaction that takes place between Beryllium metal and the etchant ions is also shown below.

$$2Fe^{3+} + Cu \rightarrow 2Fe^{2+} + Cu^{2+} \ldots\ldots\ldots\ldots\ldots\ldots\ldots\ldots\ldots\ldots (4)$$

$$Be + 2Fe^{3+} \rightarrow Be^{2+} + 2Fe^{2+} \ldots\ldots\ldots\ldots\ldots\ldots\ldots\ldots\ldots\ldots\ldots.. (5)$$

As can be seen from the extensive literature survey on Chemical machining covered in Chapter-2 of this report, it is obvious that no one has previously reported chemical machining of DTM machined, nano-finished parts made of CuBe alloy. This chapter is on the comparative experimental investigation of chemical micro machining process of DTM machined parts made out of Copper beryllium alloy vis-à-vis pure copper. This study is mainly focused to investigate various etching parameters such as concentration of etchant, bath temperature and time on etching rate and surface roughness. With this preliminary study, a suitable design of experiment was made to produce a desired micro groove depth with lowest possible surface roughness.

7.2.7 Preparation of Etchant and characterization of etch depth as well surface roughness

- Etchant concentration**:** The etchant has been prepared by dissolving weighed quantity of the solid etchant material in known quantity of pure water.
- The Measurement of Depth of Etch: The average etch depth has been computed based on weight loss (gravimetric analysis).Samples were also checked using profilometer for the etch depth.
- The Measurement of Surface Roughness: Surface roughness at two stages, both before etching as well as after etching is measured using Rank Taylor Hobsson, UK Make instrument model ‘TalySurf FTS 1200’.

7.2.8 Post etching treatment

After the chemical etching process, the specimens are treated with ethoxy ethanol solvent for complete removal of PR. Subsequently, the specimens were ultra-sonically cleaned with ASTM Type 1 water (conductivity: 0.052 µS) for two times so that no residual chemical is retained on the work piece, to avoid any further reaction during storage. Cleaning with tap-water is undesirable due to nano-finished component surface. Tap-water may lead to scale formation on the nano-finished surfaces due to dissolved salts. The final etched components are stored in silica-gel packed desiccators, till they are taken for surface roughness and etch-depth measurements.

7.2.9 Chemical etching equipment

The experimental setup developed for the present research work as shown in Figure 7.2 includes PID temperature controlled hot plate, RTD 1000 class temperature sensor etc. Table 7.3 shows the detailed parts list of this set up. It consists of a variable temperature water bath with an integrated Proportional-Integral-Derivative (PID) temperature controller. The beaker containing the etchant of known concentration was placed inside the constant temperature bath. The bath temperature could be programmed to the desired value. The parts to be chemically etched were immersed in the bath using proper fixtures. An overhead programmable stirrer of high torque and variable speed of 'Heidolph Instruments GmbH and Co. Germany' make was used to agitate the enchant bath. The speed of rotation of the stirrer could be set to the required value. The torque encountered by the stirrer while in operation is displayed on the stirrer control panel along with the speed of rotation in RPM. The timer provided on the control panel is used to program the agitation time. This stirrer is provided with gear arrangement to ensure constant speed despite change in the load seen by the stirrer.

The constant temperature bath is equipped with a chillier as well as heating coil for its proper operation at the desired temperature both in the cold/ hot region. The photograph of the chemical etching lab that houses various equipments/instruments used for the chemical etching studies, is shown in Figure 7.3**.**

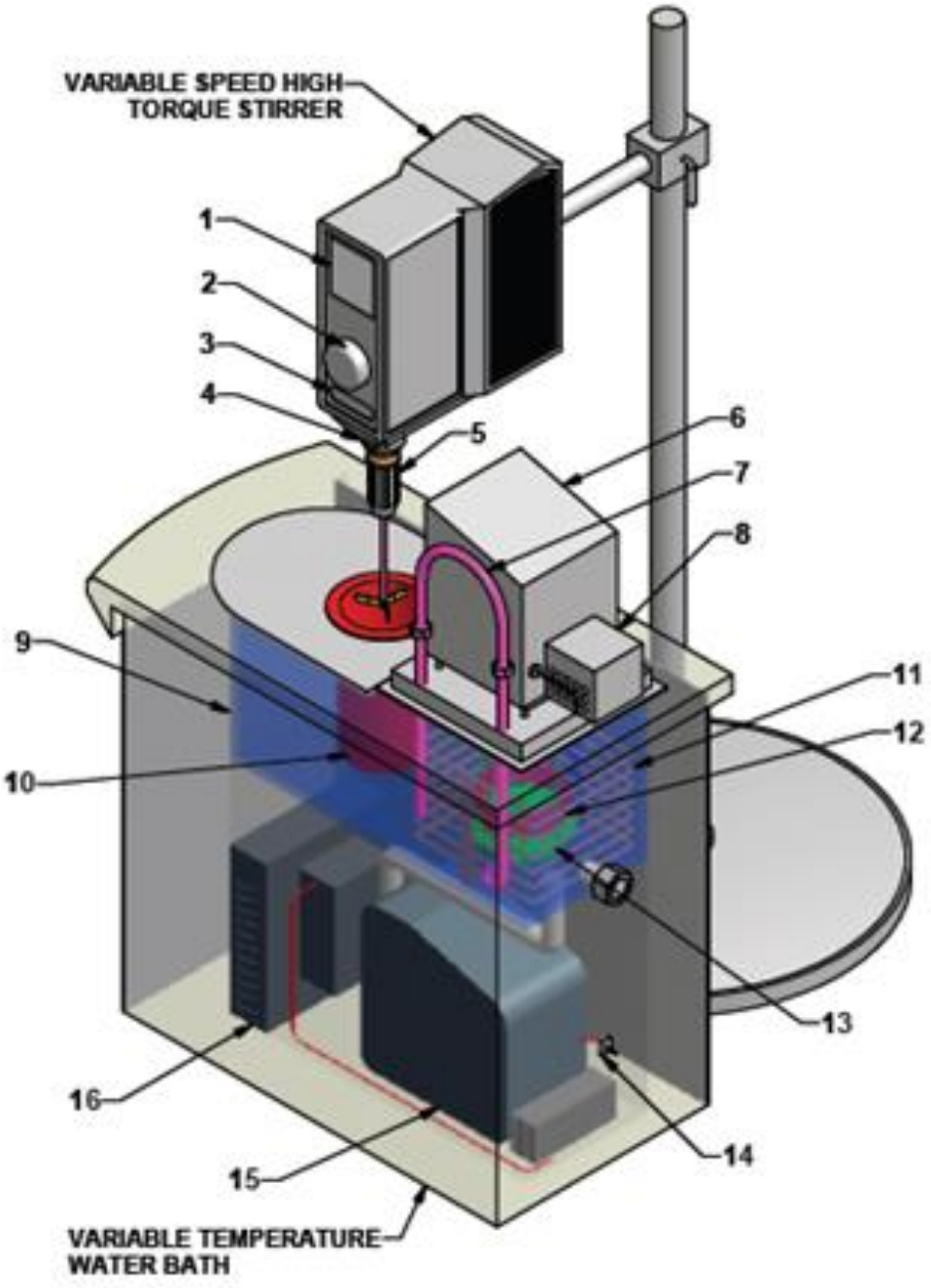

Figure 7.2 Chemical Etching set-up

Table 7.3 Part List of Chemical Etching set-up

Part No.	Description
1	Display
2	Control Knob (Speed Adjustment)
3	Slider (Switch Rotation On/Off)
4	On/Off Switch
5	Quick Chuck
6	'PID Controller and Stirrer Pump' Assembly
7	Water Recirculation Loop
8	Heater Terminal Box
9	Constant Temperature Water Bath
10	Beaker (Chemical Etching Bath)
11	Cooling Coil
12	Heating Coil
13	RTD Sensor
14	Miniature Circuit Breaker
15	Compressor
16	Condenser

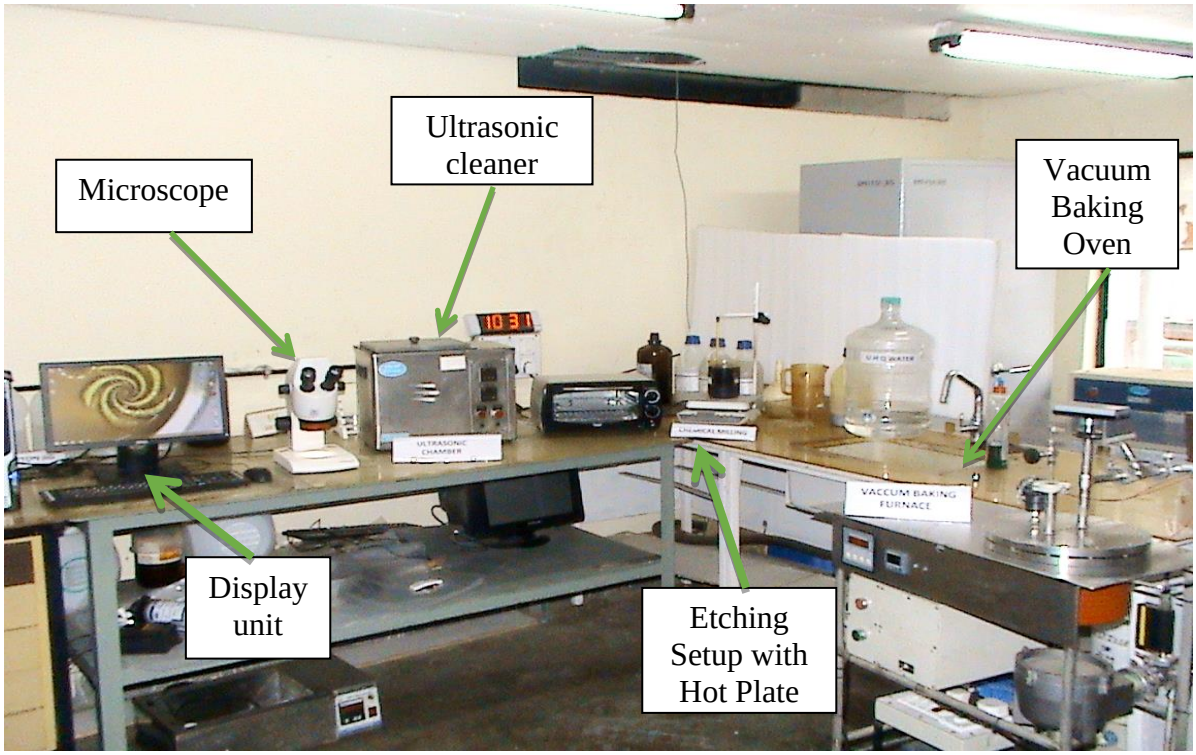

Figure 7.3 Chemical Etching Lab

7.3 Preliminary Etching Studies in 'macro scale'

For preliminary experimental understanding of the chemical etching process, a macro-scale etching study has been conducted and the results are summarized in the below given Figure 7.4. It is seen from literature that the etchant concentration is different for different applications. In general, the etchant should provide consistent etch rate from batch to batch, to get reliable value of etch depth from batch to batch. Therefore, as a preliminary study, experiments have been carried out using etchant-concentration ranging from 1M to 5M, spread over a time period of 300 minutes (5 hours). Figure 7.4 illustrates variation of etch rate with time, indicating that the etch rate behaviour is different. Though etch rate with 5M concentration is the lowest compared to other dilute solutions, there is a consistency in etch rate during the entire etching period. This study indicates that consistency of etch rates depends on etchant concentration. However, in the present case the etching requirement is to produce micro grooves having depth of order of 20 µm, for which the etching time is few

minutes. Therefore, screening of etchant concentration and optimization is desirable to produce micro grooves of predefined etch depth.

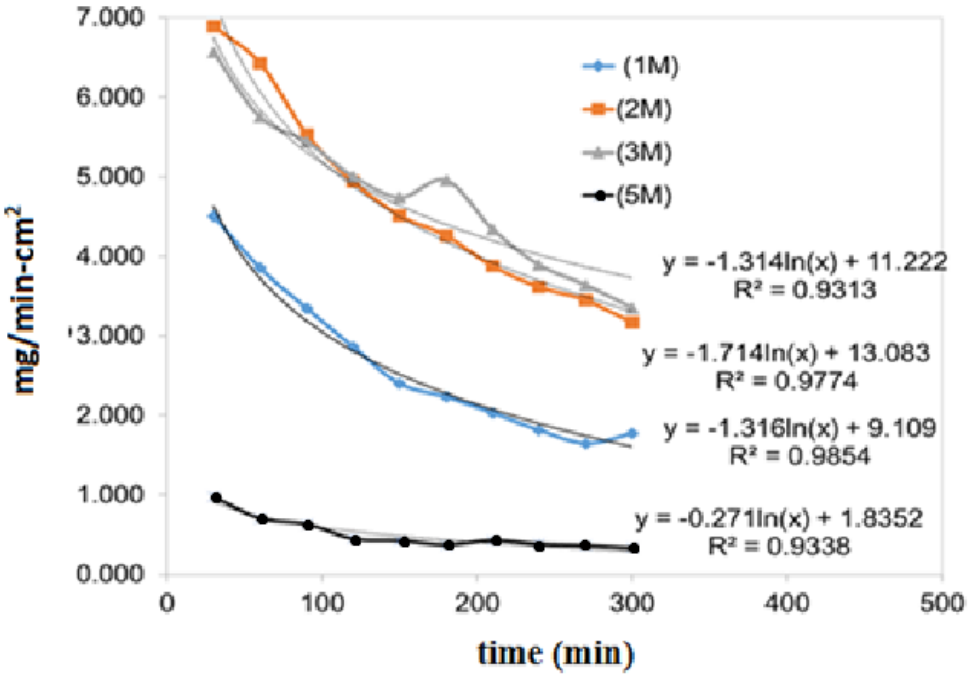

Figure 7.4 Macro-scale Mass Removal Rate Variation with Time for Different Etchant Concentrations

7.3.1 Preliminary Etching Studies in micro scale using 1M etchant concentration

Twenty-four experiments were conducted for the photochemical machining of Cu and Cu-Be alloys separately using $CuCl_2$ and $FeCl_3$ etchants of 1M concentration. Etching temperatures were varied from 40ºC to 70ºCin steps of 10°C and etching has been carried out from 5min to 30min in steps of 5min. Figure 7.5 illustrates the variation of etch depth as a function of temperature and time.

In industrial application of chemical etching of CuBe alloys, the highest possible etching temperature which the etchant machine allowed was generally around 50ºC . It is seen from the literature that lower etching temperature decreases etch rate and produces poor surface quality.

In the below given figures the label High Alloy (HA) stands for CuBe alloy having 2% Be, to distinguish it from the Low Alloy (LA) CuBe containing 0.7% Be in it.

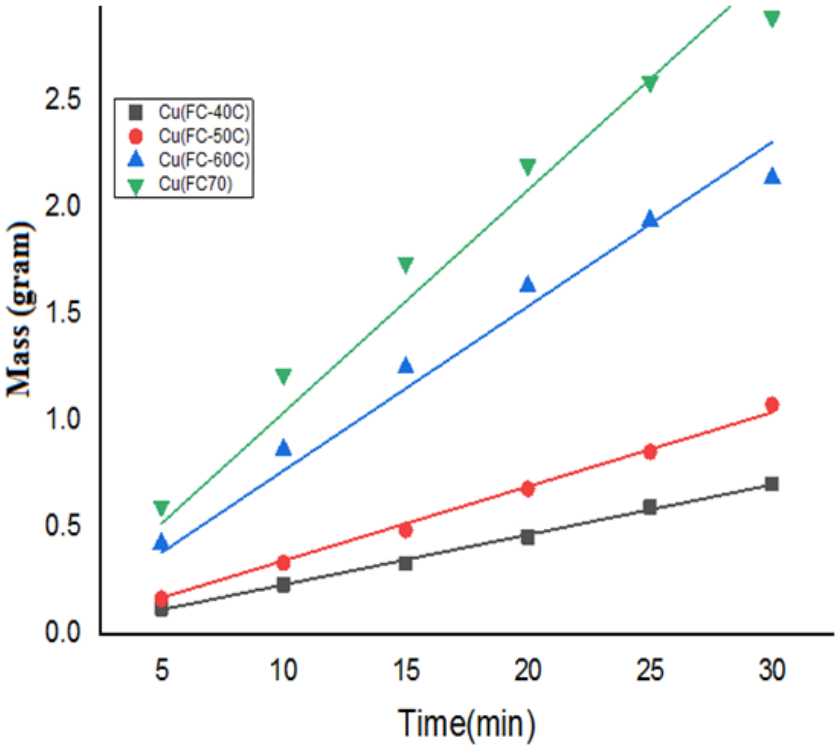

Figure 7.5 **(a)** Variation of etch rate with temperature of Cu with $FeCl_3$ etchant

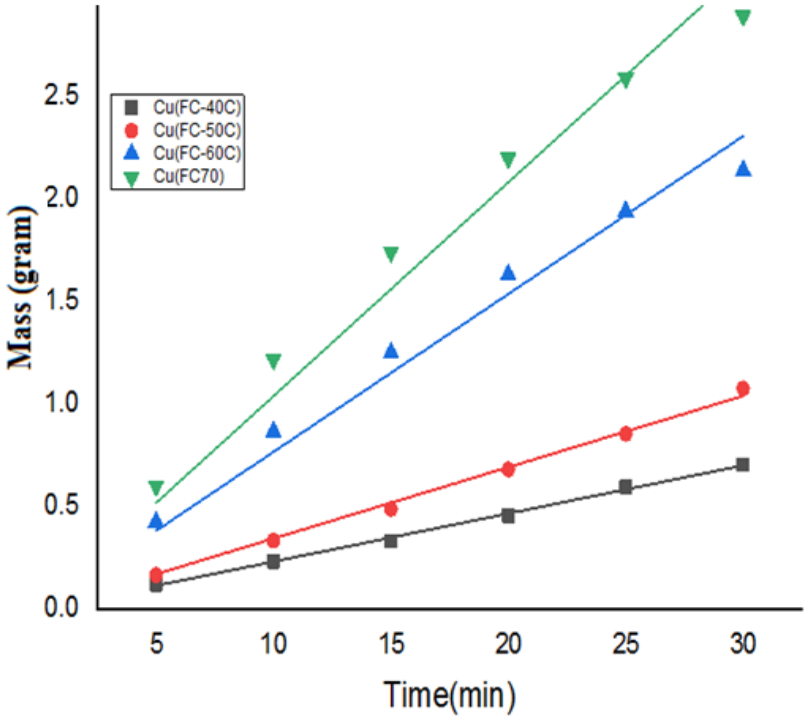

Figure 7.5 **(b)** Variation of etch rate with temperature of Cu with $CuCl_2$ etchant

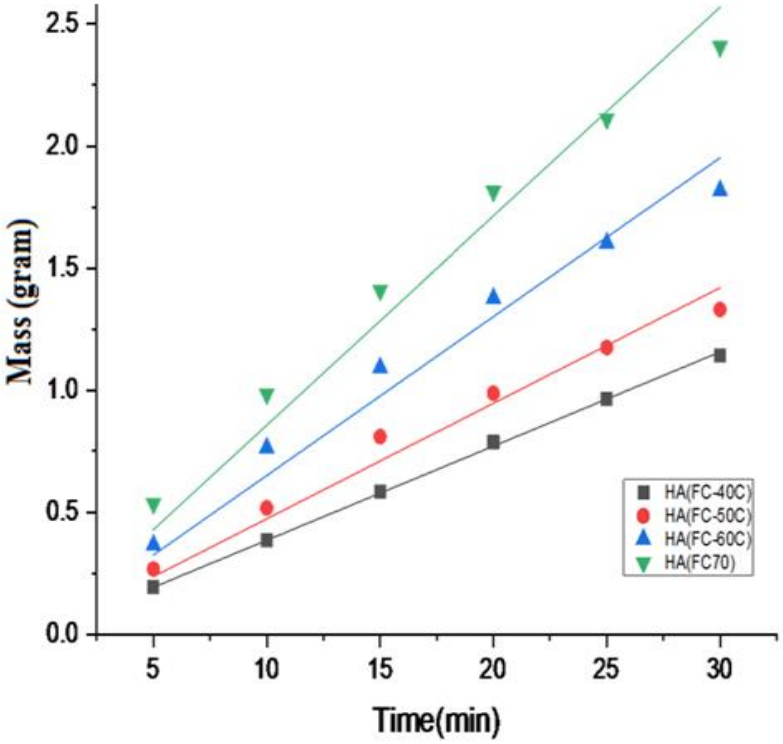

Figure 7.5 **(c)** Variation of etch rate with temperature of 2% Be-Cu alloy with $FeCl_3$ etchant

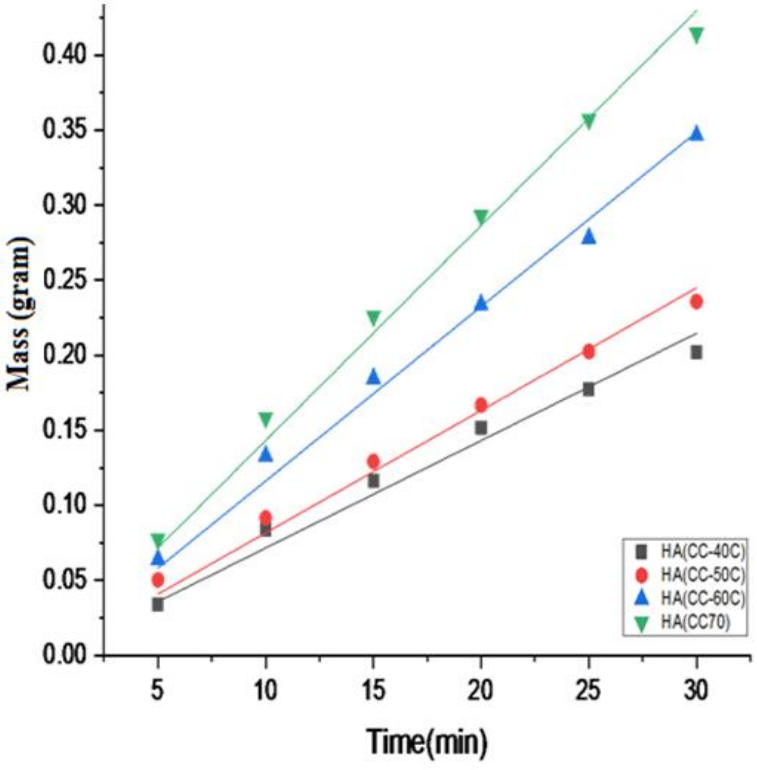

Figure 7.5 **(d)** Variation of etch rate with temperature of 2% Be-Cu alloy (CuBe) with $CuCl_2$ etchant

Above four graphs from

Figure 7.5 (a-d) shows etching of Cu and CuBe using $FeCl_3$ and $CuCl_2$ of constant concentration of '1M' at four different temperatures namely 40ºC, 50ºC, 60ºC and 70ºC.

The following inference can be derived from the study. Etch rate increases linearly with temperature for all cases. Etch rate obtained by $FeCl_3$ solutions are approximately four to five times higher than that by $CuCl_2$ solution for Cu material within the experimental range of temperature as shown in Table 7.4.

Table 7.4 Cu and CuBe Alloy Etching Rates while using $FeCl_3$ and $CuCl_2$ Etchants at Different Temperatures

Workpiece Material	**Etchant (Molar Concentration)**	**Etching rate in mg/min at different temperatures**			
		40 ºC	**50 ºC**	**60 ºC**	**70 ºC**
Cu	$FeCl_3$ (1M)	23.47	34.77	77.02	104.25
	$CuCl_2$(1M)	5.70	8.02	14.92	22.05
CuBe	$FeCl_3$ (1M)	38.55	47.33	65.07	85.68
	$CuCl_2$(1M)	7.16	8.16	11.63	14.32

As far as etching of CuBe is concerned, Etch rate obtained by $FeCl_3$ solutions are approximately five to six times higher for same temperature range compared to $CuCl_2$

solution. This shows $FeCl_3$ reacts more aggressively compared to $CuCl_2$ and produces higher etch rate as discussed earlier.

When the etch rate of CuBe and Cu using $FeCl_3$ etchant are compared, it is interesting to note that $FeCl_3$ provides higher etch rate for CuBe in the temperature range of 40ºC to 50ºC; while this etch rate of CuBe in $FeCl_3$ reduces in the temperature range of 50-70ºC, in comparison with those of Cu material as shown in Figure 7.6**.** This indicates that in case of CuBe, at lower temperature range of 40 to 55^0 C, the etching rate is more with $FeCl_3$ when compared to Cu for the same temperature range. Similar trend is noticed with $CuCl_2$ as the etchant but in the temperature range of 40 to 50^0 C. Hence for micro machining applications, wherein lesser material removal rate (etching rate) is desirable, higher temperature range above 55^0 C for $FeCl_3$ and above 50^0 C with $CuCl_2$ are preferred within this experimental range. However, $CuCl_2$ is most preferred from the point of lesser etch rate.

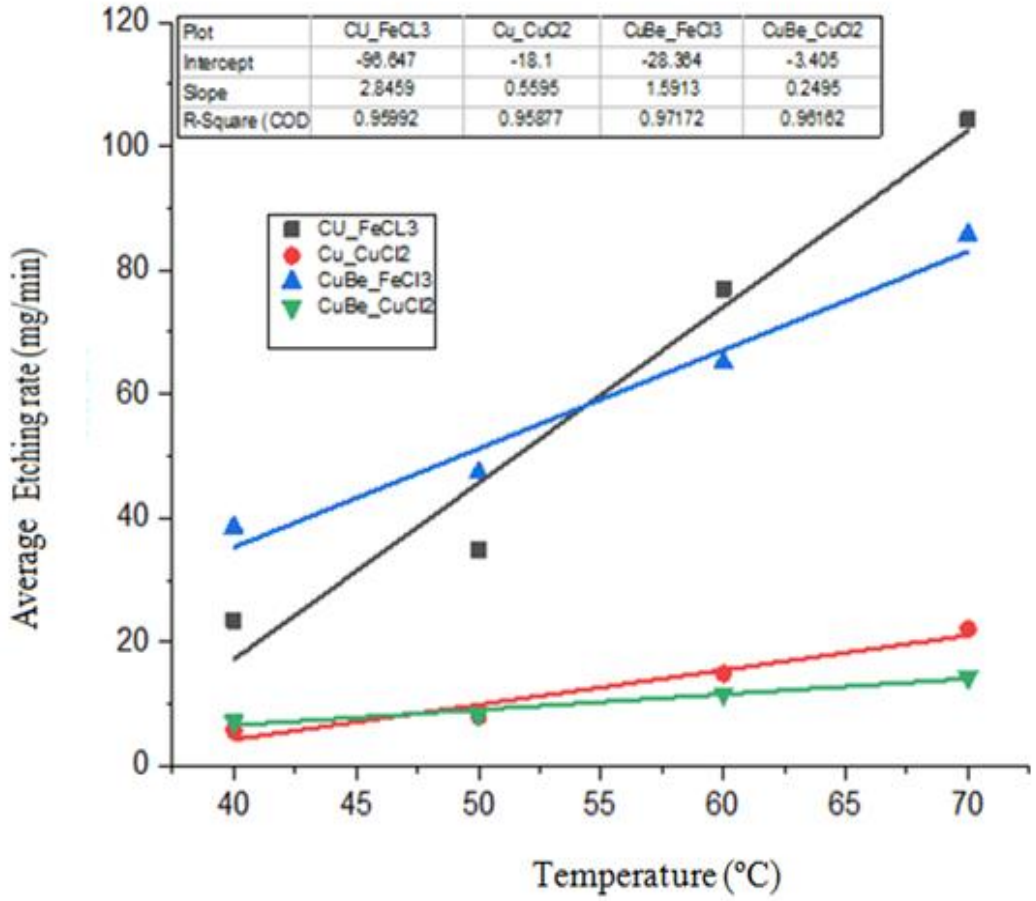

Figure 7.6 Comparison of etch rate of Cu and CuBe with $FeCl_3$ etchant with temperature from 40ºC to 70ºCin steps of 10°C and etching time from 5min to 30min in steps of 5min.

7.4 Study of Chemical Kinetics

Variation of logarithmic etch rate with reciprocal of temperature plotted with the experimental results are shown in Figure 7.7 (a-b) for $FeCl_3$ etchant and $CuCl_2$ etchant respectively. It is evident from the figures that there is a linear relation as shown by the correlation coefficient >0.9, indicating the chemical etching is in accordance with Arrhenius equation of chemical kinetics as shown below.

$$V = A\, e^{\frac{-E}{RgT}} \qquad \text{---(7.1)}$$

Where V is Etch rate or Slope of Mass etched vs. Time curve of the etching process

A is a constant

E is Arrhenius activation energy

R_g is Universal gas constant

T is Temperature in Kelvin

After taking natural logarithm of the terms on both sides of the above equation, we get:

$$\ln(K) = \ln(A) - \frac{E}{R_g}\left(\frac{1}{T}\right) \quad \text{---(7.2)}$$

From this equation it is clear that the slope of

This takes the linear form as follows:

$$y = c + mx \quad \text{---(7.3)}$$

Where y = ln(K), logarithm of etch rate

c= y intercept of the linear graph involving the terms (1/T) on the X-axis and ln(K) on Y-axis.

m= slope of the present graph which is equal to E/R.

x= 1/T

It could be observe that experimental results confirm the linear trend for the etching process which means chemical etching process of Cu or CuBe with $FeCl_3$or $CuCl_2$ follows the Arrhenius equation.

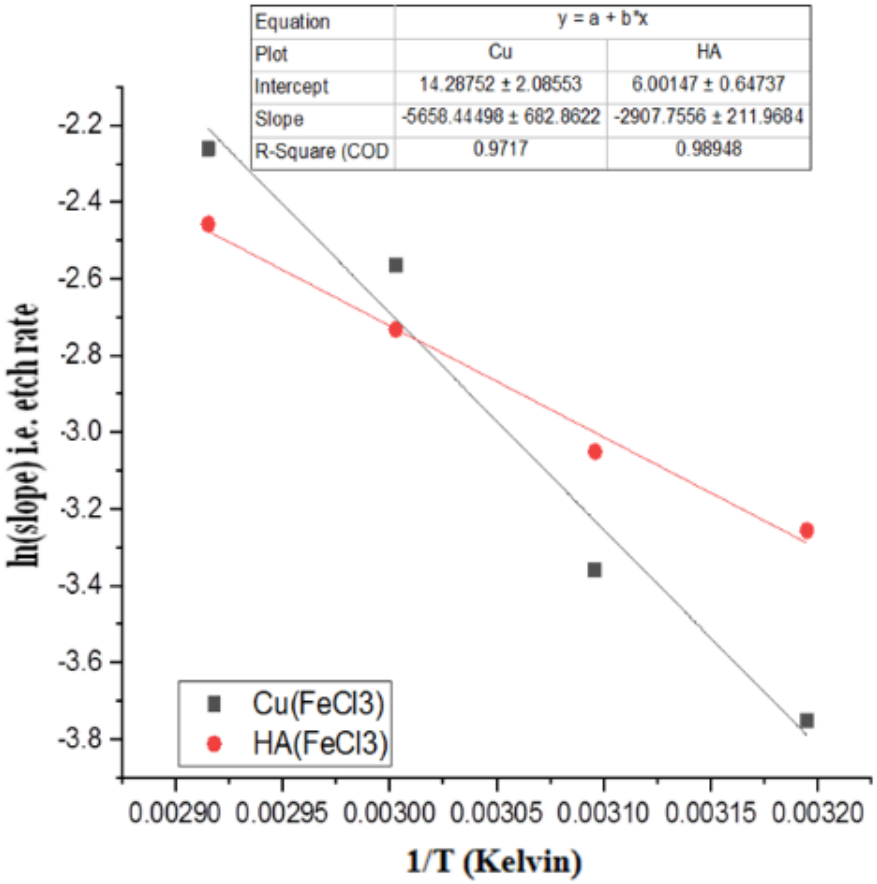

Figure 7.7 (a) Variation of logarithm of slope (reaction rate) with inverse of temperature in K for Cu and 2% Be-Cu alloy (CuBe) with $FeCl_3$ etchant

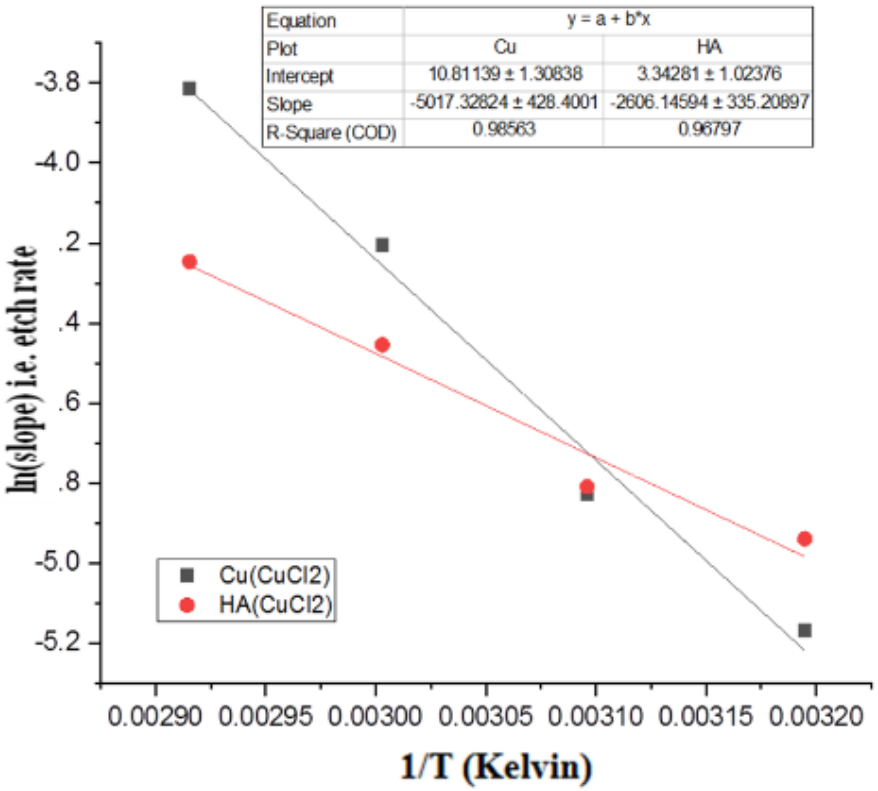

Figure 7.7 (b) Variation of logarithm of slope (reaction rate) with inverse of temperature in K for Cu and 2% Be-Cu alloy (CuBe) with $CuCl_2$ etchant

7.5 Surface Roughness Characteristics

In the chemical etching process, at microscopic level, the chemical attack takes place both at the individual grain surfaces and at the grain boundaries, usually with the different reaction rates. Therefore, fine grain size and homogeneous structure are necessary, in case fine surface finishes are to be attained on the chemically etched parts. Surface roughness, R_a value as defined in the Figure 7.8 is used throughout this research work to characterise the surface roughness.

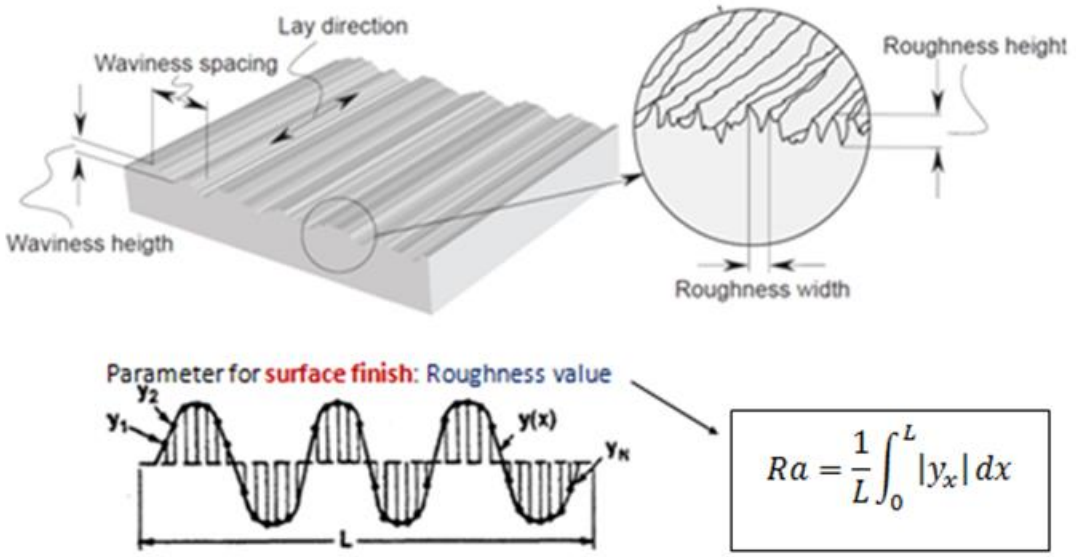

Figure 7.8 Definition of R_a value, the surface roughness parameter

The variations of surface roughness with etch depth for Cu and CuBe alloy are shown in Figure 7.9. The variation follows exponential relation with correlation coefficient of > 0.9. While Cu showed roughness of about 4 µm, CuBe alloy showed roughness of about 0.5µm for $FeCl_3$ etchant. Similar trend is also observed with $CuCl_2$ etchant.

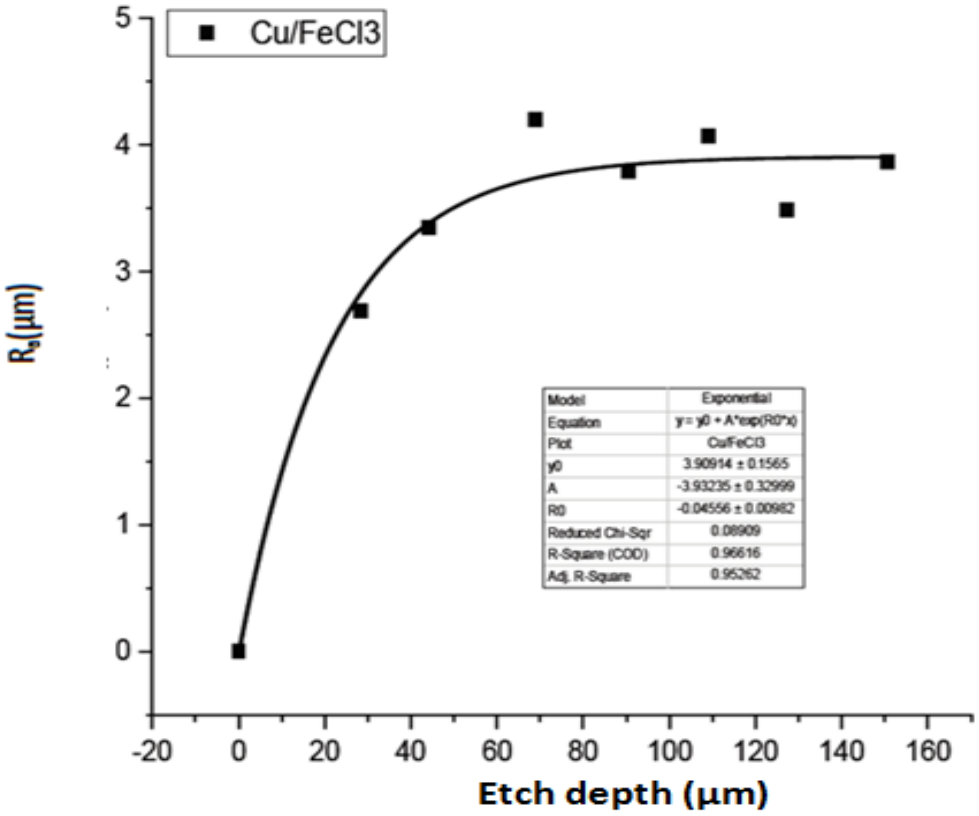

Figure 7.9 **(a)** The variations of surface roughness with etch depth for Cu with $FeCl_3$

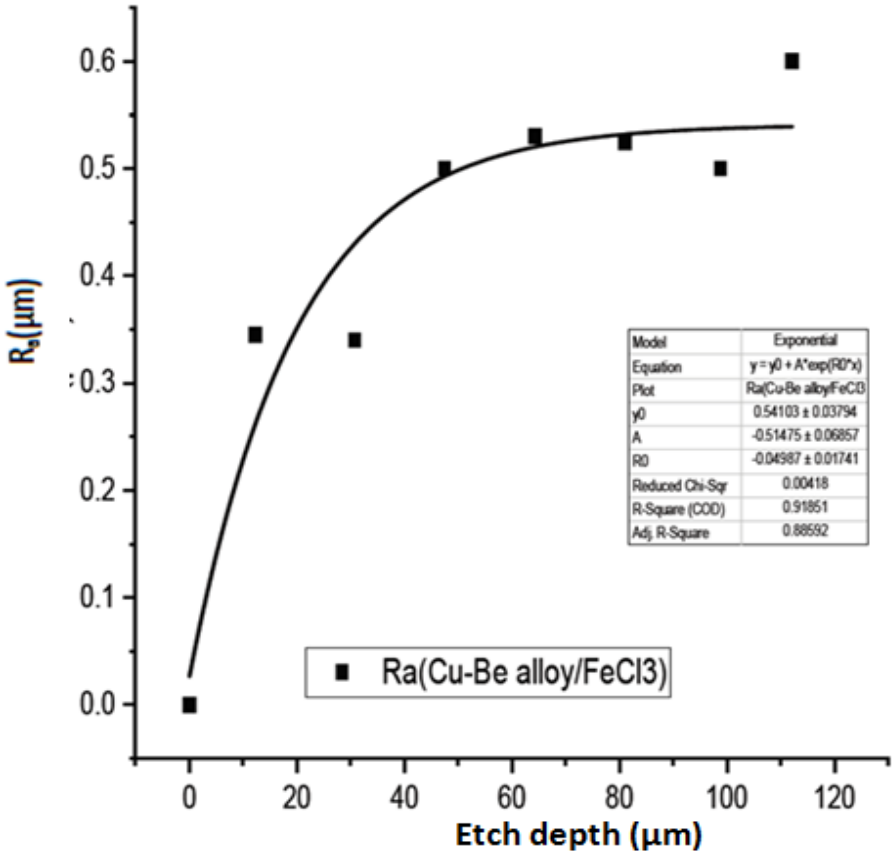

Figure 7.9 **(b)** The variations of surface roughness with etch depth for CuBe alloy with $FeCl_3$

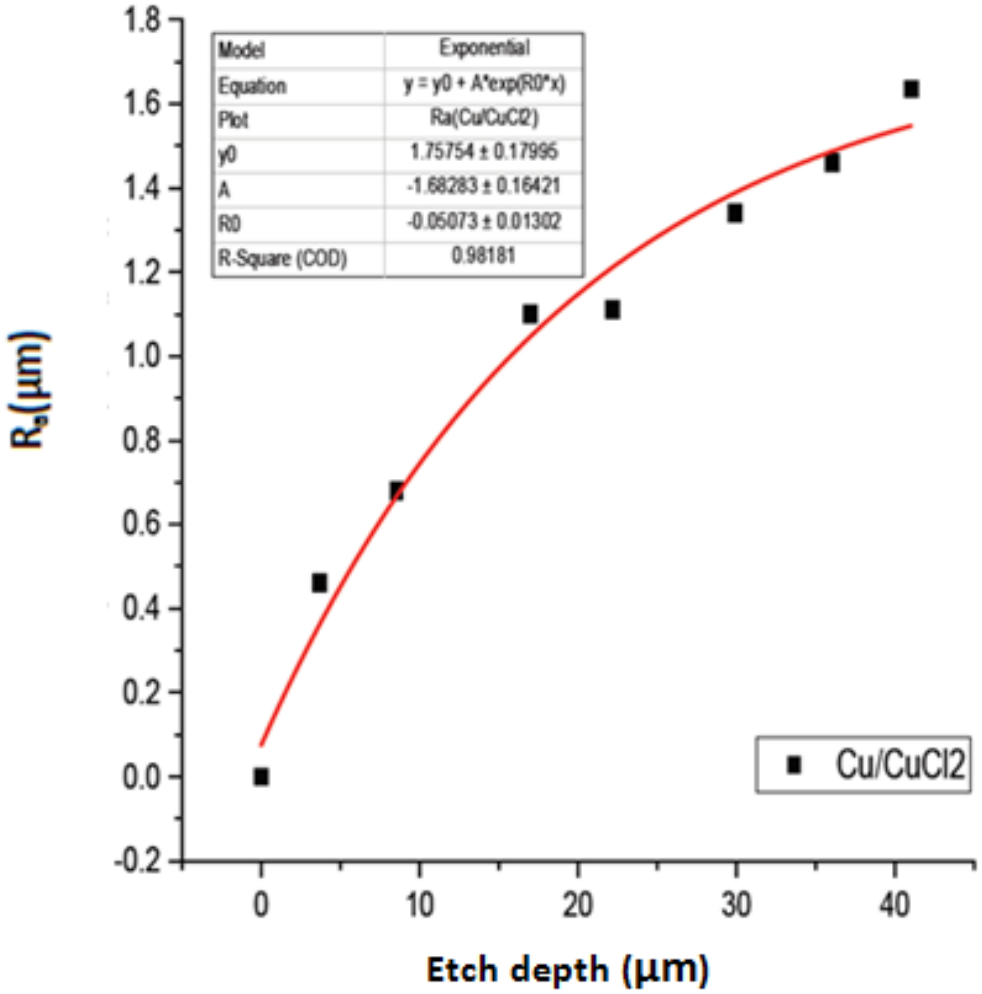

Figure 7.9 **(c)** The variations of surface roughness with etch depth for Cu with $CuCl_2$

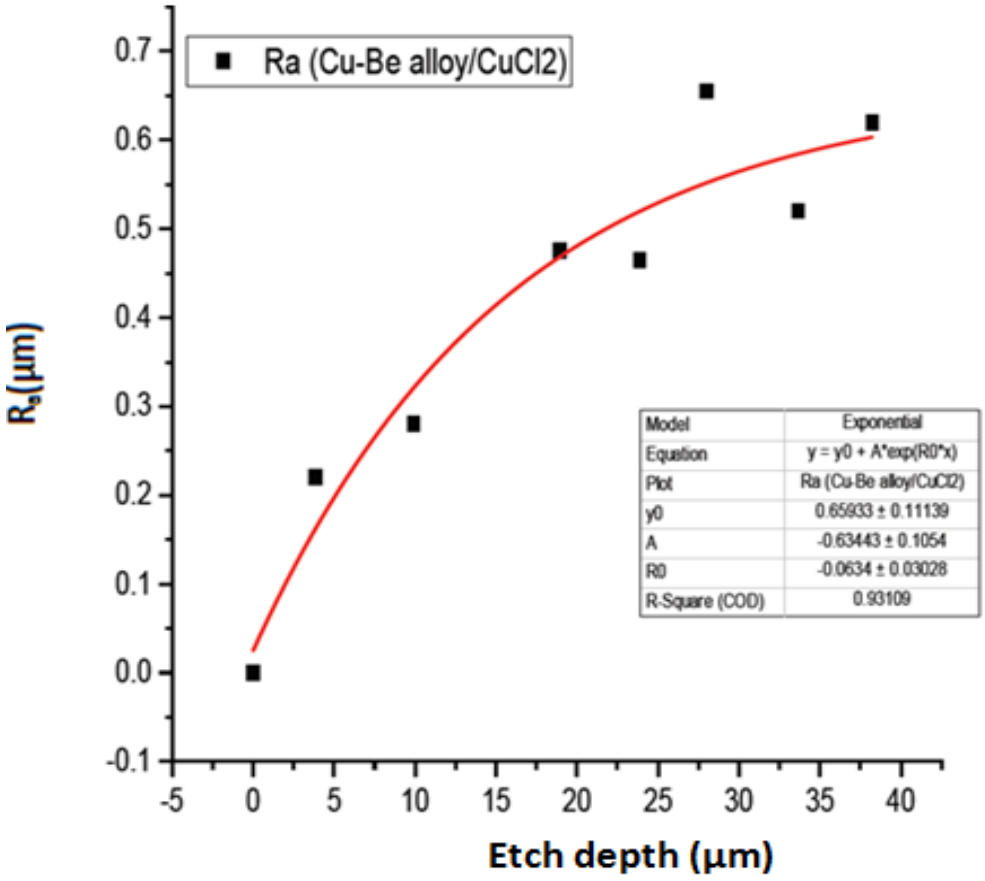

Figure 7.9 (d) The variations of surface roughness with etch depth for CuBe alloy $CuCl_2$

A comparative assessment of surface roughness of both Cu and CuBe alloy for both etchant is shown in Figure 7.10. It is obvious that there is significant difference in surface roughness for Cu among the two different etchants. However, there is no statistically significant difference for Cu and CuBe alloy for both etchants.

It is reported that ferric chloride produced the fastest chemical etch rate, while cupric chloride produced the smoothest surface quality [cakir] during the chemical etching of ETP-copper. This study is in accordance with this observation as far as copper in concerned.

It is observed that the surface roughness remains almost same for both the etchants in case of CuBe alloy. It is interesting to note that the surface roughness values of CuBe alloy remain the same (and better than that of Cu) irrespective of the etchant used.

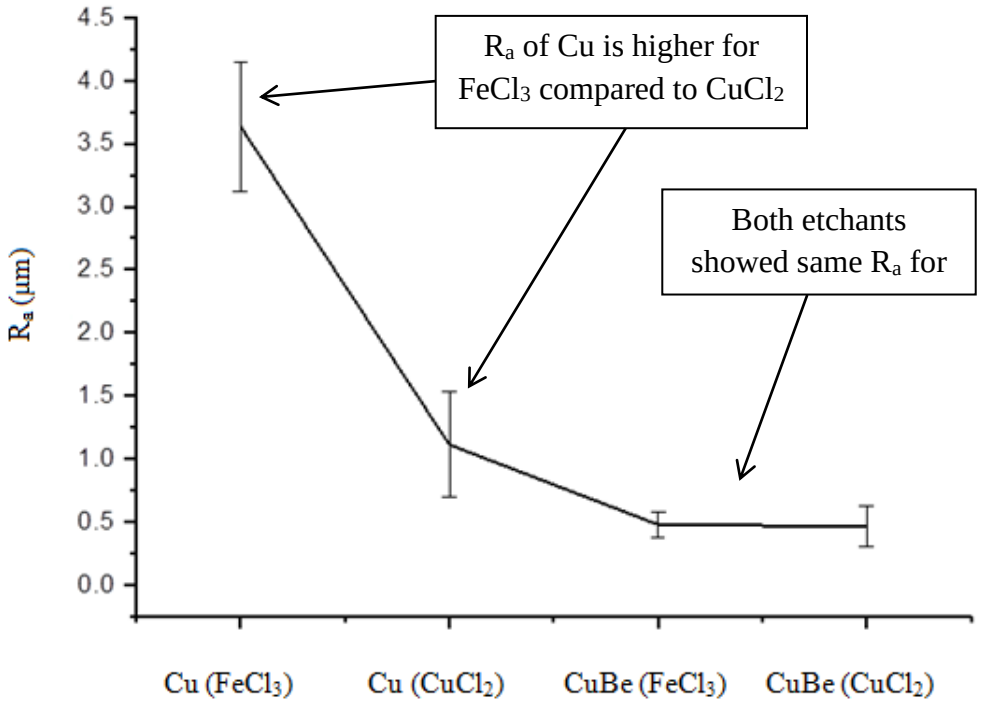

Figure 7.10 Variation of Surface Roughness for Different Combination of Etchant and Metals at a etching time of 2 minutes.

All the surface roughness measurement of the chemically etched specimens have been carried out by and large on, Taylor Hobson, UK made 3D surface topography measurement system model FTS1200. Typical surface roughness measurement plots obtained from this instrument is shown in Figure 7.11**.**

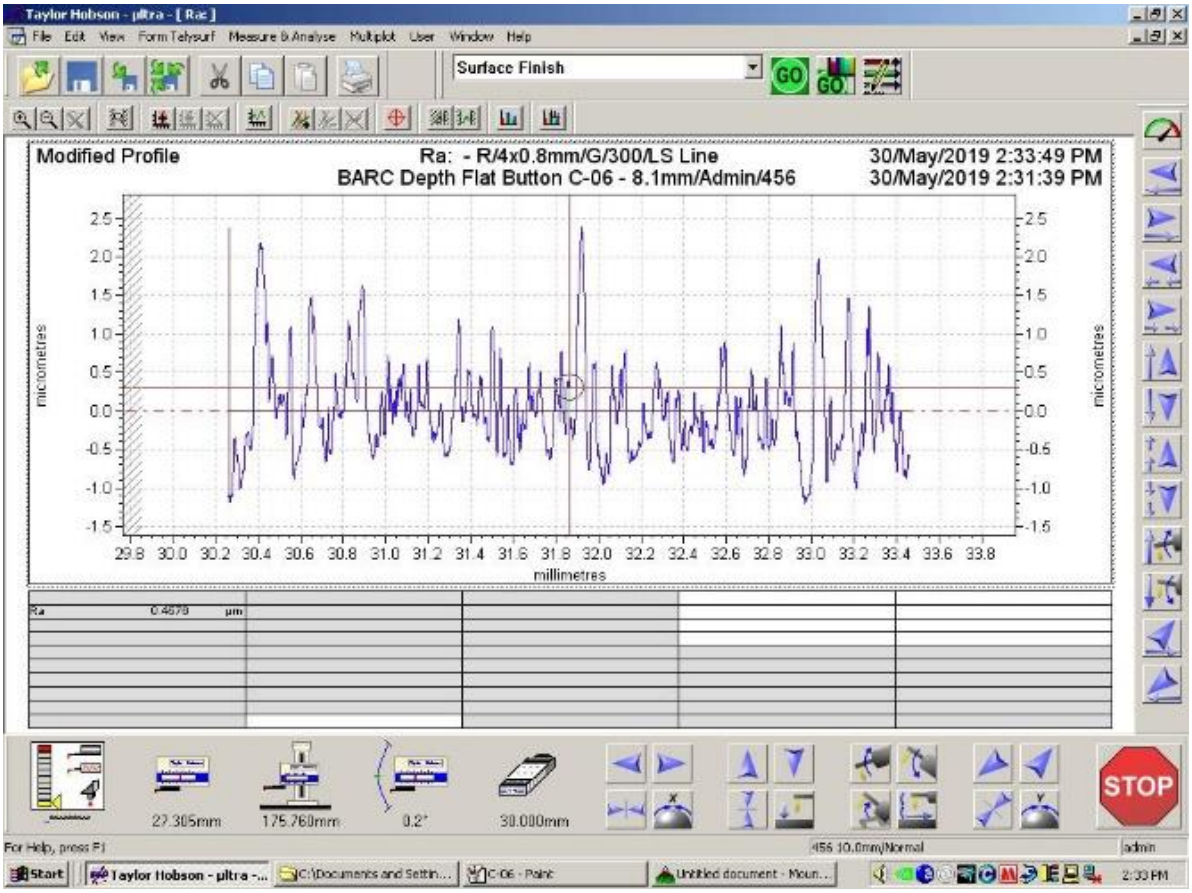

(a) Surface roughness profile for Cu; R_a: 0.45µm

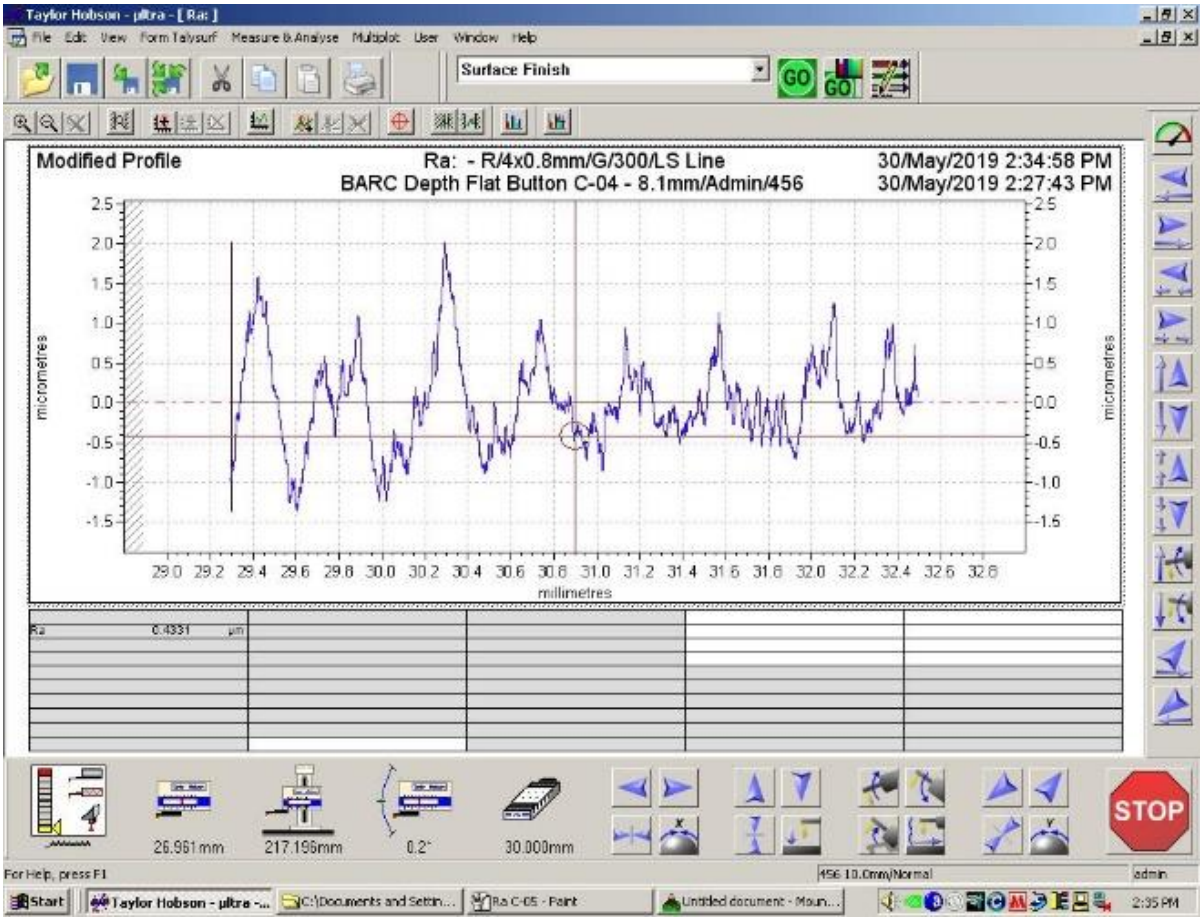

(b) Surface roughness profile for Cu;R_a:0.43µm

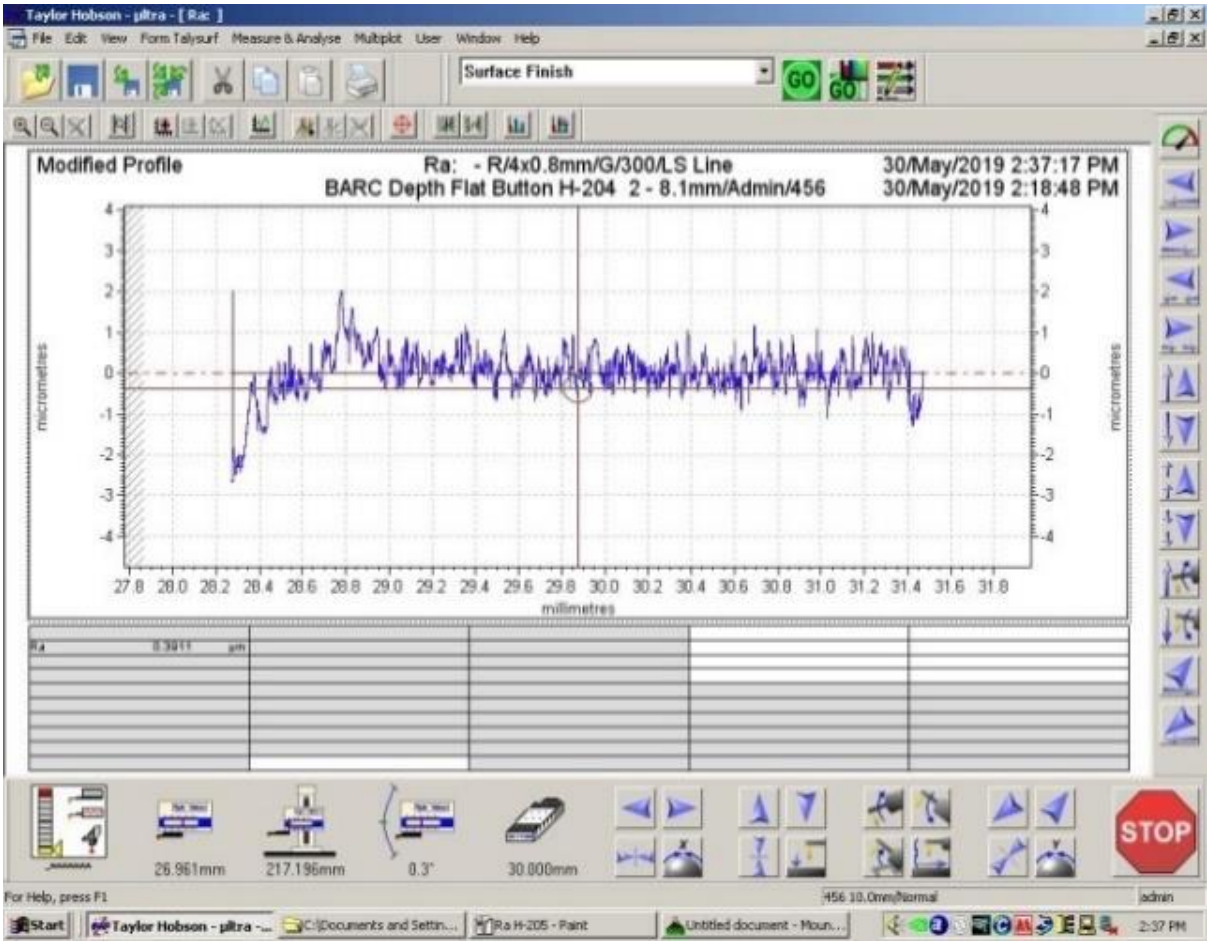

(c) Surface roughness profile for CuBe R_a:0.39µm

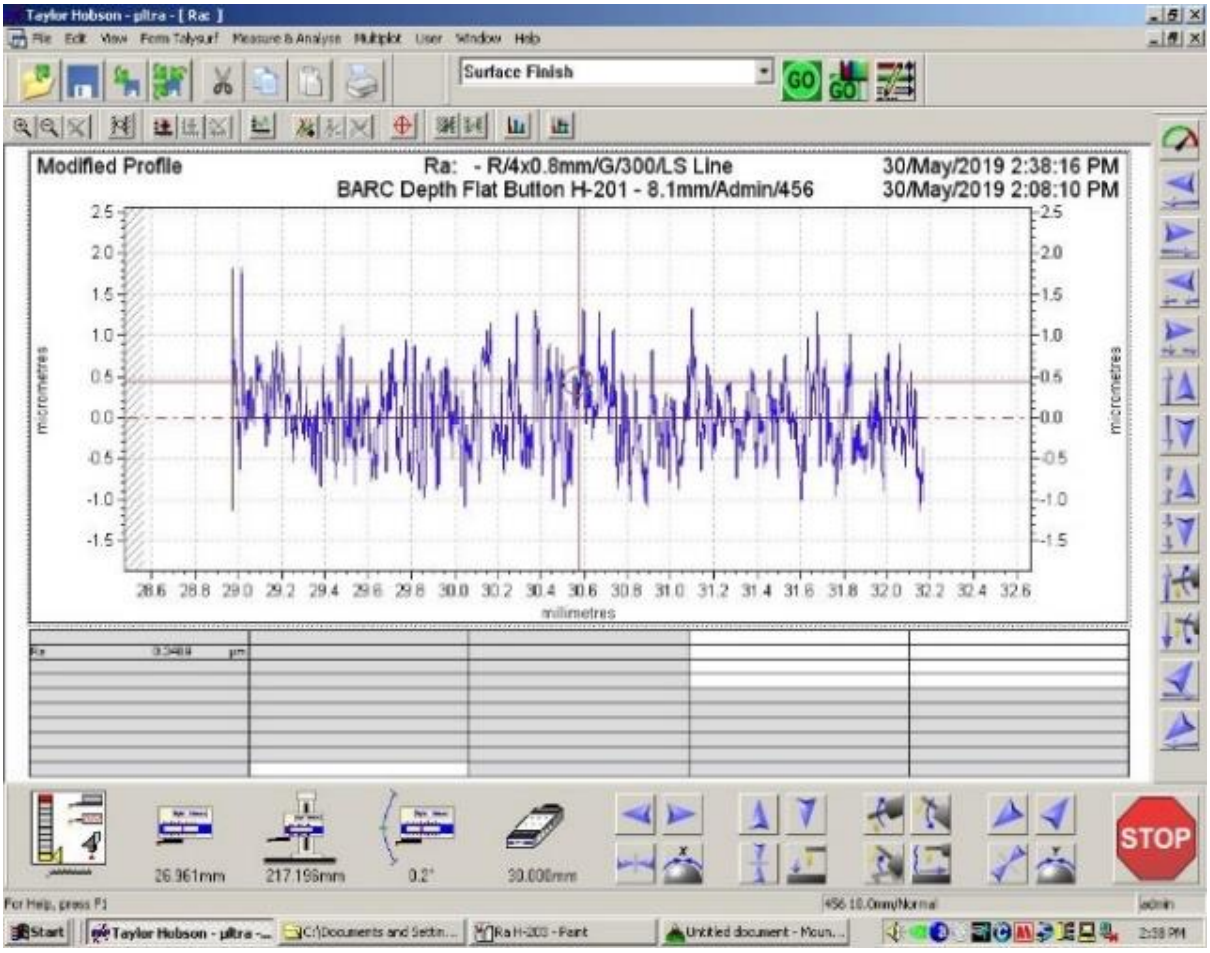

(d) Surface roughness profile for CuBe R_a:0.34µm

Figure 7.11 Typical roughness surface records of chemically etched surface of Cu and CuBe alloy (a to d) with $FeCl_3$ etchant carried out on FTS instrument

7.6 Effect of Excimer Laser Machining on the Depth of Chemically Etched Surface

The Figure 7.12 shows the importance of complete removal of the transparent photoresist coating during laser ablation process, so as to obtain uniform depth after chemical etching. These images are taken on 'Alicona'- 3DTopography Measuring Instrument.

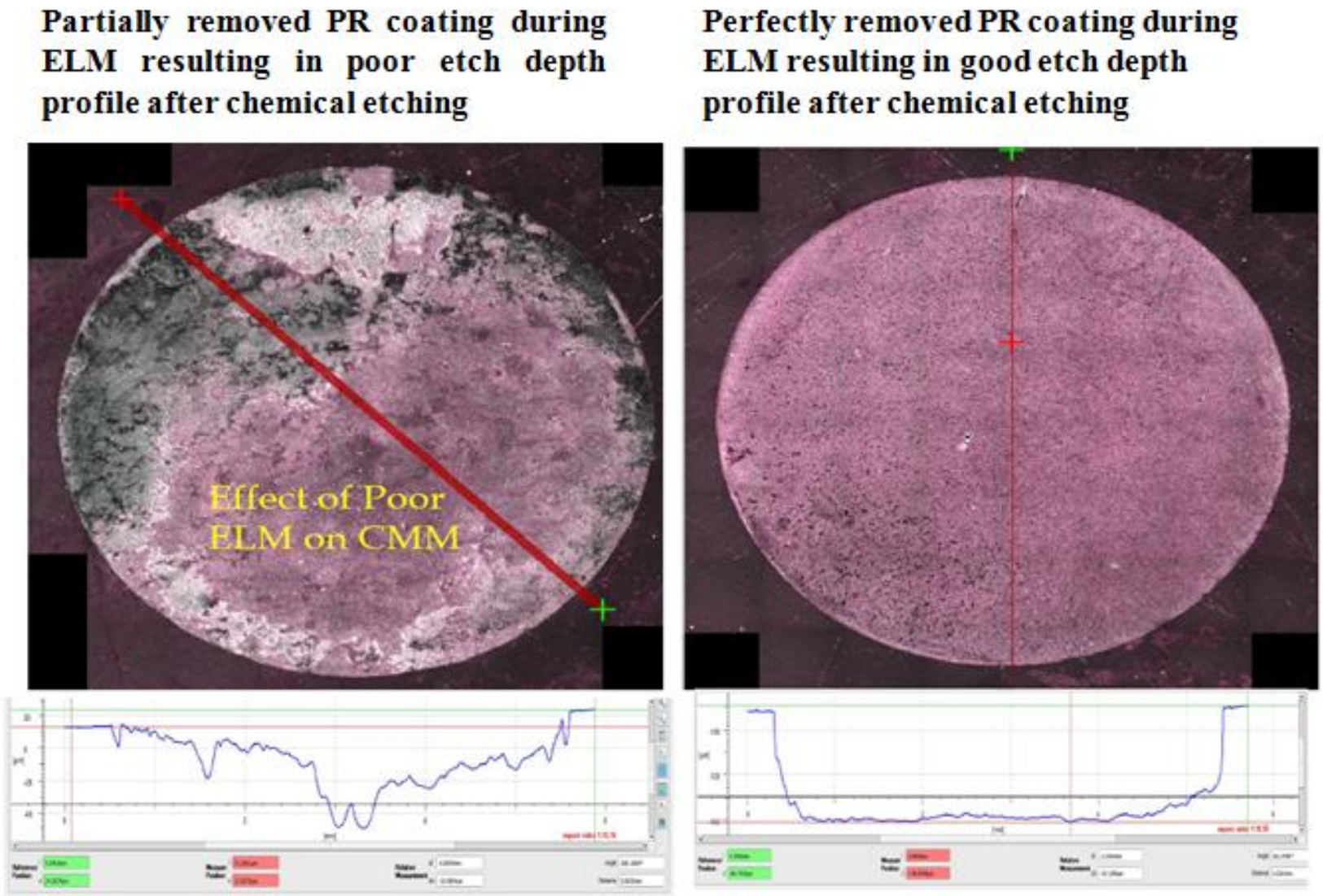

Figure 7.12 'Alicona' Images and Depth Profile after Chemical Etching of two Specimens

Photoresist is a transparent film, which will be adhering to metallic surface. Visually it will be very difficult rather impossible to decide whether 100% of the PR layer is removed from the desired location during Excimer laser ablation. On examination of the etch depth profile of the chemically etched surface after a number of experiments, it is observed that the etch depth is highly non-uniform and in some areas practically zero. On further investigation it is revealed that root cause for the observed phenomena is imperfect removal of the PR layer during laser ablation. The black patches seen in Figure 7.12, represents areas from where incomplete removal of PR has happened during the Excimer laser ablation.

7.6.1 Surface Characterization by GDOES

For an alloy containing various metals, it is natural that the etch rate of each one of the constituent element may be having different etch rate. In order to asses whether it is true for CuBe alloy, chemical etched surface is charaterised for its depth profile to assertain its compositional inhomogenity using Glow Discharge Optical Emmision Spectrometer (GDOES). The plots obtained from the GDOES instruemnts is shown in Figure 7.13.From the figure it is clear that after chemical etching the surface will become enriched with Be and consequently the etched surface would imporve its hardness. However further investigations on these aspects are not within the scope of present research work. This observation is first time reported by this study and its mechanism can be explained based on redox potential of alloying elements (electrochemical series).

Beryllium rich top surface layer

- 2.2% Be in 2% Alloy
- 1.2% Be in 0.7% Alloy

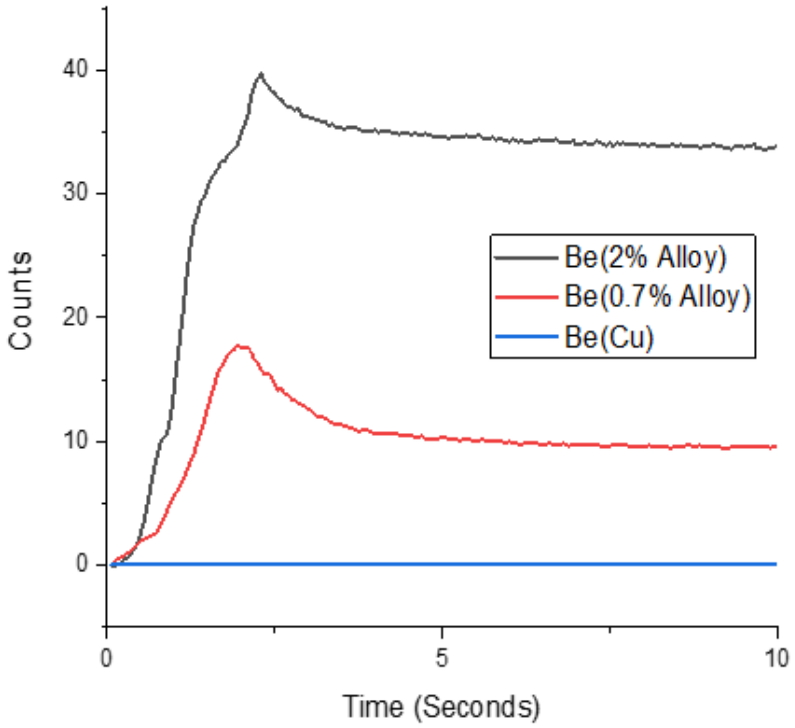

Figure 7.13 Surface Composition by GDOES

From the above experimental study, the following Observations can be inferred.

- Mass removal is linearly increasing with time.
- MRR is increasing with increase in etchant temperature.
- With $CuCl_2$ etchant, both Cu and CuBe alloy showed same etch rate.
- CuBe alloy showed different etch rate with both the etchants.
- Etch Rate of Cu > CuBe for $FeCl_3$
- Both etchants showed same Ra for CuBe
- Cu-Be alloy is having better surface finish than Cu metal.
- Ra of Cu is higher for $FeCl_3$ compared to $CuCl_2$
- Beryllium rich surface layer after chemical etching of CuBe

7.7 Manufacturing of SSGB

The overall manufacturing process sheet of SSGB and the importance of chemical etching process in this overall plan is shown below in Figure 7.14**.**

- The SSGB parts are first CNC turned to produce the hemispherical ball ended shaft and the matching hemispherical cup. Subsequently these parts are finish-machined on Diamond Turning Machine (DTM) using Single Crystal Diamond (SCD) tool to produce nanometre level surface roughness values and size and form tolerances within 1.0 and 1.2 µm respectively.

- The micro grooves are to be produced on the hemispherical cavity surface. For this the surface is coated with Photoresist (PR) and laser lithographed using Excimer laser of 240 nanometre wavelength, by the mask projection technique.

- The lithographed components are subjected to photochemical machining to produce micro grooves on the hemispherical cavity surface.

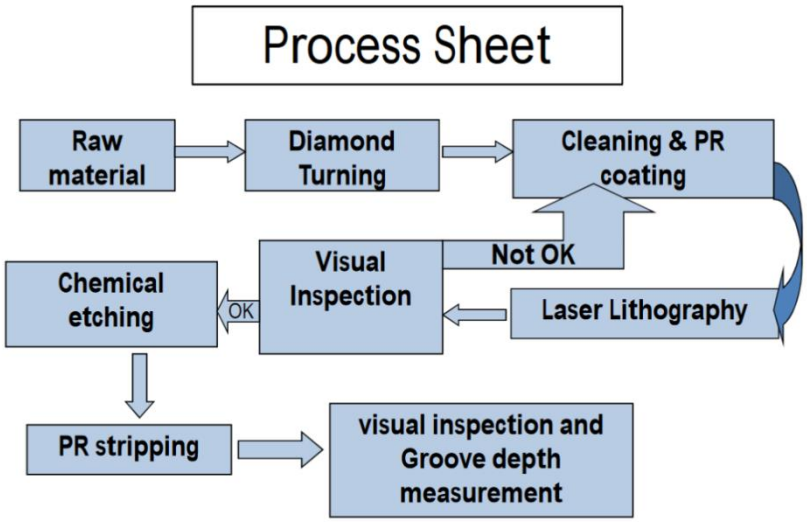

Figure 7.14 Manufacturing process flow sheet to produce micro grooves

The groove generation is accomplished with a patterned-mask (Photo mask / Stencil) as shown in Figure 7.1 (a) kept in the laser beam path. The image of the mask is projected on

to the PR coated metallic work piece. The Excimer Laser ablates the photoresist at specific locations dictated by the openings on the mask. The chemical etching process is carried out after laser lithography to produce micro features on metal surface. Subsequent etching in $FeCl_3$ solution generates the groove due to isotropic etching. In the process, metal is etched by chemical enchants to dissolve the surface of the part that has been selectively exposed using laser ablation technique. Schematic representation of Chemical etching is shown in Figure 7.15.

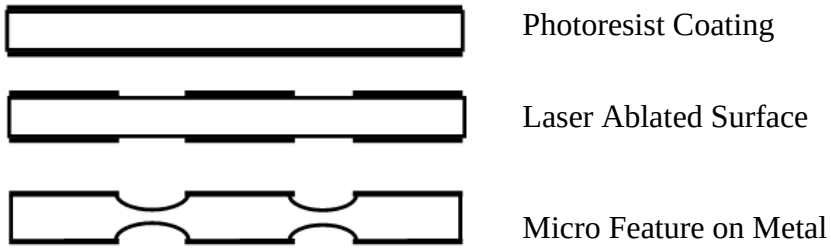

Figure 7.15 Stages of Photochemical Machining

Chemical micromachining on both pure copper and Cu-Be alloy is done and various process parameters are considered to optimize the chemical etching process. Figure 7.16 shows the experimental plan used for chemical etching.

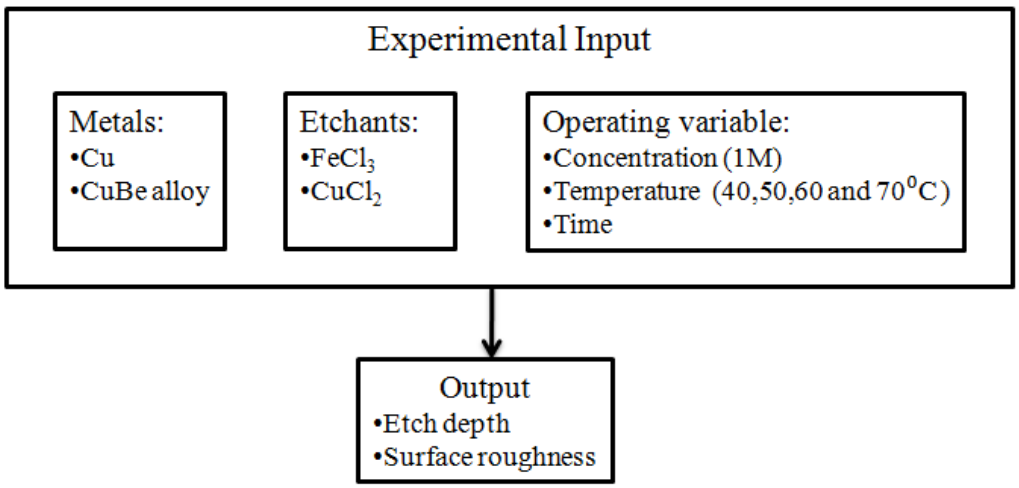

Figure 7.16 Experimental plans for Chemical etching

7.8 Optimization of Chemical Etching Process

The objective is to optimise the etching parameters of CuBe alloy component using $FeCl_3$ etchant to get the desired etch depth and the lowest surface roughness value. The data is subjected to statistical analysis using ANOVA methodology to establish the effect of concentration of ferric chloride etchant, chemical bath, temperature and etch time on etch depth and surface finish. Two data driven predictive models using Response Surface Modelling (RSM) and Artificial Neural Network (ANN) were developed and their prediction capabilities were ascertained. Further, optimization has been carried out to predict optimum parameters with respect to etchant concentration, bath temperature and etch time to achieve target values of 25±2 µm, 30±2 µm and 35±2 µm etch depth and minimum possible R_a value. The details of the study are described below.

7.8.1 Full factorial design for Chemical etching

A full Factorial experimental design was employed for the design of the experiments to evaluate the effect of three operating parameters, i.e., concentration of ferric chloride etchant (M), chemical bath temperature (^{o}C) and etch time (minutes). These selected parameters have been considered as the independent variables and the etch depth (µm) after chemical etching, and surface finish (R_a) have been treated as the dependent variable (response).

Independent variables:

- 4 levels for concentration of etchant (mole/litre): 1, 1.5, 2, 2.5.
- 5 levels for chemical bath temperature (^{o}C):45, 50, 55, 60
- 4 levels for etching time (minutes): 2, 4, 6, 8

Dependent variables:

- Etch depth, µm

- Surface finish (Ra)

The experimental ranges were obtained based on previous preliminary experiments. Accordingly, 80 experiments were defined for these three independent variables as shown in Table 7.5. The response for this experimental study i.e. average etch depth (dependent variable), for chemical etching CuBe alloy has been calculated from the mass loss in the experiments. Etch depth is computed gravimetrically from the relation, etch depth=Mass of metal removed/(area of cross section of the etched cylindrical feature x density of the material). Surface roughness has been measured using profilometer 'Form TalySurf 1200' Instrument.

Table 7.5 Experimental conditions and responses on etch depth and surface roughness for CuBe alloy

Experiment	**Pattern**	**Conc. of $FeCl_3$(M)**	**Temp. (°C)**	**Time (min)**	**Depth (µm) for 2%Be alloy**	**R_a (µm) for 2%Be alloy**
1.	111	1	45	2	6.92	0.39
2.	112	1	45	4	11.04	0.77
3.	113	1	45	6	14.01	1.09
4.	114	1	45	8	19.14	0.86
5.	121	1	50	2	9.48	0.24
6.	122	1	50	4	19.86	0.23
7.	123	1	50	6	23.23	0.19
8.	124	1	50	8	28.16	0.17
9.	131	1	55	2	11.25	0.16
10.	132	1	55	4	21.70	0.16
11.	133	1	55	6	28.66	0.19
12.	134	1	55	8	21.15	0.16
13.	141	1	60	2	11.56	0.19
14.	142	1	60	4	22.73	0.15
15.	143	1	60	6	26.89	0.26
16.	144	1	60	8	51.11	0.25

Experiment	Pattern	Conc. of $FeCl_3$(M)	Temp. (°C)	Time (min)	Depth (µm) for 2%Be alloy	R_a (µm) for 2%Be alloy
17.	151	1	65	2	13.16	1.10
18.	152	1	65	4	17.41	1.50
19.	153	1	65	6	22.33	0.96
20.	154	1	65	8	32.87	1.39
21.	211	1.5	45	2	7.71	0.20
22.	212	1.5	45	4	10.31	0.47
23.	213	1.5	45	6	24.79	0.69
24.	214	1.5	45	8	30.15	0.95
25.	221	1.5	50	2	10.93	0.16
26.	222	1.5	50	4	22.66	0.34
27.	223	1.5	50	6	33.41	0.38
28.	224	1.5	50	8	44.76	0.27
29.	231	1.5	55	2	10.27	0.33
30.	232	1.5	55	4	19.01	0.40
31.	233	1.5	55	6	28.77	0.38
32.	234	1.5	55	8	45.20	0.32
33.	241	1.5	60	2	15.17	0.21
34.	242	1.5	60	4	29.65	0.21
35.	243	1.5	60	6	38.74	0.27
36.	244	1.5	60	8	51.94	0.34
37.	251	1.5	65	2	12.66	1.07
38.	252	1.5	65	4	17.41	1.27
39.	253	1.5	65	6	39.96	1.00
40.	254	1.5	65	8	40.25	0.45
41.	311	2	45	2	8.87	0.18
42.	312	2	45	4	18.22	0.15
43.	313	2	45	6	26.89	0.28
44.	314	2	45	8	32.87	0.24
45.	321	2	50	2	12.24	0.19
46.	322	2	50	4	28.77	0.24

Experiment	Pattern	Conc. of $FeCl_3$(M)	Temp. (°C)	Time (min)	Depth (µm) for 2%Be alloy	R_a (µm) for 2%Be alloy
47.	323	2	50	6	20.89	0.12
48.	324	2	50	8	24.46	0.16
49.	331	2	55	2	14.17	0.27
50.	332	2	55	4	18.02	0.30
51.	333	2	55	6	26.82	0.15
52.	334	2	55	8	27.57	0.20
53.	341	2	60	2	16.29	0.14
54.	342	2	60	4	19.62	0.17
55.	343	2	60	6	41.74	0.30
56.	344	2	60	8	49.55	0.29
57.	351	2	65	2	16.99	0.75
58.	352	2	65	4	19.86	1.10
59.	353	2	65	6	31.25	0.48
60.	354	2	65	8	40.82	0.65
61.	411	2.5	45	2	11.36	0.31
62.	412	2.5	45	4	13.29	0.50
63.	413	2.5	45	6	26.34	0.48
64.	414	2.5	45	8	31.73	0.40
65.	421	2.5	50	2	10.90	0.24
66.	422	2.5	50	4	20.69	0.18
67.	423	2.5	50	6	15.52	0.32
68.	424	2.5	50	8	27.48	0.76
69.	431	2.5	55	2	14.61	0.51
70.	432	2.5	55	4	22.66	0.82
71.	433	2.5	55	6	32.76	0.43
72.	434	2.5	55	8	29.93	0.56
73.	441	2.5	60	2	14.39	0.46
74.	442	2.5	60	4	19.79	0.36
75.	443	2.5	60	6	33.98	0.46
76.	444	2.5	60	8	52.75	0.50

Experiment	Pattern	Conc. of $FeCl_3$(M)	Temp. (°C)	Time (min)	Depth (µm) for 2%Be alloy	R_a (µm) for 2%Be alloy
77.	451	2.5	65	2	12.81	0.54
78.	452	2.5	65	4	18.46	0.71
79.	453	2.5	65	6	34.66	0.71
80.	454	2.5	65	8	17.76	0.73

The variation of etch depth and surface roughness as a function of etchant concentration, temperature and time are illustrated in 3-D surface profile shown below in Figure 7.17. As can be seen from surface contour the relationship is non-linear.

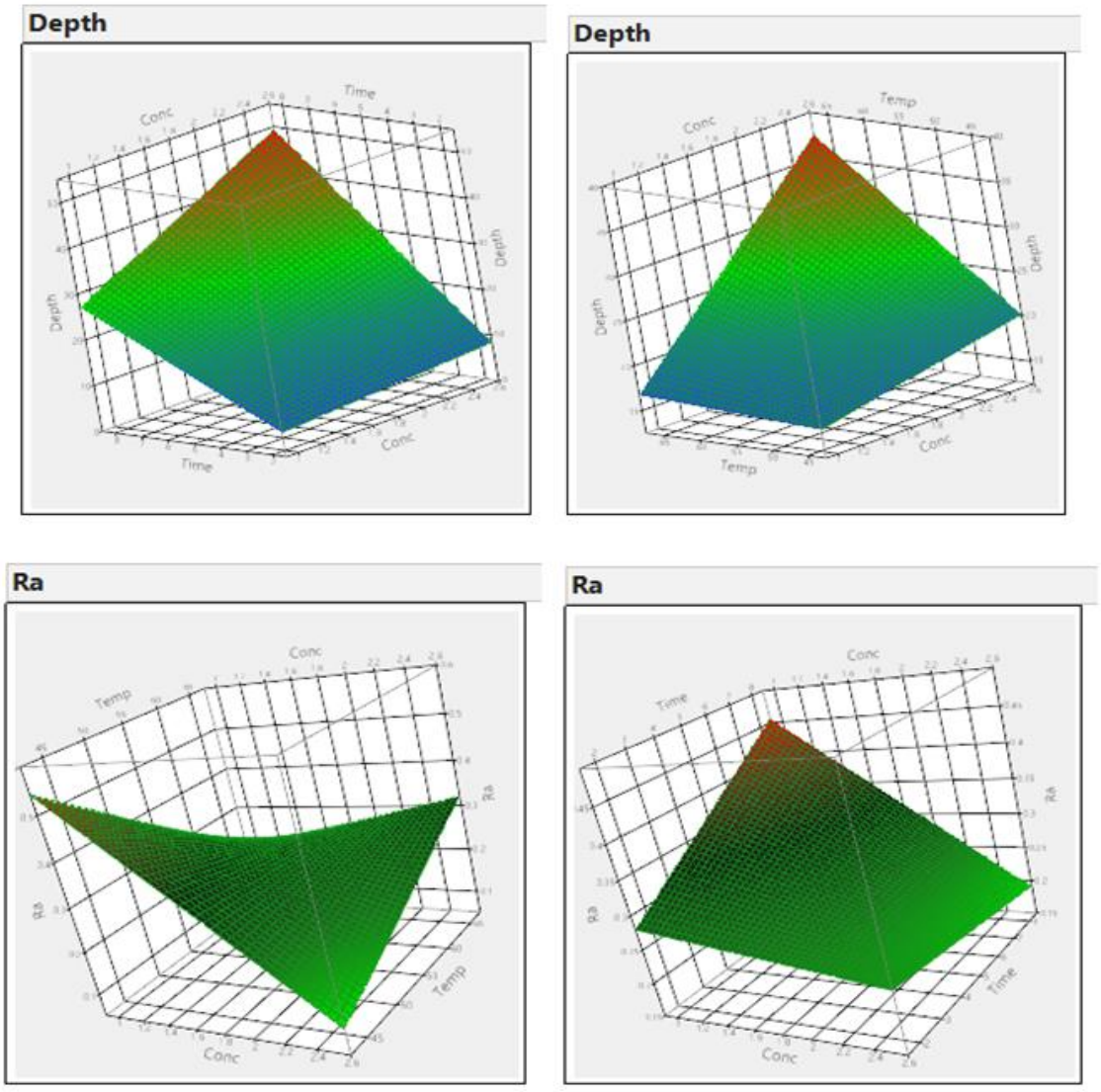

Figure 7.17 Profile Showing Relation of Responses with Independent Variables

Upon investigating the statistically significant influencing etching parameters on etch depth and surface roughness the following observations are made. As far as etch depth is concerned the following parameters are statistically significant as shown in Table 7.6.

Table 7.6 Statistical Significance for Etch Depth

Source	**Sum of Squares**	**F Ratio**	**Prob > F**	**Remark**
Concentration	1393.7161	45.0561	<0.0001*	significant
Temp	538.4477	17.4069	<0.0001*	significant
Time	8047.1138	260.1471	<0.0001*	significant
Concentration *Temp	181.8765	5.8797	0.0178*	significant
Concentration *Time	323.9674	10.4732	0.0018*	significant
Temp*Time	94.4425	3.0531	0.0848	

As far as surface roughness is concerned the following parameters are statistically significant as shown in Table 7.7**.**

Table 7.7 Statistical Significance for R_a

Source	**Sum of Squares**	**F Ratio**	**Prob > F**	**Remark**
Concentration	0.20884900	19.9993	<0.0001*	significant
Temp	0.02782563	2.6646	0.1069	
Time	0.03724900	3.5669	0.0629	
Concentration *Temp	0.22512050	21.5574	<0.0001*	significant
Concentration *Time	0.04213620	4.0349	0.0483*	significant
Temp*Time	0.01201250	1.1503	0.2870	

The prediction capabilities for both etch depth and surface roughness of full factorial design is shown in Figure 7.18**.** The correlation coefficients of 0.82, 0.42 for etch depth and

surface roughness respectively are observed. The prediction equation for etch depth and surface roughness are given in Eq (7.4) and Eq. (7.5) respectively.

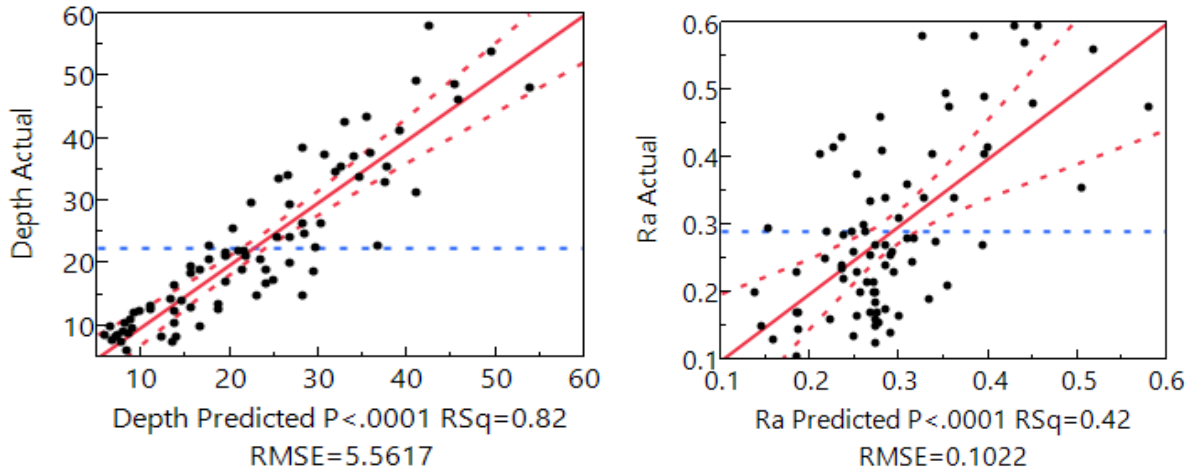

Figure 7.18 Regression graph of actual and predicted values for etch depth and R_a

$$Etch\ depth(\mu m) = -33.1087 + (7.4665 * Conc.) + (0.3668 * Temp.) + (4.4852 * time) + (conc. - 1.75) * \big((Temp. - 55) * 0.3814\big) + (conc. - 1.75) * \big((Temp. - 55) * 1.6098\big) + (Temp - 55) * ((time - 5) * 0.0687) \quad \text{---(7.4)}$$

$$Surface\ roughness, R_a(\mu m) = 0.5477 + (-0.0914 * Conc.) + (-0.0026 * Temp.) + (0.0097) * time + (conc. - 1.75) * \big((Temp. - 55) * 0.0134\big) + (conc. - 1.75) * \big((time. - 55) * (-0.0184)\big) + (Temp - 55) * ((time - 5) * (-0.0007)) \quad \text{---(7.5)}$$

7.8.2 Model Optimization by RSM

'Prediction profiles' are useful in cases where the modelling of problems/experiments involve multiple-responses. These profiles help one to optimize the model to get the desired set of responses for which the corresponding input variables/ factor values can be optimized using the complex set of criteria (desired response). Often there are multiple responses measured and the desirability of the outcome involves several or all of these responses. For

example, one might want to maximize one response, minimize another, and keep a third response close to some target value.

To derive the optimal parameters with respect to etchant concentration, temperature and time for three target values of 25±2 µm, 30±2 µm and 35±2 µm etch depth and minimum surface roughness, the 'optimization profiles' are shown in Figure 7.19**,** Figure 7.20 and Figure 7.21. In these figures the values written in red colour indicates the optimum ones. The red coloured values indicated on the Y-axis is the targeted etch depth and R_a values. The red coloured values indicated on the X-axis shows the optimum values of concentration, temperature and etching time as predicted by RSM the model.

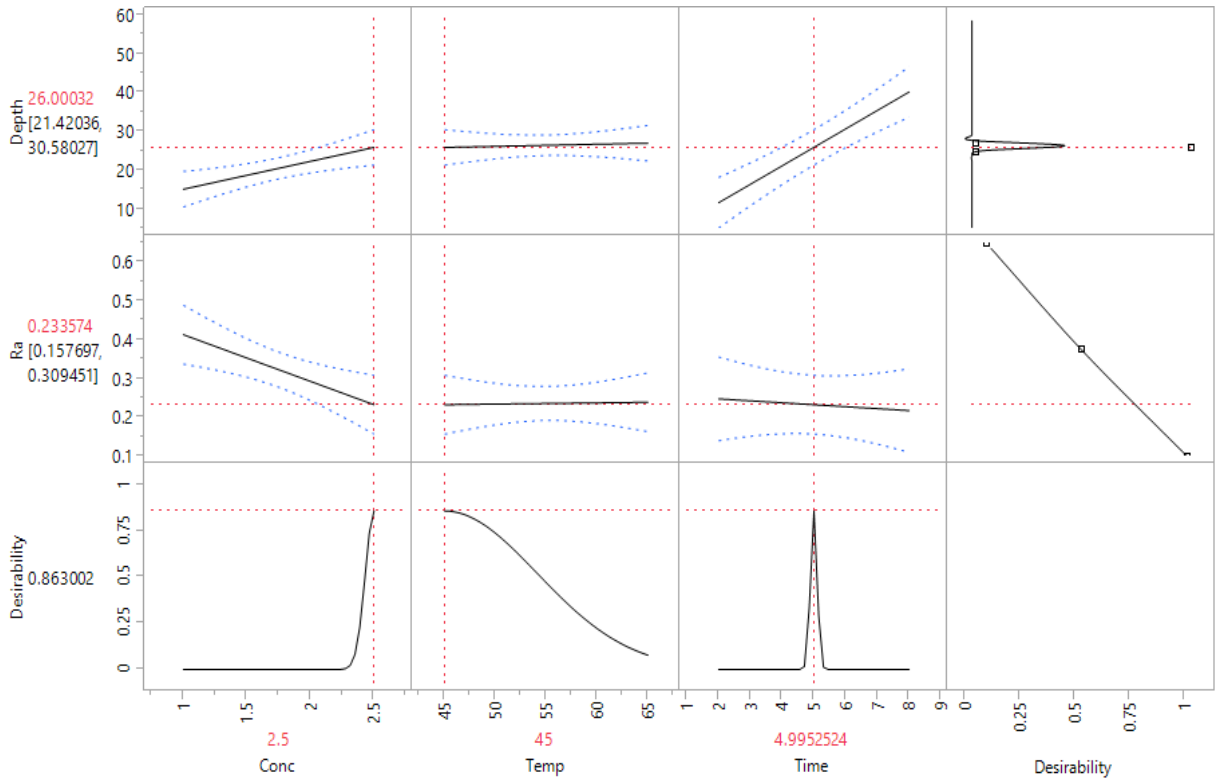

Figure 7.19 Optimization profile for Design 1 with a target value of 25±2 µm etch depth with minimum possible R_a Value by RSM

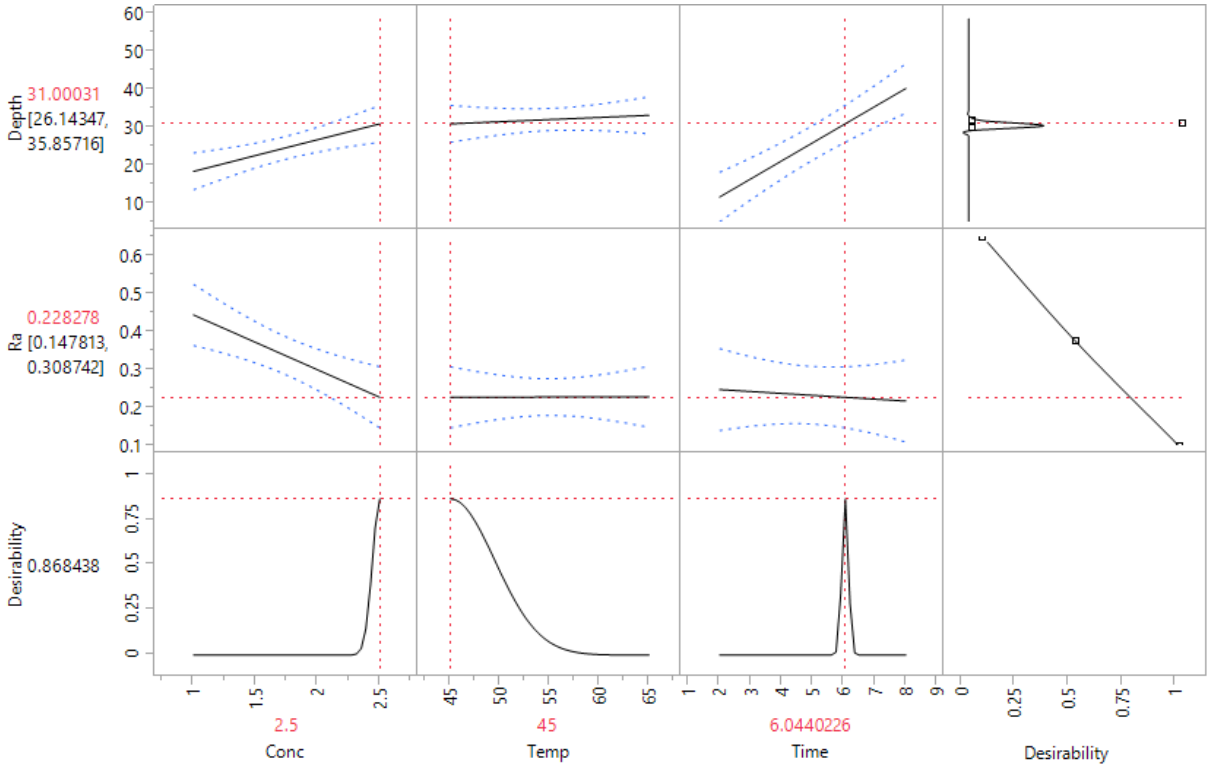

Figure 7.20 Optimization profile for Design 2 with a target value of 30±2 µm etch depth with minimum possible R_a Value by RSM

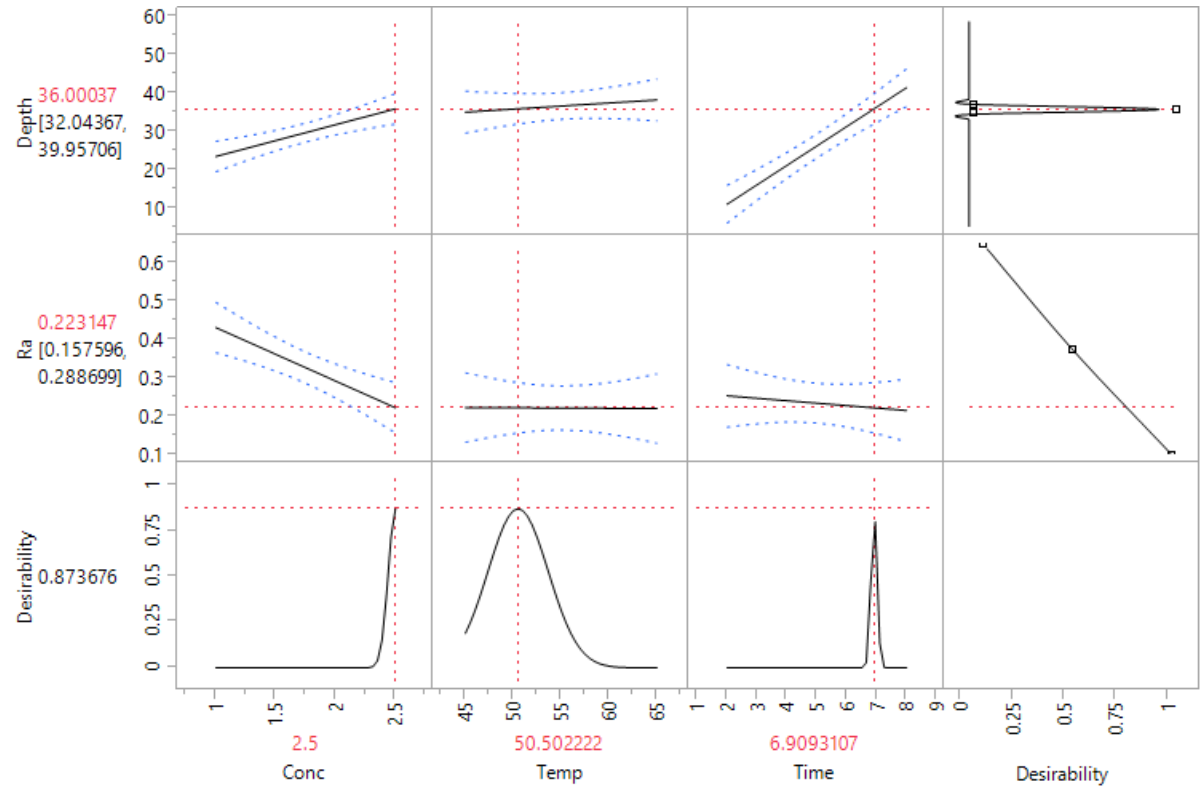

Figure 7.21 Optimization profile for Design 3 with a target value of 35±2 µm etch depth with minimum possible R_a Value by RSM

7.8.3 Modelling by Artificial Neural Network (ANN) and Optimisation

7.8.3.1 ANN Modelling

For ANN, a three-layer feed-forward neural network has been developed and trained by back-propagation gradient-descendent algorithm. The experimental data were randomly classified into two sets containing 53 and 27 data to be employed for training and validation respectively. Training data sets were used for updating weights and biases via Levenberg–Marquardt algorithm and the test data were utilized to evaluate the generalization ability of the trained network. A hyperbolic tangent sigmoid function and two linear functions were used as transfer functions for the neurons in the hidden layer and the neurons in the input and output layers respectively. The input and output layers had 3 and 2 neurons respectively. To determine the optimal number of neurons in the hidden layer, different topologies were examined during which the number of neurons varied between 3 and 15. Based on the values of R^2 and RMSE, 13 numbers of neurons were observed to be providing satisfactory results. Accordingly, ANN model has been developed with 3 inputs- 13 nodes mono hidden layer-2output concept as shown in Figure 7.22.

For this modelling purpose, 80 experiments have been carried out under different input parameters. Each of these input parameters are introduced to ANN structure by an input layer neuron. Experimental data sets have been used to train the ANN to make the general understanding of the model. Among the data sets, 2/3 of the data has been used for training ANN, while 1/3 is used for validation purpose. While training set is used to adjust the network weights and errors in each iteration, validation sets are used to optimize the ANN architecture with respect to number of neurons for the hidden layer. Based on the least mean square error as evaluation criterion, a structure of neural network with single hidden layer with thirteen nodes is observed to be appropriate one for ANN modelling as shown in Figure 7.23 and Figure 7.24. Correlation of training and validation datasets with the predicted values showed correlation coefficient>0.92 and >0.8 for etch depth and Ra respectively, indicating that the single layer thirteen neural nodes ANN model is sufficient to

explain the result satisfactorily. In Figure 7.23 the experimentally obtained values are indicated by data points and predicted values by lines.

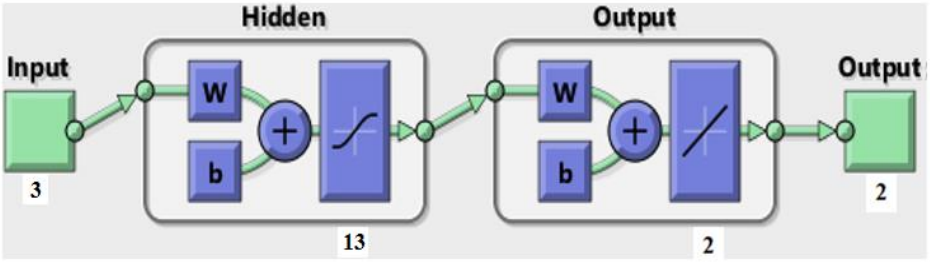

Figure 7.22 Structure of Neural Network

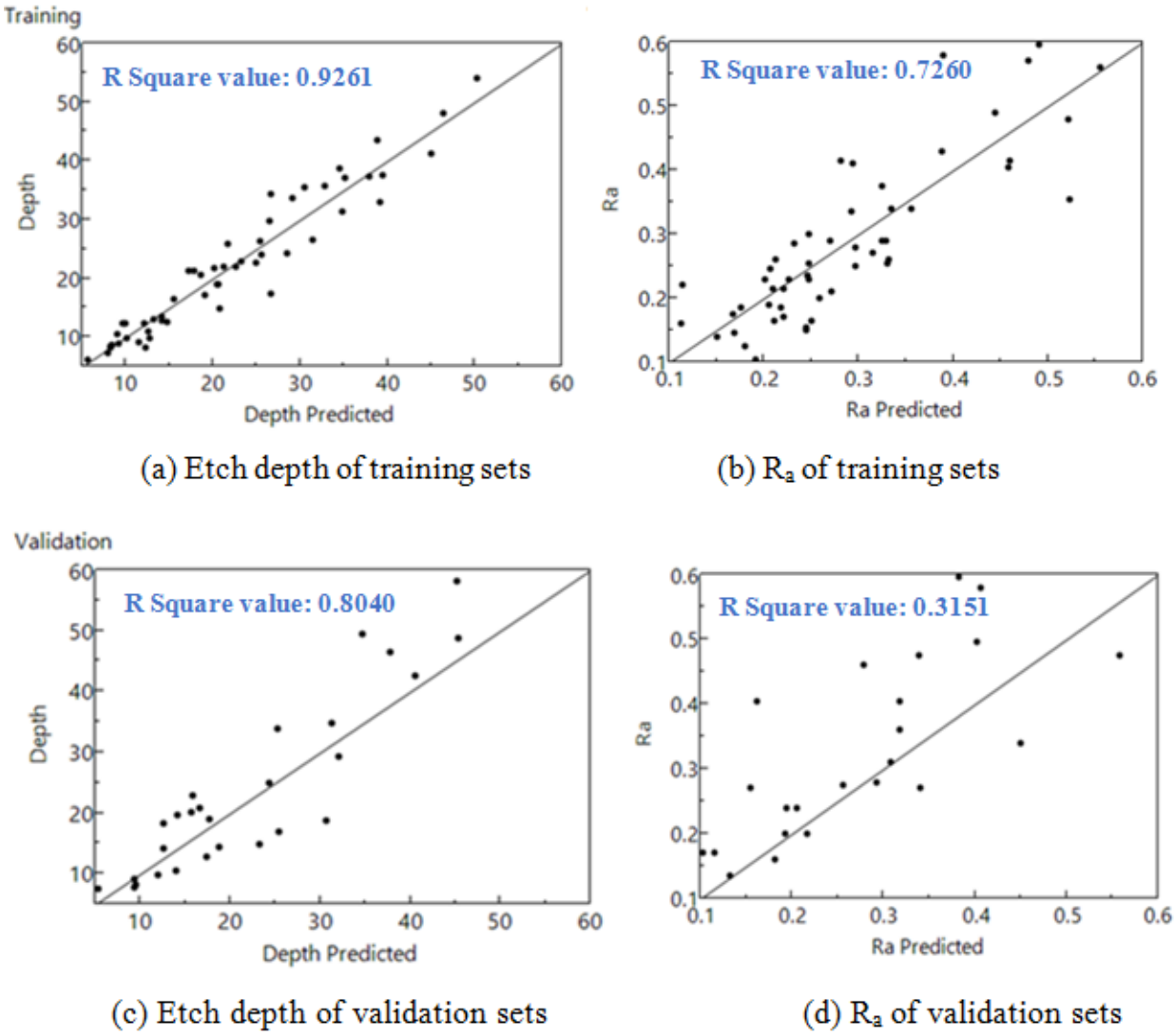

Figure 7.23 Prediction graph of actual values and predicted values

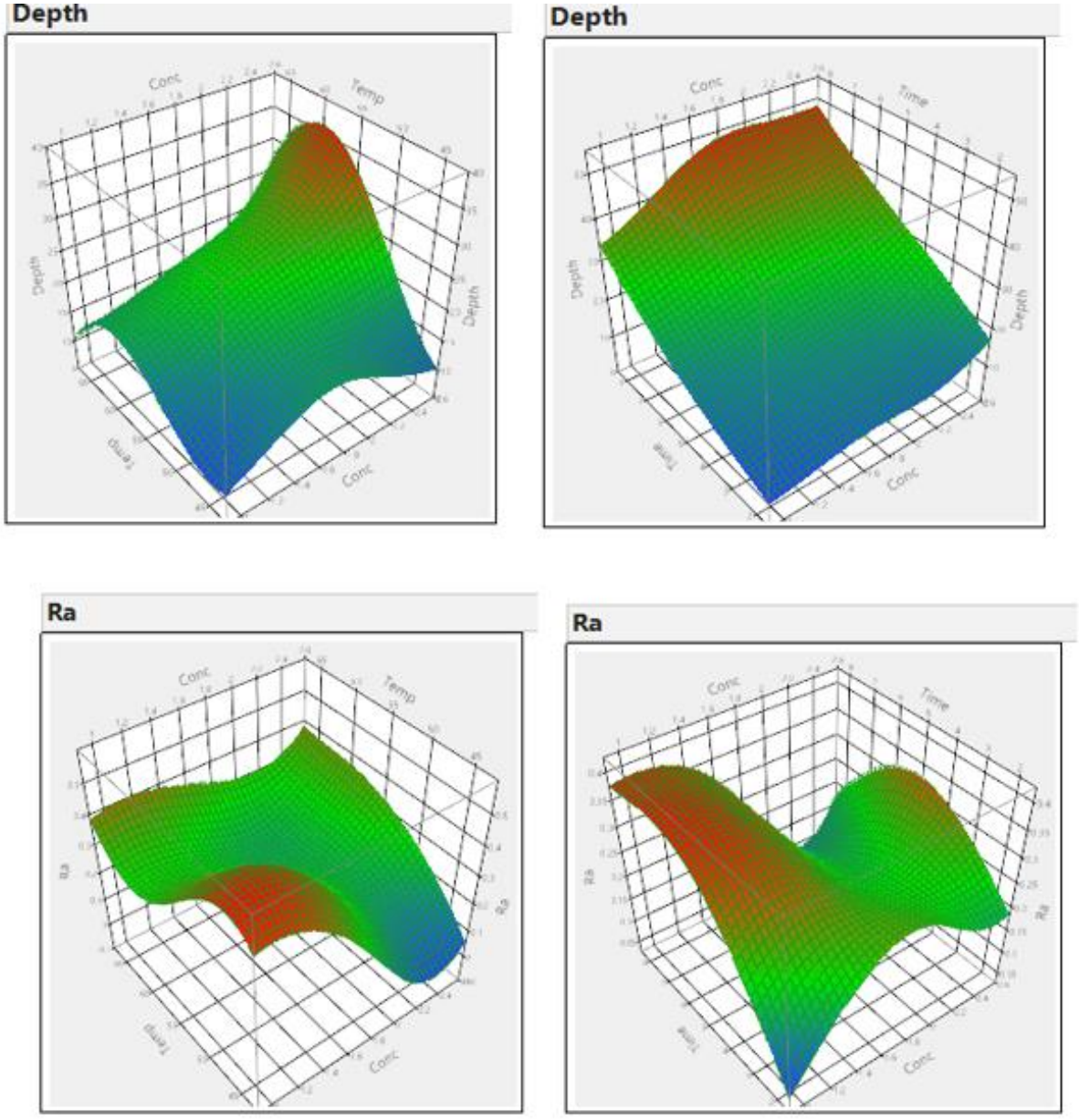

Figure 7.24 3D graphs showing the interaction effects of etching parameters on the dependent variables of etch depth and R_a value

7.8.3.2 Model optimization

To derive the optimal parameters with respect to etchant concentration, temperature and time for three target values of 25±2 µm, 30±2 µm and 35±2 µm etch depth and minimum surface roughness; 'optimization profiles' achieved after ANN model optimization are shown in the Figure 7.25, Figure 7.26 and Figure 7.27.

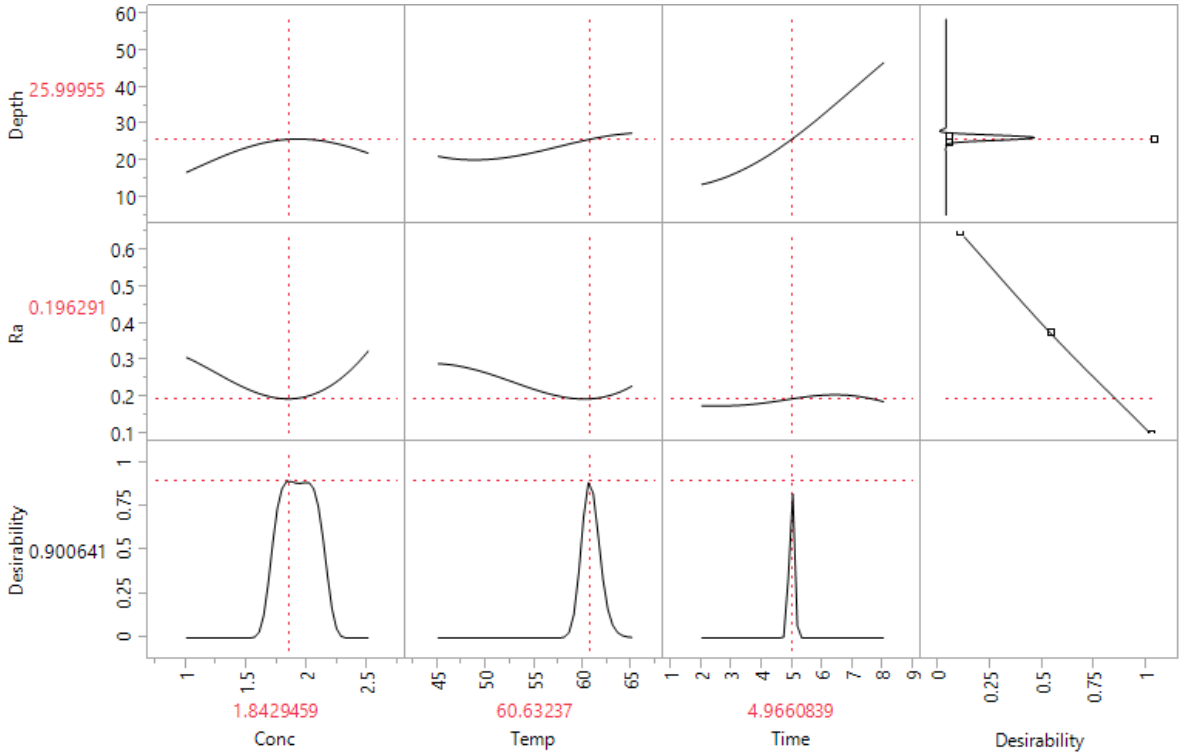

Figure 7.25 Optimization profile for Design 1 with a target value of 25±2 µm etch depth with minimum possible R_a Value by ANN

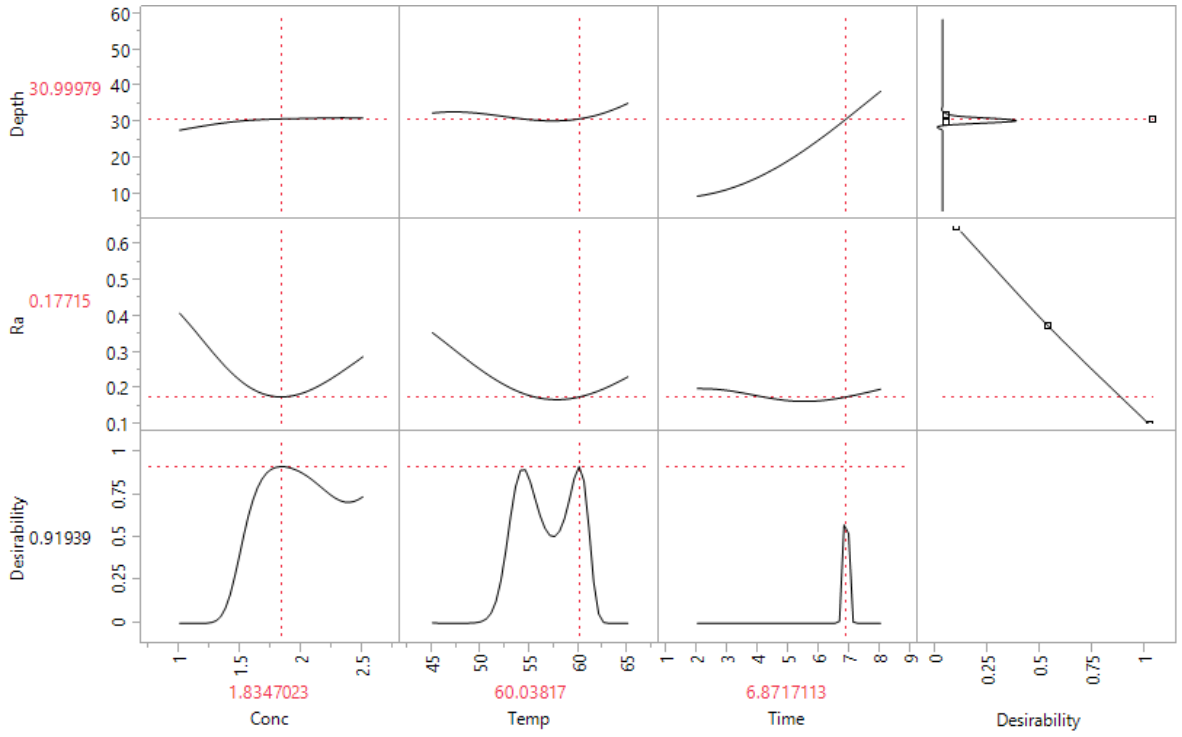

Figure 7.26 Optimization profile for Design 2 with a target value of 30±2 µm etch depth with minimum possible R_a Value by ANN

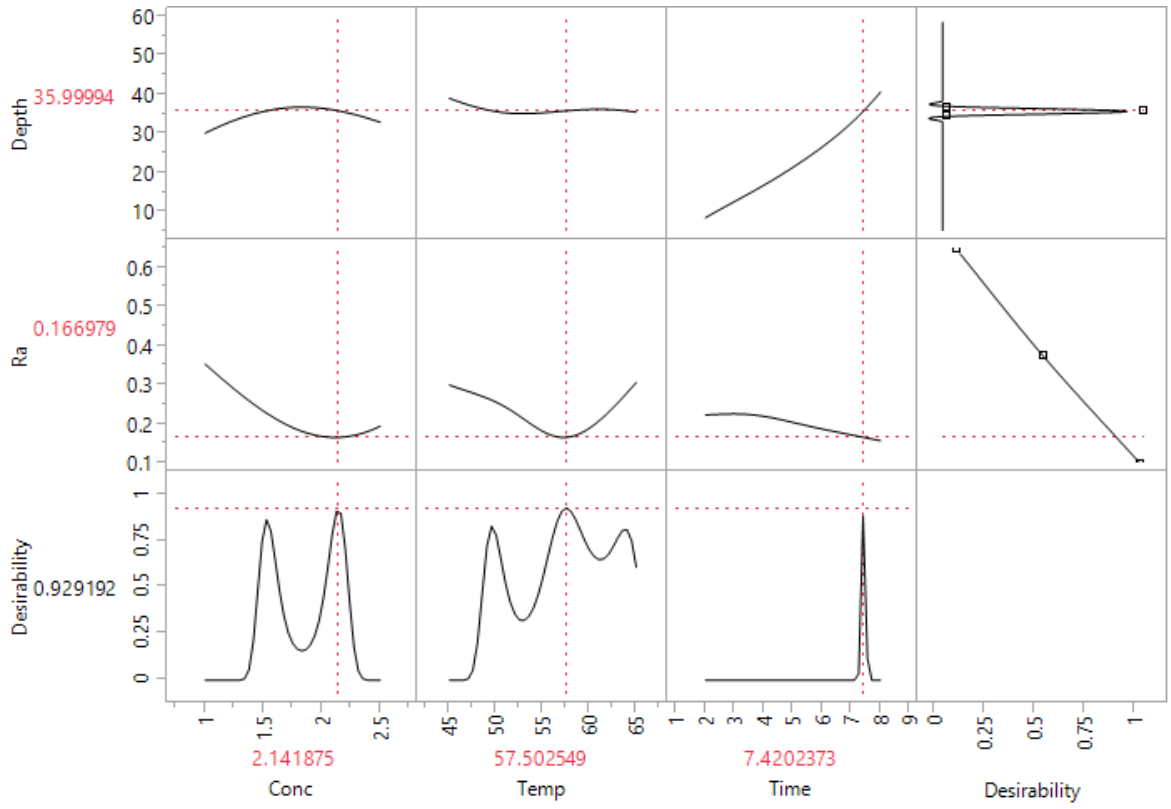

Figure 7.27 Optimization profile for Design 3 with a target value of 35±2 µm etch depth with minimum possible R_a Value by ANN

The optimized parameters achieved from the above 'optimization profiles' **(**Figure 7.25, Figure 7.26 and Figure 7.27**)** by ANN modelling for three target values of 25±2 µm, 30±2 µm and 35±2 µm etch depth and minimum surface roughness, are listed in Table 7.8.

Table 7.8 Achieved optimal parameters with respect to etchant concentration, temperature and etching time for 25±2 µm, 30±2 µm and 35±2 µm etch depth and minimum surface roughness by ANN Modelling

Optimized Parameter (units)	**Etch depth**		
	Design 1: 25±2 µm	**Design 2: 30±2 µm**	**Design 3: 35±2 µm**
Etchant concentration (M)	1.84	1.83	2.14
Temperature (°C)	60.63	60.03	57.50
Etching time (Minutes)	4.96	6.87	7.42

7.8.4 Validation of ANN Model

By comparing both the models RSM and ANN, it was observed that ANN model gives a better predictability which can be inferred from the higher R square values as shown in Table 7.9**.** However it is seen that the prediction capability for surface roughness is not very good for both the models**.**

Table 7.9 Comparison of R^2 Values of RSM and ANN Models

Targeted Parameters (units)	R^2 Values	
	RSM Model	ANN Model
Etch Depth (µm)	0.82	0.93
Surface roughness, Ra (µm)	0.42	0.73

As ANN model gives better predictability compared to RSM model, only ANN model was used for the experimental validation. Further experiments were conducted, to validate the prediction capability of ANN model, under the optimum experimental conditions for the three different sets of the target values of the etch depth and minimum possible R_a value. In order to validate the model for the three sets (Design1, Design 2 and Design 3) of targeted values as predicted by the ANN Model, three different etching experiments were conducted. Each one of these experiments was conducted at the process parameters (Concentration, temperature and etch time) predicted as the optimum values by the model. The experimentally obtained results on the etch depth (µm) and surface roughness values (R_a value in µm) are shown in Figure 7.28, Figure 7.29 and Figure 7.30.

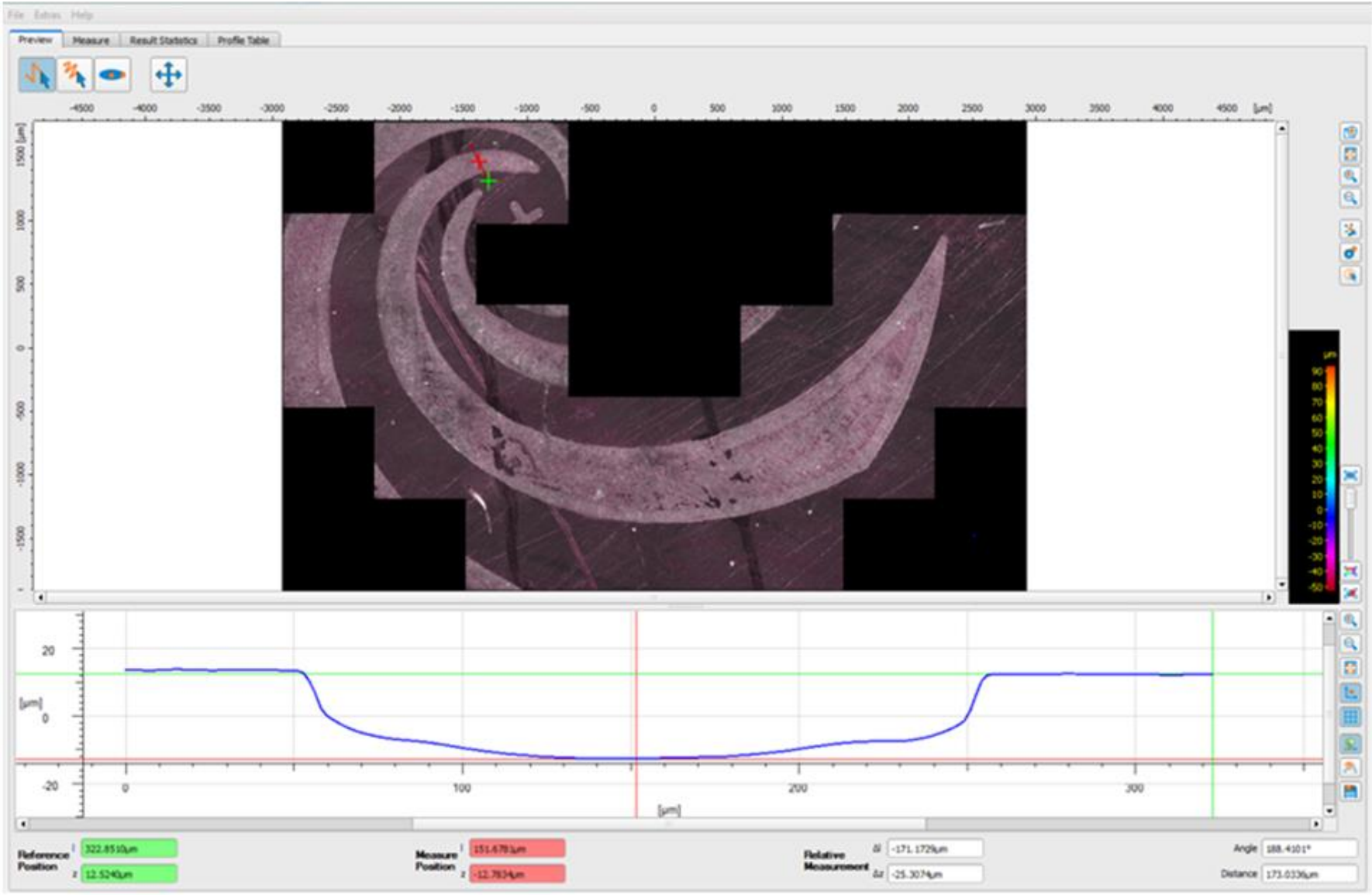

(a) Etch Depth Profile

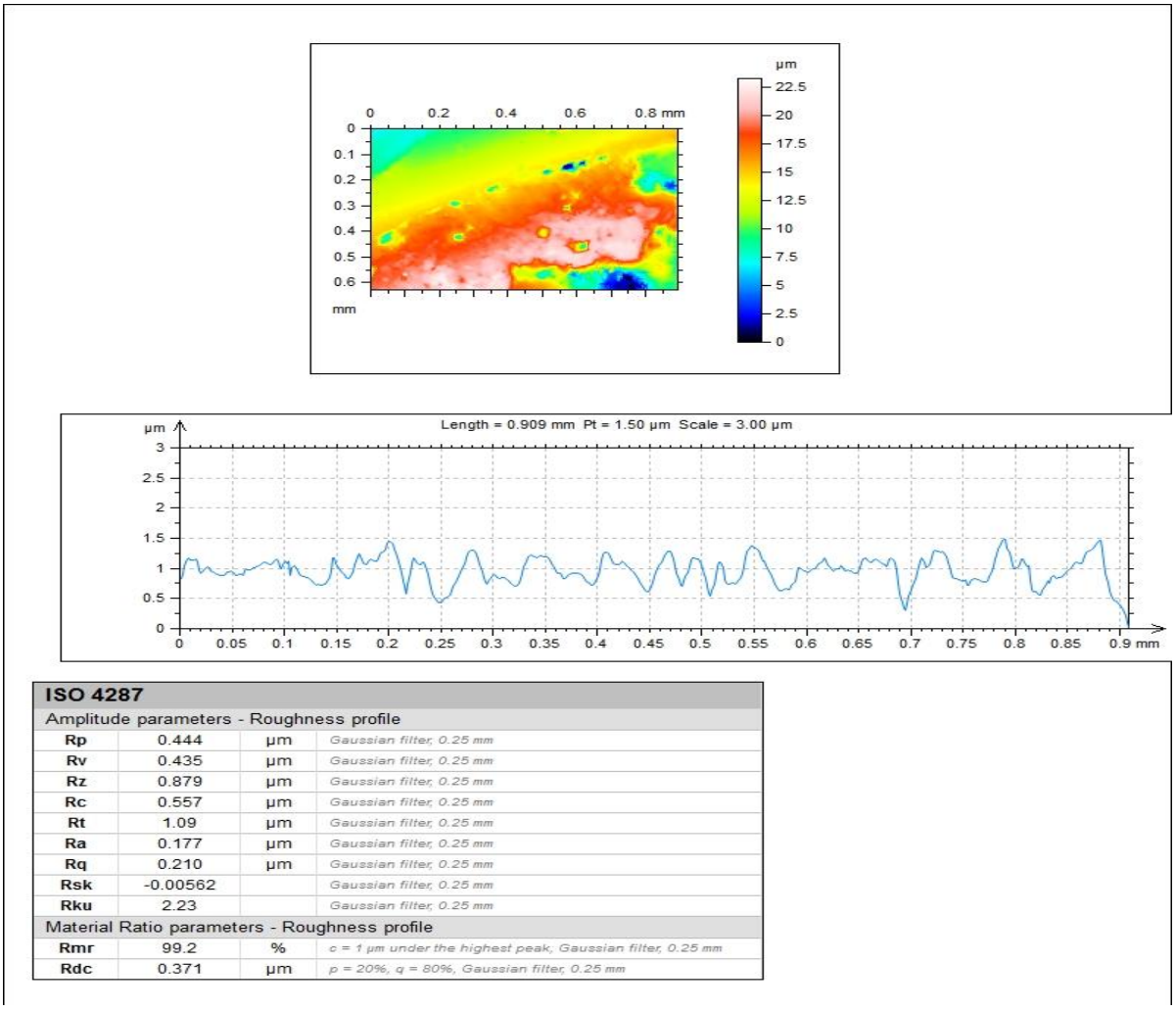

ISO 4287			
Amplitude parameters - Roughness profile			
Rp	0.444	µm	Gaussian filter, 0.25 mm
Rv	0.435	µm	Gaussian filter, 0.25 mm
Rz	0.879	µm	Gaussian filter, 0.25 mm
Rc	0.557	µm	Gaussian filter, 0.25 mm
Rt	1.09	µm	Gaussian filter, 0.25 mm
Ra	0.177	µm	Gaussian filter, 0.25 mm
Rq	0.210	µm	Gaussian filter, 0.25 mm
Rsk	-0.00562		Gaussian filter, 0.25 mm
Rku	2.23		Gaussian filter, 0.25 mm
Material Ratio parameters - Roughness profile			
Rmr	99.2	%	c = 1 µm under the highest peak, Gaussian filter, 0.25 mm
Rdc	0.371	µm	p = 20%, q = 80%, Gaussian filter, 0.25 mm

(b) Surface Roughness Profile

Figure 7.28 Experimental Validation Records for 'Design:1' of ANN

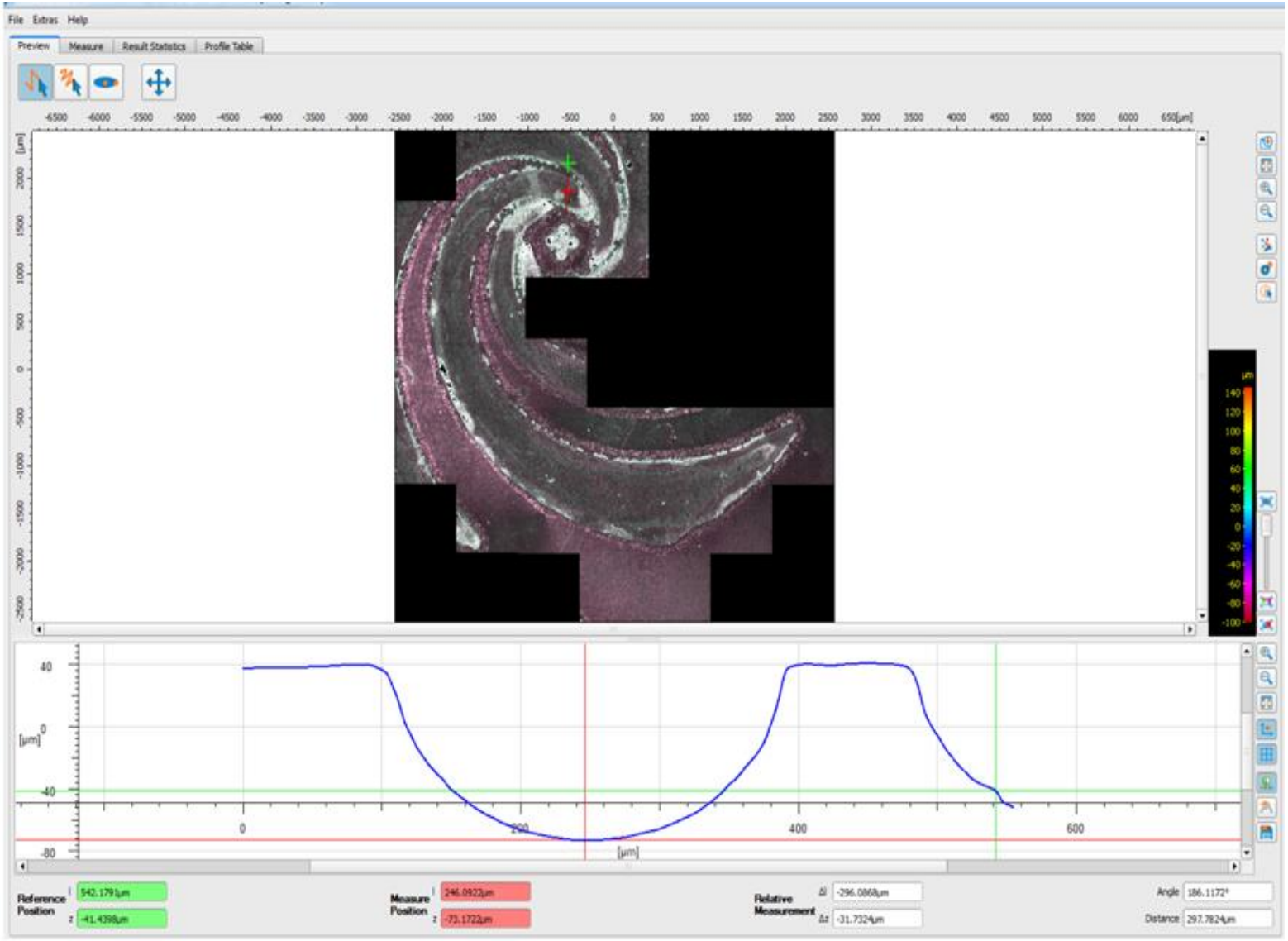

(a) Etch depth profile

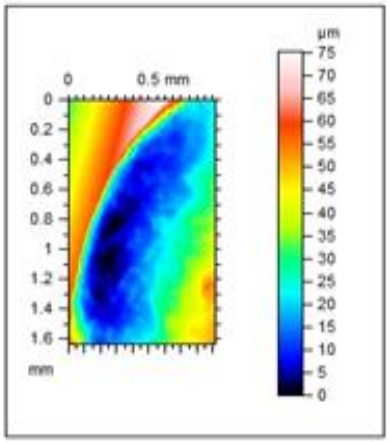

ISO 4287			
Amplitude parameters - Roughness profile			
Rp	1.09	µm	Gaussian filter 0.25 mm
Rv	0.671	µm	Gaussian filter 0.25 mm
Rz	1.76	µm	Gaussian filter 0.25 mm
Rc	0.677	µm	Gaussian filter 0.25 mm
Rt	1.85	µm	Gaussian filter 0.25 mm
Ra	0.263	µm	Gaussian filter 0.25 mm
Rq	0.343	µm	Gaussian filter 0.25 mm
Rsk	0.586		Gaussian filter 0.25 mm
Rku	3.66		Gaussian filter 0.25 mm
Material Ratio parameters - Roughness profile			
Rmr	37.3	%	c = 1 µm under the highest peak, Gaussian filter 0.25 mm
Rdc	0.420	µm	p = 20%, q = 80%, Gaussian filter 0.25 mm

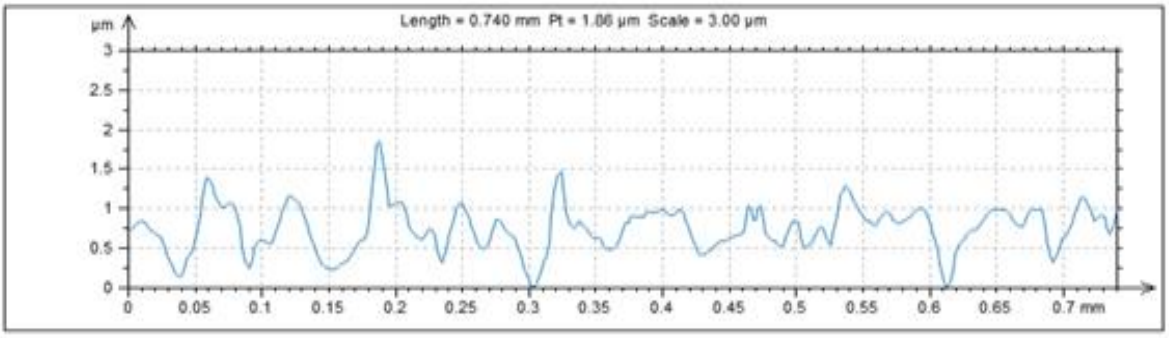

(b) Surface roughness profile

Figure 7.29 Experimental validation records for 'Design:2' of ANN

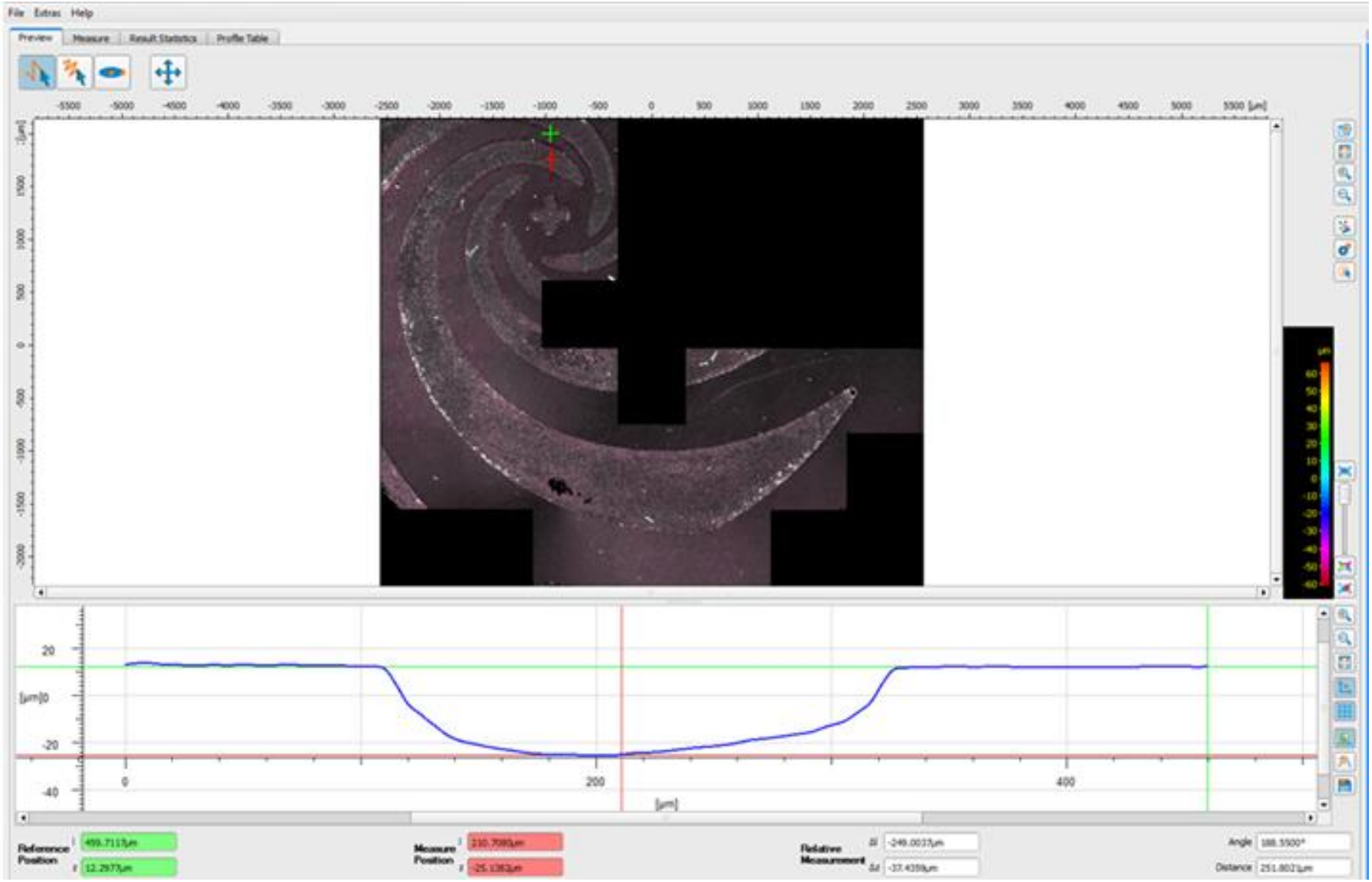

(a) Etch depth profile

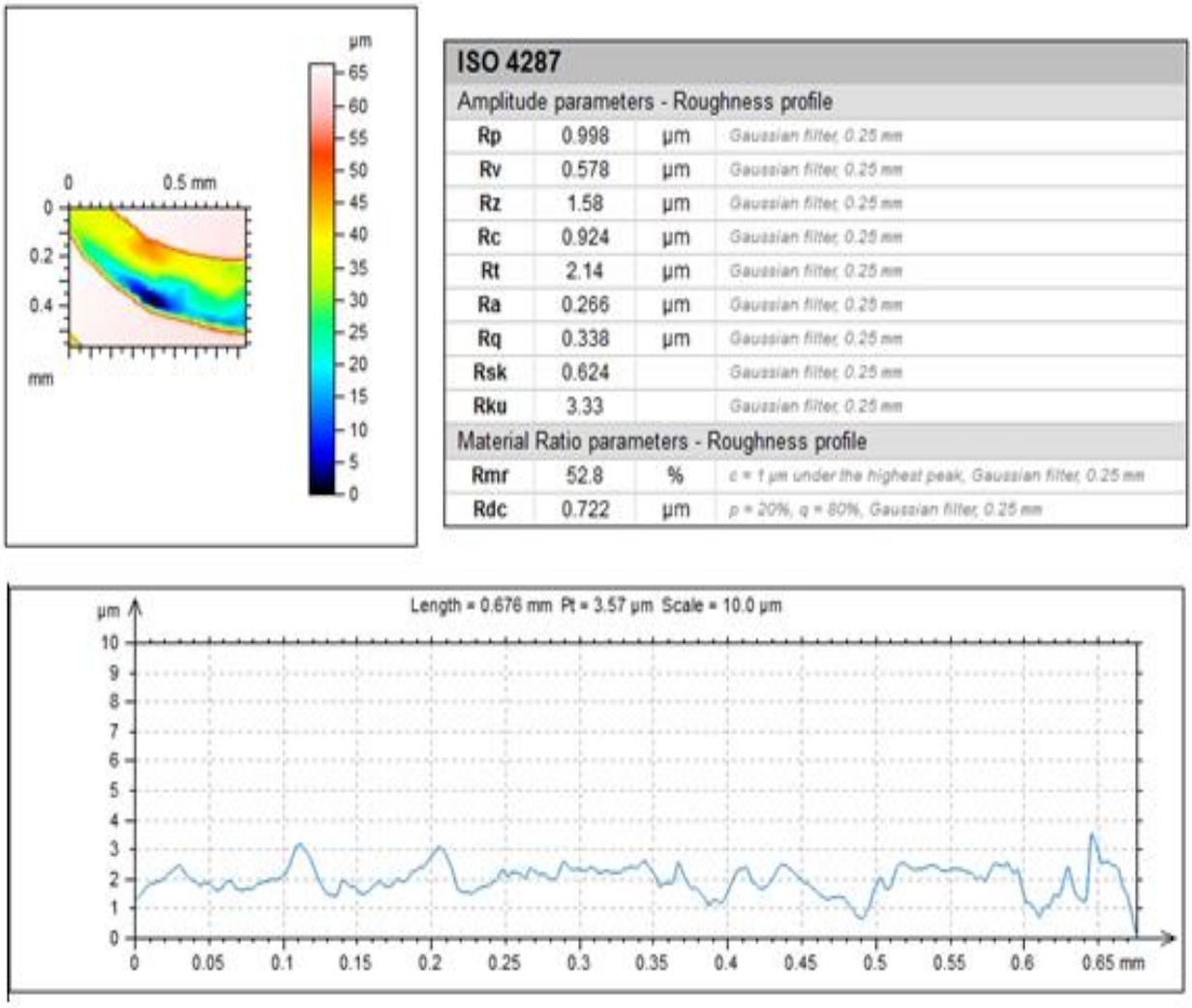

ISO 4287			
Amplitude parameters - Roughness profile			
Rp	0.998	µm	Gaussian filter, 0.25 mm
Rv	0.578	µm	Gaussian filter, 0.25 mm
Rz	1.58	µm	Gaussian filter, 0.25 mm
Rc	0.924	µm	Gaussian filter, 0.25 mm
Rt	2.14	µm	Gaussian filter, 0.25 mm
Ra	0.266	µm	Gaussian filter, 0.25 mm
Rq	0.338	µm	Gaussian filter, 0.25 mm
Rsk	0.624		Gaussian filter, 0.25 mm
Rku	3.33		Gaussian filter, 0.25 mm
Material Ratio parameters - Roughness profile			
Rmr	52.8	%	c = 1 µm under the highest peak, Gaussian filter, 0.25 mm
Rdc	0.722	µm	p = 20%, q = 80%, Gaussian filter, 0.25 mm

(b) Surface roughness profile

Figure 7.30 Experimental validation records for 'Design:3' of ANN

7.8.4.1 Experimental Validation of the Etch Depth Predicted

The compilation of the experimental results on etch depth, covered in Figure 7.28, Figure 7.29 and Figure 7.30. is given below in Table 7.10. This table shows the extent of agreement of the targeted values of etch depth predicted by the ANN Model with those of the experimentally obtained results. As can be seen from the table for all the three Design sets, the relative deviation of the predicted value from the experimental values is well within 4%, which shows that prediction capability for etch depth is very good.

Table 7.10 Comparision of Etch Depth (µm) Predicted by the ANN Model with Experimental Results

Design No. (Targeted Value)	Optimum Parameters predicted by ANN for experimental study			Experimental value (µm)	Predicted Value (µm)	Relative Deviation %
	Etchant concentration (M)	Temperature (^oC)	Etching Time (min)			
1 (25±2 µm)	1.8	60.6	4.9	25.307	25.999	2.73
2 (30±2 µm)	1.8	60.0	6.8	31.732	30.999	-2.31
3 (35±2 µm)	2.1	57.5	7.4	37.435	35.999	-3.83

7.8.4.2 Experimental Validation of the Surface Roughness

The compilation of the experimental results on surface roughness (Ra value in µm), covered in Figure 7.28, Figure 7.29 and Figure 7.30. is given below in Table 7.11**.** This table shows the extent of agreement of the targeted values of surface roughness (R_a value in µm), predicted by the ANN Model with those of the experimentally obtained results. As can be seen from the table for all the three Design sets, the relative deviation of the predicted value from the experimental values is well within 40%, which shows that prediction capability for surface roughness is not very good.

Table 7.11 Comparision of Surface Roughness (µm) Predicted by the ANN Model with Experimental Results

Design No. (Targeted Value)	Optimum Parameters predicted by ANN for experimental study			Experimental value (µm)	Predicted Value (µm)	Relative Deviation %
	Etchant concentration (M)	Temperature (^oC)	Etching Time (min)			
1 . Least possible value	1.8	60.6	4.9	0.177	0.196	10.73
2 . Least possible value	1.8	60.0	6.8	0.263	0.177	-32.69
3 . Least possible value	2.1	57.5	7.4	0.266	0.166	-37.59

7.9 Outcome of Research work in Chemical Etching

The chemical etching process to generate micro grooves on the DTM manufactured CuBe alloy component is optimised to get the desired groove depth and lowest possible Ra value. As part of this research work, few other changes were introduced in the manufacturing of SSGB which are shown below in Table 7.12. These modifications have enabled the production of superior quality SSGB components in large numbers, with consistent quality.

Table 7.12 Modifications Introduced in Manufacturng Process of SSGB

S. No.	Process flow sheet for 'SSGB spiral grooves- generation' on DTM machined spherical cups of CuBe material	Manufacturing Process steps followed before taking up the research work	Modifications incorporated for enhancing quality and productivity as part of the present Research work
1.	Ultrasonic cleaning by Ethoxy Ethanol as cleaning agent	The spherical cups were dipped in ultrasonic chamber filled with Ethoxy Ethanol (LR grade). After cleaning the cups were removed one by one by an holder. This process was time consuming.	Cleaning agent is replaced by Ethoxy Ethanol (AR grade) as the LR grade is diminishing the surface finish of DTM machined surface. The cups were held in a jig which can hold 60 no's of cups and the jig is dipped into ultrasonic cleaning chamber. This reduced the time during removal of cups after cleaning process.
2.	Water rinsing to remove traces of cleaning agent	DM water was used for rinsing. The cups were held one by one and dipped into the beaker with DM water and agitated manually. This process was time consuming.	Jet cleaning fixture is used for the process. A batch of 60 no's of cups are fixed on to the fixture and a jet of UHQ water is directed by array of nozzles on to the cup for cleaning.
3.	Drying to remove water trapped in spherical cup and centre hole	Drying was done by arranging the cups on a surface and blowing hot air over the components followed by wiping by absorbent paper. This procedure was time	A vacuum chamber is fabricated and a jig which can hold 60 no's of cups is placed in the vacuum chamber. The chamber is evacuated to the order of 1×10^{-2} mbar which enabled a thorough job

S. No.	Process flow sheet for 'SSGB spiral grooves- generation' on DTM machined spherical cups of CuBe material	Manufacturing Process steps followed before taking up the research work	Modifications incorporated for enhancing quality and productivity as part of the present Research work
		consuming and possibilities of dust getting deposited on the surface.	of vacuum drying.
4.	Photo resist polymer coating	Photo resist coating is done by dip method. The cups are dipped one by one into the photo resist and held for 10 second and removed and placed for drying.	No change in the process is employed.
5.	Drying of polymer coating	The coated cups are placed on a surface and allowed to dry by natural circulation of air	The coated cups are held on a jig and placed in vacuum chamber. The chamber is heated by electric coil to a temperature of 40degC and the chamber is evacuated to 1×10^{-2} mbar.
6.	Photo Ablation by exposing KrF Excimer Laser over the groove pattern	Laser lithography technique is used for pattern transfer from 2- dimensional laser mask to 3-dimensional spherical surface. Polymer ablation by Excimer laser is done in projection mode. The jewel is exposed to 3000 Nos. of pulses	To prevent the ablated products to deposit on the projection lens, a gas purging fixture is fixed to the projection head. The fixture has two ports, H_2 gas is purged into the chamber by one port, which provides a reducing gas atmosphere for ablation and also acts as driver gas to drive

S. No.	Process flow sheet for 'SSGB spiral grooves- generation' on DTM machined spherical cups of CuBe material	Manufacturing Process steps followed before taking up the research work	Modifications incorporated for enhancing quality and productivity as part of the present Research work
		at 20Hz keeping the Laser gun at 400mJoule of pulse energy (measured at the exit of the Laser Source). The ablated products got deposited on the projection lens thereby reducing the energy fluence on the job	away the ablated products, the other port is connected to vacuum pump to evacuate the ablated products mixed with the purging gas. Ablation is done in 1500 pulses with 400mJoule energy(measured at the exit of the Laser Source). This helped in increasing the productivity as well as reducing the operating cost of the laser micromachining system, exposure time is reduced.
7.	Chemical Etching of ablated region to form spiral groove pattern	Chemical Etching is done by dipping the ablated cups in Ferric Chloride solution with controlled temperature and time duration. The etchant was heated by hot plate by continuously monitoring the temperature by a dipped thermometer and the cups were agitated manually after a	The hot plate is replaced by a programmable heater cum stirrer (magnetically coupled Teflon coated stirrer) with for agitation. The coated cups were dipped into the beaker and were placed on the programmed heater cum stirrer with set temperature and time.

S. No.	Process flow sheet for 'SSGB spiral grooves- generation' on DTM machined spherical cups of CuBe material	Manufacturing Process steps followed before taking up the research work	Modifications incorporated for enhancing quality and productivity as part of the present Research work
		particular time interval.	
8.	Stripping of Photo Resist coat from non-ablated region by Ethoxy Ethanol as cleaning agent	Stripping of PR coating was done by dipping the cups in a beaker containing ethoxy ethanol and allowing for PR coating to peel off from the cup. Then the cups were removed one by one and cleaned by wiping with absorbent paper.	No change in the process is employed
9.	Water washing to remove traces of cleaning agent	DM water was used for rinsing. The cups were held one by one and dipped into the beaker with DM water and agitated manually. This process was time consuming.	Jet cleaning fixture is used for the process. A batch of 60 no's of cups are fixed on to the fixture and a jet of UHQ water is directed by array of nozzles on to the cup for cleaning
10.	Drying, Inspection and Testing	The coated cups are placed on a surface and allowed to dry by natural circulation of air. Visual inspection was done using a stereo zoom microscope and testing for	Drying is done in vacuum chamber which reduced time and effort and increased productivity. Visual inspection using optical zoom

S. No.	Process flow sheet for 'SSGB spiral grooves- generation' on DTM machined spherical cups of CuBe material	Manufacturing Process steps followed before taking up the research work	Modifications incorporated for enhancing quality and productivity as part of the present Research work
		deceleration was done at the Final HSR Assembly Clean Room	microscope with digital display for effortless and accurate inspection. Test set up with graphical display of test parameters is built to carryout deceleration test, which is the ultimate functional Test for acceptance of the SSGB.

7.10 Testing with Modified Process

The modified manufacturing procedure as detailed in Table 7.13 was employed for the large scale manufacture of SSGB's. After the optimisation of the SSGB etch depth and Ra values, the micro-grooved parts were produced using the optimised etching parameters of concentration, temperature and etching time. SSGB's produced in such optimised process parameters were characterized and subsequently deployed for the assembly of HSR Machines. HSR machines using such SSGB's were finally subjected to performance tests. As part of this, the HSR Machine was accelerated to a specified speed and then the power supply to the Machine was switched off. The rate at which the machine decelerate was recorded in 'Hz /sec'. The other operating conditions of the HSR machine kept unchanged, the angular deceleration value in 'Hz /sec', would be a parameter of the SSGB performance. Lower the deceleration value, better the performance of the HSR machine and in turn that of the SSGB.

The final outcome of the research work in the area of both laser ablation and chemical etching has been put to the application area of SSGB for HSR machines. A snapshot of the test set-up wherein the performance of SSGB's manufactured using the technology evolved from this research work is shown in Figure 7.31. This figure shows just the bottom part of the HSR machine, showing the location of the SSGB within the machine. The control panel houses the Variable Frequency Drive (VFD) for driving the motor of the HSR machine. The instrumentation required to process the rotational speed data received from the HSR machine, was provided as part of the control panel. From the real time data on the 'speed vs. time' the angular deceleration values were computed and displayed.

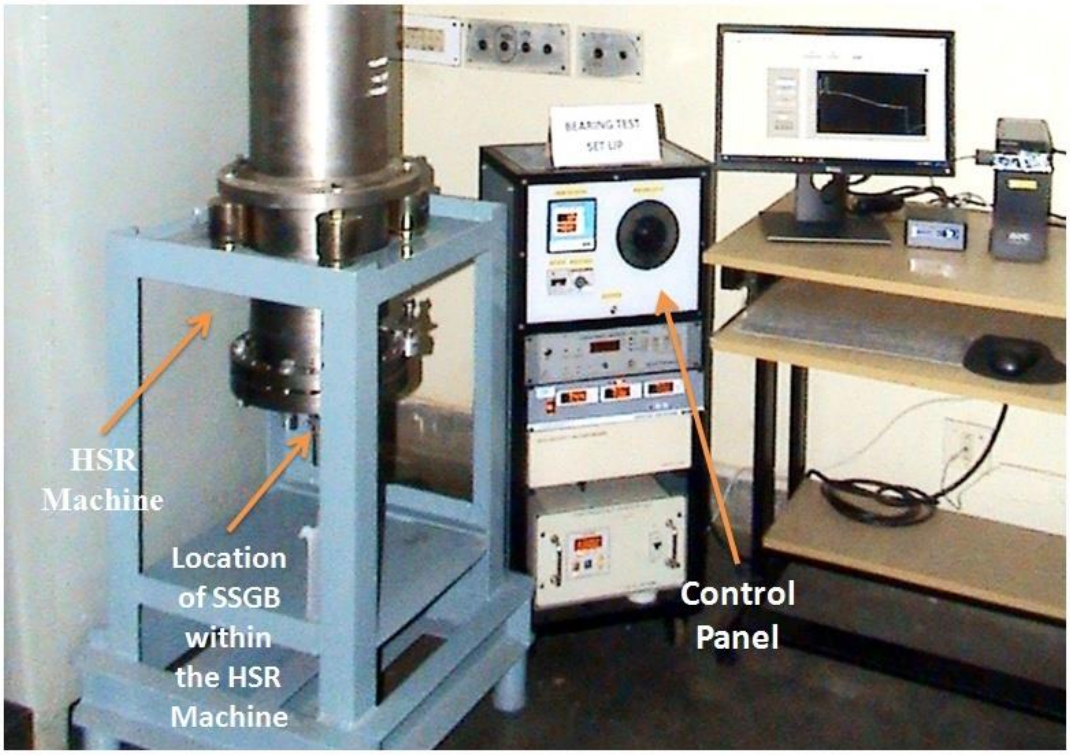

Figure 7.31 SSGB Performance Test Setup to Measure the Deceleration Value

Figure 7.32 (a) shows the mean value of the HSR machine deceleration (On the Y-axis) for a large no. of HSR machines. These mean deceleration values were computed for two types of HSR machines. One with SSGB's produced using the old technology and the other one with new (modified) technology. It also shows the enhanced performance level, accomplished by employing findings of the present research work. Figure 7.32 (b) shows the distribution and spread of the deceleration values for a large no. of HSR machines using old technology and the same is shown for new (modified) technology in Figure 7.32 (c) . The lower spread values and a shift towards lower deceleration value shows the enhanced performance as well as higher no. of HSR machines being accepted, compared to those of the old technology. This improvement has resulted in raising acceptance percentage from the earlier level of 35% to the current level of 98%.

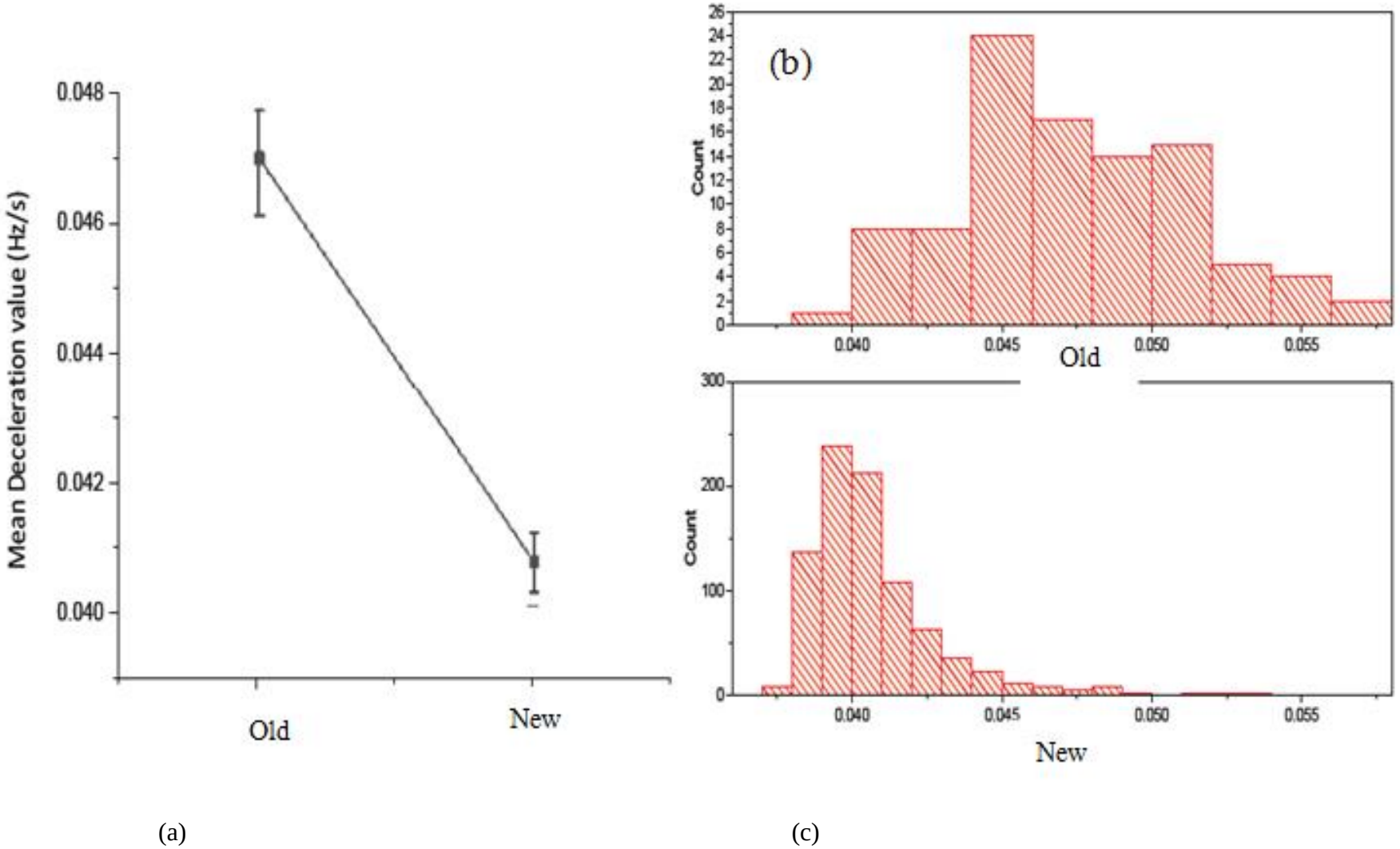

Figure 7.32 Performance Indicators and their spread: Old and New Techniques

Based on experimental study of chemical etching carried on CuBe alloy and Cu, it is found that CuBe alloy has better surface finish than Cu. Beryllium rich surface layer is formed on CuBe alloy after CMM.

7.11 Summary

- Cu-Be alloy showed better surface finish (0.5 μm) for both cupric chloride and ferric chloride etchants.
- Cu showed very poor surface finish with Ferric chloride compared to cupric chloride.
- CuBe alloy does not show significant change in surface finish, irrespective of etchant.
- GDOES study showed that Etched surface of CuBe alloy is having Be rich composition (2.2%) indicating surface is modified with high Be alloy, resulting in a higher hardness protective layer which is an advantage for SSGB functioning.
- This study provided information as to what condition the chemical milling is to be carried out to meet the performance criteria SSGB
- Acceptance level of SSGB increased substantially.

Chapter 8
Conclusions

The experimental and numerical investigations of excimer laser lithography under different gaseous media gives a novel finding about the effect of hydrogen gas on ablation of photo-resist polymer. On the basis of the present research work, following main conclusions can be drawn:

1. Excimer laser ablation of photoresist polymer under hydrogen media helps in enhancing the form and edge definition on the workpiece.

2. The presence of hydrogen media during excimer laser ablation of polymer results in a haze-free (absence of carbonaceous soot) ablation of the workpiece surface.

3. It has been found that material removal rate (MRR) is highest in case of hydrogen gas environment compared to other gaseous media while carrying out the ablation of photoresist polymer with excimer laser.

4. The increased MRR under hydrogen environment could be explained by a new phenomenon of Laser Assisted Chemical Reaction (LACR).

5. The LACR phenomenon is proposed, based on the simulation result which shows that inappreciable heating of the polymer surface occurs during excimer laser ablation under H_2 gas environment.

6. Owing to increased material machining rate, operating cost cam be considerably brought down for the laser micromachining system due to reduced consumption of the expensive pre-mix gas mixture.

7. Five different regression models namely, LR, GPR, Cubic SVM, RSM and ANN have been trained and validated. Except LR, all other models are able to predict the ablation depth quite accurately.

8. Chemical Micromachining (CMM) of the excimer laser ablated workpiece was carried under optimised chemical micro machining conditions which yielded better surface finish and desired etch depth on workpiece.

9. The optimized chemical micro machining conditions (etchant concentration, temperature and etching time) have been obtained by ANN and RSM models.

10. The processes developed during this research work has been applied to manufacture SSGB, which increased its acceptance from 35% to 98% and reduced the deviation from desired performance parameter (deceleration value) of HSR machines.

8.1 Scientific Contributions of Present Research

A new phenomenon of Laser Assisted Chemical Reaction (LACR) of polymer with hydrogen gas in presence of laser beam at the polymer hydrogen gas interface is observed to be the scientific reason behind the experimental observation of higher MRR.

Direct Impact of this work on hydro dynamic bearing: A consistently enhanced performance value and increased acceptance rate of 98% was obtained by adopting the techniques developed by this research work.

Major outcome of this research work

New hybrid process of Excimer Laser micromachining of photo resist polymer under hydrogen gas environment, followed by chemical micromachining of Cu-Be workpiece was developed. Using this technology, more than large numbers of Cu-Be SSGBs having

consistent quality with regard to microgroove geometry (depth, edge definition and uniformity in the groove depth) resulting in enhanced acceptance and improved performance indicator for the HSR machines have been accomplished.

CMM process has been optimised using both RSM and ANN modelling for its input parameters of etchant concentration, temperature and time to get the objective function of targeted etch depth and minimum surface roughness of the order of 200 nm.

The newly developed ELM process under hydrogen gas environment has got potential application in a wide field of microfabrication which also include semiconductor industry.

8.2 Future Scope of Work

- Molecular Dynamic Simulation (MDS) of the excimer laser ablation under hydrogen gas environment.
- Study of ablation process using different type of excimer laser (ArF, F2, XeCl etc.) under hydrogen gas or mixture of gases.
- Present study can be extended to cover wide range of photoresist polymers.
- Experimental study on the chemical micromachining to find out the mechanism of mass removal of Cu-Be alloy vis-a-vis Cu, which results in a better surface roughness.
- GDOES Characterization of etched surface of CuBe alloy and the investigations of the mechanism behind the Be-enriched surface of workpiece.
- Optimization process variables for chemical micromachining of CuBe using $CuCl_2$ etchant to achieve desirable etch depth and lowest possible surface roughness value.

References

[1] Benedict G. F., Non-traditional Manufacturing Processes, Mercel Decker Inc., New York, 1987, 1-4.

[2] McGeough J. A., Advanced Methods of Machining, Chapman and Hall Ltd., London, 1988, 6-8.

[3] https://www.researchgate.net/figure/Schematic-representations-of-a-centrifuge-rotor-left-and-gas-centrifuge-right-Based_fig1_279715352.

[4] Excimer Laser Technology: Laser Sources, Optics, Systems and Applications, Lambda Physik AG, Gottingen, 2001, ISBN 3-00-0063951-1.

[5] Basting D., Excimer Laser Technology, Lambda Physik, 2001.

[6] Maiman T. H., Stimulated Optical Radiation in a Ruby, Nature, 1960, 187:493-494

[7] Schawlow A. L., Science, 1965, 149:13

[8] Longo L., Window on the Laser Medicine World, SPIE, 2000

[9] Bütje R., Abtragen von,Metallenmit, Excimer-Lasernals Verfahrenzur Mikrobear-beitung, IFW, 1992.

[10] Milloni P. W., Eberly J. H., Lasers, John WIley and Sons, 1988

[11] Srinivasan R., Mayne-Banton V., Appl Phys Lett, 1982, 41:576.

[12] Garrison B. J., Srinivasan R., Laser Ablation of Organic Polymers: Microscopic Models for Photochemical and Thermal Processes, J Appl Phys 1985, 57:2909–2914.

[13] V. Srinivasan, Mark A. Smrtic, S. V. Babu, Excimer Laser Etching of Polymers, J. Appl. Phys. 1986, 59 (11):3861-3867.

[14] Desbiens J. P., Masson P., ArF Excimer Laser Micromachining of Pyrex, Sic and PZT for Rapid Prototyping of MEMS Components, Sensors and Actuators A, 2007, 136:554-563.

[15] Dyer P. E., Excimer Laser Polymer Ablation: Twenty Years, Appl. Phys. A, 2003, 77:167-173.

[16] Klotzbach U., Andrés F. L., Panzner M., Franke C., Laser Micromachining, Advanced Structured Materials 2011, DOI 10.1007/978-3-642-17782-8_2.

[17] Fedosejevs R, Argument M, Sardarli A, Kirkwood S E, Holenstein R, Tsui Y Y, Laser Micromachining for Microfluidic, Microelectronic and MEMS Applications. Proceedings International Conference on MEMS, NANO and Smart Systems, 2003, page 53, DOI10.1109/ICMENS.2003.1221964.

[18] Chen Z., Fu X., Geng N., Hu X., Effects of Parameters in Femtosecond Laser Micromachining on Ablation of Silicon, Transactions of Tianjin University, 2009, 15(3):225–228.

[19] Li J., Ananthasuresh G. K., A Quality Study on the Excimer Laser Micromachining of Electro-Thermal-Compliant Micro Devices, J. Micormech, Microeng, 2001, 11:38-47.

[20] Klotzbach U., Lasagni A. F., Panzner M., Franke V., Fabrication and Characterization in the Micro-Nano Range, Advanced Structured Materials, Laser Micromachining, Springer-Verlag Berlin, Heidelberg, 2011, 10:29-46.

[21] Friedrich J. F., Mix R., Schulze R. D., Asmus M. P., Joshi R., New Plasma Techniques for Polymer Surface Modification with Monotype Functional Groups, Plasma Processes and Polymers, 2008, 5(5):407-423.

[22] Tönshoff H. K., Hesse D., Mommsen J., Micromachining Using Excimer Lasers, CIRP Annals, 1993, 42:247-251.

[23] Dyer P. E., Bond I. W., Jackman R. B., Laser Ablation of Polymer; Photochemical Processing of Electronic Materials, Academic Press Limited, London, 1992, 360-385.

[24] Kuhnke M., Cramer L., Dickinson J. T., Lippert T., Wokaum A., Study of Photoreaktive Polymers Ablated by F_2 Excimer Laser, Poster at COAL, 2003.

[25] Lippert T. Dickinson, Hauer M., Kopitkovas G., Langfold S. C., Masuhara H., Nuyken O., Debris Formation by Excimer Laser Ablation, Appl. Surf. Sci., 2002, 197:746-756.

[26] Hauer M., Funk D. J., Lipper T., Wokaun A., Study of Excimer Laser Ablation of TP Material, Applied Surface Science, 2003, 208:107-112.

[27] Perrie W., Gill M., Robinson G., Fox P., Neill W., Femtosecond Laser Micro-Structuring of Aluminium Under Helium, Applied Surface Science, 2004, 230:50-59.

[28] Ju Sun, John P. Longtin, Effects of a Gas Medium on Ultrafast Beam Delivery and Materials Processing, J. Opt. Soc. Am. B., 2004, 21(5):1081-1088.

[29] Dowding C. F., Lawrence J., Ablation Debris Control by Means of Closed Thick Film Filtered Water Immersion, Proceedings of the Institution of Mechanical Engineers, Part B: Journal of Engineering Manufacture, 2009, 224:753 – 768.

[30] DemirG. Ali, Previtali B., Dross-free submerged laser cutting of AZ31 Mg alloy for biodegradable stents, Journal of Laser Applications, 2016, 28(3)2001-2012.

[31] Ricciardi G., Cantello M., Savant Aira G., Marking of Computer Keyboard by Means of Excimer Lasers, CIRP Annals, 1996, 45:191-196.

[32] Morshedian Nader, Specifications of Nanosecond Laser Ablation with Solid Targets, Aluminium, Silicon Rubber, and Polymethylmethacrylate (PMMA), Plasma Science and Technology, 2017, 19:1-8.

[33] Klotzbach, U., Hauptmann, J.,Potenzial der Mikromaterialbearbeitungmit UV-Lasernfürdie Photovoltaik; Laserphotonics, Carl Hanser Verlag GmbH and Co. KG, 2008.

[34] Lazare S., Vincent G., Ultraviloet Laser Photoablation of Polymers: A Review and Recent Results, Laser Chem., 1988, 10:25-40.

[35] Crafer R., Peter J., Excimer Lasers by M. C. Gower, Laser Processing in Manufacturing, Springer, Chapman and Hall, London, 1993, 163-271.

[36] Srinivasan R, Braren B., Dreyfus R. W., Ultraviolet laser ablation of polyimide films, JAppl Phys 1987, 61(1):372–376.

[37] Tian Long See, Zhu Liua, Lin Lib, Xiang Li Zhong, A Comparison of the Characteristics of Excimer and Femtosecond Laser Ablation of Acrylonitrile Butadiene Styrene (ABS), Applied Surface Science, 2016, 364:467–476.

[38] Knowles M.R.H., Rutterford G., Karnakis D., Ferguson A., Micro-machining of Metals, Ceramics and Polymers using Nanosecond Lasers: Multi-material Micro Manufacture W. Menz and S Dimov Published by Elsevier Ltd, 2007.

[39] Knowles M.R.H., Rutterford G., Karnakis D., Ferguson A., Micro-machining of Metals, Ceramics and Polymers using Nanosecond Lasers, Multi-material Micro Manufacture, 2005.

[40] Jung Mi-Hee, Choi Ho-Suk, Photoresist Etching using Ar/O_2 and He/O_2 Atmospheric Pressure Plasma, Thin Solid Films 2006, 515(2)295–302.

[41] Yi C. H., Jeong C. H., Lee Y. H., Ko Y. W., Yeom G. Y., Oxide Surface Cleaning by an Atmospheric Pressure Plasma, Surf Coat Technol, 2004, 711(17)7–8.

[42] Yi C. H., Lee Y. H., Yeom G. Y., The Study of Atmospheric Pressure Plasma for Surface Cleaning, Surf Coat Technol 2003, 171:237–240.

[43] Morinaga H., Suyama M., Ohmi T., Mechanism of Metallic Particle Growth and MetalInduced Pitting on Si Wafer Surface in Wet Chemical Processing. J ElectrochemSoc, 1994, 141(10):2834–2841.

[44] Morinaga H., Futatsuki T., Ohmi T., Fuchita E., Oda M., Hayashi C., Behaviour of Ultrafine Metallic Particles on Silicon Wafer Surface., J Electrochem Soc, 1995, 142(3):966–970.

[45] Horibe H., Yamamoto M, Kusano E, Ichikawa T, Tagawa S. Resist removal by usingatomic hydrogen. J Photopolym Sci Technol, 2008, 21(2):293.

[46] Yamamoto M, Horibe H, Umemoto H, Takao K, Kusano E, Kase M, et al. Photoresist Removal using atomic hydrogen generated by hot-wire and effects on Si-wafersurface. Jpn J Appl Phys, 2009, 48(2):026503-1-026503-7.

[47] Yamamoto M, Maruoka T, Kono A, Horibe H, Umemoto H. Substrate temperature dependence of the photoresist removal rate using atomic hydrogen generated by a hot-wire tungsten catalyst. Jpn J Appl Phys, 2010, 49:16701–6.

[48] Yamamoto M, Maruoka T, Goto Y, Kono A, Horibe H, Sakamoto M, Removal of ion-implanted photoresists using atomic hydrogen. J Electrochem Soc, 2010, 157(3):H361.

[49] Yamamoto M, Maruoka T, Kono A, Horibe H, Umemoto H., Order of reaction between photoresist and atomic hydrogen generated by a tungsten hot-wire catalyst. Appl Phys Express, 2010, 3(2):026501–0265013.

[50] S. Kuper, J. Brannon, K. Brannon, Appl. Phys., 1993, A56:43.

[51] Brook M. R., Shafeev G. A., Laser-assisted engraving of HgCdTe under a liquid layer, Appl Surf Sci, 1992, 54:336–340.

[52] Simakin A. V., Shafeev G. A., Laser-assisted etching-like damage of SiC. Appl Surf Sci, 1995, 86:422–7.

[53] Dupont A, Caminat P, Bournot P., Enhancement of Material Ablation using 248, 308, 532, 1064 nm Laser Pulse with a Water Film on the Treated Surface, J Appl Phys, 1995, 78(3):2022–2028.

[54] Geiger M, Becker W, Rebhan T, Hutfless J, Lutz N., Increase of efficiency for the XeCl Excimer Laser Ablation of ceramics. Appl Surf Sci, 1996, 3:01–15.

[55] Shafeev G. A., Laser-assisted etching of diamonds in air and in liquid media. Proc SPIE, 1998, 3484:149–57.

[56] Lou Q., Surface Alteration of Polymer by UV Laser Ablation, Proc SPIE. 1998, 3519:219–23.

[57] E. Bongiorno, E. Salinelli, A. Goia, P. Vieu, Contributions in Infinite-Dimensional Statistics and Related Topics, Esculapio, 2014.

[58] G. Aneiros, P. Vieu, Variable selection in infinite-dimensional problems, Statist. Probab. Lett.,2014, 94:12–20.

[59] Jeng-Min Chiou, Ya-Fang Yang, Yu-Ting Chen, Multivariate functional linear regression and prediction, Journal of Multivariate Analysis, 2016, 146:301–312.

[60] Ziqi Zhu, Jiayuan Zhang, Jixin Zou, Chunhua Deng, Multi-kernel Gaussian process latent variable regression model for high-dimensional sequential data modeling, Neurocomputing, 2019, 348:3–15.

[61] Peng, H., Ling X., Predicting thermal hydraulic performances in compact heat exchangers by Support Vector Machine Regression. Int. J. Heat Mass Transfer, 2015, 84, 203—213.

[62] Zaidi S, Novel application of support vector machines to model the two-phase boiling heat transfer coefficient in a vertical tube thermosiphon reboiler. Chem. Eng. Res. Des., 2015, 98, 44—58.

[63] Nusrat P., Sadaf Zaidi, Mohammad D., Support Vector Machine Regression model for predicting the sorption capacity of lead (II), Perspectives in Science, 2016, 8:629—631.

[64] Allen D. M., The Principles and Practice of Photochemical Machining and Photoetching, Adam Hilger/IOP, 1986, a:1.

[65] Harris W. T., Chemical Milling, Oxford University Press, Oxford, 1974, 1.

[66] Allen D. M., The Principles and Practice of Photochemical Machining and Photoetching, Adam Hilger/IOP, 1986, b:1.

[67] Van Deusen E. L., Chemical milling, Scientific American, 1958, 196(1):104-112.

[68] Allen D. M., The Principles and Practice of Photochemical Machining and Photoetching, Adam Hilger/IOP, 1986, 1-2.

[69] Eisler P., The Technology of Printed Circuits, Heywood and Company Ltd., London, 1959, 146-158.

[70] O.D. Black, L.H. Cutter, New method for etching copper, Indust. and Engg. Chemistry, 1958, 50(12):1539-1540.

[71] E.B. Saubestre, Chemical problems in printed wiring, Indust. and Engg. Chemistry, 1959, 51(3):281-287.

[72] E.B. Saubestre, Copper etching in ferric chloride, Indust. and Engg. Chemistry, 1959, 51(3):288- 290.

[73] Andes R.V., Factors affecting occurrence of flaws in etched wiring, Indust. and Engg. Chemistry, 1959, 51(3):291-292.

[74] Sharp L. H., P. D. Garn, Regeneration etchant for copper, Indust. and Engg. Chemistry, 1959, 51(3):293-298.

[75] Friedman H., Photochemical Machining, Metals Handbook, 1988, 16:578-593.

[76] Barkerjian R., Tool and Manufacturing Engineers Handbook, Published by Society of Manufacturing Engineers (SME), 1992, 6(11):41-44.

[77] Allen D. M., Gillbanks P. J., Palmer A. J., The selection of an appropriate method to manufacture thin sheet metal parts based on technical and financial considerations, Proc. 9th Int. Symposium for Electro-Machining, Nagoya, 1989, 246-249.

[78] Rajurkar K. P., Ross R. F., Wei B., Kozak J., R. B. Williams, The role of non-traditional manufacturing processes in future manufacturing industries, The Proceedings of Manufacturing International,1992, 23-27.

[79] Rajurkar K. P., Non-traditional manufacturing processes, Handbook of Design, Manufacturing and Automation, John Wiley and Sons Inc., 1994, 211-241.

[80] Cakir O., Copper Etching with Cupric Chloride and Regeneration of Waste Etchant, Dicle University, Turkey, 2006.

[81] Hibi Y., Yuji E., Kaoru K., Nobuo Shikata, Hisato Ogiso, Excimer Laser Assisted Chemical Machining of SiC Ceramic, Mechanical Engineering Laboratory, Tsukuba-shi, 1994.

[82] MuhlJ., George M. Alder, Direct Printing of Etch Masks Under Computer Control, The University of Edinburgh, 1995.

[83] E. Makino, T. Sato and Y. Yamada, Photoresist for Photochemical Machining of Alumina Ceramic, Hokkaido University, Sapporo, 1987.

[84] Bruzzone A. A. G., Reverberi A. P., An Experimental Evaluation of an Etching Simulation Model for Photochemical Machining, 2010, 24(4)56-61.

[85] Allen D. M., M. Simpkins and H. Almond, A Novel Photochemical Machining Process for Magnesium Aerospace and Biomedical Microengineering Applications, Materials Today: Proceedings, 2010, 6(2):559-562.

[86] Atul R. Saraf, M. Sadaiah, Application of Artificial Intelligence for the Prediction of Undercut in Photochemical Machining, The Proceedings of Manufacturing International, 2013, 54:62-65.

[87] A. Fadaei Tehrani, E. Imanian, A New Etchant for the Chemical Machining of SS304, Journal of Material Processing Technology, 2004, 149:404–408.

[88] Rajkumar Roy, Allen D. M., Oscar Zamora, Cost of Photochemical Machining, The Proceedings of Manufacturing International, 2004, 11:25-28.

[89] Deepak Kumar, Himmatrao Patil, Sadaiah Mudigonda, Investigation on Effect of Grain Orientation in Photochemical Machining of Monel 400, Materials and Manufacturing Processes, 2017, ISSN: 1042-6914.

[90] Agrawal D., Kamble D., GRA and ANN Integrated Approach for Photochemical Machining of Al/SiC Composite, Computation Proceedings, 2016, 8:43-46.

[91] Wangikar S. S., Patowari P. K., Misra R.D., Parametric Optimization for Photochemical Machining of Copper using Overall Evaluation Criteria, Materials Today: Proceedings, 2018, 5:4736–4742.

[92] Agrawal D., Kamble D., Optimization of Photochemical Machining Process Parameters for Manufacturing Microfluidic Channel, Materials and Manufacturing Processes, 2018, 34:658-662.

[93] M.J. Pryor, A.J. Brock, Process and apparatus for etching copper based materials, US Patent No:4725374, 1988.

[94] R. Ueda, Chemical machining with ferric chloride etchant, Corrosion Engineering, 1989, 38(4):271-282.

[95] Zhang., J.,Yonggang M., A study of surface texturing of carbon steel by photochemical machining. Journal of Material Processing Technology, 2012, 212:2133–2140.

[96] Bhasme, A. B., Kadam M. S., Parameter optimization by using grey relational analysis of photochemical machining. International Journal of Mechanical Engineering and Technology 2016, 3(3):992–997.

[97] D.M. Allen, O. Cakir, H.A.J. White, The photochemical machining of brass with cupric chloride etchant and a technique for the partial recovery of dissolved zinc, Proc. of the Symp. High Rate Metal Dissolution Processes, The Electrochemical Society Inc. Pub., 1995, 95(19)305-315.

[98] D.M. Allen, O. Cakir, Comparison of $FeCl_3$ and $CuCl_2$ etchants in the photochemical machining of brass, Proc. of ESDA, 6th Biennial Conf. On Engg. Systems Design and Analysis, Turkey, 2002.

[99] Visser, Beer A., Bestimmung der absorption des rothen Lichts in farbigenflüssigkeiten (determination of the absorption of red light in coloured liquids) Annalen der Physik und Chemie, 1852, 86: 78–88.

[100] James Jacob M., Shanmugavelu P., Balasubramaniam R., Ramesh K Singh, Study of excimer laser ablation of photo resist polymer in presence of hydrogen gas environment for micro-fluidic applications, IOP Publishing, Material Research Express, 2019, 6:085316.

[101] Lide David R, CRC Handbook of Chemistry and Physics. 88th edition by CRC Press, 2007, 9780849304880 - CAT# 488.

[102] Spitzyn B. V., Bouilov L. L., Derjaguin B. V., J.Cryst, Growth 1981, 52:219.

[103] Dementiev A. P., Petukhou M. N., Diamond Relat Mater, 1997, 6:486.

[104] Bäuerle D., Chapter 2 thermal, photophysical, and photochemical processes, Laser processing and chemistry. 4th ed. Berlin Heidelberg: Springer-Verlag; 2011, 13–38, https://doi.org/10.1007/978-3-642-17613-5_2.

[105] Beer, Bestimmung der Absorption des rothen Lichts in farbigen Flüssigkeiten (Determination of the absorption of red light in coloured liquids), Annalen der Physik und Chemie, 1852, 86:78–88.

[106] Takeshi Maruoka, Masashi Yamamoto , Yousuke Goto Seiji Takahashi, High removal rate of cross-linked SU-8 resist using hydrogen radicals generated by tungsten hot-wire catalyzer Thin Solid Films, 2014, 562:632–637.

[107] James Jacob, P. Shanmugavelu, R. Balasubramaniam, Investigation of the Performance of248 nm Excimer Laser Assisted Photoresist Removal Process in Gaseous Media by Response Surface Methodology and Artificial Neural Network, Journal of Manufacturing Processes, 2019, 516–529.

[108] Morinaga H., Suyama M., Ohmi T., Mechanism of metallic particle growth and metal induced pitting on Si wafer surface in wet chemical processing, J Electrochem Soc 1994, 141(10):2834–41.

[109] Tom Mitchell, Machine Learning, McGraw-Hill Computer science series, 1997

[110] Horibe H, Yamamoto M, Kusano E, Ichikawa T, Tagawa S., Resist removal by using Atomic Hydrogen, J Photopolym Sci Technol, 2008,21(2):293

[111] Garrison B. J., Srinivasan R., Laser ablation of organic polymers: microscopic models for photochemical and thermal processes, J Appl Phys 1985, 57:2909–14.

[112] David J.C., Mackay, Introduction to Gaussian Process, Cambridge University, UK.

[113] Tutorial slides by Andrew Moore, http://www.cs.cmu.edu/~awm

[114] V. Vapnik. The Nature of Statistical Learning Theory, Springer, N.Y., 1995. ISBN

[115] Burges C., A tutorial on support vector machines for pattern recognition, In Data Mining and Knowledge Discovery, Kluwer Academic Publishers, 1998, (2).

[116] V. Vapnik, S. Golowich, A. Smola, Support vector method for function approximation, regression estimation and signal processing. In M. Mozer, M. Jordan, and T. Petsche, editors, Advances in Neural Information Processing Systems,1997, 9:281– 287.

[117] Nello Cristianini, John Shawe-Taylor, An Introduction to Support Vector Machines and Other Kernel-based Learning Methods, Cambridge University Press, 2000.

[118] N. Heckman, The Theory and Application of penalized least squares methods or reproducing kernel hilbert spaces made easy, 1997.

[119] Vapnik V., Estimation of Dependencies Based on Empirical Data. Empirical Inference Science: Afterword of 2006, Springer.

[120] Olivier Bousquet, Stephane Boucheron, Gabor Lugosi, Introduction to Statistical Learning Theory.

[121] Anandhi V., Chezian R.M., Support Vector Machine Regression to Forecast the Demand and Supply of Pulpwood. Journal of Future Computer and Communication, 2013, 2:58-65

[122] Mark A. Smrtic, S. V. Babu, Benedict G. F., Manufacturing Metal Parts by the Photochemical Machining Process, in Non-traditional Machining, Proceedings of 1985 Conference, American Society of Metals, 1986, 141-144.

[123] Wang W. Di. Z., Allen D. M., Almond H. J. A., Non-traditional machining techniques for fabricating metal aerospace filters, Chinese Journal of Aeronautics, 2008, 21:441–447.